An Experimental Investigation of Flow Control for Supersonic Inlets

A thesis submitted for the degree of
Doctor of Philosophy

by Neil Titchener
Peterhouse
Work Conducted at the University of Cambridge
01/10/2009–30/05/2013

Described in this dissertation is work conducted in the Aeronautics Laboratory of the Department of Engineering, University of Cambridge. This dissertation is the result of my own work and includes nothing which is the outcome of work done in collaboration except where specifically indicated in the text. This dissertation contains fewer than 150 figures and 65,000 words.

Neil Titchener
8th February 2013

Acknowledgements

The author would like to thank the following people for their invaluable advise, guidance and criticism throughout this project: Professor Holger Babinsky, Professor Eric Loth, Dr. Paul Bruce, Rane Nolan, Simon Colliss, Dan Baruzzini, and Anthony Haynes.

The author would also like to thank the financial support of the Air Force Office of Scientific Research, Air Force Material Command, United States Air Force, under grant numbers FA8655-08-1-3091 and FA8655-11-1-3002. And in addition to this funding, the technical advice offered by Jon Tinapple and Lew Surber.

Abstract

This thesis focuses on the control of shock wave / boundary layer interactions (SWBLIs) in supersonic inlets. The overall aim of this study is to determine to what extent vortex generators (VGs) can mitigate flow separations within supersonic inlets. To achieve this, an experimental investigation was undertaken in a small-scale wind tunnel, because small-scale wind tunnels are much more amenable to numerous measurement techniques than real inlets.

A new geometry was designed and developed as part of this study to make the configuration more representative of typical inlet conditions than previous studies. The flow-field that was determined to be relevant, yet still simple, comprised of a Mach 1.4 normal shock followed by a region of subsonic diffusion created by a 6^o straight-angled diffuser. A shock holder was used to improve shock stability and the Reynolds number was set to 25 x 10^6 per metre throughout.

This flow was examined in three different shock positions. The flow was found to be highly sensitive to the relative position of the shock and diffuser: when the shock was positioned somewhat upstream of the diffuser the flow was relatively benign and, apart from small corner separations, the majority of the boundary layers remained attached; but as the shock was moved close to the diffuser, separation was introduced on the channel floor; and once inside the diffuser the entire diffuser boundary layer was separated.

In the first instance, VGs were employed on the channel floor. While the VGs were able to produce a thin attached region on the channel floor and therefore improve the centre-span region somewhat, they were detrimental to the corner separations. As a result, corner suction was employed to reduce the prominence of the corner flows. Corner suction dramatically reduced the corner separations, however, flow separation still dominated the diffuser because separation was now introduced at centre-span.

These results demonstrate that a strong coupling between the centre-span and corner flow regions exists in this configuration. When flow control was applied to one region, although the flow is improved locally, increased losses in other regions tended to offset this gain. This is because an overall improvement in the pressure within the diffuser can only be maintained if all areas can sustain the pressure-rise. As a result, only when all the problem regions were appropriately controlled—the corners using suction and the centre-span using VGs—could a notable improvement in the flow be obtained. In this combined configuration, more than 50% of the diffuser-span remained attached throughout the diffuser and there was a 15% drop in stagnation pressure losses and 6% increase in the wall-pressure recovery.

Although further VG studies are required, this investigation does suggest that VGs do have the potential to alleviate the current dependency on boundary-layer bleed for flow control in supersonic inlets.

Contents

Nomenclature

Roman Symbols

A	flow area
AR	aspect ratio
$B = 5.0$	logarithmic-law constant
$c = 3 \times 10^8$ ms^{-1}	speed of light
C	confinement ratio
C_d	discharge coefficient
$c_\mathrm{f} = \dfrac{\tau_\mathrm{w}}{\frac{1}{2}\rho_\mathrm{w} u_\mathrm{e}^2}$	local skin-friction coefficient
$C_\mathrm{p} = \dfrac{p - p_\infty}{\frac{1}{2}\rho_\infty u_\infty^2}$	pressure coefficient
$c_\mathrm{p} \simeq 1005$ JK^{-1}	Specific heat capacity of air at constant pressure
$D = \dfrac{p_{0\mathrm{max}} - p_{0\mathrm{min}}}{\bar{p}_0}$	simple distortion index
D_f	diameter at the engine-face
D_vg	spanwise distance between vortex generator pairs
d_vg	spanwise distance between a vortex generator pair
$DC(\theta) = \dfrac{p_{0\mathrm{f,av}} - p_{0\mathrm{f}\theta\mathrm{,av}}}{q_\mathrm{f}}$	typical UK distortion index
f_i	frequency of incident light
f_s	frequency of scattered light
$H = \dfrac{\delta^*}{\theta}$	incompressible boundary-layer shape factor
h_cl	cowl height
h_r	ramp height at inlet entrance
h_vg	vortex generator height
I	luminescent light intensity

I_{atm}	luminescent light intensity at atmospheric pressure
I_{un}	luminescent light intensity in the absence of oxygen (unquenched)
k	thermal conductivity
k_{sv}	Stern-Volmer constant
$K_{A2} = K_\theta + b.K_{rad}$	more complex distortion index predominantly used in the USA
L	inlet compression surface length
l	length (streamwise)
L_{diff}	inlet diffuser length
M	Mach number
p	pressure
$p_{0\text{f,av}} = \int_{A_\text{f}} \frac{p_{0\text{f}}}{A_\infty}\, dA_\text{f}$	area-averaged pressure
$p_{0\text{f,mav}} = \int_{A_\text{f}} \frac{\rho_\text{f} U_\text{f} p_{0\text{f}}}{\rho_\infty U_\infty A_\infty}\, dA_\text{f}$	mass-averaged pressure
$p_{0\text{probe}}$	probe Pitot pressure
$p_{0\text{rake}}$	stagnation pressure at the rake
$Pr = \frac{c_\text{p}\mu}{k}$	Prandtl number
$q = \frac{1}{2}\rho u^2$	dynamic pressure
$R \simeq 287$ J kg^{-1} K^{-1}	specific gas constant for air
r_{cl}	cowl radius
r_r	centre-body radius at inlet entrance
$Re = \frac{\rho u}{\mu}$	Reynolds number (per metre)
T	temperature
u	streamwise velocity
$u^{*+} = \frac{u^*}{u_\tau}$	non-dimensional velocity based on inner variables
$u^* = \frac{u_\text{e}}{A}\sin^{-1}\left(\frac{Au}{u_\text{e}}\right)$	van Driest effective velocity assuming adiabatic walls
$u_\tau = \sqrt{\frac{\tau_\text{w}}{\rho_\text{w}}}$	wall shear velocity
v	wall-normal velocity

w	spanwise velocity
w_{slot}	slot width (spanwise)
w_{tunnel}	wind tunnel width
x	streamwise coordinate
y	wall-normal coordinate
$y^+ = yu_\tau/\nu_{\text{w}}$	non-dimensional distance from the wall based on inner variables
z	spanwise coordinate

Greek Symbols

α_{d}	angle between incident beams of LDV system
α_{i}	compression ramp angle at the inlet entrance
α_{slot}	corner suction slot angle
α_{vg}	vortex generator angle of attack
β	LDV emitting head angle
δ	boundary-layer thickness based on 99% u_e
$\delta^* = \int_0^\infty \left(1 - \frac{u}{u_{\text{e}}}\right) dy$	incompressible boundary-layer displacement thickness
δ_{sc}	boundary-layer thickness based on the curve-fitting method of Sun and Childs (1973)
ϵ	lowest measurement point within the boundary layer
$\eta = y/\delta$	non-dimensional position within the boundary layer
$\eta_{\text{f}} = \frac{p_{0\text{f,av}}}{p_{0\infty}}$	area-averaged pressure recovery
$\gamma = c_{\text{p}}/c_{\text{v}} = 1.4$	ratio of specific heat capacities for air
$\kappa = 0.41$	von Karman/logarithmic-law constant
λ	wavelength
μ	dynamic viscosity
μ_{oil}	dynamic viscosity of oil for oil-flow visualization
$\nu = \mu/\rho$	kinematic viscosity
ϕ	Pitot probe diameter
ψ	compression surface ramp angle

τ_w	shear stress at the wall
$\theta = \int_0^\infty \frac{u}{u_e}\left(1 - \frac{u}{u_e}\right) dy$	incompressible boundary-layer momentum thickness

Subscripts

0	stagnation conditions
∞	far upstream
atm	atmospheric
av	area-averaged
aw	adiabatic wall conditions
cl	cowl
d	Doppler
diff	subsonic diffuser
e	boundary-layer edge
f	engine face location
fs	freestream
gauge	relative to atmospheric conditions
i	inlet entrance station
mav	mass-averaged
n	nozzle exit station
o	start of interaction
orifice	orifice plate
p	sideplate
r	ramp
s	location downstream of shock wave(s)
sc	based on Sun and Childs (1973)
sep	location of separation
slot	corner suction slot
sw	location of shock wave
t	inlet throat station

vg	vortex generator
w	wall

Other Symbols

$\bar{\dot{m}} = \frac{\dot{m}\sqrt{c_p T_0}}{A p_0}$	non-dimensional mass flow function
$\Delta x_{\text{throat}} = x - x_{\text{throat}}$	distance downstream of the nozzle throat
$\Delta x_{\text{vg}} = x_{\text{sep}} - x_{\text{vg}}$	distance between point of flow separation and vortex generator trailing edge
$\frac{A_i}{A_\infty}$	mass flow ratio
$\frac{p_{0\text{f,av}}}{p_{0\infty}}$	area-averaged pressure recovery
$\frac{p_{0\text{f,mav}}}{p_{0\infty}}$	mass-averaged pressure recovery
$\dot{m}$	mass flow

Abbreviations

AGARD	Advisory Group for Aeronautical Research and Development (Paris, France)
AIP	Aerodynamic Interface Plane
CFD	Computational Fluid Dynamics
IWM	Imperial War Museum, UK
LDV	Laser Doppler Velocimetry
NASA	National Aeronautics and Space Administration (Washington DC, USA)
NPL	National Physics Laboratory (Teddington, UK)
ONERA	Office National d'Études et de Recherches Aérospatiales (Paris, France)
RAE	Royal Aircraft Establishment (formely Farnborough, UK)
RAF	Royal Air Force, UK
SAE	Society of Automotive Engineers (Warrendale, PA, USA)
SWBLI	Shock wave / boundary layer interaction
UK	United Kingdom
USA	United States of America

VG	Vortex Generator
VKI	von Karman Institute for Fluid Dynamics (Rhode-St-Genese, Belgium)

Chapter 1

Introduction

As we endeavour to design more advanced and more efficient air vehicles, one area that continues to pose much difficulty in aeronautical engineering is the vehicle's propulsion system. This problem is particularly acute at supersonic speeds and above. In supersonic designs significantly more attention must be paid to what is known as the inlet or intake as this integral part of the propulsion system must efficiently supply the engine with its required mass flow across the entire flight envelope of the aircraft.

The role of the inlet is more complex at supersonic speeds due to the phenomenon known as shock wave / boundary layer interaction (SWBLI). In most air vehicle designs, the air-flow required by the engine must be decelerated before the engine, and above Mach 1 this is almost always achieved via a system of shock waves. Unfortunately, these shock waves often interact with the boundary layers inside the inlet. This interaction results in boundary-layer thickening and in some instances separation—both of which lead to distortion and increased losses within the inlet duct. This degrades inlet performance which adversely affects payload and range, and hence the economic and environmental costs.

Some form of boundary-layer control is often employed to alleviate the detrimental effects of SWBLIs. The most common form of control is what is known as boundary-layer bleed or suction, which involves removing some of the near-wall flow from the inlet. Although extremely effective, there has long been interest in alternatives for the purpose of separation mitigation as a boundary-layer bleed system tends to be complex, heavy, and has drag associated with its use.

Over the years, a wide variety of alternative techniques have been suggested and in a number of instances trialled. One such control method that is thought to have significant promise employs vortex generators (VGs). These devices have the advantage of being passive (i.e., they do not consume any power and hence have no associated auxiliary equipment) and are highly economical once installed. Yet, the development and evaluation of new flow control techniques is expensive. Consequently, with increasing pressure on defence budgets, there is a need to develop more cost effective development methods. In this investigation, one such cost effective experimental setup is presented, and extensive experiments undertaken using the small-scale supersonic wind tunnel in the Cambridge University Aeronautics Laboratory to help us move forward in the evaluation of VGs for the control of SWBLIs are detailed.

In order to conduct this investigation effectively, the current state of understanding in this area of applied aerodynamics is first reviewed.

Chapter 2

Inlet Design–A Brief Introduction

2.1 Introduction

In order to conduct an effective experimental research program on inlet flow control, an appreciation of inlet design and the relevant flow physics is required. Accordingly, this chapter and the two following chapters are dedicated to topics relevant to supersonic inlet design. An overview of inlet design is given in this chapter. Firstly, inlet performance is discussed with emphasis on internal performance and how it is measured. In chapter 3 SWBLIs are discussed in detail to illustrate why this phenomenon is so crucial in determining internal inlet performance in supersonic inlets. Lastly, chapter 4 concentrates on inlet flow control, how it has developed over time, and why there is still interest in continuing the development of flow control techniques.

2.2 The role of the inlet

The role of the engine inlet (American English) or engine intake (British English) in air-breathing-propulsion-systems is to provide the engine with the appropriate supply of air-flow across the operating range of the aircraft, with the least possible loss in total pressure or head, the best attainable flow distribution, and the least amount of aircraft drag. This is a nice and concise definition that probably has its origins in a paper produced at GE (1952). This definition is still valid today, although, in addition, one may wish to also include the desire for a lightweight, compact and economical design.

A very simplified schematic of a Pitot inlet is shown in figure 2.1 to illustrate the salient features of a supersonic inlet. The important features of the inlet are indicated in this figure:

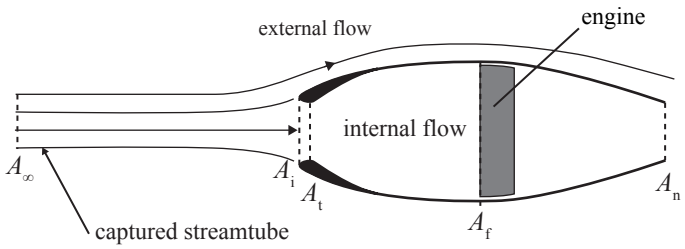

Figure 2.1: Aerodynamic duct showing main propulsion system features

the inlet entrance which is also the location of the cowl lip, i; the inlet throat, t; the location of the engine, f; and the nozzle exit, n. In the case of turbine-based systems, which are the only propulsion systems discussed here, the flow must be decelerated from the supersonic freestream Mach number, M_∞, to a subsonic Mach number at the engine face, M_f. The engine face Mach number must usually be in the range 0.5–0.8. The location of the throat and the area variation between A_i and A_e very much depend on the type of inlet employed and these details are discussed in depth in section 2.5.

The job of the inlet designer is to devise the best internal and external profile between stations i and f to accomplish the task laid-out in the first sentence of this section within the design constraints of the aircraft. The inlet must be contoured on the inside such that the flow is decelerated uniformly and with low entropy creation while being compact and hence lightweight. At the same time, the inlet's external shape should be contoured such that the external drag is kept low by retaining the aerodynamic profiling of the airframe. However, this project is primary concerned with inlet internal performance, and the following discussion is therefore confined to this topic.

2.3 Internal inlet performance

2.3.1 Pressure recovery

An inlet's internal efficiency is usually quantified by a parameter known as the pressure recovery. In high-speed flows this is most simply defined as the ratio of average stagnation pressure at the engine face to freestream stagnation pressure. This ratio is either calculated on a mass-averaged or an area-averaged basis (see equations 2.1 and 2.2 respectively). Usually the area averaged value is preferred (mainly due to the ease with which it can be calculated), and hence this definition is used throughout the remainder of this report. A low value of pressure recovery is probably the first indication that flow control may be required.

$$\frac{p_{0\mathrm{f,mav}}}{p_{0\infty}} = \int_{A_\mathrm{f}} \frac{\rho_\mathrm{f} U_\mathrm{f} p_{0\mathrm{f}}}{\rho_\infty U_\infty A_\infty p_{0\infty}}\, dA_\mathrm{f} \tag{2.1}$$

$$\eta_\mathrm{f} = \frac{p_{0\mathrm{f,av}}}{p_{0\infty}} = \int_{A_\mathrm{f}} \frac{p_{0\mathrm{f}}}{A_\infty p_{0\infty}}\, dA_\mathrm{f} \tag{2.2}$$

To determine inlet performance during testing, pressure recovery is calculated using an array of Pitot probes mounted just upstream of the engine-face location, which is also often referred to as the Aerodynamic Interface Plane (AIP). Pressure recovery is often calculated using a standardized 40-hole Pitot rake. A rake of this type is shown in figure 2.2 where (a) shows such a rake installed in NASA's F-18 test aircraft, (b) is a schematic showing the location of pressure transducers, and (c) is a resulting contour map of pressure recovery. To standardize the approach in determining η_f there is a generally accepted probe configuration which is formally described in the SAE standard ARP 1420 (see SAE (2002)). By utilizing the same engine-face instrumentation, it is hoped that more direct comparisons can be made between a variety of configurations and facilities.

The sources of loss that result in a reduction of inlet pressure recovery can in broad-terms be split into three categories:

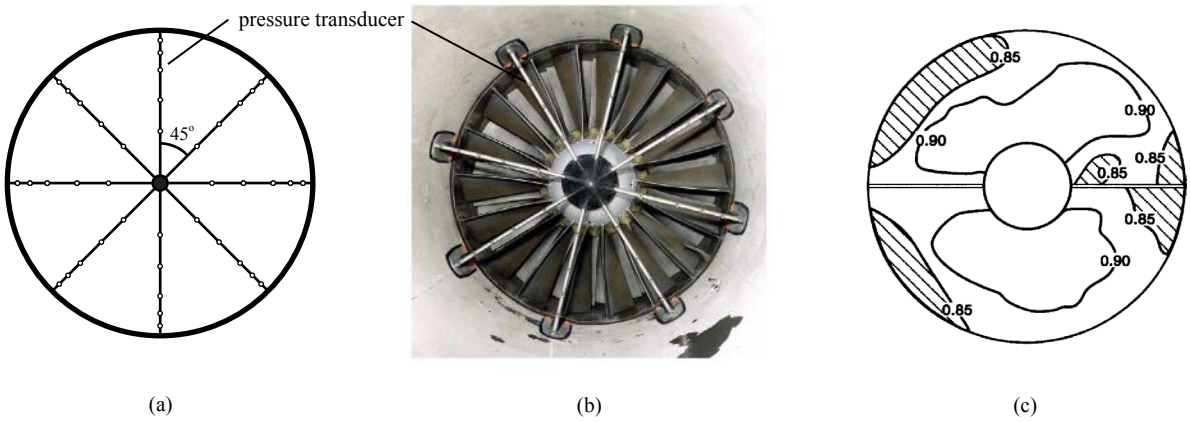

Figure 2.2: The SAE standard, ARP 1420, 40-hole Pitot rake: (a) schematic; (b) rake installed in the NASA F-18 High Alpha Research Vehicle (HARV)[1]; (c) pressure contours ($p_{0f}/p_{0\infty}$) from Wasserbauer et al. (1996)

- frictional losses,
- losses caused by turbulence generation, and
- shock losses.

These three types of loss are illustrated in the inlet shown in figure 2.3: There is the frictional loss due to the thin attached boundary layer associated with on the internal surface of the cowl; the turbulent loss due to the presence of a separation bubble on the floor; and the shock-loss due to the shock which is required to decelerate the flow from a supersonic to subsonic velocities.

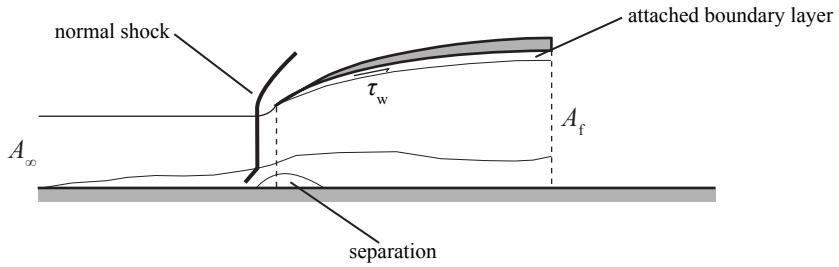

Figure 2.3: Sources of loss in an inlet

These three factors are highly interlinked. Importantly, not only is there a shock loss due to the presence of the shock-wave, but the shock-wave also introduces a significant adverse-pressure-gradient. Unfortunately, these regions of high adverse-pressure-gradient have a detrimental impact on the inlet boundary layers, and strongly increase the risk of flow separation (a topic known as shock-wave/boundary layer interactions or SWBLI). Hence, the addition of shock-waves will impact strongly on the other two factors and, accordingly, on the entire performance of the inlet. These discontinuities in pressure, velocity, temperature and density, are therefore a

[1]Source: NASA Image EC94-42514-11 (currently available at http://www.nasa.gov/centers/dryden/multimedia/imagegallery/F-18HARV/EC94-42514-11.html)

prominent feature of all supersonic inlets and their designs are therefore heavily based around the particular shock system that they produce.

2.3.2 Flow distortion

In addition to the pressure recovery, the distribution of pressure at the engine-face is important. The pressure contour map shown in figure 2.2 illustrates some spatial variation and this is often referred to as spatial distortion. Large differences in pressure (whether spatial differences or temporal differences) are undesirable because they degrade engine performance and in severe cases can lead to engine surge.

In the early days of inlet design pressure recovery was generally considered the most important parameter in inlet flow, however, the development of axial compressors with higher tip speeds and blade loadings and the requirement for more extreme vehicle operating envelopes has led to an increased importance in distortion. Now, in many instances, distortion is just as important as pressure recovery. Therefore, even if an inlet has high pressure recovery, it may be desirable to use flow control to help evenly distribute the losses.

It is necessary to introduce a distortion descriptor which can describe both the quality of the inlet flow and the tolerance of the engine. Yet, in contrast to pressure recovery, there is no general consensus as to what this should be, and this is in large part due to difficultly in quantifying distortion. In general, engine manufacturers use their own distortion variables, and a detailed account of these is not given here (many are proprietary, in any case). Nevertheless, three simple descriptors are shown for reference.

$$D = \frac{p_{0\max} - p_{0\min}}{p_{0\mathrm{f,av}}} \tag{2.3}$$

$$DC(\theta) = \frac{p_{0\mathrm{f,av}} - p_{0\mathrm{f}\theta,\mathrm{av}}}{q_{\mathrm{f}}} \tag{2.4}$$

$$K_{A2} = K_{\theta} + b.K_{rad} \tag{2.5}$$

For each of these distortion descriptors the data is obtained from an AIP rake like that shown in figure 2.2. The first descriptor, equation 2.3, is a very simple descriptor which calculates distortion, D, as the maximum difference in stagnation pressure obtained using the 40-hole AIP rake as a proportion of the average stagnation pressure (i.e. the pressure recovery). Thus D quantifies the maximum variability across the engine-face. In the UK, a more complex descriptor is that given by equation 2.4, where $p_{0\mathrm{f}\theta\mathrm{av}}$ is the mean stagnation pressure in the worst sector of the AIP flow of angle θ. 60^o and 90^o are typical values of θ; thus a commonly used parameter is DC(60) or DC(90). The third example, equation 2.5, is a more complex descriptor which was developed in the USA. This descriptor differentiates circumferential and radial distortion using a weighting factor between the two, b, which is a function of the engine type.

For a long while distortion was quantified on the basis of steady-state pressures, yet, this method tends to miss peak distortion levels which last for only a few milliseconds. As high distortion, lasting only one blade revolution (a few milliseconds), is often enough to cause engine surge, high-frequency pressure transducers should be used alongside their steady-state counterparts to time-resolve the distortion descriptors shown above.

For more details on distortion, especially the influence of unsteadiness, the reader should refer to the details of the flight testing trouble encountered with the F-111 described in Seddon and Goldsmith (1999) and Burcham Jr. and Bellman (1971).

2.3.3 Mass flow

At the same time as supplying the engine with as high a pressure recovery and as low distortion air as possible, the inlet must provide the correct mass flow of air across the operating range of the vehicle. The mass flow entering the inlet is that contained within the captured streamtube, A_∞. Hence, the operating characteristics of an inlet as a function of mass flow can be obtained by plotting η_f and D versus A_i/A_∞ for a given M.

An example of such an operating characteristic is shown in figure 2.4 for a simple Pitot inlet operating supersonically at some M_∞. The inlet is shown operating at three different points: (a) subcritically, where the inlet requires a mass flow less than that given by A_i and flow must spill behind the terminal shock-wave; (b) critically with no spillage, $A_\infty = A_\mathrm{i}$; and (c) supercritically, where the inlet desires more mass flow but this cannot be achieved and so the shock-wave is instead pulled inside the inlet.

It can be seen that over quite a wide range, i.e., from A to B the inlet has good performance in terms of both pressure recovery and distortion. Whereas the performance drops off very quickly as the shock-wave is pulled inside the inlet.

When flow control is employed, it is clearly desirable to improve performance across the entire range, i.e., from A to C. However, as subcritical operation is much more common than supercritical operation more emphasis is usually placed on A to B. In subcritical operation the inlet can encounter an unsteady phenomenon known as "inlet buzz" where high shock oscillations are obtained, and flow control is often utilized to try and suppress this shock unsteadiness. These conditions are discussed in more detail later.

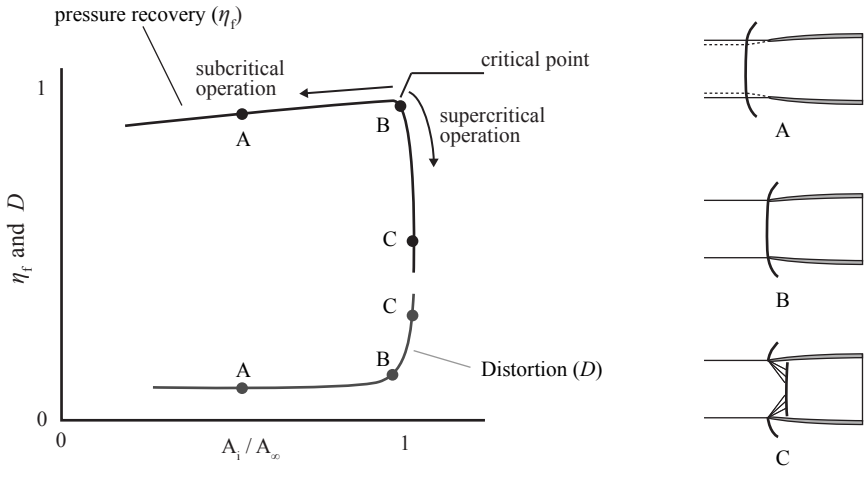

Figure 2.4: Inlet operating modes

2.4 Inlet external performance

As even a short description of inlet drag would fill numerous pages, it is felt that a discussion of inlet drag would not be appropriate as inlet drag in itself is not of major importance to this current project. For a detailed discussion on inlet drag see Seddon and Goldsmith (1999).

Nevertheless, it should be noted here that the two main components of drag are spillage drag and cowl wave drag. These drag components are mentioned in the following sections as they have a strong bearing on the choice of inlet configuration. However, for a full appreciation of these, the reader should refer to the literature mentioned above.

2.5 Types of inlet

2.5.1 Introduction

Inlets for supersonic air-breathing-propulsion-systems can generally be split into four groups: Pitot inlets; external compression inlets; internal compression inlets; and mixed compression inlets. These are shown respectively in figure 2.5. In this section these inlets are discussed in order of increasing complexity; from the simple Pitot inlet (figure 2.5a) to the highly complex mixed compression inlet system (figure 2.5d), and examples of each are described. In each case, turbine-based configurations are discussed although much of what follows is also relevant to ramjet and scramjet configurations.

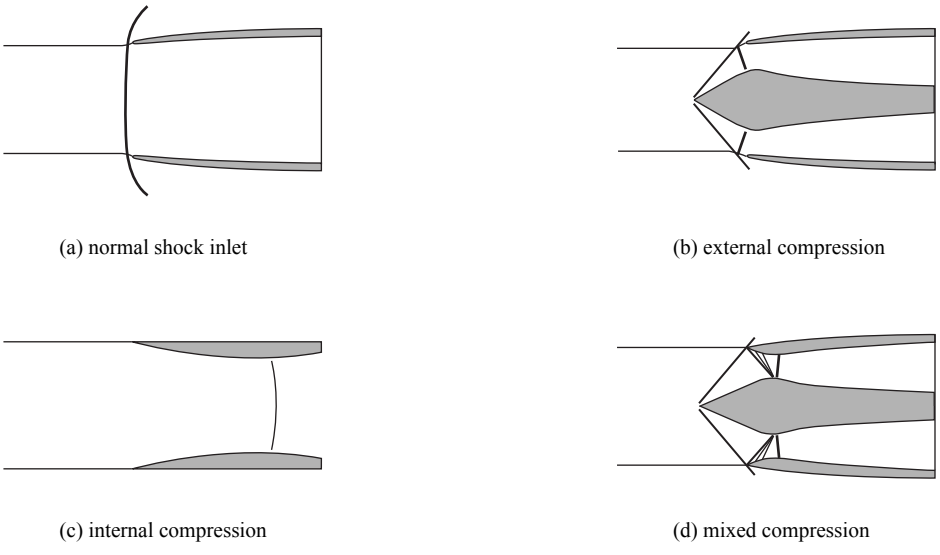

Figure 2.5: Different inlet types

2.5.2 Pitot inlets

The simplest supersonic inlet design arises from the use of a single shock-wave to decelerate the flow. This type of inlet is often referred to as a Pitot inlet (in honour of the aerodynamicist Henri Pitot). This design is not dissimilar to a typical subsonic inlet configuration; the only difference being the addition of a terminal shock upstream of the inlet entrance. An example of

such an inlet configuration is shown in figure 2.6, which presents both a schematic drawing and a picture of the Pitot inlet of the Lockheed Martin F-16 Fighting Falcon (see Hawkins (1976) for a good description of this particular inlet configuration).

The main advantage of a Pitot inlet is its innate simplicity. In addition, if the Pitot inlet is nose mounted then the only shock-wave will not interact with any boundary layers. More common, however, is a Pitot inlet similar to that shown in figure 2.6. In this instance, the terminal shock interacts with a boundary layer from a splitter plate (which divides the boundary-layer diverter and the inlet). Even though there is now a SWBLI, the boundary layer on the splitter plate is usually thin and hence there is little viscous loss associated with this SWBLI (see chapter 3). Accordingly, there is not often a need to employ flow control in Pitot inlets and this is another significant advantage.

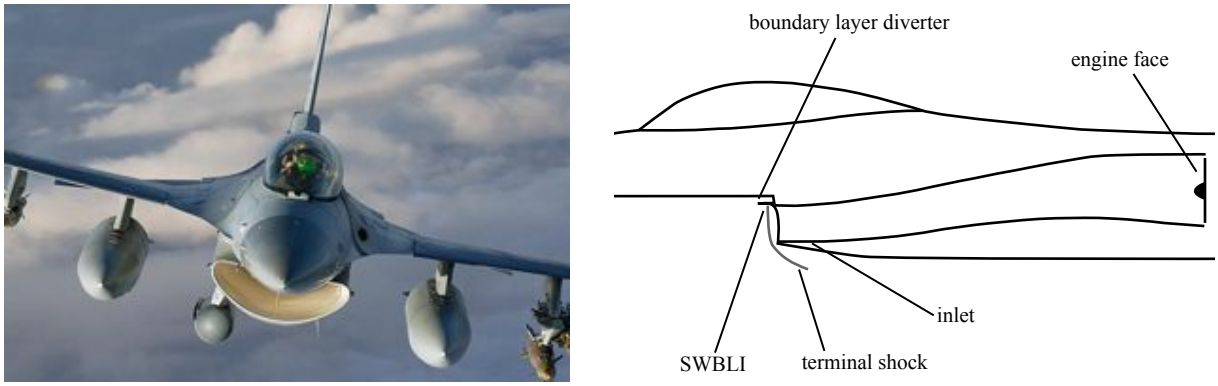

Figure 2.6: Lockheed Martin F-16 (a) front view showing inlet[2] and (b) inlet schematic adapted from McCallum (1989)

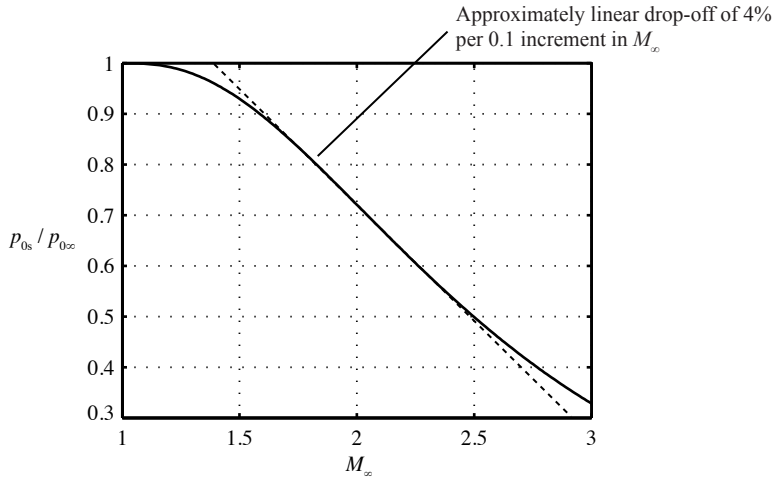

Figure 2.7: Post-normal shock pressure recovery as a function of M_∞

Despite these advantages, the main downside of such a design is that at relatively low Mach

[2]Source: Lockheed official photo (currently available at http://www.lockheedmartin.co.uk/us/products/f16.html)

numbers the pressure recovery starts to drop-off substantially due to the shock loss of the terminal shock. This trend is illustrated in figure 2.7, in which post-normal shock stagnation pressure losses are plotted versus freestream Mach number. Performance up until Mach 1.4 is good (at Mach 1.4 $p_{0s}/p_{0\infty} = 0.96$), however, after this point the curve exhibits a steep drop-off and by Mach 2 the performance is probably unacceptable for most applications.

2.5.3 The need for multi-shock inlet designs

The way to reduce the large stagnation pressure losses associated with the Pitot inlet at high M_∞ is to introduce multiple shock waves into the inlet system (such as the inlets shown in figures 2.5b–d). The advantage of this approach is well illustrated in figure 2.8, which shows the variation of obtainable pressure recovery using a two and three shock system respectively. These results are based on simple planar shock theory (see Equations, tables and charts for compressible flow by Ames Research Staff). It can be seen that big improvements in pressure recovery are achievable using simple compression ramps upstream of the inlet cowl. For example, at Mach 2.5, with a Pitot inlet ($\delta = 0$) the recovery is 50%, with a single compression ramp this can be increased to 75%, and with two ramps this can be increased to 87%. The advantage of this multi-shock approach was first noted by Oswatitsch (1944).

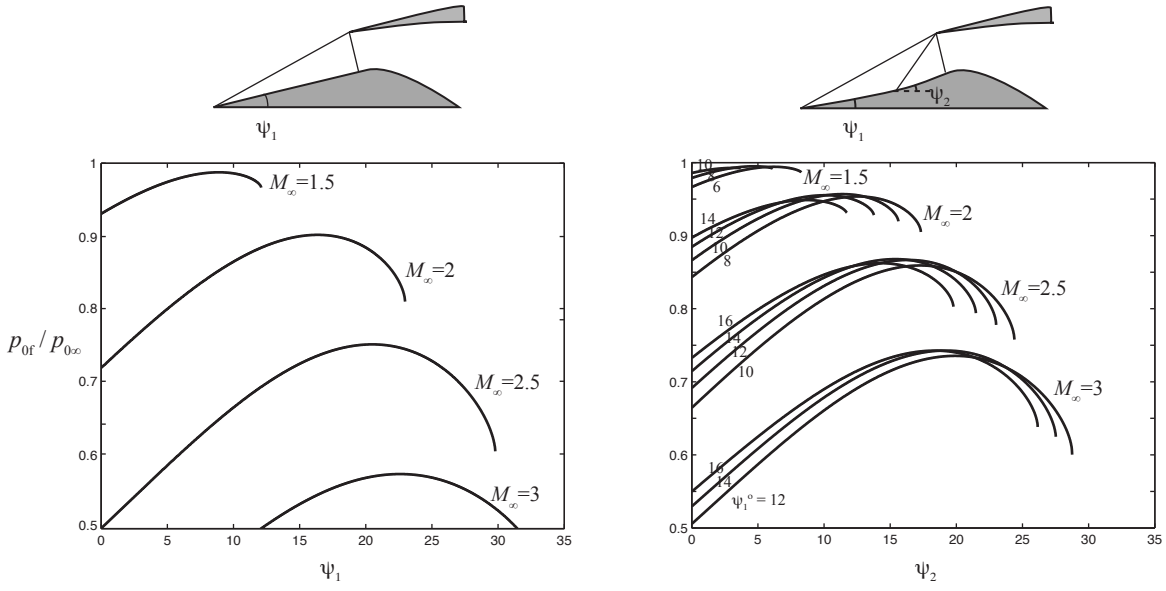

(a) two shock inlet

(b) three shock inlet

Figure 2.8: Variation of pressure recovery with M_∞ and δ for a planar 2 shock and 3 shock inlet

2.5.4 External compression inlet

The simplest multi-stage compression design is the external compression inlet (figure 2.5b). To reduce the strength of the terminal shock, a compression surface is employed ahead of the inlet entrance. In a axisymmetric configuration this surface is referred to as a centerbody and in a planar configuration as a compression ramp or wedge. This type of inlet is referred to as an external compression inlet as all the supersonic compression takes place upstream of the inlet entrance (the inlets shown in figure 2.8 are examples of simple external compression inlets). The

advantages of this type of inlet were noticed quite early on in the development of supersonic jet aircraft and early designs utilizing this configuration include the Lockheed F-104 and the English Electric Lightning. A more complex external compression design, that employed on the Boeing F-15, is illustrated in figure 2.9 (for more details see Sams (1975) and Imfeld (1976)).

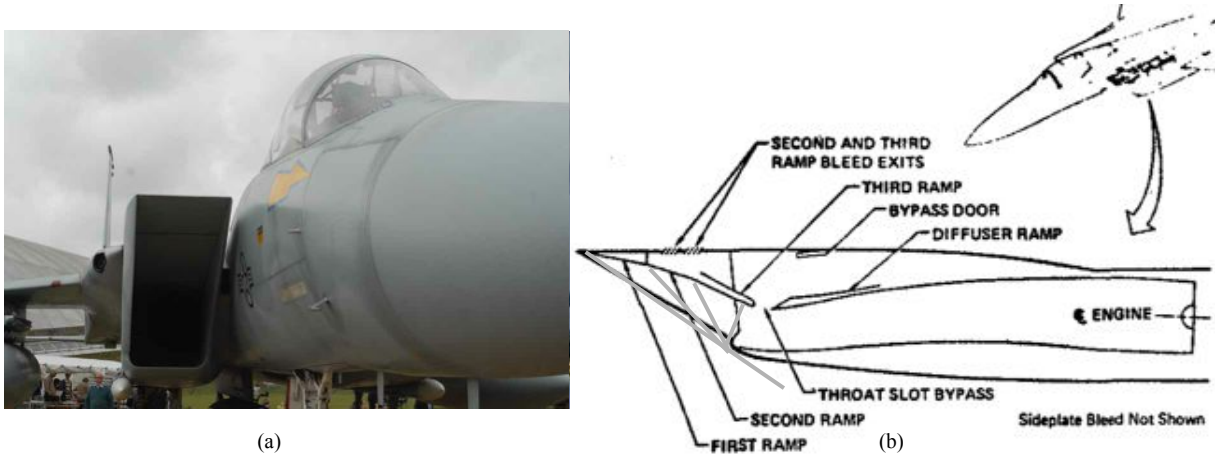

(a) (b)

Figure 2.9: Boeing F15 (a) front view of inlet[3] and (b) inlet schematic adapted from Sams (1975)

Unfortunately, alongside the improvements in pressure recovery resulting from external compression, this strategy results in more prominent SWBLIs. Whereas, with the Pitot inlet, SWBLIs can either be avoided all together (figure 2.5a) or kept to a minimal level as in the case with the F-16 (figure 2.6), with the external compression inlet the terminal shock inevitably terminates on the compression surface. Moreover, there is more wetted area than before and so viscous effects become more important. In addition, if multiple ramps are used, as is the case with the F-15 (see figure 2.9) there are multiple SWBLIs. Consequently, some form of boundary-layer control is often required (this is also shown in figure 2.9). At higher Mach numbers, the outward turning of the flow can also become a problem as this tends to lead to an high cowl angle which results in high cowl drag and in some instances high spillage drag.

2.5.5 Internal compression inlets

To reduce the drag caused by the outward flow turning of external compression inlets, an inlet with internal compression can be utilized (figure 2.5c). Such a design actually has zero cowl drag as the outer part of the cowl is parallel to the flow. Unlike either the Pitot or external compression configuration, in this configuration the terminal shock-wave is actually stands inside the inlet.

The problem with such a design, however, is two-fold. Firstly, viscous losses are even higher than in the external compression case as there are likely to be more SWBLIs and there is almost always more wetted-area. Secondly, there is the flow starting problem that is illustrated in figure 2.10 (the terminal shock-wave must be sucked inside the inlet). In this figure the difficulty in getting the inlet 'started', i.e., getting the shock system into the desired position is described.

[3]Personal image of F-15A currently exhibited at the IWM Duxford

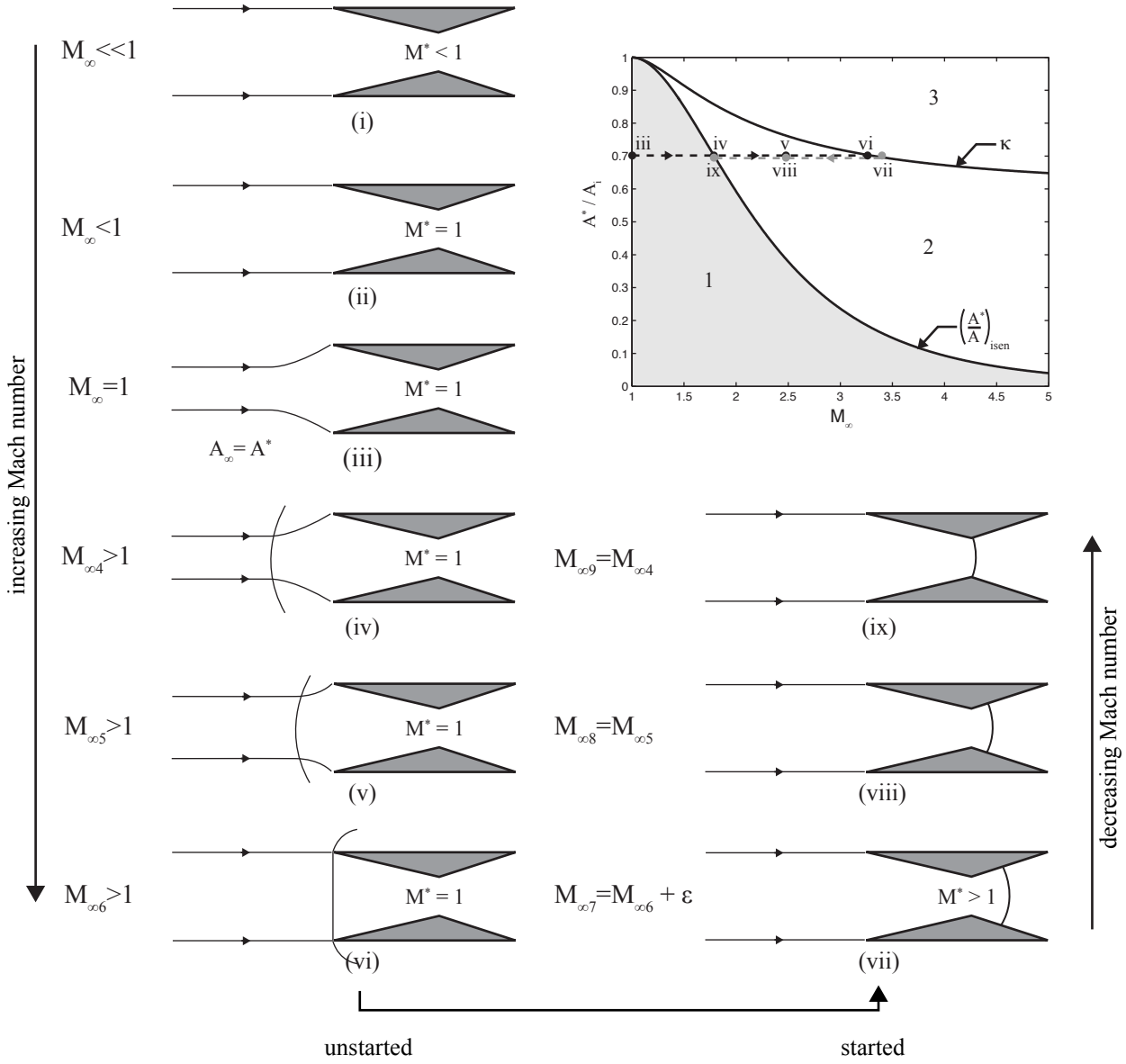

Figure 2.10: "Over-speed" flow starting of a supersonic internal compression inlet

As the inlet is accelerated from rest, it is difficult to get the terminal shock positioned within the inlet as the throat of the inlet soon becomes choked (ii), and, consequently, as M_∞ increases beyond 1, a normal shock must be setup to spill the unwanted mass flow around the inlet. The loss across the normal shock further decreases the mass flow for choking (iv), and accordingly, greatly increases the difficulty of ingesting the shock. This phenomenon is illustrated in the graph shown in figure 2.10 which shows the isentropic area ratio versus M_∞ and another line (labelled κ) which is often referred to as the Kantrowitz line (after Kantrowitz and Donaldson (1945)). The difference between the two lines is caused by the loss across the terminal shock wave and without this the inlet would "start" (the shock would be ingested) at point (iv). However, without changing the inlet geometry (not changing your position on the y-axis), the only way to get the inlet started from here is to increase M_∞ to $M_{\infty 7}$ (vii) and then reduce it back to $M_{\infty 4}$. This is known as over-speeding the inlet. In general, it is unlikely that you will have

over-speeding capability and often variable geometry is instead required. Variable geometry adds significant weight and complexity, though.

In addition to this serious problem, the difficulty of setting up a desirable shock system in a purely internal compression inlet system over a range of Mach numbers makes the internal compression inlet impractical. For this reason, no flight vehicles have utilized purely internal compression, to the author's knowledge. For details on some early internal configurations, see Pfyl and Watson (1959) and Mossman and Pfyl (1956).

2.5.6 Mixed compression inlets

To make a more practical design than the internal compression inlet but at the same time reduce drag, features of both the external and internal compression inlet can be combined to create a mixed compression inlet (figure 2.5d). In such a configuration, there is some external compression and consequently some cowl drag; yet, this can be reduced when compared to the external compression inlet by introducing some internal compression. This is illustrated by the mixed compression inlet shown in figure 2.11 which shows the NASA 60/40 mixed compression inlet. An internal oblique shock is utilized at the cowl to reduce the cowl angle (and hence cowl drag) with the terminal shock positioned slightly downstream of the geometric throat.

Although this type of configuration can give high pressure recovery and low drag this comes at the price of significant complexity. The problem of viscous losses especially those due to SWBLI is considerable and variable geometry is often required to allow flow starting as described in section 2.5.5. The only operational mixed compression inlet to be employed thus far is that on the Lockheed SR-71. The NASA 60/40 inlet shown in figure 2.11 was designed for the Boeing supersonic transport project (Boeing SST / Boeing 2707) which was cancelled before production. However, the inlet associated with this project has seen continued use for fundamental inlet and SWBLI research. An appreciation of the complexity of these types of inlets can be gained from the review of the inlet work for the Boeing SST given by Tjonneland (1971).

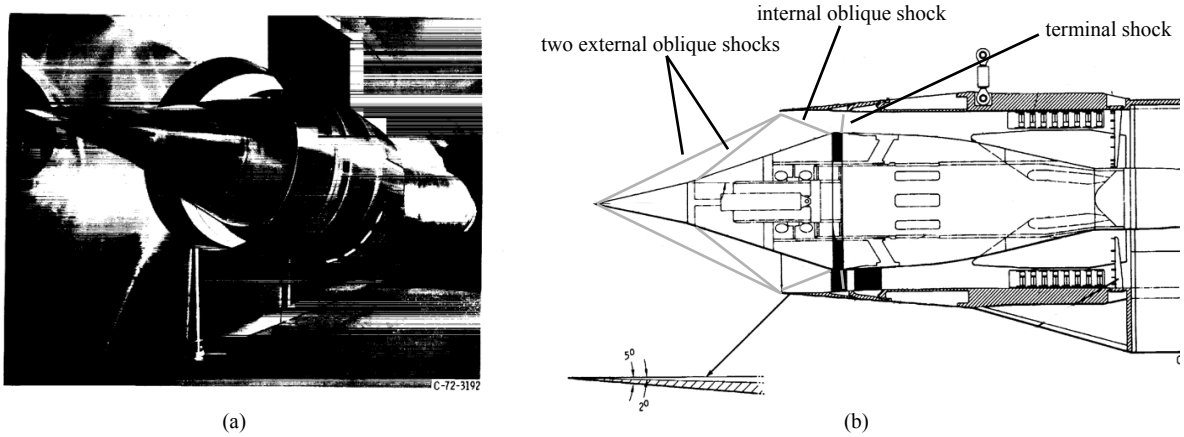

Figure 2.11: NASA 60/40 mixed compression inlet from Wasserbauer et al. (1975): (a) inlet mounted in NASA Glenn 10 by 10 foot supersonic wind tunnel and (b) schematic drawing

2.5.7 The subsonic diffuser

An aspect of all the inlets described above that has not yet been mentioned is the subsonic portion of the inlets. However, in each of these turbine-based propulsion systems, downstream of the terminal shock, further deceleration is required to reduce the incoming flow to an acceptable Mach number at the engine-face. Unfortunately, this puts further strain on the boundary layers. Three scenarios in which this is the case are illustrated in figure 2.12.

In each of these scenarios the terminal shock-wave is accompanied by further subsonic diffusion downstream: In the external compression inlet on-design (figure 2.12a) flow turning and expansion close to the inlet entrance induce a second adverse-pressure-gradient on the inlet; when the same inlet runs subcritically (figure 2.12b) flow spillage behind the terminal shock induces an expansion of the captured streamtube with a corresponding flow deceleration; and in the mixed compression inlet system (figure 2.12c) the terminal shock-wave is required to be within the diverging section of the channel for stability reasons and hence there is also an immediate second adverse-pressure-gradient.

The presence of a downstream adverse-pressure-gradient can only be eliminated if the inlet is of external compression type, is operating on-design and has no flow turning or area expansion in the vicinity of the terminal shock. However, delaying the expansion and flow turning until some distance downstream of the shock will result in increased drag, wetted area and weight—

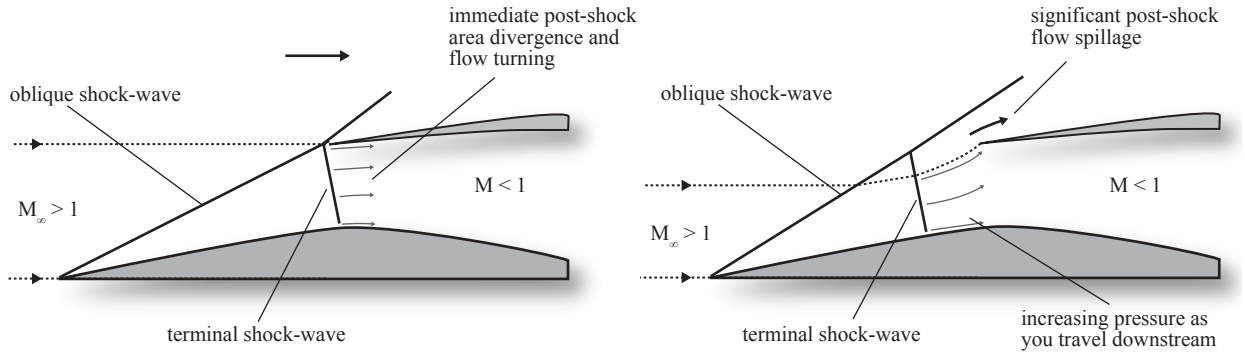

(a) Simplistic external compression inlet; on design

(b) Simplistic external compression inlet; highly subcritical operation

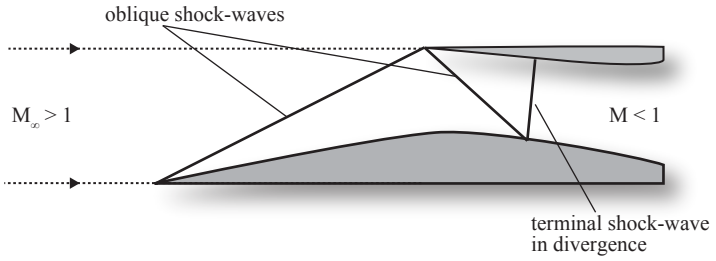

(c) Simplistic mixed compression inlet; slightly supercritical operation

Figure 2.12: Schematic diagram of inlet scenarios with combined terminal shock-wave and diffuser

all undesirable effects. Thus, in almost all instances there are two adverse-pressure-gradients in quick succession. As a consequence, there is a high risk of separation in this region.

This risk is also higher than across other SWBLIs as the pressure across the terminal shock alone is higher than other SWBLIs. The boundary layers also tend to be thicker at this location when compared to other SWBLIs, and this will further amplify viscous losses. As a result, the terminal SWBLI and subsonic diffuser region often requires boundary-layer control. For this reason, the flow control investigation here, is targeted at this region. The terminal SWBLI, which is more often called the normal SWBLI when detailed in isolation, is discussed next.

Chapter 3

Shock Waves, Boundary Layers and their Interaction

3.1 Boundary layers and shock waves

Before a detailed review of normal SWBLIs is given, some introductory comments about the basic concepts of turbulent boundary layers and shock waves are made. It is worth noting that the following discussion is limited to interactions between turbulent boundary layers and shock waves, as inlet boundary layers are almost always fully turbulent by the time the first SWBLI is reached.

As the performance of the boundary layer is pivotal in many areas of fluid mechanics (one example being the supersonic inlet as demonstrated in chapter 2) it is often beneficial to define a number of characteristics of the boundary-layer to help quantify its behaviour. To this end, the boundary-layer is commonly characterised by its thickness (δ), displacement thickness (δ^*), momentum thickness (θ), and shape factor (H). These are collectively known as the integral boundary-layer parameters.

To calculate the integral boundary-layer parameters in a compressible flow knowledge of the density variation across the boundary layer is required in addition to the velocity distribution. However, at supersonic speeds ($M_\infty < 5$) the incompressible or kinematic definitions of the integral parameters are often retained. The reason for this preference is two-fold. Firstly, the boundary-layer density variation is difficult to determine, and this uncertainty is easily removed by assuming a constant density. Furthermore, Morkovin's Hypothesis[1] states that the dynamics of shear layers are not appreciably influenced by compressibility (within the range $M_\infty < 5$). Hence, there is a strong case for utilizing the incompressible parameters, and the validity of this approach has been demonstrated by a number of authors including Winter and Gaudet (1970). For these reasons, the incompressible variants are used throughout this report.

The shape factor H can be a particularly useful parameter as it gives a measure of the current resistance of the boundary-layer to separation. As such, it is often referred to as a measure of the fullness or health of the boundary-layer. It is generally accepted that turbulent boundary-layer

[1]Morkovin's hypothesis, after Morkovin (1962), states that for boundary layers with $M_\infty < 5$ fluctuations in density and enthalpy do not modify the turbulence structure because fluctuations in Mach number are much less than unity

separation occurs somewhere around $H > 2.5$ (see Kline et al. (1983)). Hence, one indication of separation can be established by looking at the evolution of the boundary-layer shape factor.

Shock-waves are finite amplitude discontinuities that arise in compressible flows. To abide by the 2nd Law of Thermodynamics, these finite amplitude waves or shock-waves must be compressive. Thus, the shock-wave creates a strong discontinuity from low to high pressure. In this section shock waves that decelerate the flow from supersonic to subsonic velocities are discussed. Although such discontinuities are usually normal shock waves there are circumstances in which a strong oblique shock wave may be produced from the solution of the Rankine-Hugoniot equations. Throughout this investigation when referring to a situation where the flow is decelerated to subsonic speeds the term terminal shock wave is used.

For more in-depth descriptions of boundary layers and shock waves the reader should consult any modern fluid mechanics textbook—good examples include White (2006) for details on boundary layers and Anderson (2004) for details on shock waves.

3.2 Shock-Wave / Boundary-Layer Interactions (SWBLIs)

3.2.1 Introductary remarks

While this section is primarily devoted to the interaction of a turbulent boundary layer with a normal shock wave much of the flow physics detailed is also relevant to other SWBLIs. For a more general overview of SWBLI though, the reader should refer to Green (1969), Delery and Marvin (1986), or Babinsky and Harvey (2011).

Alongside these reviews, some of the best data obtained with the simplest normal SWBLI configuration (the normal SWBLI in a constant area channel) is that reported by East (1976) and Sawyer and Long (1982) at the RAE. For this reason, the data presented in the following section is from these investigations.

3.2.2 The normal SWBLI

The interaction between a normal shock wave with an upstream Mach number of 1.3 and a turbulent boundary layer obtained at RAE is shown in figure 3.1. In this figure, measurements of the overall flow structure are shown using schlieren in figure 3.1a and from LDV measurements in figure 3.1b. Alongside these, the measured wall-pressure distribution is presented in figure 3.1c and measurements of the boundary-layer parameters in figure 3.1d. The images have been aligned such that the same streamwise extent is shown in each.

Firstly, looking at the schlieren image of figure 3.1a, it can be seen that the shock wave is significantly smeared in the streamwise direction near the wall. This region is often referred to as the shock-foot and is also clearly visible in the LDV measurements of figure 3.1b. This smearing starts well upstream of the inviscid shock location, and the distance between here and the inviscid shock location is often referred to as the upstream influence. Due to the upstream influence, the boundary layer upstream of the shock wave thickens in response to the shock wave's adverse-pressure-gradient (see figure 3.1d), and, as a result, compression waves propagate into the outer-flow. This results in a more gradual pressure rise in the near wall region which is visible not only from the contours of Mach number in figure 3.1b but also in the wall pressure distribution of figure 3.1c.

If the pressure increase across the shock wave is not too high (i.e., if the upstream Mach number is not too high), the thickening of the subsonic layer occurs slowly enough that a near-isentropic compression fan is setup in the shock foot region. This near-isentropic compression reduces the normal shock Mach number close to the wall and this reduces the stagnation pressure losses due to the shock in this region.

Although the shock losses are reduced locally, the development of the boundary-layer parameters in figure 3.1d shows that there is a significant thickening of the viscous region across the interaction. Although some thickening is inevitable to satisfy continuity, significant turbulence kinetic energy is produced across the interaction and this increases the losses in the near-wall region, further thickening the boundary layer.

In addition to creating substantial losses, the rapid thickening of the boundary layer restricts the flow downstream of the shock wave reaccelerating the flow in this region. As a result, the pressure remains well below the inviscid pressure level for sometime after the shock wave. Slowly, however, the boundary layer will relax to an equilibrium state (although much thicker than before) and at the same time the wall pressure will tend towards the inviscid pressure level. While the production of turbulent kinetic energy across the shock wave increases the viscous losses it also aids the downstream relaxation process. Nevertheless, this can still take tens of incoming boundary-layer thicknesses.

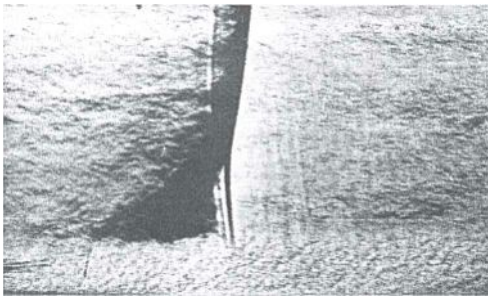

(a) schlieren

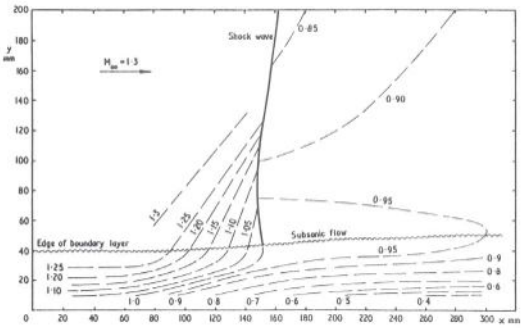

(b) LDV

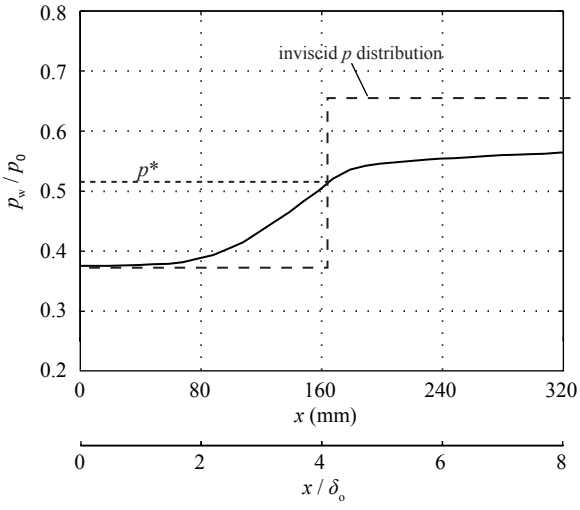

(c) wall pressure

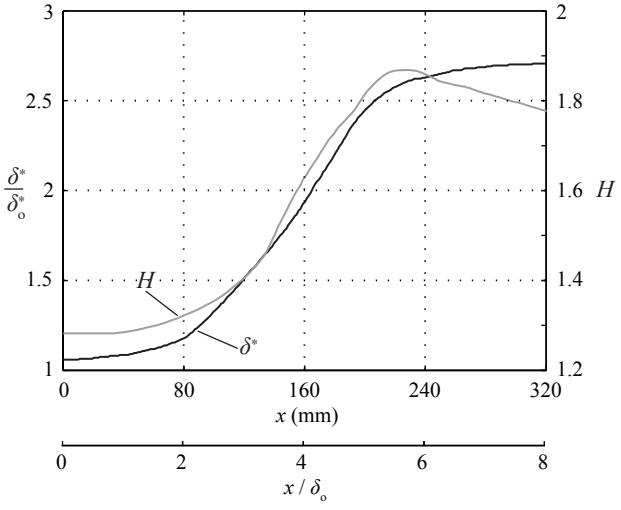

(d) boundary-layer parameters

Figure 3.1: A weak transonic SWBLI; adapted from East (1976) and Sawyer and Long (1982)

While the data presented here demonstrates performance in a typical constant-area Mach 1.3 normal SWBLI, it is important to note that the flow will behave substantially differently in other geometrical configurations—especially in the subsonic region of the flow. This factor is discussed in more detail later.

As the upstream Mach number is increased the interaction slowly changes from the smeared interaction shown in figure 3.1 to the interaction presented in figure 3.2. This figure shows data in the same wind tunnel configuration but with an upstream Mach number of 1.5. Comparing the schlieren images between the two figures illustrates that there is quite a difference between the two interactions. In this instance, at Mach 1.5, there is a clearly defined three-shock structure, in contrast to the smeared shock system at Mach 1.3. This three-shock structure somewhat resembles the Greek letter λ and is therefore often referred to by the term 'lambda foot'. It is important to note that there is no Mach number at which there is a step-change from the smeared to the lambda foot interaction, and it is generally accepted that this occurs gradually between Mach 1.3 and 1.5 (see Atkin and Squire (1992) for a detailed description of the development of the normal SWBLI as the upstream Mach number is increased).

The lambda foot structure starts to develop as boundary-layer thickening underneath the shock wave becomes more sudden, and, as a result, the compression waves that result start to coalesce and form a weak oblique shock wave. As this sudden thickening of the boundary layer often accompanies the presence of separation, the lambda foot is therefore often seen as a first indicator of separation. Behind this weak oblique shock wave there is strong oblique shock wave to terminate the supersonic flow. This three-shock structure is nicely illustrated in the LDV measurements of figure 3.2b.

The lack of boundary-layer separation at Mach 1.3 and its presence at Mach 1.5 are nicely illustrated by the oil-flow visualizations taken by Sawyer and Long (1982). These are reproduced here in figure 3.3. Unfortunately, the quality of the original images is poor. However, on close inspection it can be seen that extensive separation exists at Mach 1.5. In contrast, at Mach 1.3 the flow is predominantly attached.

Much like before, the wall-pressure distribution, shown in figure 3.2c, is smeared over a significant streamwise distance, and due to the separation the pressure resides even further below the downstream inviscid pressure level directly downstream of the shock wave.

The distributions of δ^* and H, shown in figure 3.2d, illustrate that the boundary layer grows more strongly than before (note the difference in the vertical axis between figure 3.1d and figure 3.2d). In this instance, H has increased well above the accepted value for separation, confirming that a separated region is present. The presence of the separation leads to the creation of much higher viscous losses than in the unseparated case (the production of turbulent kinetic energy is even higher than before).

In addition to the high viscous losses, recent work such as Dussauge et al. (2006) suggests that there is a clear link between the presence of separation and the magnitude of shock oscillations—shock oscillation amplitude increasing with increasing separation. Flow separation therefore not only introduces significant viscous losses, but also flow unsteadiness. (It should be pointed up that both the unsteadiness and the production of turbulent kinetic energy in a normal SWBLI are not well understood, both of these phenomena still require significant attention as indicated by Dolling (2001).) Notwithstanding this, the increase in viscous losses and the

possible unsteadiness both make the separated normal SWBLI undesirable to the inlet designer.

3.2.3 Shock-induced separation: the influence of M and H

Predicting under what conditions a normal SWBLI will cause separation and the accompanying increase in viscous losses is clearly important. Hence, much effort has been expended trying to predict the shock-induced separation limit, M_{sep}.

Until recently, the most complete discussion of this limit was probably that of Delery (1985). In this investigation, it is concluded that the main factors which determine whether separation occurs or not are:

- The Mach number just upstream of the shock wave, M_{o} (sometimes referred to as the shock strength) and
- the boundary-layer shape parameter, H_{o}, at the onset of the interaction (while the more commonly considered Reynolds number effect is encompassed to a large extent in H_{o}).

The dependency of flow separation on M_{o} and H_{o} determined by Delery (1985) is shown in figure 3.4, where hollow symbols signal attached flow and filled symbols separated flow. This

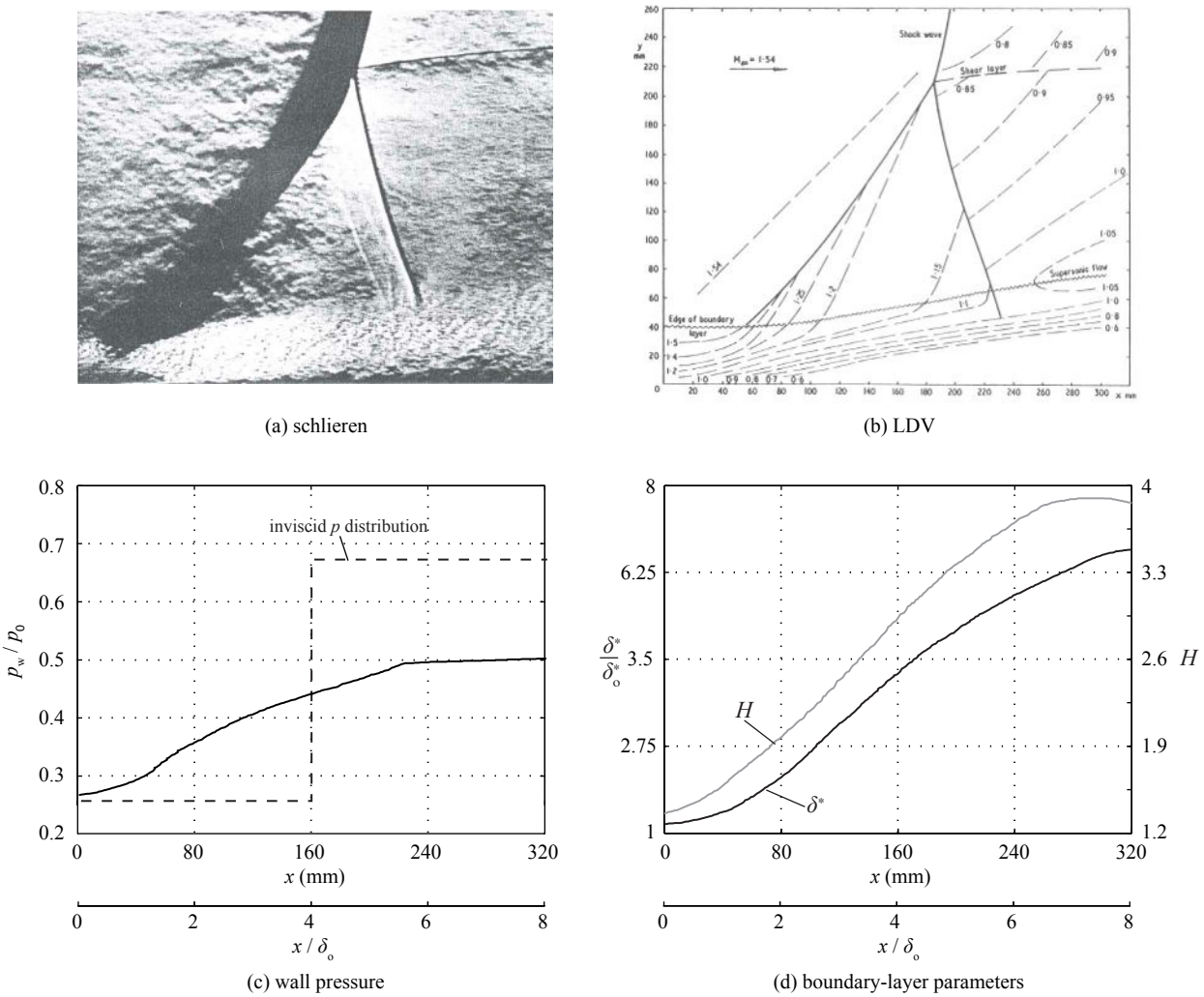

Figure 3.2: Details of a strong transonic SWBLI from East (1976) and Sawyer and Long (1982)

(a) Mach 1.3

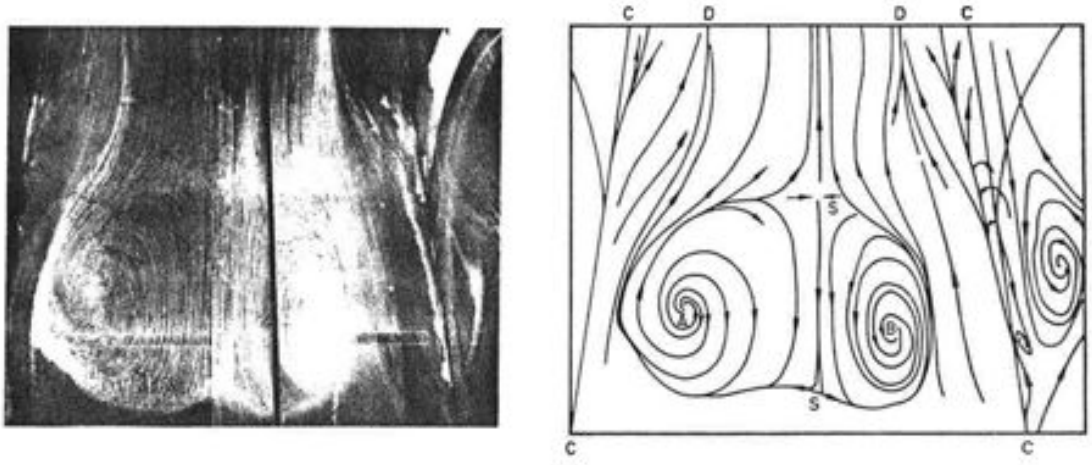

(b) Mach 1.5

Figure 3.3: Oil-flow visualizations for the weak and strong transonic SWBLI (quality of original document low)

figure indicates that while the separation limit is a function of both upstream Mach number and upstream shape factor it is the upstream Mach number which is of primary importance—separation in general occurring near Mach 1.3.

The upstream Mach number is important because this determines the overall pressure rise imposed on the boundary layer (which with a normal shock wave is solely a function of the upstream Mach number). Although it is a high adverse-pressure-gradient that leads to a boundary-layer separation and not a high overall pressure rise, only a certain degree of streamwise smearing can be achieved by the boundary layer. Consequently, a higher overall pressure rise will ultimately lead to a higher adverse-pressure-gradient and therefore flow separation.

The reason for the insensitivity to the boundary-layer shape factor is more subtle. In principle a lower shape factor should lead to a boundary layer more resilient to separation. However, in a supersonic flow, a lower shape factor also thins the subsonic portion of the boundary layer, and this makes it more difficult for information about the shock wave to travel upstream. Accordingly, the shock is less smeared resulting in a stronger adverse-pressure-gradient. The

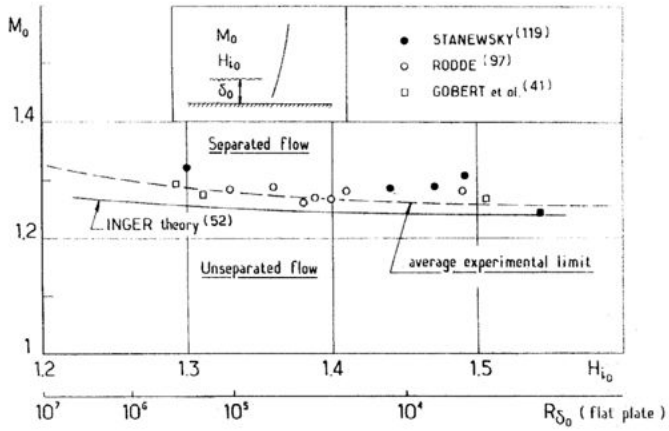

Figure 3.4: Experimental shock-induced separation limit in transonic flows; Delery (1985)

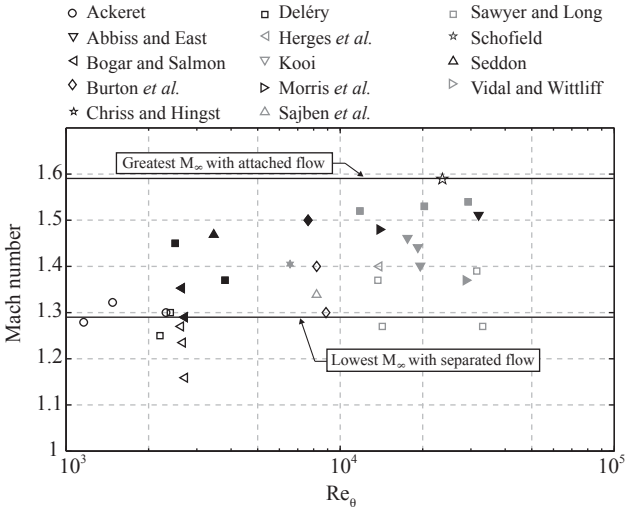

Figure 3.5: Experimental shock induced separation limit, Mach number vs Re_θ; unseparated flows (open symbols) and separated flows (closed symbols); Bruce et al. (2010)

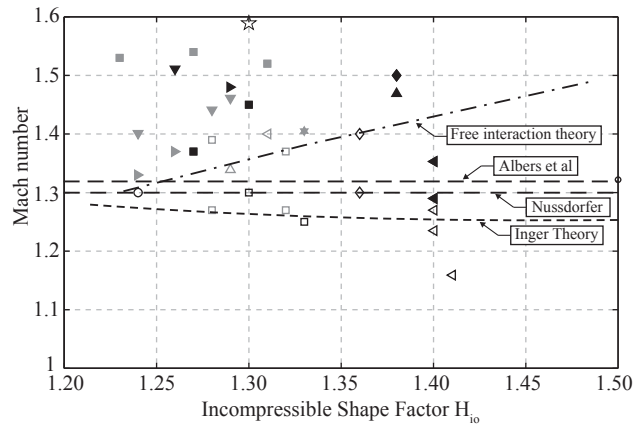

Figure 3.6: Experimental shock induced separation limit, Mach number vs H_o; unseparated flows (open symbols) and separated flows (closed symbols); Bruce et al. (2010)

increased boundary-layer resilience is therefore counteracted, and these two factors tend to negate one another to a large extent.

Despite the insensitivity of the separation limit to the boundary-layer shape factor, Delery and Marvin (1986) did observe that a lower shape factor tended to reduce the extent of separation. It is therefore still beneficial to reduce the shape factor when trying to minimize viscous losses due to separation.

The findings of Delery (1985) are generally in agreement with earlier investigations such as Ackeret et al. (1947) who found that the shock-induced separation limit is $M_{\text{sep}} = 1.3$, Alber et al. (1973) who determined $M_{\text{sep}} = 1.3 - 1.32$, and Nussdorfer (1956) who also indicated that separation occurred at $M_{\text{sep}} = 1.3$. Yet, in more recent investigations, authors including Chriss et al. (1989), Sajben et al. (1991) and Bruce et al. (2010) have not observed such similar behaviour.

When Sajben et al. (1991) discovered that they could produce attached flow at Mach 1.34, they decided to collate data from a wide variety of normal SWBLI studies. As a result of collating a much wider range of data than Delery (1985), Sajben et al. (1991) produced a plot with substantially more scatter. These data plotted upstream Mach number versus Reynolds number (based on θ) were then replotted but with additional data by Bruce et al. (2010). This plot is reproduced as figure 3.5. Notable in this figure are the extremes: the attached flow at Mach 1.58 obtained by Chriss et al. (1989) and the separated flow at Mach 1.29 by Salmon et al. (1983). To create a direct comparison with the data of Delery (1985), these data were also plotted against shape factor by Bruce et al. and this is shown in figure 3.6. The scatter in figures 3.5 and 3.6 is in clear contrast to the data of Delery (1985) (figure 3.4).

Also plotted in figure 3.6 are some of the experimentally observed shock-induced separation limits (as discussed above) and the analytically derived separation limits from Inger and Mason (1976) and from the Free-Interaction-Concept (see Chapman et al. (1957) and Erdos and Pallone (1962)). It can be seen that the data does not adhere to any of these suggested trends.

It is possible that these differences can to some extent be caused by variations in the definitions of separation between the wide array of investigations presented in Bruce et al. (2010). Although it would be preferable to use the classical definition of separation ($P(u < 0) = 0.5$) for each investigation, this is not always possible and a variety of less precise separation detection methods have to be utilized instead. Yet, this uncertainty cannot account for the extent of the scatter observed. There are clearly other factors influencing whether separation is initiated or not.

3.2.4 Shock-induced separation: other factors

To comprehend why there is such a discrepancy in the shock-induced separation limit between investigations, it is worth considering that these studies were undertaken in a variety of facilities. It therefore seems plausible that this may be having an influence on the flow physics of the interactions. In other words, the differences may be due to variations in the wind tunnel geometries. Although a seemingly obvious consideration, this factor is often overlooked. Even though Delery (1985) did indicate that geometry could be influential, he did not evaluate geometrical variations in detail.

To illustrate that geometry and factors related to geometry have a strong influence on the

resulting flow-field, measurements of wall-pressure for a variety of what are nominally Mach 1.3 normal SWBLIs have been collated by the author and are presented in figure 3.7. Visible in this figure is a large variation in the resulting wall-pressure distributions. While upstream of the sonic pressure ratio the distributions are very similar (as predicted by Free-Interaction-Theory), downstream of this location the distributions are not. This difference is thought to be largely due to geometrical differences between the experimental configurations.

Of the geometrical factors that are influential, the effect of streamwise area variation in the vicinity of the normal SWBLI is important as this has an impact on the post-shock pressure gradient. The effect of a downstream area expansion is visible in figure 3.7. In this figure, it can be seen that both Delery (1985) and Ackeret et al. (1947) obtained much higher wall-pressure recoveries, and this is largely because these investigations did not utilize a constant-area duct like the investigations shown in section 3.2.2 (this type of configuration is also shown schematically in figure 3.8). Instead these studies utilized what is often referred to as a two-dimensional bump configuration. This configuration is shown in figure 3.9. Improved wall-pressure recovery is obtained with this experimental setup as the area expansion is used to further reduce the Mach number downstream of the shock.

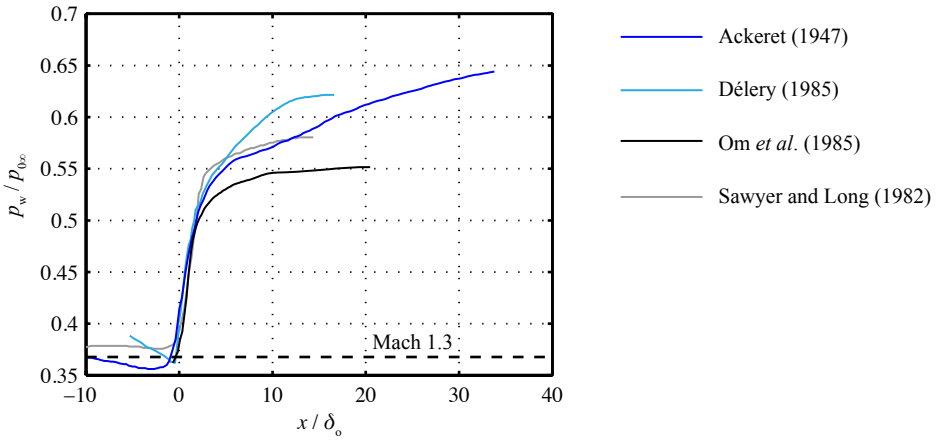

Figure 3.7: Wall pressure measurements from a variety of nominally Mach 1.3 transonic SWBLIs

The two-dimensional bump setup is often utilized because it is easy to vary the Mach number upstream of the shock wave by varying the position of the shock. However, the two-dimensional bump has the disadvantage that the shock-induced adverse-pressure-gradient is always strongly coupled to area variation in the vicinity of the shock wave. This may be beneficial in instances where the downstream pressure gradient for the application of interest is known (such as a particular airfoil design), but in all other instances it just introduces a new degree of freedom which cannot be easily controlled.

If a further downstream adverse-pressure-gradient is desirable—which it is in almost all inlet applications—it is preferable to prescribe a particular downstream pressure gradient independently of the shock strength. An example of such a configuration is shown in figure 3.10. A configuration similar to this has been utilized by both Morris et al. (1992) and Schofield (1985). Yet, in neither of these investigations was the downstream area variation varied, and as a consequence, it is difficult to make conclusions about the influence of the downstream adverse-

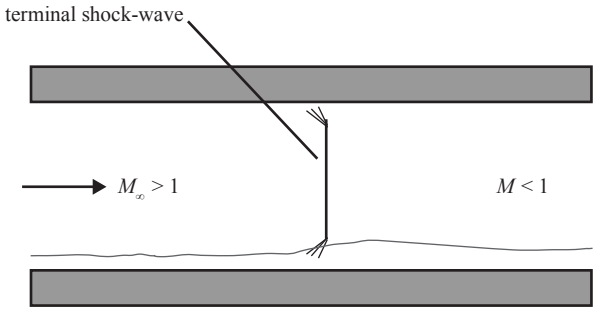

Figure 3.8: Schematic of simplest terminal SWBLI setup; the constant area duct

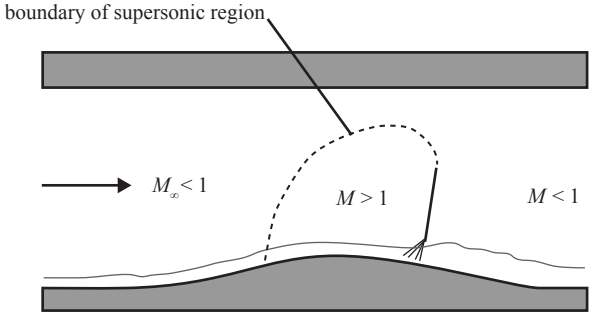

Figure 3.9: Two-dimensional bump based terminal SWBLI setup

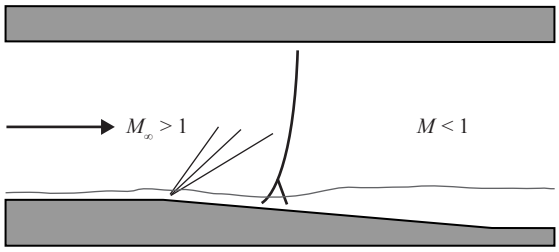

Figure 3.10: Duct-diffuser based terminal SWBLI

pressure-gradient. A number of more inlet orientated investigations have been undertaken to try and determine this coupling (MacMiller (1969) and Syberg and Surber (1980) are good examples). Unfortunately, in these investigations it is difficult to determine the precise influence of the downstream adverse-pressure-gradient due to the large number of variables involved and the lack of instrumentation available near the SWBLI.

As a downstream area variation has a substantial influence on the wall-pressure distribution, it has a strong effect on the interaction. Much further work is still required on the impact of this factor.

The other factor that is highly influential is three-dimensionality. Although all of the flows discussed thus far are clearly three-dimensional, all discussion so far has been assuming near

two-dimensional behaviour with all the measurement shown obtained at the centre-span of the wind tunnel. While this is not likely to be a problem in axisymmetric configurations, two-dimensional rectangular geometries are far more prevalent. This point is also illustrated in figure 3.7: Comparing the distributions of Sawyer and Long (1982) and Om et al. (1985) it can be seen that there is a substantial difference between these two interactions. Yet, they are at very similar Mach numbers (1.27 versus 1.29), similar Reynolds numbers (10.2 versus 9.9 million per metre), and even have similar confinement ratios—a measure of the inflow area taken up by the boundary layers (14% versus 16%). In addition, both experiments were undertaken in a constant area working section. The main difference between the two is that the investigation by Sawyer and Long (1982) was undertaken in a rectangular working section, whereas that of Om et al. (1985) was undertaken in an axisymmetric working section.

The notion that three-dimensional effects are important is not new: Green (1969) duly noted its importance in 1969. Despite this, it is difficult to determine the influence of three-dimensionality. This is because it is both difficult to acquire measurements of the flow-field in three-dimensions and because it is very difficult to vary the three-dimensional characteristics of a particular configuration (for example the height and width of the wind tunnel). Despite this difficulty, the three-dimensional nature of a SWBLI has been investigated by Kornilov (1997). In this investigation, Kornilov was able to vary the aspect ratio of his wind tunnel configuration by employing artificial sidewalls inside the working section. Kornilov found that the width had an important influence on factors such as the vortical flow-field produced in the corners (at the junction of sidewall and floor) and on the streamwise extent of the separation.

In terms of three-dimensionality in normal SWBLIs, the only notable experiments are those of Bruce et al. (2010). In addition to the the analysis shown in figures 3.5 and 3.6, the impact of three-dimensional effects—specifically the influence of corner interactions in a rectangular working section—were investigated experimentally. The experiments of Bruce et al. demonstrate that the normal SWBLI can lead to a highly three-dimensional flow. What is more, by manipulating the corner flows, it was shown that there is a strong coupling between the separation present in the corners and the centre-span separation: when the size of the corner separation was increased the size of the centre-span separation could be reduced (note that although three-dimensionality makes the definition of separation more complex, the definition of reversed flow in the centre-span region is maintained as our definition throughout this section).

Further evidence to support this coupling of the corner and centre-span separations is presented in the paper of Bruce et al. (2010). In this investigation, the data in figure 3.5 is again replotted but with a width-based confinement/aspect ratio parameter, $\delta^*/w_{\text{tunnel}}$, on the x-axis (suggested as a rudimentary measure of corner size). This plot is shown in figure 3.11. In this figure, there is less scatter than either figure 3.5 or 3.6 and there appears to be a trend of increasing shock-induced separation limit with increasing $\delta^*/w_{\text{tunnel}}$. In instances where corner separations are more prominent (larger $\delta^*/w_{\text{tunnel}}$) shock-induced separation in the centre-span is delayed. It is then postulated that this is because the blockage caused by the corner separations smears the pressure rise in the centre-span region; therefore reducing the centre-span adverse-pressure-gradient. More details on this phenomenon are discussed in Burton and Babinsky (2012). Nevertheless, more work is still required on the coupling between the centre-span and corners flows.

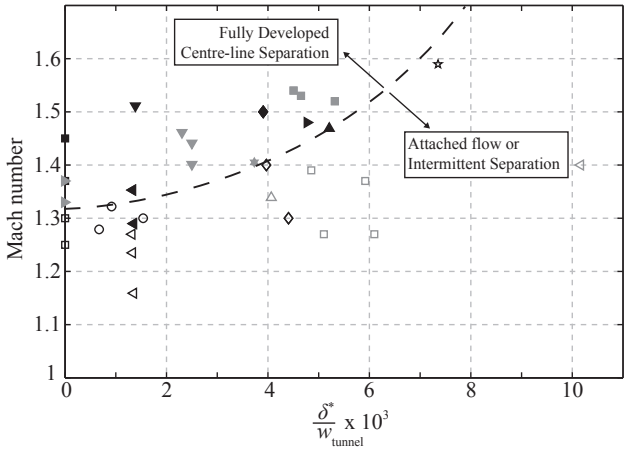

Figure 3.11: Experimental shock induced separation limit, Mach number vs geometry ($\delta^*/w_{\text{tunnel}}$); unseparated flows (open symbols) and separated flows (closed symbols); Bruce et al. (2010)

The differences between the distributions shown in figure 3.7 and the separation limits shown in figure 3.11 are evidence that the flow geometry is critical. This explains the extensive scatter produced in figure 3.6 when compared to figure 3.4 (due to the wider range of facilities in the former). Consequently, it can be concluded that the shock-induced separation limit and therefore the extent of viscous loss in an interaction is more complex than the plot of Delery (1985) implies: the shock-induced separation limit is going to vary between configurations and facilities due to three-dimensionality and streamwise area variation (and perhaps other factors). While some progress has been made to quantify these factors further work is required.

This discussion therefore allows it to be concluded that a number of factors including, upstream Mach number, streamwise area variation, and three-dimensionality are clearly important to inlet design, as they all influence the likelihood of separation. These all need to be taken into account when investigating flow control for supersonic inlets.

Chapter 4

Inlet Flow Control

4.1 Boundary-layer bleed

4.1.1 Introduction

Of the methods currently available for reducing the adverse viscous effects of SWBLIs, the most widely used technique to control the inlet boundary layers is boundary-layer bleed. Using this approach, the inlet's boundary layers are at least partially removed from the main inlet stream before they are able to reach the engine face. This increases the fullness of the boundary layer (reduces H) and decreases the boundary-layer thickness, both of which help to reduce viscous losses and separation as discussed in chapter 3. The bleed flow is then either ducted to the exterior or, less often, re-injected into the nozzle flow.

When designing a bleed system, the bleed configuration needs to be tailored to the particular type of inlet, the vehicle requirements, and to the engine's operating characteristics. Accordingly, it is difficult to make generalizations on bleed system design. Nevertheless, the author feels that a general overview of inlet bleed systems would be beneficial to those involved in boundary-layer flow control for inlet applications. Unfortunately, such a survey is lacking in the literature. The best summaries are probably given by Seddon and Goldsmith (1999) and in a lecture series at VKI (1988), but neither are particularly detailed.

4.1.2 Bleed configurations

Broadly speaking there are three main types of bleed configuration available, and these three configurations are shown in figure 4.1. There is slot or flush bleed (figure 4.1a), scoop or ram bleed (figure 4.1b), and the distributed or perforated bleed region (figure 4.1c).

In the early days of inlet design, slot and scoops were generally preferred as the simple two shock external compression inlet designs only had one SWBLI (that due to the terminal shock) and hence control was only really required in this one region. The inlets were actually somewhat similar in design to that shown in figure 4.1a. Some of the earliest examples of this type of bleed configuration were tested at NACA by Obery et al. (1952) and Obery and Cubbinson (1954) and at RAE by Griggs (1958). In these early examples, the slot or scoop was generally placed underneath the terminal SWBLI and in many instances gave substantial improvements in pressure recovery due to its ability to mitigation separation. In some instances improvements of as much as 10% could be obtained. Further to this, large reductions in the

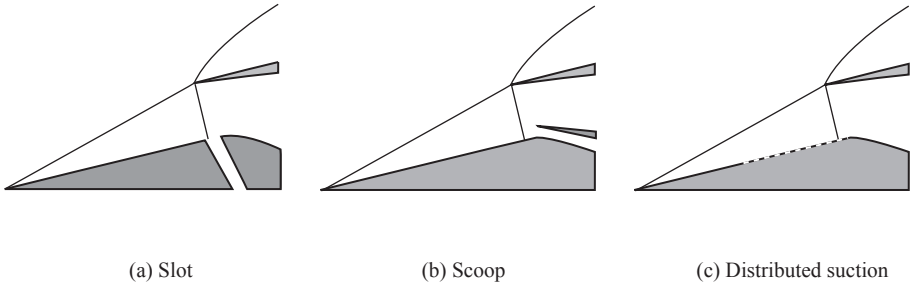

Figure 4.1: Types of boundary-layer bleed system typically available

level of shock unsteadiness at low mass flow ratios (often referred to as 'inlet buzz') could also be achieved with these slots and scoops. In some instances a 10–20% reduction in A_i/A_∞ could be maintained over the uncontrolled case without severe shock oscillations. This reduction in the level of shock oscillations has been investigated in more detail by a number of authors and is usually attributed to the reduction in separation resulting from the use of boundary-layer bleed, much like Dussauge et al. (2006). See Griggs (1958) and Fisher et al. (1972) for more details.

In the external compression tests by Obery and Cubbinson (1954) and Griggs (1958) it was found that the slot tended to give preferential performance to the scoop, and this bleed type ended up on a wide variety of external compression inlets. Some examples being the F-104 and F-4 (Surber and Robinson (1983)), F-14 (Hinz et al. (1970)), F-15 (Imfeld (1976)), Concorde and Tornado (which had similar designs; see Leynaert (1966)).

In inlets where there are multiple SWBLIs distributed suction is often employed. Fukuda et al. (1977) suggest that a major reason for this lies in the complexity of these inlets which leads to a heavily iterative bleed system design. In such a case, a model with a large number of distributed holes that can be easily switched on and off helps to lead the design to optimal solution more quickly. Consequently, the complex mixed compression inlet system on the SR-71 (see Smeltzer et al. (1975)) and the Boeing/NASA SST inlet (see Tjonneland (1971)) both utilize substantial areas of distributed suction. As do the F-4, F-14, and F-15 which have multiple compression ramps on which distributed suction was deemed necessary.

In addition to the distributed bleed on the SR-71, the inlet also employed a shock-trap bleed to stabilize the terminal shock. Similar to a scoop bleed this configuration seems to give very good performance on design, and some very nice experiments on this configuration were conducted by Luidens and Flaherty (1958).

More recently, inlet designers have tended to move away from slots and scoops and even in simple external compression cases have utilized just distributed suction. Examples being the F-18, both the original YF-17/ F/A-18A–D design (see Wong (1974)) and the caret inlet of the F/A-18 E/F (see Hall et al. (1993)), and more recently on the F-22 (see Hamstra and McCallum (2010)). The reason for this change is probably increased flexibility and the negative impact that scoops and slots have on the inlet structure.

Even though there have been a large number of studies into bleed system type, very little is known about the precise flow physics as most of these investigations took place in large wind tunnels with very complex models. This makes it difficult to determine the relative performance

advantages of these different types of bleed. In addition, to the author's knowledge, no direct comparison of the slot and distributed bleed exists.

In addition to the type of bleed system, the location of bleed is also important. If the bleed position is not optimal low pressure recovery may result and excessive bleed may be required to maintain desired performance.

The general preference when using a slot appears to have been to bleed just downstream but in the close vicinity of the SWBLI—with most of the slots discussed in this section finding this location optimal. Such a location is seen as beneficial as the high pressure behind the shock wave can be used to drive the flow into the slot, while at the same time the slot is close enough to the SWBLI to suppress the boundary-layer thickening and possible separation before it is able to considerably attenuate inlet performance. In addition, this position is near the geometric throat and this is the location where the inlet is particularly sensitive to small changes in area (as the flow is near sonic).

A noteworthy computational example of a slot suppressing shock induced separation in this position is illustrated in figure 4.2. It can be seen that the flow downstream of the SWBLI is much improved with the addition of the slot. Both the benefit to distortion and the reduction in losses are apparent in this figure.

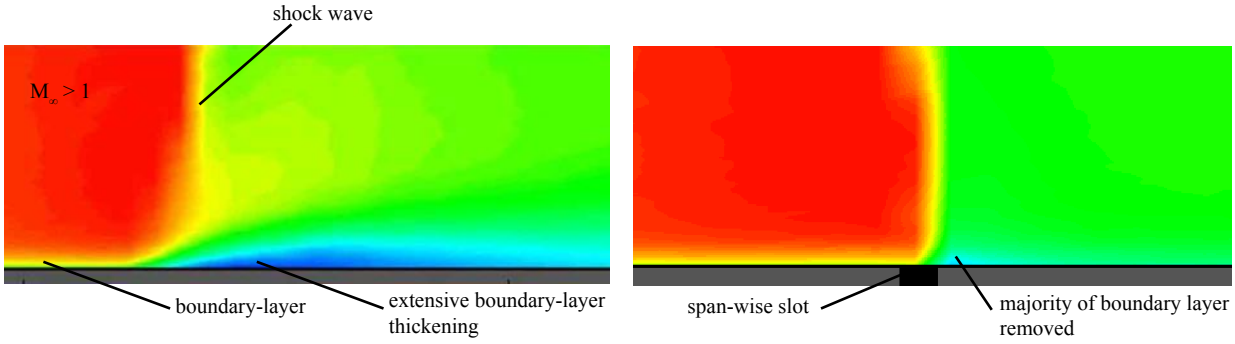

Figure 4.2: Mach number contours through a terminal SWBLI. Computation by Stanewsky et al. (1997)

Fukuda et al. (1977) found that the just downstream location also gives the most favourable performance for the distributed suction case. Furthermore, it was concluded that bleeding across the interaction (both upstream and downstream of the shock) is undesirable as this generally leads to recirculation from within the bleed plenum, which can actually increase losses over the baseline case. However, if recirculation can be avoided Wong (1974) found that bleeding both upstream and downstream can result in good performance. There are also instances where upstream bleed tends to perform well, with one noteworthy example being the more fundamental study of Morris et al. (1992). Yet, the author has no concrete reason why such variations have been observed between investigations. More work in this area would be desirable to help to optimize bleed location and reduce the possibility of unnecessarily high bleed rates.

The amount of mass flow removed from the inlet is the other main factor to consider. If the bleed rate is too low there will be little benefit and the bleed may even act as surface roughness and increase the losses slightly (Willis and Davis (1996)). On the other hand, if too much bleed

is applied, unnecessary mass flow is removed from the inlet stream which will inevitably increase drag. This bleed drag penalty is discussed more in 4.1.3.

To give some indication of the amount of mass flow typically bled, the bleed system mass flows for a variety of inlets during typical operation are shown in figure 4.3. These include Pitot, external compression, mixed compression and fully internal compression inlets. Many of the inlets plotted are fundamental inlet studies undertaken in large scale wind tunnels. However, some production inlets are included, including the SR-71, F-15A, and F-18A.

It is visible from figure 4.3 that boundary-layer bleed requirements are mainly in the region 3–10% of the inlet capture flow. Furthermore, some interesting trends are visible from this plot. It can be seen that in general there appears to be a trend towards using higher mass flow rates at higher freestream Mach numbers. This is to be expected as more deceleration is required as the flight speed is increased, and, consequently, the boundary layer is more susceptible to separation. In addition, there is a clear trend with the type of inlet: as the inlet complexity increases, so does the bleed requirement. For the Pitot inlet no boundary-layer bleed is required. While the external compression inlet generally requires some bleed this is not as much as the mixed compression systems. And even higher than the mixed compression inlet, the fully internal compression inlets require a significant amount of bleed. This trend is due to the increase in internal wetted area and the number of SWBLIs experienced as the inlet goes from external to mixed and then internal compression (as was discussed in chapter 3).

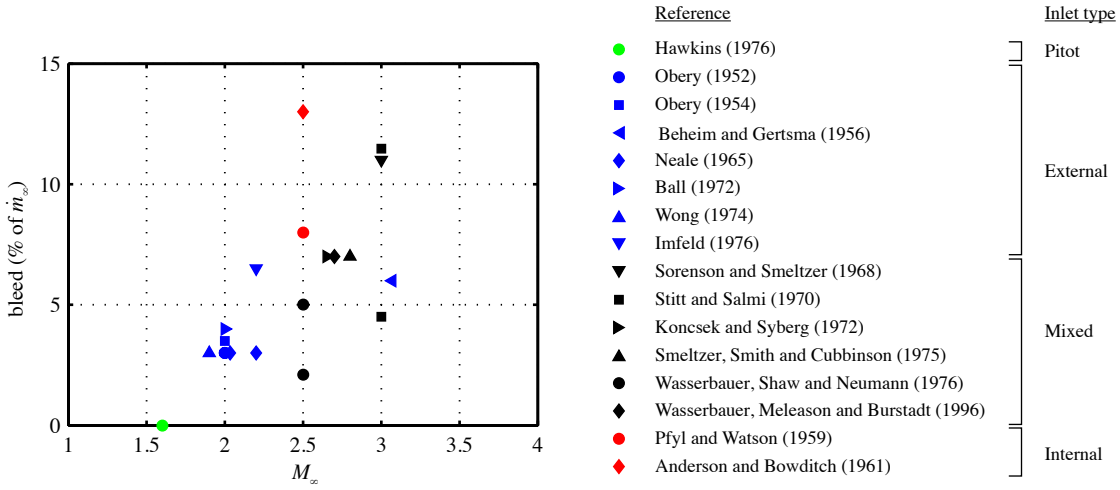

Figure 4.3: Bleed rate versus freestream Mach no. for a variety of supersonic propulsion systems

4.1.3 Bleed Drag

The information in figure 4.3 indicates that a considerable amount of the air-flow is often consumed by the bleed system. As a consequence, there is likely to be a noticeable drag penalty associated with the bleed system.

While the bleed penalty will inevitably be different for each application, to illustrate that bleed drag can be a significant contributor to overall aircraft drag, figure 4.4 shows the range loss associated with the bleed system components employed on the Boeing SST as calculated

by Tjonneland (1971). From figure 4.4, it is visible that bleed contributes substantially to aircraft drag, with each section of bleed contributing a 0.5–1% reduction in range. In total, the system utilizes about 6.5% of the inlet mass flow and its total contribution to aircraft drag is thought to be around 6%. This is a considerable penalty. For this reason, there has always been interest in reducing inlet dependency on bleed. For the reader's interest, more details on the trade-offs for the Boeing SST can be found in Sorenson and Bencze (1974) where some further work on improving the SST inlet is described.

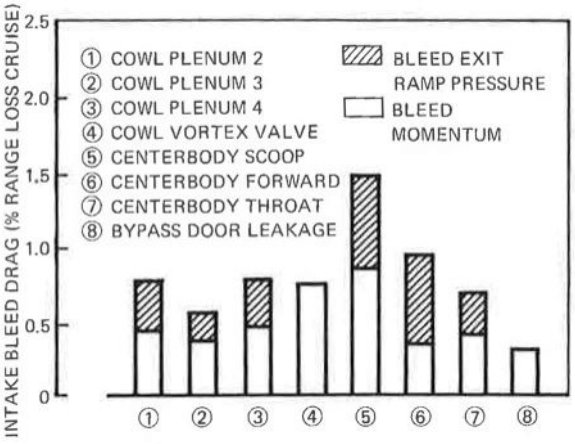

Figure 4.4: Boeing SST range loss due to inlet drag (Tjonneland (1971))

4.2 Benefits of boundary-layer bleed other than SWBLI control

In addition to improving the inlet pressure recovery and possibly reducing shock oscillations by removing at least some of the inlet boundary layers, boundary-layer bleed has a number of other advantages that should not be overlooked. These benefits are discussed in detail in a recent paper by Domel et al. (2012).

There are two main other advantages. One of these is the ability to use the boundary-layer bleed system as a crude form of variable geometry—as by varying the bleed mass flow the inlet can be tailored to give the engine a variable mass flow. This improves inlet-engine matching and can be used to reduce shock motion caused by slight inlet-engine mismatching. A good example of a bleed system that is capable to correcting for slight inlet-engine mismatching is that utilized on the BAC Concorde (see Leynaert (1966)). The bleed system is also capable of reducing the displacement effect of the boundary layers. This is especially important in mixed compression inlets where excess boundary-layer thickening can lead to an over-contraction, and therefore an inlet unstart. These benefits greatly increase inlet flexibility.

From this short discussion, it has been shown that while boundary-layer bleed is highly capable of reducing the negative impact of SWBLIs, it can contribute significantly to drag. Therefore reducing the amount of bleed employed is highly desirable. Nevertheless, it should be kept in mind that bleed is often used for benefits other than separation suppression and these other advantages cannot be replaced by other boundary-layer control methods.

4.3 Vortex Generators (VGs)

4.3.1 Introduction

Vortex generators (VGs) are a promising alternative to boundary-layer bleed for the mitigation of flow separation. Although VGs are not new (for example see Taylor (1950)) there has only recently been a surge in interest in using them for shock-induced separation control.

VGs generate a streamwise vortex into the near-wall flow, and the simplest type of VG, the vane, is shown in figure 4.5. VGs produce vortices in a very similar way to that produced at the wing-tip of an airfoil, where the flow wraps up at the end of the wing due to the pressure difference between the suction and pressure surfaces—the vane type vortex generator is effectively a very low aspect ratio airfoil protruding from the surface.

The generation of streamwise vorticity is advantageous as it increases mixing in the wall-normal direction. Through this mixing process, higher momentum fluid is transferred down towards the wall and lower momentum fluid is transferred upward away from the wall. As a

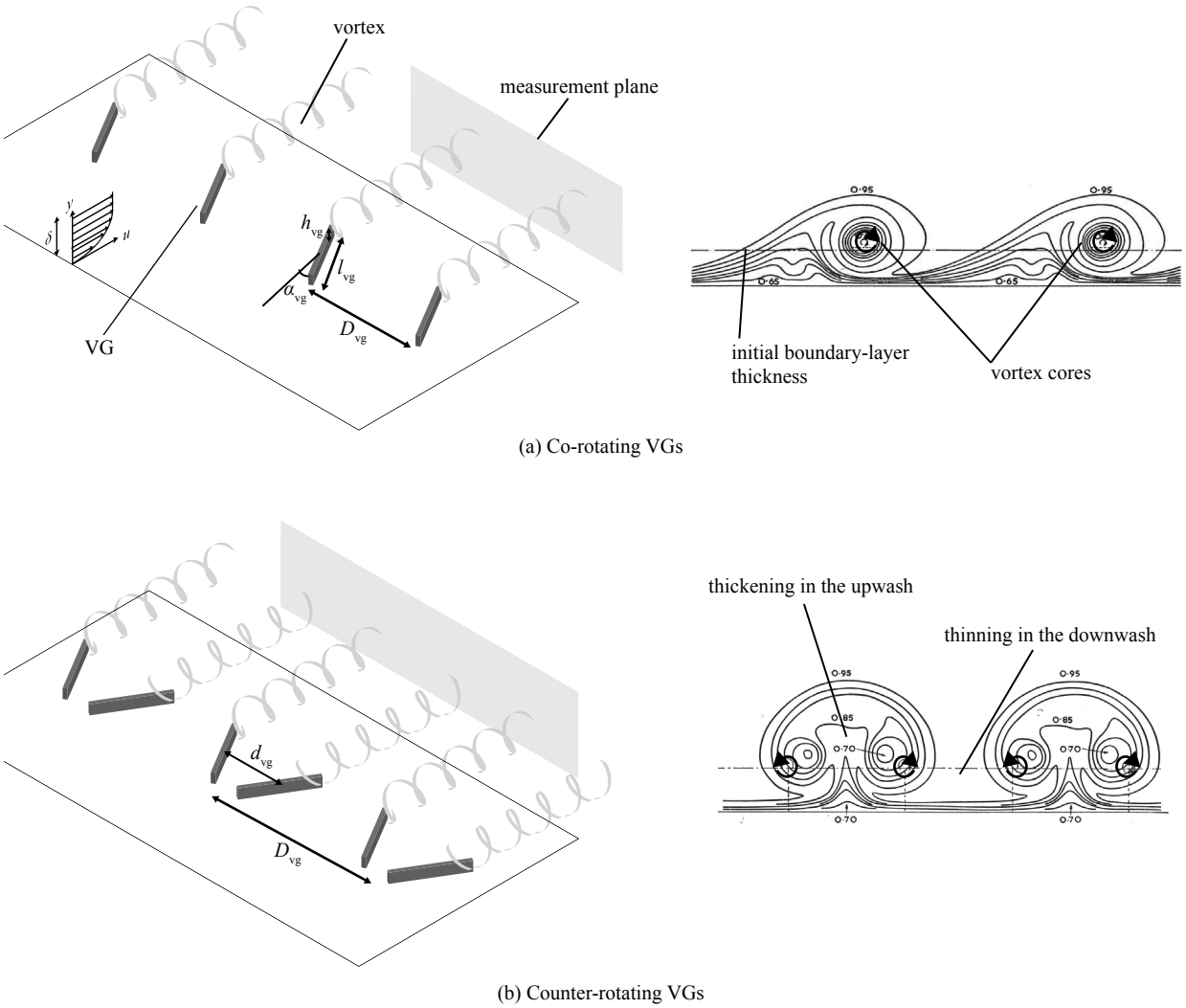

(a) Co-rotating VGs

(b) Counter-rotating VGs

Figure 4.5: Typical VG configurations. Schematic drawing of VGs (left) and resulting flow-field at the measurement plane from Pearcey (1961) (right)

single VG only spans a small area, VGs are nearly always employed in an array. This mixing process is nicely illustrated in figure 4.5.

4.3.2 Vortex generator configurations

One of the first comprehensive studies of vane-type VGs was conducted by Pearcey (1961). In this investigation, Pearcey (1961) expended much effort examining different VG arrays in terms of their spacing and orientation, and found that as these parameters strongly influence the vortex trajectories, they also largely determine the vortices ability to inhibit flow separation. Pearcey (1961) termed this ability to reduce flow separation 'VG effectiveness', and this term has been much used throughout the literature since. Overall, Pearcey (1961) determined that VG effectiveness improved in instances where the vortices dissipated most slowly and when the vortices stayed close to the wall. What soon became clear from the study of Pearcey (1961) and others is the large number of degrees of freedom that are associated with VG design including factors such as VG height, spacing, orientation, streamwise positioning, and VG type.

What is more when VGs are then introduced into an inlet configuration the problem is further complicated. Although some success has been gained using VGs for control in the subsonic portion of inlets (see Wasserbauer et al. (1975)) when introduced for supersonic flow control there are now many additional variables such as shock position and shock strength. Studies using VGs for supersonic flow control in inlets therefore tend to be extremely complex, and, because of this, the few studies that have taken place have generally given inconclusive results (see Mitchell (1971) and Wasserbauer et al. (1996) for example). For this reason amongst others (there is also the reason of cost but this is not detailed here), many more recent investigations have taken place in very simple flow-fields. These have the advantage of being inexpensive, simple and are easy to take measurements in.

One result of more recent fundamental studies has been a general trend towards smaller VGs than those used by Pearcey (1961). While Pearcey (1961) used VGs of a size similar to the boundary-layer thickness ($h \approx \delta$), Rao and Kariya (1988) found that near-comparable separation reduction performance to standard VGs could be obtained using VGs embedded within the boundary layer. This type of VG is often referred to as sub-boundary-layer VGs or micro-VGs (although here they are still just called VGs) and their size is illustrated schematically in figure 4.6. In this investigation, it was found that VGs of height, $h/\delta = 0.3$, gave comparable VG

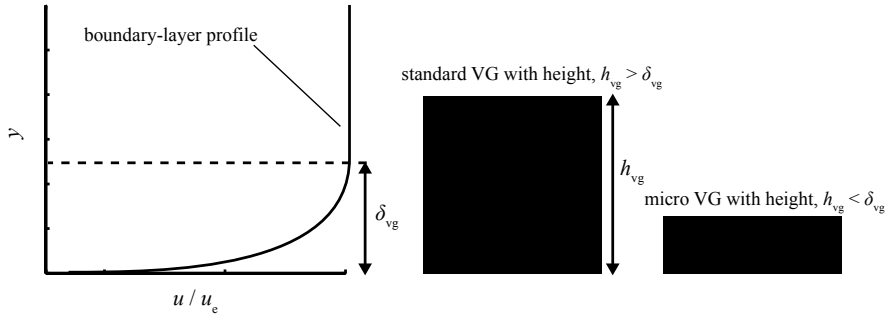

Figure 4.6: Schematic comparison of standard VGs and sub-boundary-layer VGs

effectiveness but with only a fraction of the drag penalty. The reason behind this comparable performance is because momentum transfer is really only required very close to the wall for turbulent boundary layers. Furthermore, the drag benefit of smaller VGs is even greater at supersonic speeds due to the presence of wave drag.

To gain this drag benefit, small VGs, $h/\delta = 0.4$, were utilized by McCormick (1993) who conducted one of the earliest fundamental studies on the control of a SWBLI using VGs. In this investigation, these VGs were found to alleviate the shock-induced separation quite well.

The benefits of small VGs has also been observed in fundamental studies specifically aimed at separation mitigation for supersonic inlet applications, where, both experimentally and computationally, VGs with heights less than the boundary-layer thickness have been found to be optimal. In addition, a preference for smaller VGs as the freestream Mach number is increased has also been noted. For optimal control at transonic speeds (Mach 1.3–1.5) the computational studies of Rybalko et al. (2010) and Lee et al. (2011) concluded that a size $h/\delta = 0.5 - 1$ is near optimal, while in a supersonic oblique SWBLI at Mach 2.5, the experiments of Babinsky et al. (2009) indicate that VGs of size $h/\delta = 0.3$ are preferable. A similar result was obtained in the computations of Lee et al. (2010) at Mach 3.

While height can be semi-optimized by concentrating on a single VG, lateral spacing is more difficult because when trying to eradicate a finite span-wise separation, lateral spacing, height and array size are all highly interlinked. Nevertheless, in general, spacings in the region $7.5h$ have been found to give good VG effectiveness, and insensitivity to this parameter has been demonstrated up to $11.5h$ by Rybalko et al. (2010). In terms of streamwise positioning Rybalko et al. (2010) determined that the flow-field was insensitive across the range $5 - 20h$ upstream of the separation point, and similar observations have been noted by other authors. Other good fundamental VG studies where factors such as spacing were also investigated include Pauley and Eaton (1988) and Ashill et al. (2002).

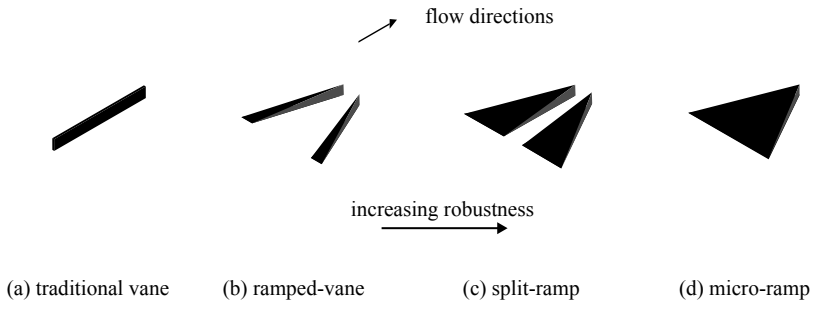

Figure 4.7: A variety of recently employed VG shapes

Due to concerns over the mechanical robustness of vane-type VGs for inlet applications, numerous studies have also investigated other more robust VG shapes. Some of these shapes are shown in figure 4.7. The most widely publicized robust shape is the micro-ramp, a design optimized computationally by Anderson et al. (2006). Since this optimization, the micro-ramp has been one of the most widely used device and the performance of this VG has been investigated by numerous authors, recent examples include Babinsky et al. (2009), Herges et al. (2010), Hirt

et al. (2012), Lee et al. (2010), and Ghosh et al. (2010). While the micro-ramp is certainly robust, other recent studies, however, suggest that the micro-ramp is not the optimal device and hybrid shapes between the ramp and vane have been shown to perform better. In the studies of both Rybalko et al. (2010) and Lee et al. (2011) the ramped-vane (robustness between the vane and ramp) performed significantly better than both the split-ramp and the micro-ramp.

Another area that requires significant attention is the influence of VGs in three-dimensional flows—and specifically near corner flows. Barely any work has been conducted in this area, although some very preliminary investigative work by Li (2008) and Sami (2012) suggests that VGs can be used to manipulate the flows in the corners.

One example of the many recent investigations conducted to determine the potential of VGs for separation mitigation through a SWBLI is shown in figure 4.8. In this figure experiments by Babinsky et al. (2009) and computations by Ghosh et al. (2010) on the same oblique SWBLI are shown side-by-side. This attempt to control an oblique SWBLI is typical of many recent investigations: In both the experiments and the computations the VGs are able to break up the separation but are not able to remove it completely, even after substantial VG optimization.

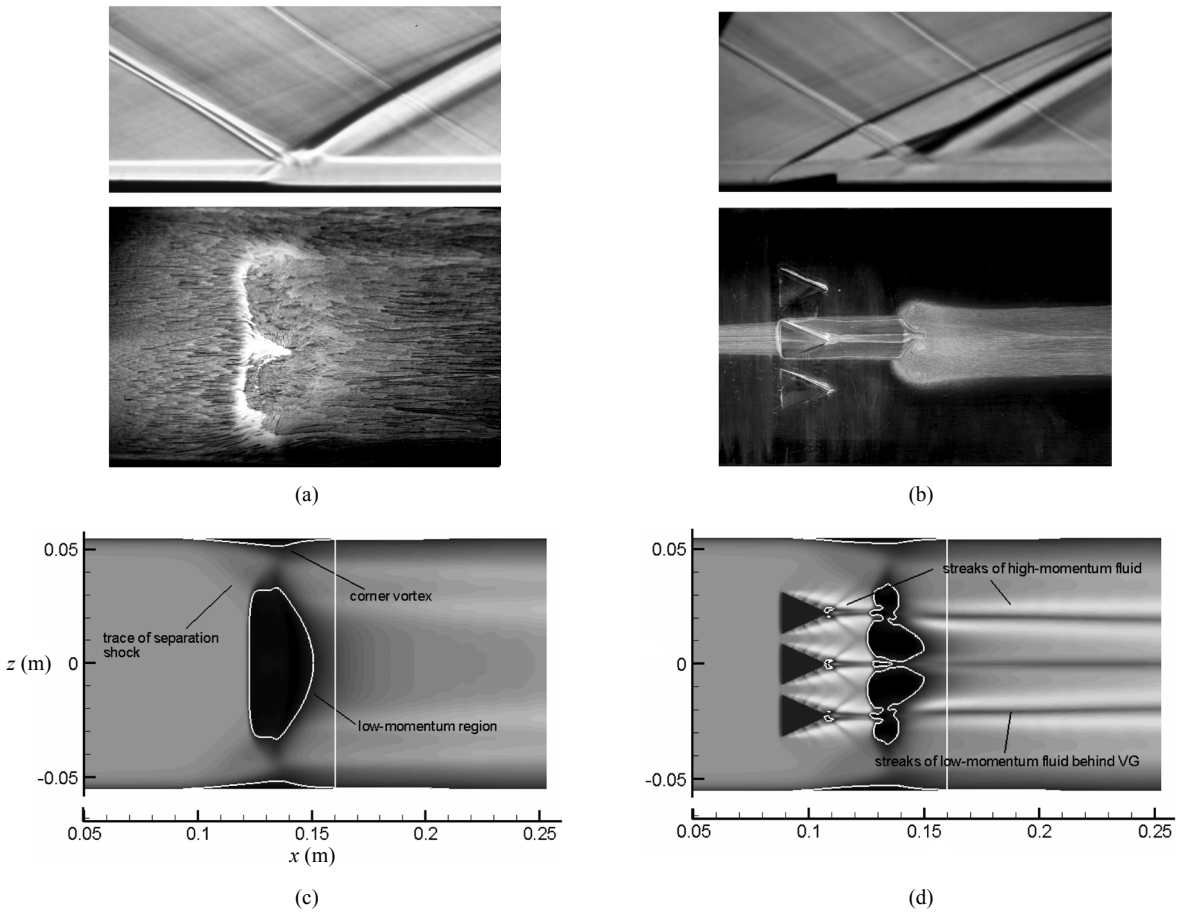

Figure 4.8: Mach 2.5, 7 deg., oblique, reflected SWBLI: (a) schlieren and oil-flow visualization from experiments for the uncontrolled case; (b) schlieren and oil-flow visualization from experiments for the case with VGs (c) near surface velocity contours from computations (light high velocity; dark low velocity); and (d) near surface velocity contours from computations. Experiments by Babinsky et al. (2009) and computations by Ghosh et al. (2010)

Nevertheless, some improvement in the near wall region is obtained downstream of the VGs; in particular, the shape factor downstream is improved across the span. Yet, the inability to eliminate the shock-induced separation indicates that the flow remains undercontrolled.

The main problem with studies such as those shown in figure 4.8 is that they were undertaken in very simple geometries. In this instance, the flow-field is a simple oblique SWBLI but there are also many with a constant-area normal SWBLI. While these configurations make it easy to obtain extensive measurements, it is very difficult to extrapolate from these measurements (often boundary-layer profiles) to real inlet performance. This is because in a real inlets, like those shown in section 2.5, the flow experiences further adverse-pressure-gradients before the engine-face. Yet, in simple geometries these additional flow features are not included. Importantly, it is not obvious how the downstream flow in these simple geometries would perform in these more complex arrangements. For example, while there may be an improvement in the near-wall region in the vicinity of the SWBLI as shown in figure 4.8 it is not known how this different boundary layer would affect the subsequent terminal SWBLI. And in the terminal SWBLI case, it is not clear how VGs would fair through a terminal shock which is immediately coupled to, and therefore strongly influenced by, subsequent diffusion. Accordingly, it is difficult to know how the performance gains obtained in fundamental configurations thus far would translate to improvements in pressure recovery and distortion.

4.4 Other inlet flow control methods

In addition to VGs, many other flow control techniques exist. Some of these also probably have the potential to reduce our dependency on bleed for separation mitigation. Nevertheless, most of these techniques are even less well developed than VGs, and like VGs they have not been utilized in a production inlet, to the author's knowledge.

Some alternatives include tangential blowing, plasma actuators, passive cavities and slots, and air-jet vortex generators. Of course, each of these have their advantages and disadvantages. However, presenting a short review of these alternatives here would not do each of them justice—especially as the author is not an expert in these methods. Instead, for a comprehensive review of recent developments in flow control the reader should refer to Ashill et al. (2005). This paper also has a comprehensive list of references which should help the reader to find further details on each of the flow control methods previously mentioned. Much like VGs much work is still needed before these techniques could be employed on a production aircraft.

Yet, if there is one point to note here, it is that a number of these still involve a significant amount of added inlet complexity which will inevitably increase inlet weight and cost. In comparison, VGs do not suffer from this issue; they are probably the most inherently simple flow control method under development.

Chapter 5

Summary and Objectives

The review of the available literature given in the chapters 2-4 has demonstrated that SWBLIs and their control is one of the most important aspects of supersonic inlet design.

Across an air-vehicle's operating range it is desirable for the inlet to produce high pressure recovery, low spatial and temporal distortion, and low external drag; while at the same time being as lightweight, compact and economic as possible. As a result, flow control is often required to mitigate the detrimental impact of SWBLIs.

Until now, in the majority of supersonic inlets flow control has been provided by a boundary-layer bleed system. At least partial removal of the inlet's boundary layers has a number of benefits, one of which is the mitigation of flow separation. Boundary-layer bleed can be highly successful at dramatically reducing or even eliminating flow separation. While this provides significant performance benefits at the engine-face there is an accompanying drag penalty.

Due to the penalties associated with boundary-layer bleed, there is interest in using other flow control techniques for separation mitigation. Of the alternatives, VGs have shown the most promise. Yet, while some success has been achieved in reducing shock-induced separation, no investigation has demonstrated an overwhelming improvement. This is somewhat concerning. Moreover, unlike the vast majority of bleed systems, most experimental studies of VGs have not taken place in real inlets, but in small fundamental facilities. These are not good representations of inlet flow-fields, and it is therefore difficult to translate the results obtained in these investigations into those that would be achieved in a real inlet. As a consequence, it is impossible to know whether the poor performance in the presence of VGs is due to the VGs themselves or the flow conditions. In addition to the scarcity of investigations with VGs in real inlets, these inlet tests are difficult to interpret and have thus far been inconclusive.

As a result of these difficulties and the numerous advantages of small-scale fundamental experiments, it is suggested that there is much to be gained from further fundamental experiments as long as they are better tailored to make them more inlet relevant. Based on the survey presented here it is thought that a more relevant fundamental normal shock flow-field could be achieved if a downstream adverse-pressure-gradient is introduced downstream of the shock. It is important to include a downstream region of diffusion because inlets almost always have an adverse-pressure-gradient immediately downstream of the terminal shock, and what is important is the flow at the end of this region of further diffusion, i.e., the engine-face. Further to this, in the section on normal SWBLIs it was demonstrated that the presence of a downstream

adverse-pressure-gradient had a highly influential effect on the flow-field.

The aim of this project is therefore two-fold. The first aim is to create a more relevant flow-field than previous studies. This flow must exhibit substantial flow separation so that separation mitigation control methods can be examined using this configuration. The second aim is to then examine VGs in this flow-field to demonstrate whether VGs are a viable alternative to boundary-layer bleed for the purpose of separation mitigation.

Chapter 6

Determining an Inlet Relevant Flow-field

6.1 Overall flow-field configuration

In light of the detailed analysis of the literature, it is thought that for an effective evaluation of inlet flow control in a fundamental scenario it would be preferable for the terminal SWBLI flow-field to exhibit the following features:

- a fixed terminal shock Mach number and incoming boundary-layer thickness
- fully supersonic inflow (outside the boundary layer)
- subsonic diffusion downstream of the transonic shock-wave
- an uncontrolled condition that exhibits large-scale separation such that boundary-layer control is required

In addition to these features the configuration must be amenable to measurements especially the ability to evaluate pressure recovery, and spatial and temporal distortion at some downstream location. It has already been discussed that the three most widely used terminal SWBLI setups—the constant-area duct; the two-dimensional bump; and the diverging duct—do not provide these features. The constant-area duct does not meet bullet point three and possibly four depending on the facility. While, the two-dimensional bump flow does not deliver on either point one or two. The diverging duct configuration fares better but does not meet point one.

A flow-field that is thought to capture all four of these features is shown schematically in figure 6.1. This configuration is here named the spillage-diffuser configuration. The shock holder is utilized in this configuration to help stabilize the shock and should not be compared with a traditional cowl. Without the shock holder it has been shown that it can be difficult to keep the shock at a near-constant streamwise location (see Babinsky and Ogawa (2006). Near to the location of the shock holder, the lower channel which contains the primary flow has an area increase to act as a diffuser. With the terminal shock sitting somewhere upstream this configuration therefore subjects the boundary layer to the combined effects of the adverse-pressure-gradient from the shock-wave followed by the adverse-pressure-gradient from the diffuser. At the same time, importantly, as long as the shock is positioned upstream of the diffuser entrance, the

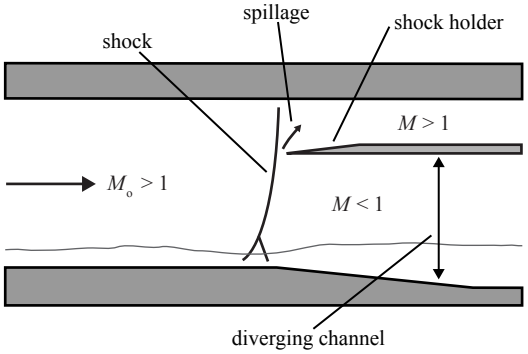

Figure 6.1: Schematic of spillage-diffuser configuration

shock strength and upstream boundary-layer thickness are independent of the spillage, of any downstream separation, and of any flow control. Thus, flow control concepts can be evaluated with consistent conditions.

This flow-field can be considered in either a two-dimensional or axisymmetric configuration. As the wind tunnel used for this investigation is rectangular this configuration is the only one utilized here. The features of this flow-field which are discussed above illustrate that this configuration captures qualitatively the desired flow physics.

6.2 Quantitative considerations related to the spillage-diffuser configuration

To be fully relevant, the test conditions and geometric parameters should also be quantitatively relevant. In order to quantify these parameters a survey of a number of inlets was conducted to determine appropriate values. The inlets that were surveyed have been grouped into two categories: Inlets that were used primarily for investigative inlet studies in wind tunnels, whether as part of the design phase for an active aircraft program or as a standalone fundamental research project. These inlets are referred to as Investigative Inlets, and information about their geometries and the conditions under which they were tested was obtained from the reports that accompanied these programs. These Investigative Inlets and their associated references are listed in the upper half of table 6.1. The second group compromises of inlets that are currently or were previously in service. Details of these inlets are more difficult to obtain from the public domain. For this reason, measurement of the inlet geometries for the majority of these inlets were obtained by physically measuring examples of the aircraft at either the Royal Air Force (RAF) Museum, RAF Cosford or at the Imperial War Museum (IWM) Duxford[1]. The test conditions for each of these aircraft is then based on published data of typical supersonic operating conditions for each design.

It is worth noting that all the inlets surveyed here are of external compression type. This choice was taken to limit the extent of the survey. Such a choice does not indicate that the configuration of figure 6.1 is only relevant to external compression configurations. The spillage-diffuser configuration is thought to have the ability to encompass some of the aspects of both external and mixed compression configurations. While the shock holder does act much like a cowl would in an external compression configuration, its primary purpose is the improvement of shock stability.

The inlet features quantified in this survey are shown in the inlet schematic of figure 6.2, and the inlets that were surveyed are shown in table 6.1.

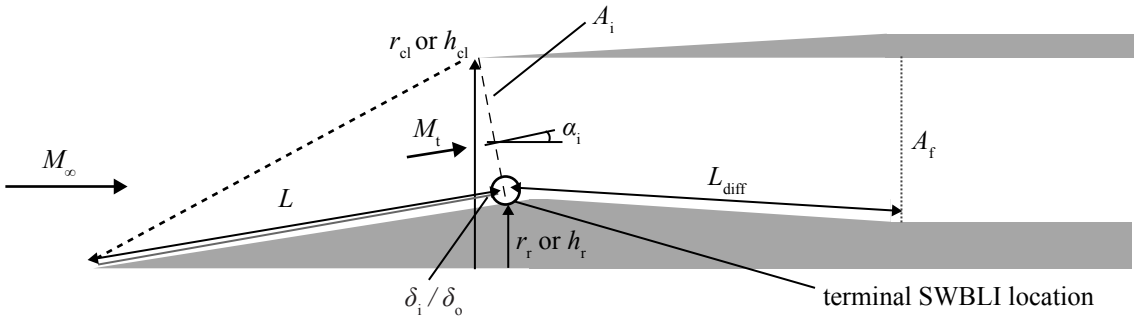

Figure 6.2: Schematic drawing of typical external compression inlet with important parameters labelled

[1]The author gratefully acknowledges the RAF Museum, RAF Cosford and the Imperial War Museum (IWM) Duxford for their cooperation and assistance in obtaining such measurements

Table 6.1: Inlets Surveyed

Inlet Investigations	Inlet type	Reference	Year	Symbol
NACA simple conical	Axisymmetric; 1 oblique shock	Obery et al.	1952	
NACA simple half-conical	Half-axisymmetric; 1 oblique shock	Piercy and Johnson	1953	
NACA simple ramp	2D; 1 oblique shock	Campbell	1954	
NACA double ramp	2D; 2 oblique shock	Obery and Cubbinson	1954	
RAE simple conical	Axisymmetric; 1 oblique shock	Goldsmith	1956	
NACA double ramp no. 2	2D; 2 oblique shock	Beheim and Gertsma	1956	
NACA double cone	Axisymmetric; 2 oblique shock	Conners et al.	1957	
RAE double ramp	2D; 2 oblique shock	Neale and Lamb	1962	
NACA double cone no. 2	Axisymmetric; 2 oblique shock	Calogeras and Meleason	1968	
RAE double ramp no. 2	2D; 2 oblique shock	Fisher et al.	1972	
RAE double ramp no. 3	2D; 2 oblique shock	Brown and Goldsmith	1975	
NASA HiMAT inlet	2D; Pitot with upstream splitter plate	Neumann et al.	1980	
MCAIR double ramp	2D; 2 oblique shock	Mark et al.	1989	
Unitary Plan double ramp	2D; 2 oblique shock	Loth et al.	2004	
Techland parametric inlet	3D; 1 oblique shock plus isentropic compression	Slater et al.	2005	
Gulfstream conical	Axi; 1 oblique shock plus isen. compression	Rybalko et al.	2010	

Inlets	Inlet type	Reference	Year	Symbol
English Electric Lightning	Axisymmetric; 1 oblique shock	IWM Duxford	1957	
McDonnell Douglas F-4J	2D; 2 oblique shock	IWM Duxford	1958	
BAC TSR2	Half-axisymmetric; 1 oblique shock	RAF Cosford	1964	
General Dynamics F-111A	Quarter-cone; 2 oblique shock	IWM Duxford and Burcham Jr. and Bellman	1964	
SEPECAT Jaguar	2D; Pitot	RAF Cosford	1968	
Aérospatiale/BAC Concorde	2D; 2 oblique shock	IWM Duxford	1969	
McDonnell Douglas F-15A	2D; 2 oblique shock	IWM Duxford	1972	
General Dynamics YF-16	3D; Pitot with splitter plate	Hawkins	1974	
Northrop YF-17	3D; 1 oblique shock	Wong	1974	
Panavia Tornado	2D; 2 oblique shock	RAF Cosford	1974	
Eurofighter Typhoon	2D; 1 oblique shock	IWM Duxford	1994	
McDonnell Douglas F/A-18E	3D; Caret	Hall et al.	1995	

6.3 Choice of terminal shock Mach number

As was discussed at length in chapter 3 one of the most influential parameters in the terminal SWBLI is the terminal shock strength (M_t). To ascertain the range in which M_t typically falls for inlets, where reported or computable, M_t for inlets in table 6.1 were collated and these data are plotted versus M_∞ in figure 6.3. Investigative inlets are shown in figure 6.3a and inlets that are/were operational are shown in figure 6.3b. Although there is significant scatter, looking more closely some trends are evident. In the investigative studies there is a trend of increasing M_t with M_∞, and this is probably due to the inability to produce ever-more compression without undesirable levels of complexity as M_∞ increases. Interestingly, this trend is not evident in the plot of operational inlets. More information, which may help to explain these observations, can be inferred from these figures, if you look at the chronological development. In the investigative studies there is a general trend of decreasing M_t over time, with the vast majority of high M_t studies being very early—many of which produced unacceptably low pressure recovery. On the other hand, the trend for operational inlets is more conservative: early inlets such as the Lightning and F-4 utilized low M_t close to 1.3 while more recent designs have employed higher M_t such as the YF-17 and F/A-18E. This desire to use higher M_t is almost certainly to reduce inlet complexity. The reason why this trend is not also observed in the investigative studies is unclear; however, it is perhaps because investigations with higher M_t are usually for military applications and recent data for such aircraft is either classified or at least proprietary. Even with all the conflicting objectives for the inlet designer, in both plots there is a visible clustering of data around Mach 1.4. Accordingly, this is a reasonable starting point for a fundamental study for boundary-layer flow control. Yet, investigations at Mach numbers in the range 1.3-1.8 would also be relevant and desirable.

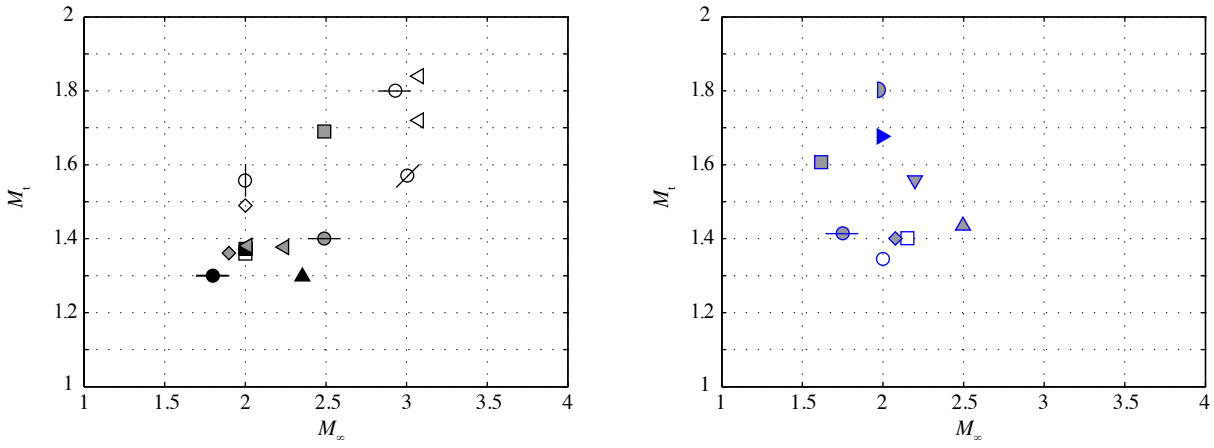

(a) Investigative studies

(b) Flight inlets

Figure 6.3: The variation of terminal shock Mach number with freestream Mach number

6.4 Choice of subsonic diffuser

The other adverse-pressure-gradient that needs to be considered is that of the subsonic diffuser. The subsonic diffuser total area change and the area variation as a function of streamwise distance for the inlets in table 6.1 were calculated where attainable. These quantities were then put in non-dimensional form such that the overall/diffuser area ratio was the area at the engine face divided by the area at the cowl ($A_\mathrm{f}/A_\mathrm{i}$) and the diffuser length was divided by the engine face diameter ($L_\mathrm{diff}/D_\mathrm{f}$).

The relationship between $A_\mathrm{f}/A_\mathrm{i}$ and $L_\mathrm{diff}/D_\mathrm{f}$ gives a first-order approximation of the severity of the adverse-pressure-gradient within the diffuser. This first-order approximation is shown for a number of the inlets in table 6.1 in figure 6.4. The further up and to the left the point, the more aggressive the subsonic diffuser is. This fact is emphasised by the addition of three curves in figure 6.4 which indicate different performance regimes for incompressible two-dimensional diffusers as found by Kline et al. (1983): the line A-A separates stalled diffusers from those with no appreciable stall; the line max C_p indicates the maximum performance configuration; and above line B-B the flow is fully stalled. Viewed in this context, it can be seen that the relatively low area ratio of the majority of the inlets results in a large number of inlets lying below the stall and maximum performance curves. When comparing investigative studies and operational inlets there is less difference than before; although there is a general trend for the operational inlets to be more cautious (further to the right).

The fact that nearly all the points lie below curve A-A is not necessarily surprising, as unlike the boundary layer in the experiments of Kline et al. inlet boundary layers must endure the adverse-pressure-gradient of the terminal shock and then the adverse-pressure-gradient of the diffuser. Yet, in almost all of these inlets, boundary-layer bleed is utilized indicating that the SWBLI is highly detrimental to the performance of the inlet. It can be postulated that if bleed or another control method could be improved such that the viscous flow downstream of the throat is no worse than the nature turbulent boundary-layers of Kline et al. then the subsonic diffusers of a number of these inlets could be made somewhat more aggressive.

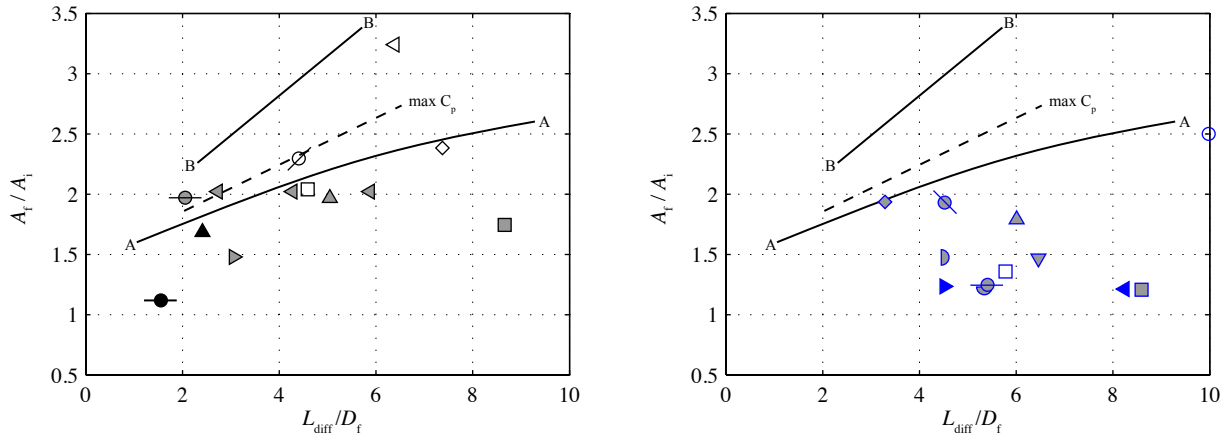

(a) Investigative studies

(b) Flight inlets

Figure 6.4: Diffuser area ratio vs. non-dimensional length (curves from Reneau et al. (1967))

In instances where the streamwise variation through the diffuser was also available these data were also collated and are plotted in figure 6.5. In this figure, the local area variation is shown normalized by the net area increase, and the length along the diffuser is normalized by the total diffuser length. Figure 6.5 illustrates that there is a wide range in the way diffusers are profiled. In general, though, the area increase tends to increase gradually then reach a maximum slope near the middle of the diffuser and taper off gradually. Some designs even exhibit a slight contraction downstream of the cowl lip with the aim of providing a short region of favourable-pressure-gradient just downstream of the terminal shock. This can sometimes lead to too much re-acceleration and has generally been avoided in more recent designs.

In addition to some of the inlets of table 6.1, the area distributions of two well-known diffuser designs are also shown in figure 6.5: the Stratford distribution (Stratford (1959)) and a standard linear Mach number distribution. The Stratford distribution is an aggressive diffuser design with the aim of decreasing the skin-friction losses by keeping the boundary-layer near the point of separation. It turns out that this can be accomplished by using strong diffusion in the initial part of the diffuser which is then gradually decreased thereafter. In contrast, in the linear Mach number configuration is a much more conservative design which employs slow diffusion near the entrance which gradually increases downstream. These two curves nicely bound the data and imply that a compromise between these two has generally been found to be preferable. This suggests that a subsonic profiling somewhere between these two extrema would be suitable for a canonical test case. The most obvious profiles that lie within this are the linear area variation and the sinusoidal area variation. These are seen as good starting points as both of these are reasonable approximations (at least on average) to the designs in figure 6.5 and they are very simple with the linear area profile being the simplest design possible.

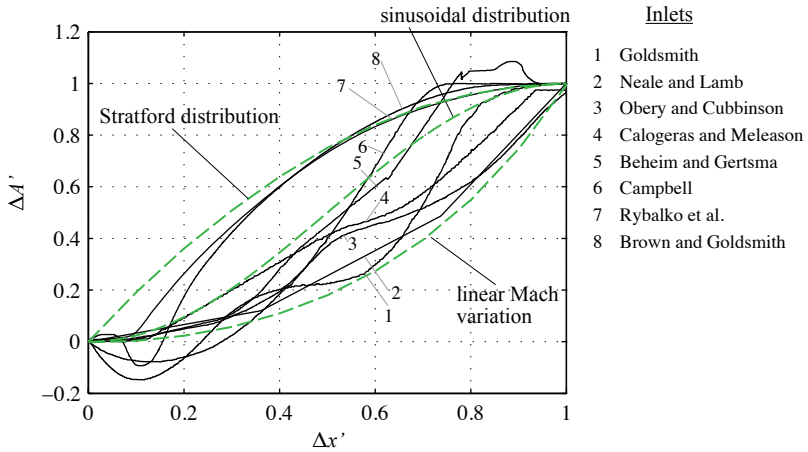

Figure 6.5: Non-dimensional area variation in diffusers of sample inlets

6.5 Choice of confinement ratio

Turning to the influence of the extent of viscous flow at the start of the interaction, the confinement, C, is calculated with knowledge of the boundary-layer thickness. Hence to calculate C for the inlets in table 6.1 the boundary-layer thicknesses at the terminal shock must be known. Unfortunately, in the vast majority of these wind tunnel inlet tests, the boundary-layer thickness was not measured. As a result, it was decided to estimate the boundary-layer thickness empirically based on the compression surface length, L, and the compression surface Reynolds number, Re_L, which according to White (2006) can be approximated as

$$\delta_{\mathrm{o}} \simeq \delta_{\mathrm{i}} \simeq 0.16 L Re_L^{-1/7}, \tag{6.1}$$

where Re_L is based on wind tunnel test conditions in the investigative studies and based on the maximum design Mach number of the operational inlets at typical atmospheric conditions, i.e., based on M_∞, ρ_∞, and T_∞. It is also assumed that the boundary-layer thickness at the start of the interaction, δ_{o}, is equal to that at the inlet entrance, δ_{i}, which is a good approximation as long as the terminal shock is close to the inlet entrance—which it is under most conditions.

With this estimate for δ_i and knowledge of the inlet geometry, C can be estimated. For axisymmetric configurations C can be calculated according to equation 6.2.

$$C_{\mathrm{axi}} \simeq \frac{2\pi(r_{\mathrm{r}}/cos\alpha_{\mathrm{i}})\delta_{\mathrm{i}}}{(\pi r_{\mathrm{cl}}^2 - \pi r_{\mathrm{r}}^2)/cos\alpha_{\mathrm{i}}} = \frac{2\delta_{\mathrm{i}}/r_{\mathrm{r}}}{(\frac{r_{\mathrm{cl}}}{r_{\mathrm{r}}})^2 - 1} \tag{6.2}$$

where each variable is defined in figure 6.2. For the two-dimensional cases, there are often two different boundary layers at the plane of the interaction: the boundary layer on the ramp (δ_{ir}) and the boundary layer on the sideplates/sidewall (δ_{ip}). δ_{ir} can be calculated in much the same way as in the axisymmetric case but with addition of the inlet width as well as the cowl and compression surface heights. However, the contribution from the sideplates is a little more involved as the sideplates usually extend from the start of the compression surface to the cowl. Thus there is a variation in the sideplate length which varies from the compression surface length, L, at the compression surface to 0 at the cowl. While you could integrate the contributions across the sideplates this would be unnecessarily complicated—especially when so many simplifying assumptions have already been made. Consequently, it is just roughly estimated that $\delta_{\mathrm{ip}} = \delta_{\mathrm{ir}}/2$ as the length of the sideplates will be on average approximately half the compression surface length. The resulting equation for C is given by equation 6.3.

$$\begin{aligned} C_{\mathrm{2d}} &\simeq \frac{w_{\mathrm{r}}\delta_{\mathrm{ir}}}{w_{\mathrm{r}}(h_{\mathrm{cl}} - h_{\mathrm{r}})/cos\alpha_{\mathrm{i}}} + 2\left(\frac{(h_{\mathrm{cl}} - h_{\mathrm{r}})(\delta_{\mathrm{ip}})/cos\alpha_{\mathrm{i}}}{w_{\mathrm{r}}(h_{\mathrm{cl}} - h_{\mathrm{r}})/cos\alpha_{\mathrm{i}}}\right)_{\mathrm{sideplate}} \\ C_{\mathrm{2d}} &\simeq \left(\frac{1}{(h_{\mathrm{cl}} - h_{\mathrm{r}})/cos\alpha_{\mathrm{i}}} + \frac{1}{w_{\mathrm{r}}}\right)\delta_{\mathrm{ir}} \end{aligned} \tag{6.3}$$

The confinement data calculated using this approach are presented versus M_∞ in figure 6.6. In figure 6.6a values of C are also shown for instances where boundary-layer data was available from either CFD or experiments from the Investigative Inlet study (the same symbol is shown repeated with a superscript to indicate the method of calculation). While the empirical approach

to calculating C presented here is relatively crude, it can be seen that good agreement is obtained between this data and that obtained by experiments and CFD, with a deviation of around 10%.

Looking at the variations in C, what is immediately clear is the difference between the confinement of the investigative and that of the operational inlets. While the investigative studies have C values extending from 2-20%, those of operational inlets are all less than 8%. The cause of this difference is thought to be the combined effects of lower unit Re and smaller-scales in the investigative studies—both of which lead to thick boundary layers.

Aside from this difference, both sets of data exhibit a trend of increasing C with M_∞. This is consistent with the desire for more compression at higher speeds which results in a smaller cowl area relative to compression surface length. The compression surface also ends up being longer due to the decreasing shock angle at higher Mach numbers.

The two outliers in figure 6.6a are worth noting. These early configurations have low confinements for their Mach number because they utilized only minimal supersonic compression. While this reduced confinement is desirable it comes with an unacceptably high M_t (see figure 6.3) which results in very low pressure recovery. Even leaving these outliers to one-side it is difficult to conclude what a typical level of confinement is. Nevertheless, as a starting point for a canonical test-case somewhere in the region of 5-10% is acceptable.

Strongly coupled to the confinement is the influence of the Reynolds number itself. For a fundamental study this should ideally lie somewhere in the range typically experienced in flight, i.e., 5 to 25 $\times 10^6$ /m.

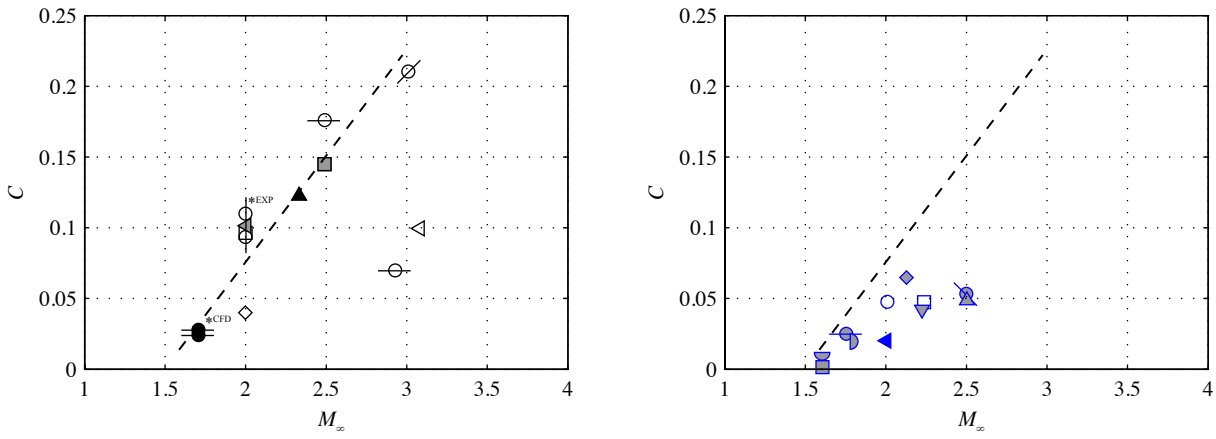

(a) Investigative studies

(b) Flight inlets

Figure 6.6: The variation of confinement with freestream Mach number

6.6 Aspect ratio

Another factor that is important when considering a two-dimensional 'spillage-diffuser' configuration is the aspect ratio (AR), where

$$\begin{aligned} AR &= w_\mathrm{i}/h_\mathrm{i} \\ &= \frac{w_\mathrm{i} cos\alpha_\mathrm{i}}{h_\mathrm{cl} - h_\mathrm{r}} \end{aligned} \tag{6.4}$$

Although partially constrained by the wind tunnel geometry, the aspect ratio can be varied by moving the height of the shock holder. The aspect ratio for the inlets in table 6.1 were calculated to determine a range of typical aspect ratios.

The resulting data are presented in Fig. 6.7, where $1/AR$ is plotted versus freestream Mach number. In Fig. 6.7 it can be seen that there is significant scatter, but that inverse aspect ratios of 0.5 or less are common at higher Mach numbers and that none of the inverse aspect ratios are more than 0.8. This suggests that the 'spillage-diffuser' configuration should be ideally employed with an aspect ratio of unity or more ($1/AR \leq 1$). Furthermore, the influence of the sidewalls in the 'spillage-diffuser' configuration will be exaggerated when compared to an actual inlet. This is because the 'spillage-diffuser' will have a sidewall boundary layer thickness similar to that along the floor; whereas in a real inlet configuration the sidewall boundary layers are generally thinner that that on the compression surface since the sideplates are (on average) shorter than the ramps.

As a result, it is suggested that a two-dimensional 'spillage-diffuser' geometry ideally employ an aspect ratio in the region 2 to 3 ($1/AR \leq 0.33 - 0.5$).

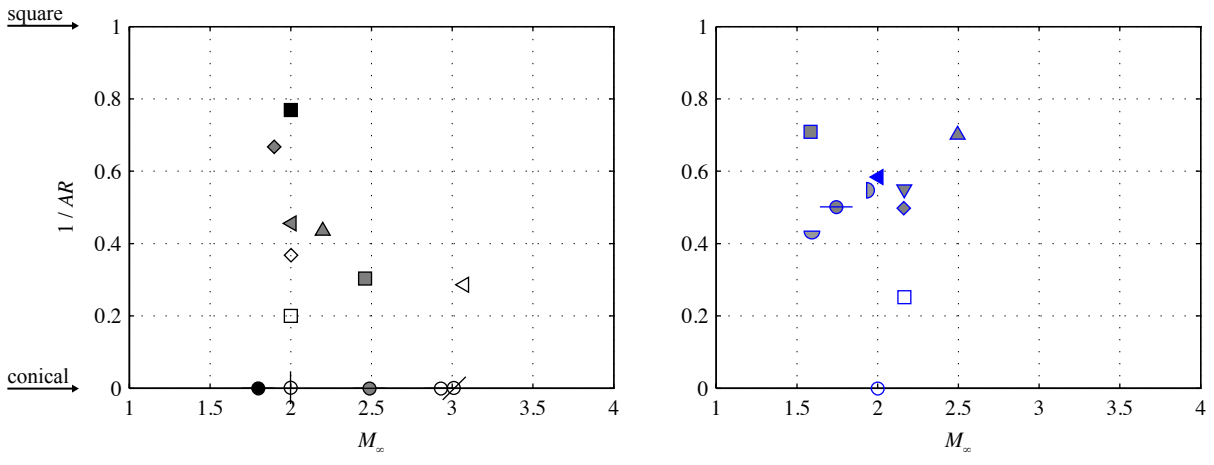

(a) Investigative studies

(b) Flight inlets

Figure 6.7: The variation of aspect ratio with freestream Mach number

Chapter 7

Experimental Configuration

7.1 Wind tunnel facilities

7.1.1 Overview

The experiments conducted herein were undertaken in supersonic wind tunnel no. 1 in the University of Cambridge Aeronautics Laboratory. This wind tunnel, which was built in the late 1950's, is an intermittent blowdown type tunnel with a working section 178 mm high and 114 mm wide (7 in by 4.5 in) and is capable of Mach numbers in the range 0.7 to 3.5.

The layout of this wind tunnel is shown schematically in figure 7.1. The wind tunnel is powered by two compressors which are used to pressurize 24 storage tanks of total capacity 15 m^3 (528 cubic feet). These storage tanks are held at a constant temperature of 60°C to avoid low temperatures at the exit of the tanks (the necks of the bottles) during depressurization. The charging of the storage tanks typically takes 20 to 30 minutes and wind tunnel runs last between 20 seconds and 1 minute depending on the configuration.

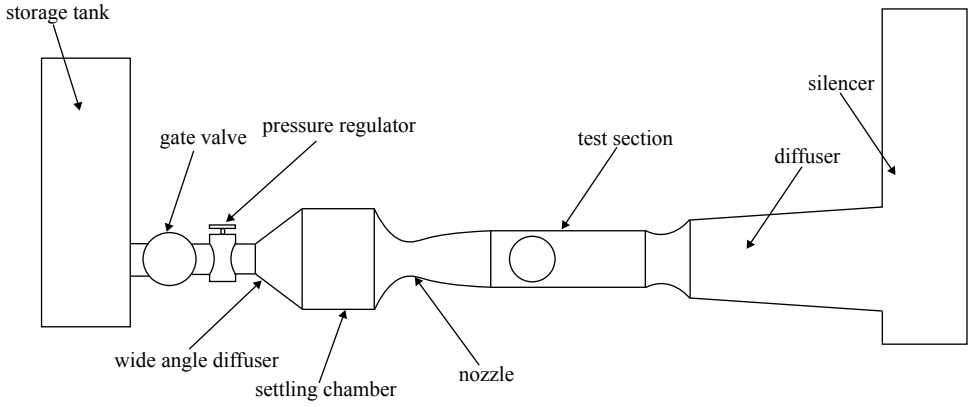

Figure 7.1: Diagrammatic layout of intermittent blowdown wind tunnel (adapted from Pope and Goin (1965))

The release of air from the storage tanks is controlled by the tunnel operator who controls the pressure regulator which alters the mass flow of air through the system. Once past the pressure regulator, the air is mixed in the wide angle diffuser and cleaned up in the settling chamber. It then passes through the convergent-divergent nozzle which accelerates the flow to

the required supersonic Mach number, before entering the test section. It is in this region that measurements are taken before the air is exhausted to atmosphere via a diffuser and silencer.

7.1.2 The wide angle diffuser and settling chamber design

The wide angle diffuser and settling chamber are integral parts of the wind tunnel as they play a critical role in determining the characteristics of the flow entering the working section. As the details of these sections of the wind tunnel are not particularly well-known, while they were recently accessible detailed measurements of these section was collated. It is thought worthwhile to report these details here, and, for this reason, a detailed schematic is shown in figure 7.2, and a short description of their operation follows.

As shown in this figure, the flow enters the diffusing section from the storage tanks via the driving valve in a turbulent and unsteady manner. In addition to diffusing the flow to reduce its velocity, a large cruciform flow spreader is used to thoroughly mix the flow before it enters the settling section. In this section, the flow passes through a number of devices to improve the flow quality. Firstly, a fine mesh screen to further promote uniformity and to reduce the turbulence level. Secondly, through honeycomb straighteners to eliminate swirl so that the flow is purely axial and then a spacer section followed by three more screens. Finally the flow is contracted while at the same time the area changes from a circular to rectangular cross section, before passing into the nozzle.

Recent measurements at the end of the settling section / beginning of the nozzle (far right of figure 7.2) indicate that the flow is very uniform at this location. Using an array of Pitot probes no variations larger than the measurement error of the transducers (less than 0.1% of p_0) was detected at this plane.

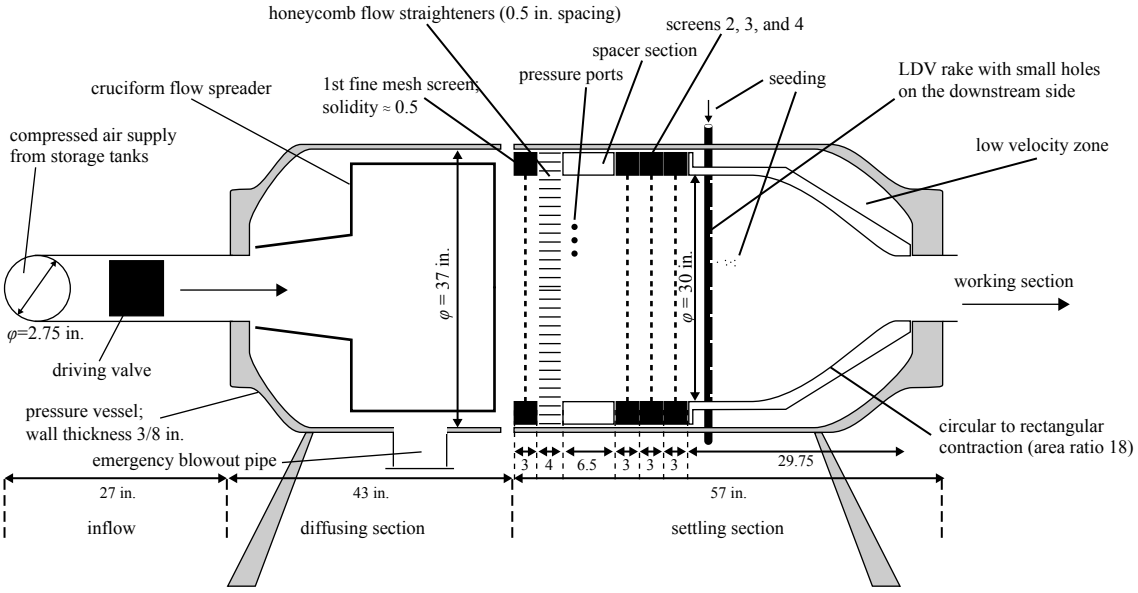

Figure 7.2: Schematic diagram of wind tunnel wide angle diffuser and settling section (dimensions in in.)

7.1.3 The Nozzle and test section design

The nozzle and test section geometry can be varied easily as the wind tunnel was designed to accommodate interchangeable blocks. Consequently, the nozzle exit Mach number can be easily changed by interchanging the nozzle blocks, and the geometry downstream of the test section can be altered so that a variety of geometries can be accommodated.

The wind tunnel nozzles and working section utilized throughout this investigation is shown in figure 7.3. Further, pictures of this configuration installed in the wind tunnel are shown in figure 7.4.

As discussed in chapter 6, this geometry was designed to provide a more representative flow-field for inlet applications than previous studies. To produce supersonic flow, symmetric nozzle blocks are positioned at the upstream end of the test section. As each set of nozzle blocks is

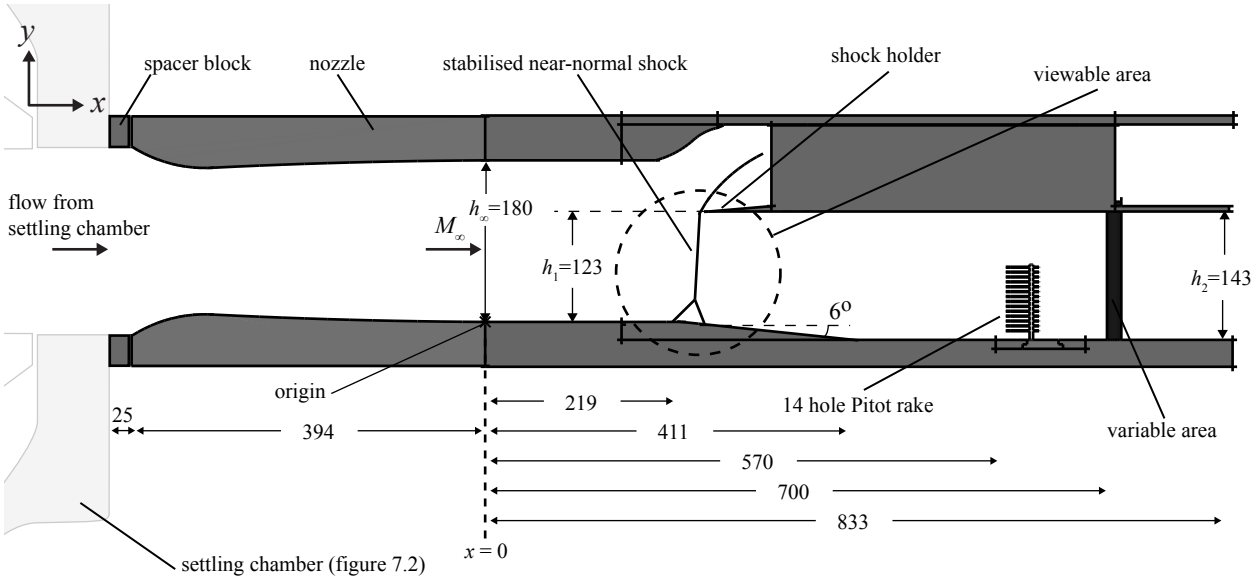

(a) side-view of nozzle and test section

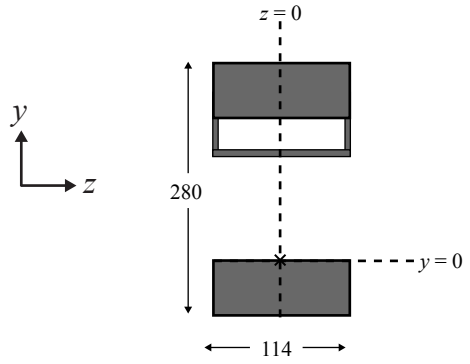

(b) end view of nozzle and test section
(view from settling chamber)

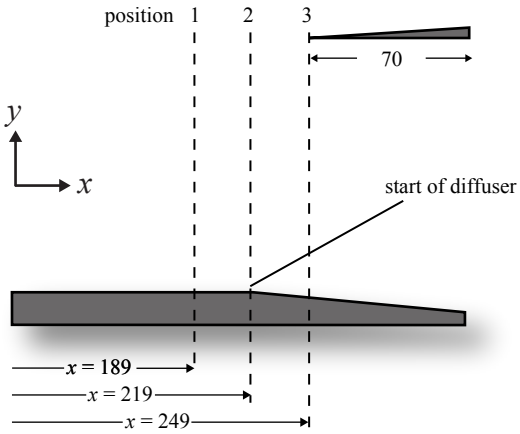

(c) more detailed side-view of shock holder and diffuser region

Figure 7.3: Nozzle and test section configuration

of fixed geometry a variety of nozzle blocks are available for this facility and are interchanged to create the desired Mach number. As Mach 1.4 was determined to be an appropriate Mach number in chapter 6 this nozzle set was utilized throughout this investigation.

Downstream of the nozzles, a new working section geometry was fabricated to produce the desired terminal shock and diffuser configuration. This configuration was designed and built in-house. The upstream portion of the configuration is just a parallel section, which is included downstream of the nozzles for two reasons. Firstly, to allow the boundary layer to return to a zero-pressure-gradient state as the nozzle provides a high favourable-pressure-gradient. More importantly, though, the parallel section continues to the location of the window so that the primary area of interest, the end of the parallel section and the start of the diffuser, is viewable through the tunnel windows.

On the basis of the review of inlet subsonic diffuser profiles, it was decided to create the diffusing section in the lower channel using a simple linear area expansion from the position $x = 219$ mm. This was decided as this is the easiest design to manufacturer. The area available for diffusion is limited by the physical constraints of the wind tunnel working section, and this led to an area ratio, h_2/h_1, of 1.16, which was achieved using an angle of 6^o and this gives a similar non-dimensional overall sizing as the Gulfstream inlet shown in figure 6.4a.

To position the terminal shock near to the diffuser entrance, the shock holder is also located within this region. The mounting for the shock holder was developed so that its streamwise position can be varied to adjust the adverse-pressure-gradient immediately downstream of the shock. This introduces flexibility which is desirable as there was quite a variation of the initial adverse-pressure-gradient in the inlet survey. As a result, the shock holder could be positioned in three different positions: directly above the diffuser entrance, and 30 mm upstream and downstream of this location.

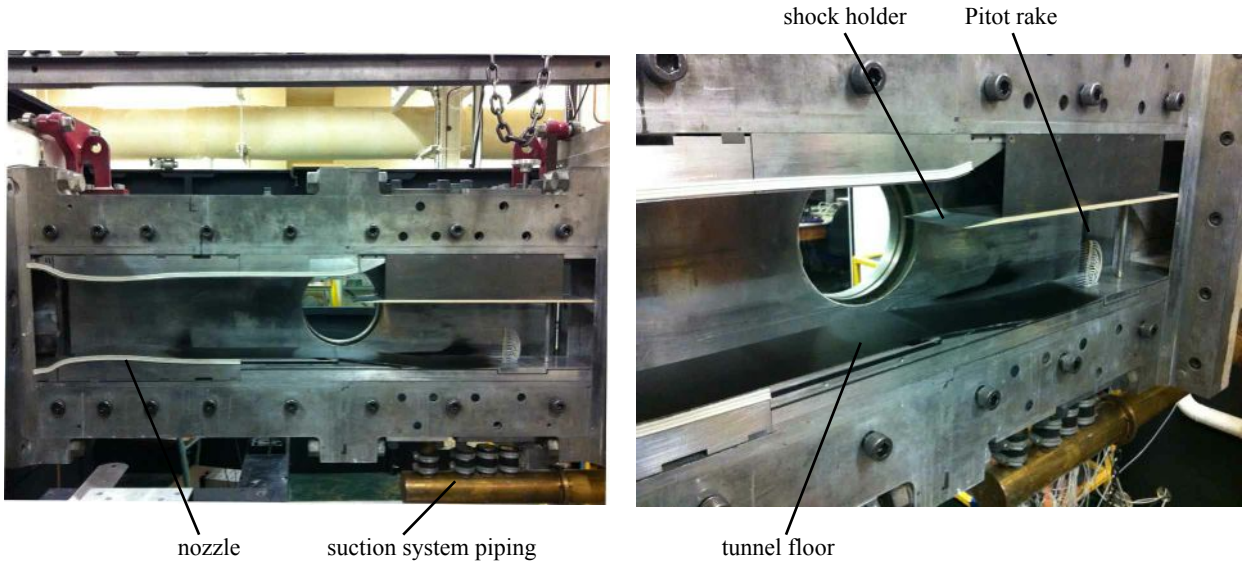

Figure 7.4: Pictures of the wind tunnel configuration used throughout this investigation

The vertical position of the shock holder was chosen to be consistent with previous studies at $h_1 = 123$ mm (for example those of Babinsky and Ogawa (2006), Bruce (2008) and Sami (2012)).

This leads to an approximate confinement of around 13% based on a boundary layer thickness at the start of the interaction of 6.5 mm (see chapter 9). This height also set the aspect ratio, $AR = 0.93$ (the tunnel tunnel width is permanently fixed at 114 mm). While this geometry results in a confinement that is higher and an aspect ratio that is lower than those of typical inlet configurations, it was decided not to adjust this because this would introduce unwanted complexity, in the form of redesigning the section above the shock holder. Furthermore, while reducing the height of the shock holder would increase AR, it would also increase C further, and vis versa. Thus, it was decided to leave the shock holder unchanged. Above the shock holder, the working section is expanded to avoid choking so that the flow over the shock holder remains supersonic someway downstream.

The positioning of the Pitot rake is clearly visible from the figure which acts as the effective AIP. Downstream of here, there is an elliptical cylinder which is used to vary the area at the downstream end of the lower channel to allow the position of the shock to be altered. The positioning of the elliptical cam could be altered during a tunnel run which was used in conjunction with the schlieren system to position the shock. Details of the precise location of the salient features of this configuration are shown in figures 7.3 and 7.4.

7.2 Wind tunnel operating conditions

The wind tunnel stagnation pressure is set by the wind tunnel driver and was set to 15 psi (103.4 kPa) gauge throughout this investigation—the maximum pressure permissible with the rectangular windows utilized throughout. The gauge pressure can be controlled to a degree of accuracy better than 0.5% by the wind tunnel driver. This pressure variation combined with the variation in the atmospheric pressure from day-to-day are shown in table 7.1, and these result in an absolute pressure range of 200–210 kPa.

The stagnation temperature of the flow has been measured to be in the range 293 ± 3K using a thermocouple placed into the settling chamber. The stagnation temperature does not tend to vary substantially with the atmospheric conditions because the storage tanks are held at a constant temperature.

Combining these conditions with the nozzle exit Mach number allows the Reynolds number to be determined from equation 7.1.

$$Re = \frac{\rho_\infty u_\infty}{\mu_\infty} = \left[1 + \frac{(\gamma - 1)}{2} M_\infty^2\right]^{-1/\gamma - 1} \left(\frac{\gamma}{R T_{0\infty}}\right)^{1/2} \frac{M_\infty p_{0\infty}}{\mu_\infty} \tag{7.1}$$

where μ_∞ is calculated using Sutherland's law:

$$\mu_\infty = \frac{(1.458 \times 10^{-6}) T_\infty^{3/2}}{(T_\infty + 110.4)} \tag{7.2}$$

Table 7.1: Wind tunnel test conditions

quantity	mean value (SI units / measured units)	variation
p_{atm}	101.6 kPa (30 inHg)	±5.1 kPa (±1.5 inHg)
$p_{0\infty\text{gauge}}$	103.4 kPa (15 psi)	±0.35 kPa (±0.05 psi)
$p_{0\infty}$	205 kPa	± 5 kPa
$T_{0\infty}$	293 K (20°C)	±3 K
M_∞	1.40	±0.01
Re	31.5×10^6	$\pm 1.5 \times 10^6$

The result is a Reynolds number in the range 30–33 $\times 10^6$ with the variation occuring due to the atmospheric variation in stagnation pressure and temperature. While there is a maximum possible variation in the Reynolds number of 10% this is insignificant at such high Re. All of these data are summarized in table 7.1.

At a Mach number of 1.4 and a unit Reynolds number of 31.5 million wind tunnel run times are in the region of 20 seconds.

7.3 Wind tunnel suction system

In some of the experiments conducted during this investigation, boundary-layer suction was required. This was provided by an ejector system that was added to the wind tunnel during the 1990's. The ejector system is powered by the high pressure air from the wind tunnel which is used to drive a hypersonic nozzle which has a very low working pressure. This low pressure air is used to entrain flow from the working section. The operation of the wind tunnel ejector system is nicely illustrated in the schematic diagram shown in figure 7.5

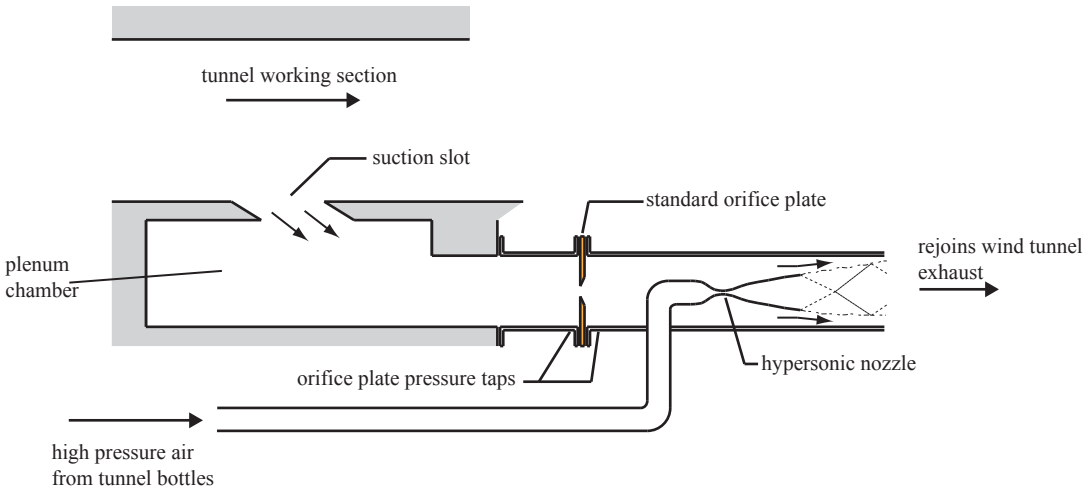

Figure 7.5: Schematic diagram of wind tunnel ejector system

The suction system plenum chamber is usually placed beneath the location in which suction is required. In this instance, the plenum chamber was positioned directly below the parallel section between the nozzle blocks and the start of the diffusing section. This section was manufactured in such a way that the top 5 mm of this section was interchangeable which allowed different plates to be incorporated here. When no suction was required, as in the baseline case, the plate was just blank with no holes or slots. However, when suction was required, this plate was manufactured to integrate suction slots at the desired location. An example plate with integrated suction slots is shown schematically in figure 7.6. Only results obtained with the suction slots in this position are presented in this investigation. This position and slot configuration was chosen as it was found to work well in the preliminary suction experiments of Bruce et al. (2011) and the experiments of Sami (2012). This position is thought not to be too far upstream such that the influence of the slots is diminished, but at the same time upstream of the terminal shock such that a complex shock/slot interaction is not introduced.

The mass flow bled from the working section is measured using an orifice plate downstream of the plenum chamber according to the following equation:

$$\dot{m} = \bar{\dot{m}}(M)\frac{C_d A_{\text{orifice}} p_{0,\text{orifice}}}{\sqrt{c_p T_{0,\text{orifice}}}} \tag{7.3}$$

If a small enough orifice plate is utilized such that the ejector is powerful enough to choke

the suction system at the orifice plate then the non-dimensional mass flow function is constant at 1.281 and the coefficient of discharge for the orifice plate can be approximated as 1 (see Bragg (1960)). In such cases, the mass flow can be calculated with the knowledge of $p_{0,\text{orifice}}$ which is obtained from the upstream wall-pressure tapping (with the downstream tapping only used to verify the flow is choked), A_{orifice} which is fixed, and $T_{0,\text{orifice}}$ which is assumed equal to the settling chamber $T_{0\infty}$. The wall pressure tappings used to measure $p_{0,\text{orifice}}$ and to check the orifice plate is choked are shown in figure 7.5.

Hence the mass flow should be relatively straightforward to obtain. However, during this project it is thought that some variation in the mass flow rate of suction was observed between test sessions; although no significant difference between the experimental setups was present. It is suspected that the difficultly in sealing the plenum and the suction system between the slots and orifice plate led to leaks in the suction system meaning that the mass flow measured at the orifice plate was not necessarily the same as that through the slots. As a result, the mass flow through the slots should only be taken as an estimate. Further work is currently being undertaken to try and eradicate this problem. Yet, it is thought that in each of the cases shown in this investigation to mass flow bled through the suction system is somewhere in the region 20–40 grams/s. With the total mass flow through the tunnel around 8.9 kg/s this is somewhere between 0.22% and 0.45% of the total inflow. While this appears to be a small amount it can be put in better perspective by comparing this quantity to that contained with boundary-layer

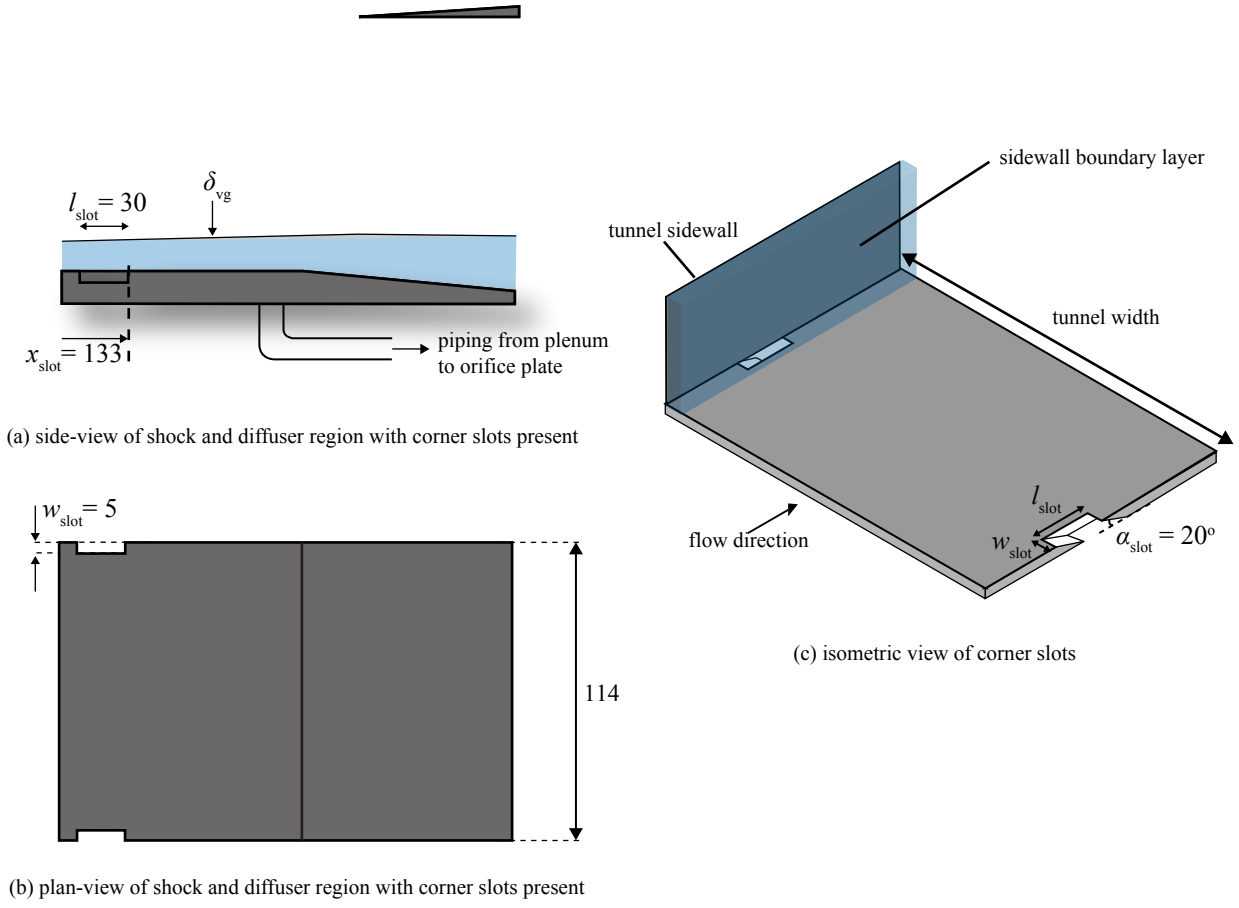

(a) side-view of shock and diffuser region with corner slots present

(c) isometric view of corner slots

(b) plan-view of shock and diffuser region with corner slots present

Figure 7.6: Schematic of corner suction configuration

itself. The mass flow in the floor boundary layer is around 0.25 kg/s; hence the corner suction is removing a mass flow equivalent to 8–16% of the floor boundary layer. As the slots themselves only cover 9% of the tunnel span (4.5% on each side) it is possible that the slots are removing the entirety of the boundary layer below which they span. However, their position in the corners means that they will certainly also be entraining flow from the sidewall boundary. As a result, without taking measurements near to the slots it is difficult to conclude the precise boundary layer region being removed from the inflow.

7.4 Vortex generator configurations

The only VG configuration investigated in this study is the ramped-vane. The ramped-vane is thought to be a good compromise between effectiveness and robustness and it has been extensively examined using CFD (see Rybalko et al. (2010) and Lee et al. (2011), and section 4.3 for a more details). This VG shape was therefore chosen for this investigation.

The ramped-vane investigated here is shown in figure 7.7. The dimensions of the ramped-vane and the spacing between pairs were selected on the basis of the optimization by Lee et al. (2011), in which the optimal spacing between pairs was determined to be $D_{\mathrm{vg}} = 10h_{\mathrm{vg}}$ and the optimal spacing between vane pairs was found to be $d_{\mathrm{vg}} = 5h_{\mathrm{vg}}$. With respect to VG sizing, VGs with a height close to half the local boundary-layer thickness were found to be optimal; the optimal height to give an $h_{\mathrm{vg}}/\delta_{\mathrm{vg}} = 0.5$ here is around 3 mm (see chapter 9 for details on the incoming boundary-layer properties). Thus, $h_{\mathrm{vg}} = 3$ mm was chosen for this investigation . All other dimensions then scale with this factor.

The streamwise position of the VGs, x_{vg}, was selected such that the distance between the VGs and the baseline separation, $x_{\mathrm{sep}} - x_{\mathrm{vg}} = \Delta x_{\mathrm{vg}}$, was similar to the optimal distance found in the computational studies discussed above; while being convenient from a wind tunnel access perspective. As a result, $\Delta x_{\mathrm{vg}}/h_{\mathrm{vg}} = 15$ was chosen (see section 4.3 for more details on VG positioning). Consequently the trailing edges of the VGs were positioned 174 mm downstream

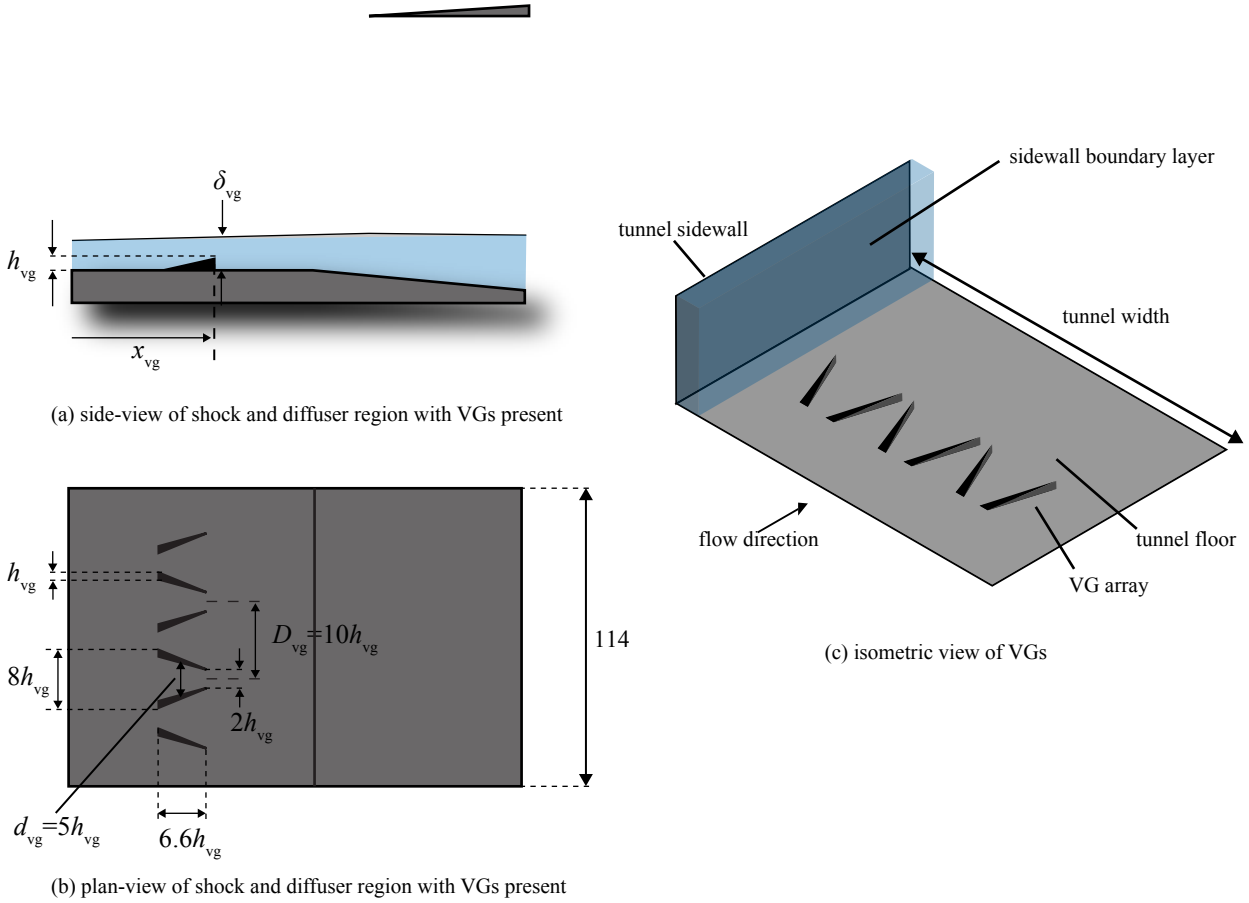

(a) side-view of shock and diffuser region with VGs present

(c) isometric view of VGs

(b) plan-view of shock and diffuser region with VGs present

Figure 7.7: Schematic of VG configuration

of the nozzle exit, $x_{vg} = 174$ mm.

While the optimization fully defines the spanwise arrangement for a configuration with a infinite span (or axisymmetric configuration), the spanwise configuration is more complex in the three-dimensional case. In the three-dimensional case, the number of vanes needs to be decided as does the conditions at centre-span. For this investigation six ramped-vanes were utilized as this array spanned the tunnel, yet vanes were not positioned too close to the sidewall to avoid a complex corner flow / VG interaction. In addition, it was decided that downwash would be preferable at centre-span to produce a positive influence of VGs at this location. The resulting VG array is schematically shown including all dimensions in figure 7.7.

Chapter 8

Measurement Techniques

8.1 Introduction

In this chapter the measurement techniques used in this investigation are presented alongside details of the data processing undertaken for each technique. In addition, the quality of the data is discussed and possible sources of error are considered and appropriately quantified. For each technique only a short description of the underlying physics is given. Nevertheless, the reader is directed to references with more in-depth descriptions in each section.

8.2 Schlieren flow visualization

A simple technique which is widely used to visualize the flow-field in transonic and supersonic wind tunnels is a schlieren system. This technique relies on the phenomenon of refraction due to density gradients which allows areas with high pressure-gradients such as shock waves to be observed.

The optical configuration utilized here is often referred to as a two-mirror schlieren system.

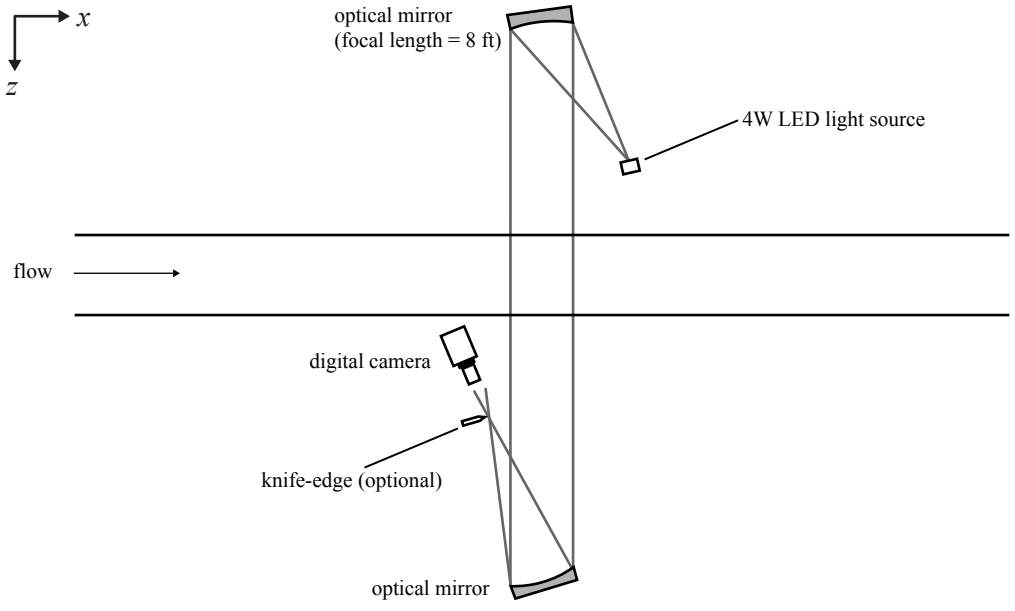

Figure 8.1: Schematic diagram of schlieren flow visualization setup

This setup is shown in figure 8.1. A small LED light source is used in conjunction with a concave mirror to create a beam of columnated light which is then passed perpendicular to the flow through the wind tunnel test section. This light is then reflected off a second concave mirror and passed into a digital camera which records the image.

The dark regions in the image created by this method look much like a shadow of an object in the wind tunnel, and, consequently, such an image is known as a shadowgraph. Further optical sensitivity can be gained by introducing a knife-edge at the focal point in front of the camera (as shown in figure 8.1). By partially blocking the light entering the camera in this way what is known as a schlieren image is produced. Further details on this optical method can be found in Holder and North (1963).

8.3 Oil-flow visualization

One way of visualizing the streamlines passing near to a surface is by using a paint, which, at first, flows in the direction of the local flow and then dries leaving streaky deposits that can be photographed and studied after the wind tunnel is shut down. This technique is often referred to as surface-flow visualization or oil-flow visualization. The surface of interest should be coated with a paint consisting of a finely powdered pigment, a suitable oil medium and in some instances a dispersant. To achieve the best visualization the exact balance of ingredients depend upon the application. See Maltby (1962) for further details.

According to Maltby, who collated the experiences with oil-flow visualizations at a number of wind tunnel facilities, the quantity $\mu_{\text{oil}}/qc_{\text{f}}$ tends to correlate well with the run time required to form a pattern according to the empirical formula:

$$t = (36,000 \pm 12,000)(\mu_{\text{oil}}/qc_{\text{f}}) \tag{8.1}$$

Accordingly, the lower the kinematic viscosity of the oil medium, the higher the dynamic pressure, and the higher the shear stress, the quicker a pattern is setup—as one might expect. Consequently, kerosene was chosen here as the oil medium as it has a relatively low kinematic viscosity, and hence does not take long to flow which is necessary due to the low wind tunnel run times in intermittent blow-down wind tunnels (around 25 seconds here). Titanium dioxide (TiO_2) is used as a pigment. The proportion of TiO_2 to kerosene was optimized by experimentation and depended on the exact configuration, but generally fell between the values of 2/5 – 2/3 parts TiO_2/oil suggested by Maltby. In addition, one drop of oleic acid was found to work as a good dispersant to reduce coagulation.

Care must be taken when analyzing oilflow-visualizations as in regions of high gradient the oil does not necessarily follow the flow exactly and small discrepancies have been noted by Atkin and Squire (1992) and Müller et al. (2001). However, these discrepancies are usually small, and, in any case, oil-flow-visualization is predominantly only utilized as a qualitative technique.

8.4 Laser Doppler velocimetry (LDV)

8.4.1 Basic principles

Laser Doppler Velocimetry (LDV) is a technique which utilizes the phenomenon of Doppler shift to calculate the velocity of a moving object. A very brief description of the underlying physics is given below before the LDV system used throughout this project is presented.

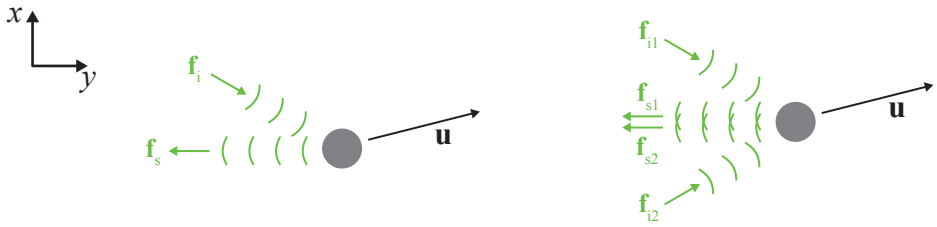

(a) Doppler shift to a single beam

(a) Dual beam Doppler shift

Figure 8.2: Schematic diagram of schlieren flow visualization setup

The velocity of an object such as the particle shown in figure 8.2 can be evaluated by shining an incident beam of light onto the particle at a known frequency and orientation, $\mathbf{f}_\mathrm{i} = f_\mathrm{i}\hat{\mathbf{e}}_\mathrm{i}$, and measuring the frequency of the light scattered from the particle, $\mathbf{f}_\mathrm{s} = f_\mathrm{s}\hat{\mathbf{e}}_\mathrm{s}$. These frequencies can then be related to the particle velocity by the equation:

$$f_\mathrm{s} = \left(\frac{c - \mathbf{u}.\hat{\mathbf{e}}_\mathrm{i}}{c - \mathbf{u}.\hat{\mathbf{e}}_\mathrm{s}}\right) f_\mathrm{i} \tag{8.2}$$

where c is the speed of light. As $|\mathbf{u}/c| << 1$, this formula can be linearized to give:

$$f_\mathrm{s} = (1 + \mathbf{u}/c.(\hat{\mathbf{e}}_\mathrm{s} - \hat{\mathbf{e}}_\mathrm{i}))\, f_\mathrm{i} \tag{8.3}$$

Nevertheless, because $|\mathbf{u}/c| << 1$, it is difficult to accurately determine the change in frequency using this single beam approach. Consequently, it is preferable to use a dual beam configuration like that shown in figure 8.2b. By utilizing two incident beams, two scattered beams are produced and the difference in frequency between these two beams can be used to determine the velocity using:

$$f_\mathrm{d} = f_\mathrm{s1} - f_\mathrm{s2} = (1 + \mathbf{u}/c.(\hat{\mathbf{e}}_\mathrm{s1} - \hat{\mathbf{e}}_\mathrm{i1}))\, f_\mathrm{i1} - (1 + \mathbf{u}/c.(\hat{\mathbf{e}}_\mathrm{s2} - \hat{\mathbf{e}}_\mathrm{i2}))\, f_\mathrm{i2} \tag{8.4}$$

If $\mathbf{f}_\mathrm{i1}$ and $\mathbf{f}_\mathrm{i2}$ are coherent, i.e., $\mathbf{f}_\mathrm{i1} = \mathbf{f}_\mathrm{i2}$, and the reflections are in the same direction, i.e., $\hat{\mathbf{e}}_\mathrm{s1} = \hat{\mathbf{e}}_\mathrm{s2}$, then the frequency difference, f_d, which is often called the Doppler frequency, is given by:

$$\begin{aligned} f_\mathrm{d} &= \mathbf{u}/c.(\hat{\mathbf{e}}_\mathrm{i2} - \hat{\mathbf{e}}_\mathrm{i1}) f_\mathrm{i1} \\ &= \frac{2\sin(\alpha_\mathrm{d}/2) u_x}{\lambda} \end{aligned} \tag{8.5}$$

Hence the x-component of velocity in this arrangement, u_x, can be calculated from knowledge of the Doppler frequency, f_d, the wavelength of the beams, λ, and the angle between the incident beams, α_d. The main advantage of this approach is that f_d can be very accurately determined by looking at the interference pattern created by the two scattered beams $\mathbf{f}_{s1}$ and $\mathbf{f}_{s2}$.

8.4.2 LDV configuration

The LDV setup used throughout this investigation is shown schematically in figure 8.3. This configuration is typical for an LDV system setup in forward-scatter mode. In this instance, an argon ion laser provides a beam of light to the beam manipulators which splits the output from the laser into specific frequencies. The system used here is setup to measure two components of velocity. Hence four beams are required: two for each velocity component. In this instance, two in the green part of the visible light spectrum and two in the blue part of the spectrum. To differentiate positive and negative velocities, a Bragg cell is used to shift the frequency of one of each the blue and green channels by 40 MHz.

Each of the four beams then pass through individual fibre optic cables to the laser head where their orientation is set. The two green beams are shown in figure 8.3. The region where the two beams cross is called the measurement volume as it is only in this volume that light is scattered from both incident beams.

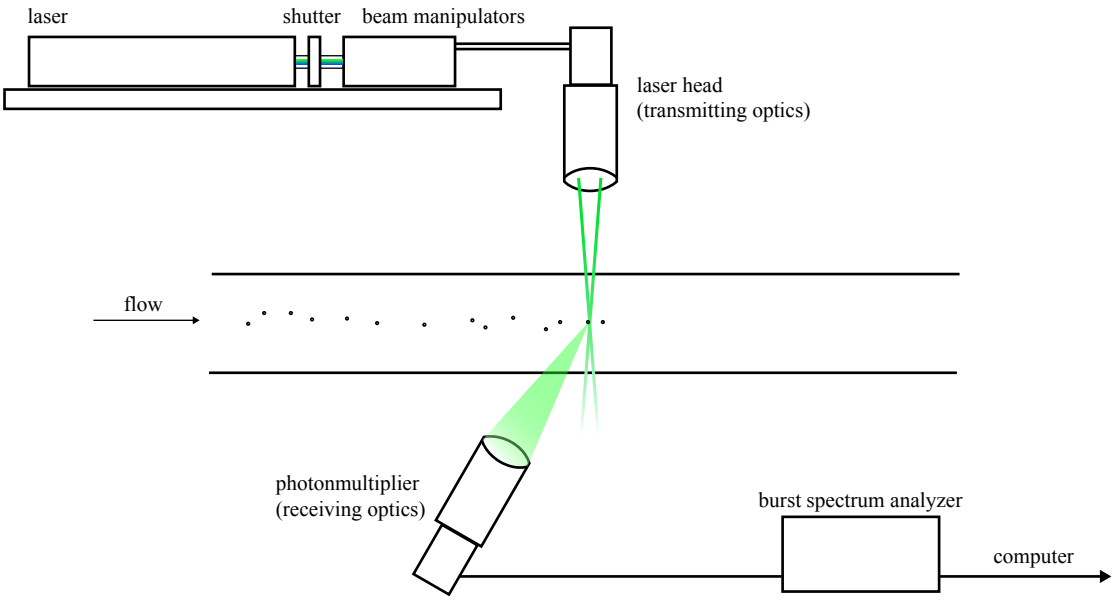

Figure 8.3: Schematic diagram of LDV setup

The receiving optics are focussed on the measurement volume and collect light scattered by the particles that pass through the measurement volume. The receiving optics is placed on the other side of the wind tunnel to the emitter so that it picks up light scattered in the forward direction. This improves the signal quality as more light is scattered in this direction (Lorenz–Mie solution to Maxwell's equations). Such positioning is usually referred to as forward scatter mode. In addition, the receiver is positioned off-axis from the emitter to avoid direct reflections from the laser beams entering the receiver.

Both the laser head and the receiver are mounted on a traverse system so that the position

of the measurement volume can be easily moved while keeping the position of the receiver and laser head relative to one another constant.

The receiving optics uses a photomultiplier to convert the intensity of the light scattered from the particles into a voltage signal (proportional to the intensity). An example of a typical signal produced by the interference of the two beams is shown in figure 8.4. This voltage signature is known as a 'Doppler burst'. These bursts are then verified by the burst spectrum analyzer, and the time between peaks is converted into the Doppler frequency and hence velocity using:

$$f_d = 1/t_d \tag{8.6}$$

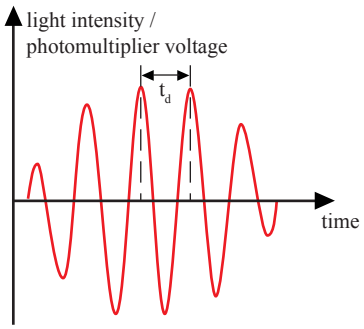

Figure 8.4: Example of a 'Doppler burst'

The LDV signal and burst acceptance criteria were manipulated to optimize the quality of the LDV output data. The settings that were optimized were the voltage gain on the photomultipliers (PMT voltage), the voltage threshold below which the burst was discarded (burst threshold), the range of frequencies/velocities simultaneously inspected (band pass filter width), and the software selectable signal-to-noise ratio. These settings were optimized to achieve a high acceptance rate and to maximise the data rate (excluding noise). As noise produced by the LDV system generally tended to first appear near the limits of the band pass filter width the onset of noise could easily be distinguished from actual particles by deliberately setting the band pass filter width to be wider than the anticipated data.

An example of a typical LDV traverse is shown in figure 8.5. Data is only obtained by the system when the traverse is stationary and this splits the data into blocks as can be seen. At each traverse location, the LDV system sampled for 250 ms; the total number of samples typically obtained in this time are shown in figure 8.5b. The drop-off in the data-rate as the wall is approached is clearly visible. Up to 0.2 mm away from the wall the data-rate is usually respectable, but at the last point, 0.1 mm from the floor, there is little data. This was typically the case, and is thought to be due to a combination of low seeding in this region and the presence of strong floor reflections. Due to the uncertainty at 0.1 mm this data was not used to calculate integral boundary layer parameters as detailed in section 8.8.1.

Also shown in figure 8.5a are the mean values of velocity at each location in addition to the location of four standard deviations either side of these means—data outside of these four standard deviations is assumed to be noise and is rejected from further processing. Nevertheless, visible from this figure is the increasing standard deviation as the wall is approached due to the

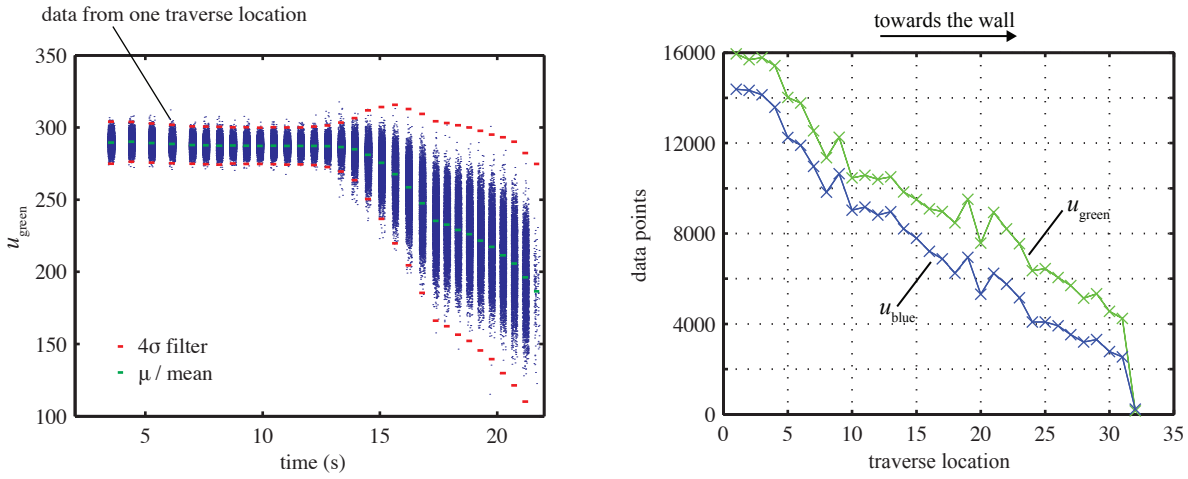

Figure 8.5: Example of a typical LDV boundary-layer traverse at centre-span

enhanced turbulence in this region.

Typical LDV settings are noted in table 8.1. However, it is important to remember that these were adapted on a daily basis depending on factors such as laser and receiver alignment and should only be used as a guide for future reference.

For a more detailed description of LDV technology, the reader should refer to Hanson (1974) and Durst et al. (1981).

A more detailed view of the positioning of the transmitting optics is shown in figure 8.6a. The location and orientation of the beams in an LDV system is important because this directly effects the velocities that are measured. In a two component system, the simplest configuration is to use one pair of beams to measure the streamwise velocity, u, directly and to use the other pair of beams to measure either the wall-normal velocity, v, or the span-wise velocity, w, directly (in this investigation u and v were measured). Nevertheless, as v is nearly always much smaller than u, it is preferable to set up the apparatus such that the green and blue channels measure similar velocities by orientating the probe at 45^o in the xy–plane, so that the two velocity components shown in figure 8.6b are measured. Such an orientation reduces the noise observed on v when compared to measuring v directly.

In addition to this 45^o orientation, it can be seen in figure 8.6a that the emitting head is also orientated slightly downward at an angle $\beta = 2.5^o$. The reason for this is that the lower green and blue beams actually point sightly upward from the emitting head at an angle $\alpha_d/2$ (so that the two pairs of beams cross). Consequently, if the emitting head were to be placed horizontal when taking measurements close to the tunnel floor the lower beams would be cut off by the presence of the floor. The head angle, β, must be greater than $\alpha_d/2$ to avoid any cut-off. Such a tilt, alters the velocity vectors measured by the LDV system, as can be seen by looking at figure 8.6b, and this must be accounted for when calculating u and v.

Adjusting for the head angle and the 45^o orientation u and v were determined from u_{blue} and u_{green} as follows:

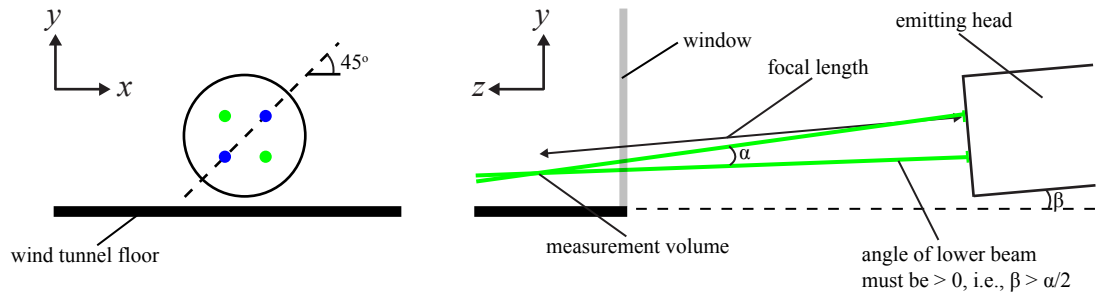

(a) Positioning of LDV emitting optics

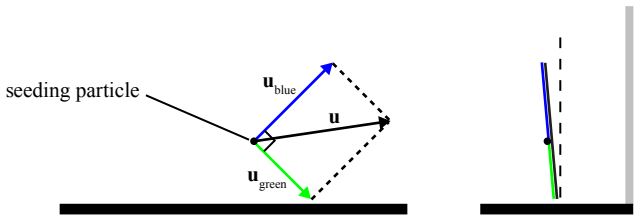

(b) Resulting velocity triangles

Figure 8.6: Schematic diagram of LDV emitting head and the resulting velocities measured

$$u = \mathbf{u}.\hat{\mathbf{e}}_x = u_{\text{blue}} \cos(\pi/4) + u_{\text{green}} \cos(\pi/4) \tag{8.7}$$

$$v = \mathbf{u}.\hat{\mathbf{e}}_y - w \sin\beta \cos\beta \approx (u_{\text{blue}} \sin(\pi/4) - u_{\text{green}} \sin(\pi/4)) \cos\beta \tag{8.8}$$

It can be seen from equation 8.8 that the combination of a head angle and a span-wise velocity component introduce a small error in the calculation of v (as w is unknown). Yet, this error is small as both w and β are relatively small (see section 8.4.4).

Some additional information on the LDV system utilized throughout this project is given in table 8.1.

Equipment	Version
Laser	Coherent Innova 70C-5 5W Argon-Ion
Beam manipulators	TSI FBL-2 fiberlight box
Emitting head	TSI TR260 with 363 mm or 512 mm lens
Receiving head	TSI RV 70 with 500 mm lens
Spectrum Analyzer	TSI PDM 1000-2 photodetector box and TSI FSA 4000-2 frequency spectrum analyzer
Software	TSI flowsizer: PMT voltage 500 green, 600 blue; burst threshold 100 mV on both green and blue; band pass filter width 40–120 M on both; and signal-to-noise medium on both
Channel 1	Green (514.5 nm)
Channel 2	Blue (488 nm)
Measurement volume:	
363 mm lens	diameter 90 μm; length 1.3 mm
512 mm lens	diameter 127 μm; length 2.7 mm
Beam half-angle ($\alpha_d/2$)	3.95^o (363 mm lens); 2.8^o (512 mm lens)

Table 8.1: LDV system information

8.4.3 LDV flow seeding

The flow was seeded with paraffin droplets created by an in-house seeding system. The seeder is made up of two parts: the vaporiser and the impactor. In the vaporiser, a double Laskin nozzle is used to atomize the paraffin and such a design is thought to produce particles in the vicinity of 1 μm (see Echols and Young (1963)). These particles then pass into the impactor which is a simple passive channel with a large number of sharp bends which blocks heavier/larger particles. The seeder is shown schematically in figure 8.7.

A recent investigation by Colliss (2011) concluded that mean diameter of the droplets reach-

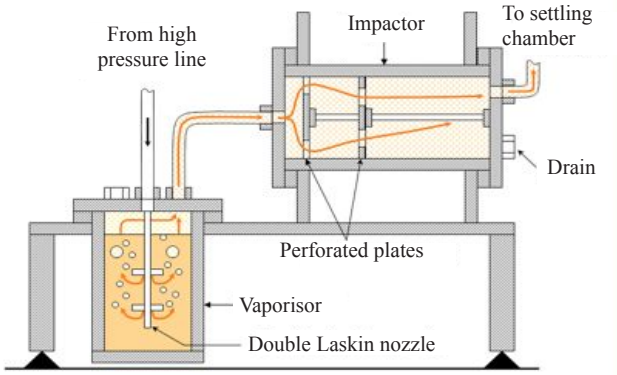

Figure 8.7: Schematic of seeding apparatus

ing the working section is in the range 0.2 μm - 0.5 μm. This gives a Stokes number (relaxation time of droplets / Kolmogorov timescale) close to 1, indicating that these droplets follow the flow for all but the smallest timescales.

Once the seeded air leaves the seeder it is passed into the rake which is positioned within the settling chamber as shown in figure 7.2. The seeding rake features a large number of radial holes on its downstream edge and it is through each of these holes that the seeding particles pass into the flow. The high-pressure air used to power the seeder was operated at a pressure of 40 psi gauge. The seeding produced by this arrangement spans the region $z = -10$ to $+10$ mm.

LDV is often referred to as a non-intrusive technique as no physical objects need to be placed within the working section. The injection of seeding, however, can cause flow disturbances. Here the positioning of the seeding rake far upstream within the settling chamber to minimize any disturbance. This fact is backed up by measurements shown in section 8.7.2 where boundary-layer profiles taken with LDV and a Pitot probe show that little difference is measured by the two—suggesting that the seeding rake creates minimal disturbance.

8.4.4 Sources of error

There are a number of sources of error in the LDV measurements. The first is caused by a discrepancy between the angle of the emitting optics head and the wind tunnel floor which was nominally set to 45^o throughout this investigation (as described in section 8.4.2). Due to wind tunnel block misalignment and possible misalignment of the emitting head this is thought to be accurate to within $\pm 1^o$. This results in an uncertainty on u of 0.3% but a much higher uncertainty on v of 10% (as it is much smaller). Secondly, the beam angle, α_{d}, which directly influences u through equation 8.4 is thought to be accurate to $\pm 0.05^o$. Hence, there is a possible error on u and v due to α of 1.25%. Thirdly there is the error associated with finite sampling. This error occurs because the flow is not perfectly steady, and, as a result, the measured mean velocities at each traverse location are not necessarily equal to the true mean velocities. Using a simple statistical approach[1] it has been determined that at a 95% confidence interval the error incurred due to finite sampling is ± 1% close to the wall (at 0.5 mm and below) but quickly becomes negligible towards the freestream (due to the very high data rates away from the wall). For a full description of statistical uncertainties in fluid mechanics see Benedict and Gould (1996).

These errors on the LDV system are combined with the repeatability of the wind tunnel flow itself (determined by repetition of measurements under the same conditions) to give a total uncertainty on supersonic boundary layer measurements of ± 1.6% on u and 11% on v. These data are summarized in table 8.2.

[1] Use of the central limit theorum and basic confidence interval analysis. See Chatfield (1983) for a detailed description.

Quantity	sources of error	error
u_{green}, u_{blue}	finite sampling rate	± 1%
u	head angle	± 0.30%
	beam angle (α_{d})	± 1.25%
	wind tunnel repeatability (supersonic)	± 0.25%
u	**total (supersonic)**	**± 1.6%**
v	head angle	± 10%
	beam angle (α_{d})	± 1.25%
	wind tunnel repeatability (supersonic)	± 4%
v	**total (supersonic)**	**± 11%**

Table 8.2: Flow velocity measurement errors

8.5 Wall pressure measurements

8.5.1 Wall pressure tappings

Measurements of steady-state wall pressure were obtained from floor tappings connected to pressure transducers mounted outside of the wind tunnel. The transducer system used here is a 16 channel self-contained NetScanner 9116. This transducer system has a sampling rate of 100 Hz; therefore 1500 samples were collected during a typical run.

The long length of plastic tubing connecting the transducers and the wall tappings (often 300 mm or more) and the small internal diameter of the tapping holes themselves (internal diameter 0.33 mm) mean that the response time of this type of arrangement is low. A previous study by Bruce (2008) concluded that with this type of arrangement the frequency response is around 33 Hz. Accordingly, this technique can only be used to measure time-averaged wall pressures.

Alongside these measurements, the settling chamber stagnation pressure is measured using a wall-tapping positioned in the side of the settling chamber (this position is shown in figure 7.2). Additionally, the atmospheric pressure is recorded using a mercury manometer on each day of testing.

To non-dimensionalize the wall pressure measurements, the measured wall pressures are divided by the settling chamber stagnation pressure.

8.5.2 Sources of error

The errors in the determination of wall pressures in this investigation are shown in table 8.3. The error incurred due to the uncertainty of the pressure transducers is relatively low with the combined effect of measurement resolution and calibration error resulting in a less than 0.03% error on the measured pressure (as quoted by the specifcation provided by the manufacturer).

Thus, the uncertainty due to finite sampling and the inability to achieve perfect wind tunnel repeatability are more significant. The error resulting from finite sampling assuming a 95%

Quantity	source of error	error
p_{atm}	reading of atmospheric pressure	± 0.02%
p, p_0	measurement/data acquisition resolution	± 0.0015%
	transducer drift and calibration	± 0.025%
	finite sampling error	± 0.25%
p / p_0	combined error on p_{atm}, p and p_0	± 0.35%
	wind tunnel repeatability (upstream)	± 0.50%
	wind tunnel repeatability (downstream)	± 1.0%
p / p_0	**total (upstream)**	± **0.60%**
p / p_0	**total (downstream)**	± **1.1%**

Table 8.3: Uncertainty in wall-pressure measurements

confidence interval has been calculated to be at worst ±0.25% (again see Benedict and Gould (1996)). More significant, however, is the uncertainty caused by the inability to achieve perfect wind tunnel repeatability. This uncertainty is calculated based on the repetition of wind tunnel runs, both during one wind tunnel test session and between different sessions conducted months apart. For the wall pressure measurements undertaken here, this uncertainty is around 0.5% of the wall pressure upstream of the normal shock wave in the supersonic flow. Downstream in the subsonic flow there is the additional variation of the shock position (±1.5 mm) which leads to a variation in the downstream wall pressure of around 1%. This is therefore the main contributor to the error.

The uncertainty in the settling chamber stagnation pressure due to it being measured with a wall-tapping is negligible because the flow velocity in the settling chamber is low (around 10 ms^{-1}).

8.5.3 PSP measurements

Wall pressure measurements obtained using wall-tappings were combined with a pressure sensitive paint (PSP) system. This technique utilizes a paint which luminesces at an intensity proportional to the local pressure to create a map of the wall pressure field. This gives a much higher spatial resolution than a few wall tappings, with the resolution restricted only by the camera resolution. In addition, if care is taken to apply only a thin layer of paint this technique is near non-intrusive. A detailed description of PSP can be found in the literature—see McLachlan and Bell (1995) and Liu et al. (1997) for good reviews. Only a very brief description of the technique is given here.

A luminescent dye is suspended in a binder paint which is then applied onto the surface of interest. When this paint is excited using an ultraviolet (UV) light source, the dye luminesces at a particular frequency (depending on the dye) which in this case is set to be within the visible light spectrum. Yet, oxygen molecules within the paint inhibit some of this luminescent emission (a phenomenon known as quenching). The amount of emission inhibited is proportional to the number of oxygen molecules which is a quantity proportional to both the partial pressure of oxygen and the air pressure.

The resulting light emission is dictated by the Stern-Volmer relation:

$$I_{\mathrm{un}}/I = 1 + k_{\mathrm{sv}}(T)p \tag{8.9}$$

where I is the intensity of light emitted (luminescence), p is the local pressure, k_{sv} is the Stern-Volmer constant (a characteristic of the paint), and I_{un} is the luminescent light intensity in the absence of oxygen (unquenched).

The luminescence, can be measured using a CCD camera and if I_{un} and $k_{\mathrm{sv}}(T)$ are known then the local pressure can be determined. Furthermore, the need to determine I_{un} can be mitigated by measuring the luminescence at atmospheric conditions (I_{atm}, p_{atm}) as well as at the conditions of interest (I, p) to give:

$$\frac{I_{\mathrm{atm}}}{I} = \frac{1 + k_{\mathrm{sv}}(T)p}{1 + k_{\mathrm{sv}}(T)p_{\mathrm{atm}}} = a(T) + b(T)\frac{p}{p_{\mathrm{atm}}} \tag{8.10}$$

By obtaining a few wall pressure tapping measurements at the same time as the PSP image, the image can be calibrated so that a and b are determined, and from this the pressure field is then

known. If the surface temperature is constant, then from equation 8.10, the calibration should be a linear fit with inverse luminescence directly proportional to local pressure.

An example of a calibration characteristic is shown in figure 8.8. In this example, it can be seen that the calibration here is near linear, and this suggests that the wall temperature is in fact relatively constant across the area of interest. When temperature variations exist, this can be somewhat compensated for by adjusting the fit, however, care must be taken when extrapolating far from the available calibration points. In this investigation some temperature variation was noted due to variations in the thickness of the various wind tunnel floor blocks. Consequently, the calibrations were adjusted to compensate for this when possible.

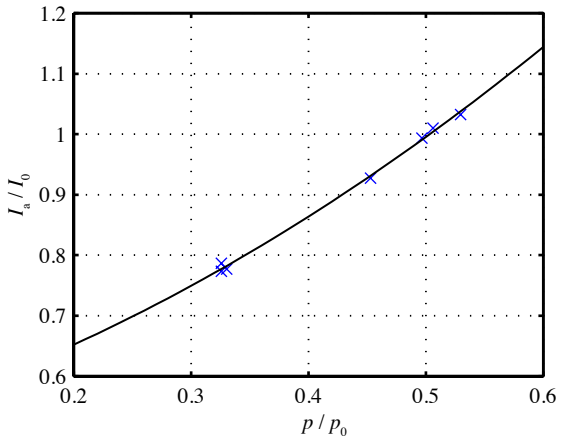

Figure 8.8: Example PSP calibration line

The setup of the PSP system is shown in figure 8.9 and some more detailed information about the equipment, including the paint, is given in table 8.4.

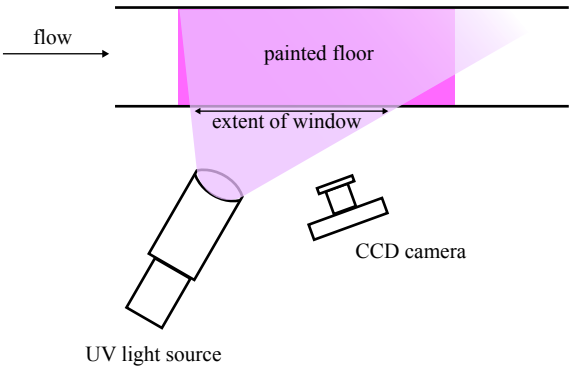

(a) Schematic diagram of PSP setup

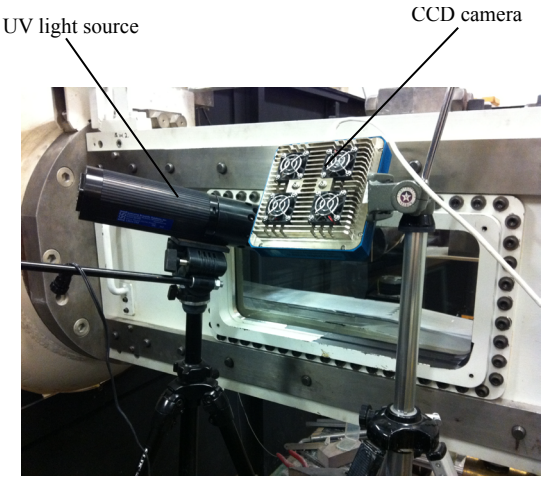

(a) Picture of PSP setup

Figure 8.9: PSP configuration

Equipment	Version
UV light source	4W LED light source (400 nm)
camera	Apogee Alta U2000C 2-megapixel, 16 bit CCD
paint	ISSI UniCoat Pressure Sensitive Paint

Table 8.4: PSP system information

8.5.4 Sources of error

The errors incurred in the PSP system are strongly dependent on the number of calibration points. As a consequence, the number of wall tappings was maximised (approximately 5-6) to minimise the error. Other than this, the main sources of error are those caused by camera noise, local temperature variations (that cannot be compensated for in the calibration) and paint imperfections. These errors are thought to be visible in figure 8.8 as the small deviations of some of the points from the fit. From a number of calibration curves the total error as a result of camera noise, local temperature variations and paint imperfections has been calculated to be ±2.0%. Although this error is much higher than from the wall tappings themselves, the ability to map an entire two-dimensional field far outweighs this increase in error. The errors in wall pressure measurements resulting from the use of the PSP system are shown in table 8.5.

Quantity	sources of error	error
p / p_0	camera noise, local temperature drift, and paint imperfections	± 2.0%
	wind tunnel repeatability (upstream)	± 0.50%
	wind tunnel repeatability (downstream)	± 1.0%
p / p_0	**total (upstream)**	± **2.1%**
p / p_0	**total (downstream)**	± **2.3%**

Table 8.5: PSP wall pressure measurement errors

8.6 Pitot measurements

8.6.1 Introductory remarks on Pitot measurements

As Pitot probes are often invasive, this measurement technique is often sidelined these days in favour of technologies such as LDV (see section 8.4) and PIV. Despite this, there can be significant advantages to using a Pitot probe. Firstly, Pitot pressure is an important quantity, in itself, as it is this that defines the potential of the fluid to do mechanical work. As such, is a good measure of efficiency or potential, and it is this quantity which is of the upmost importance to the inlet designer (see section 2.3). Additionally, Pitot measurements can be taken throughout the flow without the need for appropriate seeding and optical access, and, consequently, extensive Pitot measurements were taken throughout this investigation.

8.6.2 Pitot probe

Due to difficulties in obtaining even seeding across the wind tunnel span some incoming boundary layer characterization was undertaken using a flat-head Pitot probe. This probe is shown in figure 8.10. The probe was driven in a wall normal direction by a stepper motor that was controlled via Labview. The probe was traversed slowly enough such that the lag between the pressure transducer and the probe (again around 33 Hz) was negligible, while at the same time fast enough to accomplish a good spatial range. An appropriate speed was found to be close to 1 mm/s allowing a 25 mm traverse over a typical 25 second run. The tip of the probe was flattened so that the probe can be manoeuvred closer to the floor than its round-head equivalent.

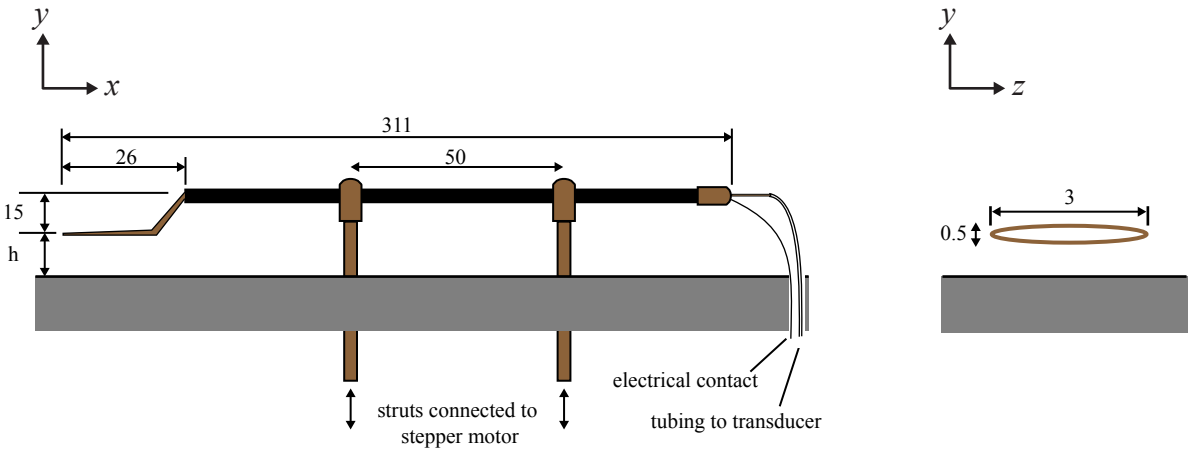

Figure 8.10: Schematic drawing of Pitot probe arrangement

8.6.3 Pitot rake

The Pitot rake positioned at the simulated AIP is shown in detail in figure 8.11. The rake has 14 Pitot probes evenly spaced from $y = 5$ mm to 70 mm. Unlike the Pitot probe of figure 8.10, the probes here are of the round-head type, as all the probes are far from the wind tunnel floor. In addition to the rake itself, there is a wall pressure tapping just upstream of the tips of the rake which allows the Mach number at the rake to be esimated. To obtain measurements across the entire span of the tunnel, the rake was designed so it could be shifted in the span-wise direction

between tunnel runs. As a result, the rake allows a contour map of the downstream flow to be obtained in the yz–plane with a 5 mm resolution in y and a 16 mm resolution in z.

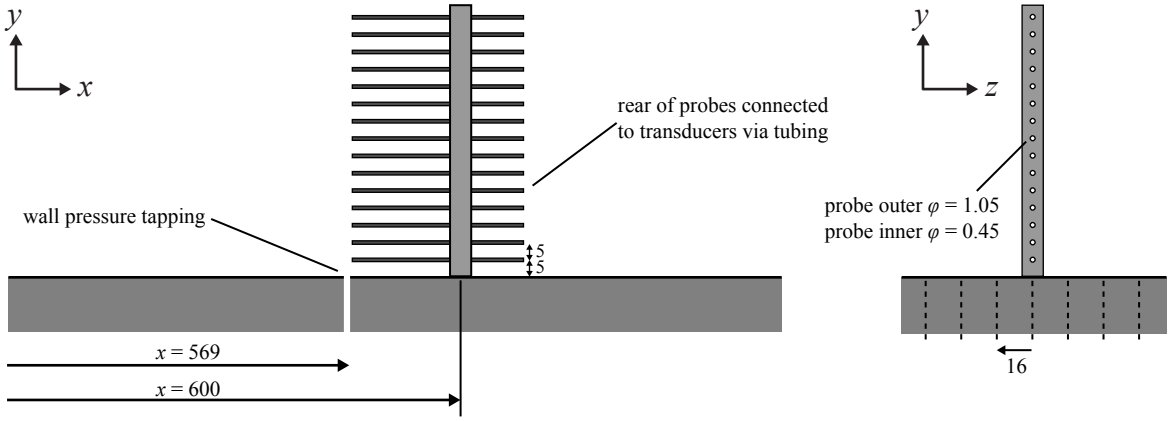

Figure 8.11: Schematic drawing of Pitot rake arrangement

8.6.4 Sources of error

The error in measurements taken by both the Pitot probe and the Pitot rake are shown in table 8.6. Error in the determination of the settling chamber stagnation pressure is also included as the Pitot pressures are always non-dimensionalized by this quantity. Again, much like the wall-pressure measurements, the uncertainty introduced due to variations in shock positioning ($\pm$1.5mm) is much higher than the absolute error in the measurement of the Pitot pressure. Note that for the Pitot probe, different slightly different pressure transducers were utilized with a higher transducer drift.

Quantity	sources of error	error
p_{atm}	reading of atmospheric pressure	± 0.02%
$p_{0\text{rake}}$, $p_{0\infty}$	measurement/data acquisition resolution	± 0.0015%
	transducer drift and calibration	± 0.025%
	finite sampling error	± 0.25%
$p_{0\text{rake}}$ / $p_{0\infty}$	combined error on p_{atm}, p and p_0	± 0.35%
	wind tunnel repeatability (downstream)	± 2.0%
$p_{0\text{rake}}$ / $p_{0\infty}$	**total**	± **2.0%**
$p_{0\text{probe}}$, $p_{0\infty}$	measurement res. and transducer drift	± 0.5%
	calibration error	± 0.5%
	finite sampling error	± 0.25%
$p_{0\text{probe}}$ / $p_{0\infty}$	combined error of that on $p_{0\text{probe}}$ and $p_{0\infty}$	± 0.75%
	wind tunnel repeatability (upstream)	± 0.9%
$p_{0\text{probe}}$ / $p_{0\infty}$	**total**	± **0.5%**

Table 8.6: Pitot pressure measurement errors

8.7 Calculation of Mach numbers and velocities from Pitot pressure data

8.7.1 Pitot pressure to Mach number

A typical Pitot probe traverse taken in the supersonic inflow is shown schematically in figure 8.12. When the Pitot probe is located outside of the boundary layer, as long as there are no upstream shock waves, the non-dimensional Pitot pressure ($p_{0\text{probe}}$ / $p_{0\infty}$) can easily be converted to Mach number using equation 8.11. Once inside the boundary layer, however, equation 8.12 must be used instead because the flow is no longer isentropic. Accordingly, the local static pressure, $p(y)$, needs to be known alongside the Pitot pressure. Unfortunately, it is very difficult to accurately measure the static pressure variation across the boundary layer. Fortunately, if there is little or no streamline curvature across the boundary layer (which will be the case for inflow boundary layers) there will be little or no wall-normal pressure gradient. It can therefore be assumed that $p(y) \neq \text{fn}(y) = p_\text{e}$ across the boundary layer, where p_e is the static pressure at the boundary-layer edge. This pressure can be calculated from the Mach number at the boundary-layer edge, M_e, which can be calculated using equation 8.11. This static pressure at the boundary-layer edge can then be used in equations 8.12 and 8.13 to determine the Mach number inside the supersonic and subsonic regions of the boundary layer respectively.

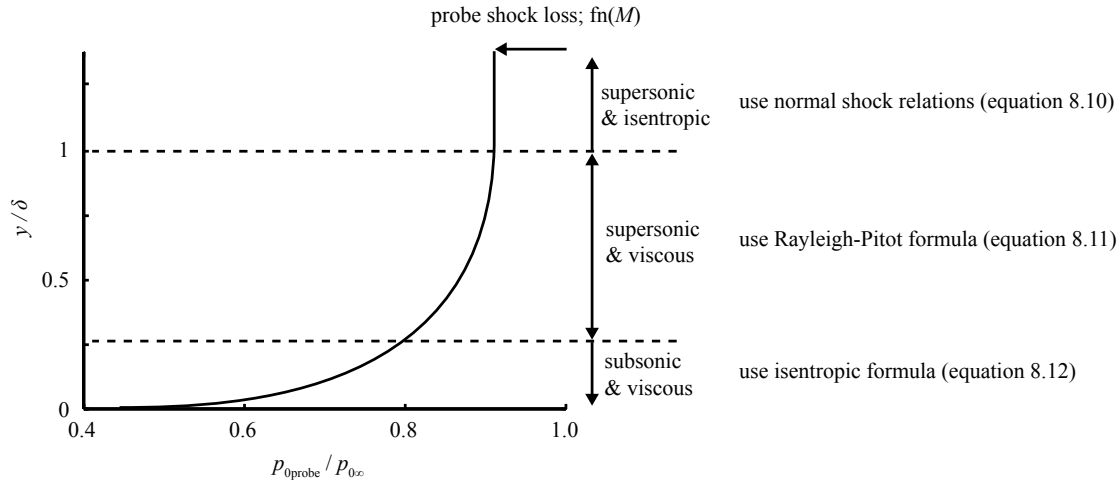

Figure 8.12: Flow regions in a typical Pitot probe traverse

$$\frac{p_{0\text{probe}}}{p_{0\infty}} = \left(\frac{\frac{\gamma+1}{2}M^2}{1+\frac{\gamma-1}{2}M^2} \right)^{\frac{\gamma}{\gamma-1}} \left(\frac{2\gamma}{\gamma-1}M^2 - \frac{\gamma-1}{\gamma+1} \right)^{\frac{1}{1-\gamma}} \tag{8.11}$$

$$\frac{p_{0\text{probe}}}{p} = \left(\frac{2\gamma M^2 - \gamma + 1}{\gamma+1} \right) \left(\frac{(\gamma+1)^2 M^2}{4\gamma M^2 - 2(\gamma-1)} \right)^{\frac{\gamma}{\gamma-1}} \tag{8.12}$$

$$\frac{p_{0\text{probe}}}{p} = \left(1 + \frac{\gamma - 1}{2} M^2\right)^{\frac{\gamma}{\gamma - 1}} \tag{8.13}$$

The validity of this assumption is nicely illustrated by the example shown in figure 8.13. In this figure, the boundary layer of the wind tunnel configuration examined here was computed at $x = 0$ using the NASA WIND CFD package[2]. A computational result is presented here as it is very difficult to obtain wall-normal boundary-layer static pressure variations experimentally.

The static pressure variation across this computed boundary layer is shown in figure 8.13a alongside the accompanying Pitot pressure and Mach number variations in figure 8.13b. The computational results presented in blue shows a weak, but not insignificant, pressure gradient across the boundary layer. The other curves indicate the profiles that involve differing simplifications. The green curves are those assuming $p(y < \delta) = p_\text{e}$, as discussed above. It can be seen that there is little difference between the Mach number profiles with this assumption and the computational result, indicating that this is not a bad assumption for inflow boundary layers with weak wall-normal pressure gradients. If the wall-pressure, p_w, is also measured, this can be used in conjunction with static pressure at the boundary-layer edge to determine if the assumption of no wall-normal pressure gradient is appropriate and to provide an approximate fit between the two if necessary (the light blue line). This gives an even better approximation of the Mach number profile. Importantly, the assumption $p(y) = p_\text{w}$ should not be used as this results in an error in the Mach number profile away from the wall. Compare the blue and red profiles in figure 8.13b. While this error is dependent on the difference between p_w and $p(y)$ and therefore may or may not be appreciable, it is not necessary to make this assumption. Consequently, such an assumption should always be avoided.

8.7.2 Mach number to velocity

To calculate the velocity profile from the Mach number profile, or vice versa, the temperature distribution across the boundary layer must be known. As this is also very difficult to measure, here the Crocco-Busemann relation is assumed to be valid which relates the temperature distribution to the velocity distribution by

$$T \approx T_\text{w} + (T_\text{aw} - T_\text{w})\frac{u}{u_\text{e}} - \frac{r u^2}{2 c_\text{p}} \quad \text{where, } r = \frac{T_\text{aw} - T_\text{e}}{T_{0\text{e}} - T_\text{e}} \approx \text{Pr}^{1/3} \tag{8.14}$$

The Crocco-Busemann relationship is relatively well backed up by experimentation (see Fernholz and Finley (1980) for a detailed review of available data). Some profiles are seen to deviate from this distribution especially when the boundary layer has an upstream history. In addition, an "overshoot" region at the outer edge of the boundary layer which is often observed cannot be accounted for with this method (again, see Fernholz and Finley (1980)). However, the Crocco-Busemann relationship is known to be a good approximation for incoming zero-pressure-gradient boundary layers like that examined in this investigation.

[2]The nozzle flow of this investigation was computed as part of an as yet unpublished project. For this computation, the nozzle was computed on a two-dimensional mesh using 16,000 grid points, to 2nd order accuracy, using the Mentor SST turbulence model. For more details see the WIND User Guide currently available at http://www.grc.nasa.gov/WWW/winddocs/index.html

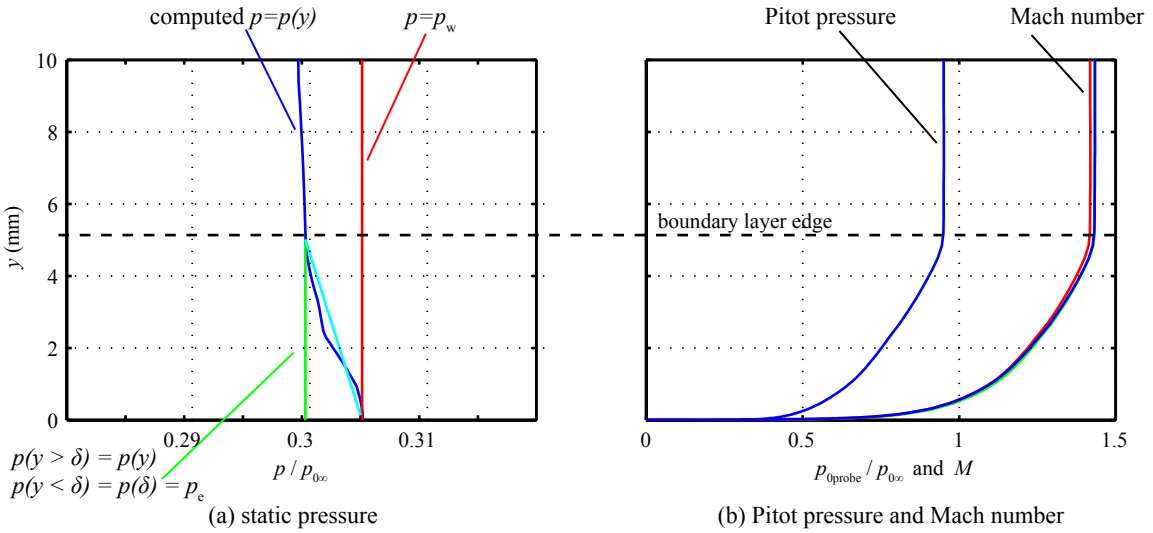

Figure 8.13: Boundary layer static pressure, Pitot pressure and Mach number profile based on computations with additional curves that involve differing simplifications

Conversion from Mach number to velocity can then be achieved after introducing $u = M\sqrt{\gamma RT}$, which, after some rearrangement, leads to

$$\frac{u}{u_e} = fn(M, Pr, T_w) \tag{8.15}$$

To determine the validity of the Crocco-Busemann assumption for the flow downstream of the nozzle blocks in this investigation, an inflow boundary layer in terms of velocity measured using a Pitot probe is compared to that produced by the LDV system in figure 8.14. The velocity profile from the Pitot probe has been created assuming that the wall temperature, T_w, is equal to the adiabatic wall temperature, T_{aw} (as T_w will be ambient at the beginning of each run and as T_{aw} is close to ambient there will be little heat transfer during each run). In figure 8.14 results assuming a Prandtl number of 0.87 and 1 are shown.

In general good agreement is obtained between the two. In the near wall region it can be seen that some deviation exists between the two techniques and it is thought that this discrepancy is probably in large part due to errors in the Pitot measurements very close to the wall which are predominantly caused by interference and finite probe thickness. The measurement inaccuracy induced by these factors, especially in relation to their influence on integral boundary-layer parameters is discussed in detail in section 8.8.1. On the other hand, the LDV is not susceptible to these errors, and is therefore thought to provide better resolution near the floor.

In addition, another disadvantage of the Pitot probe is the difficulty in determining its exact position relative to the wall (due to bending and its finite thickness). Although an electrical contact was used to determine when the probe had touched the floor, the accuracy is only thought to be 0.15 mm. The expected uncertainty from such Pitot measurements is discussed in the next section (in the profiles shown in figure 8.14 the uncertainty in y was removed by adjusting the Pitot pressure profile to overlay with the LDV).

Results for two Prandtl numbers are presented to illustrate the negligible influence of this parameter in this instance; the two profiles are almost identical. While it is clearly more ac-

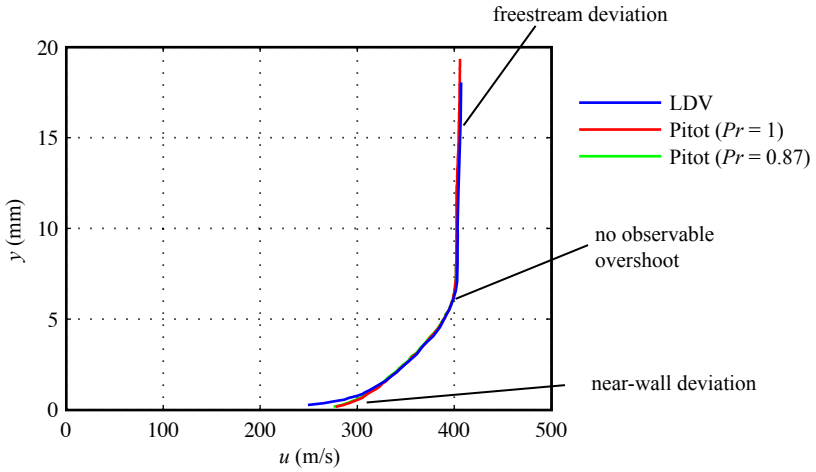

Figure 8.14: Comparison of Pitot and LDV velocity data

curate to use the more accurate $Pr = 0.87$ for air, the reason why $Pr = 1$ is also shown is because the curve-fitting method of Sun and Childs (1973) used in section 8.8.1 is only valid using this assumption. The legitimacy of this assumption is therefore demonstrated here. This simplification is valid here because of the lack of any substantial heat transfer in this flow, and this significantly reduces the influence of the Prandtl number.

Further to demonstrating the validity of the Crocco-Busemann relation and the adiabatic wall assumption, the quality of the fit between the two profiles also illustrates two other important points. Firstly, the profile obtained with the Pitot probe was obtained without the presence of the seeding rake and this indicates that the method of seeding used here (the rake positioned in the settling chamber, see figure 7.2) is not intrusive. This was further confirmed by comparisons of Pitot pressure surveys with and without the rake present. Secondly, the Pitot pressure profile was calculated on the assumption of constant stagnation temperature and that $T_{0\infty} = 290$ K, the atmospheric temperature at the time of the measurements. (The settling chamber thermocouple was not available at this time, and $T_{0\infty}$ is required to calculate an absolute velocity from the equation of non-dimensional velocity given in equation 8.15). The excellent fit between the two profiles in the freestream indicates that there is little variation in the wind tunnel stagnation temperature across a run and that the stagnation temperature is close to the atmospheric temperature. This observation was later verified by the settling chamber thermocouple as discussed in section 7.2.

8.8 Calculation of boundary-layer parameters

8.8.1 Method of calculation

Although it has been shown that the errors introduced by both the LDV and Pitot probe are small in themselves (see sections 8.4.4 and 8.6.4), when using this data to calculate boundary-layer parameters additional errors are incurred. These are predominantly due to two factors: the difficultly in determining where the probe location is relative to the wall; and the inability to obtain measurements in a region very close to the wall (this is especially a problem for the Pitot probe as was just illustrated).

From raw data measurements alone it is difficult to obtain accurate estimates for the boundary-layer parameters. This fact is illustrated in figure 8.15 where measurements (shown as crosses) are compared to a hypothetical equilibrium turbulent boundary layer (the dashed line). Due to the resolution limitations of the measurement technique, no data are available below $y = \epsilon$, and, as a result, nothing is known about the profile below this point.

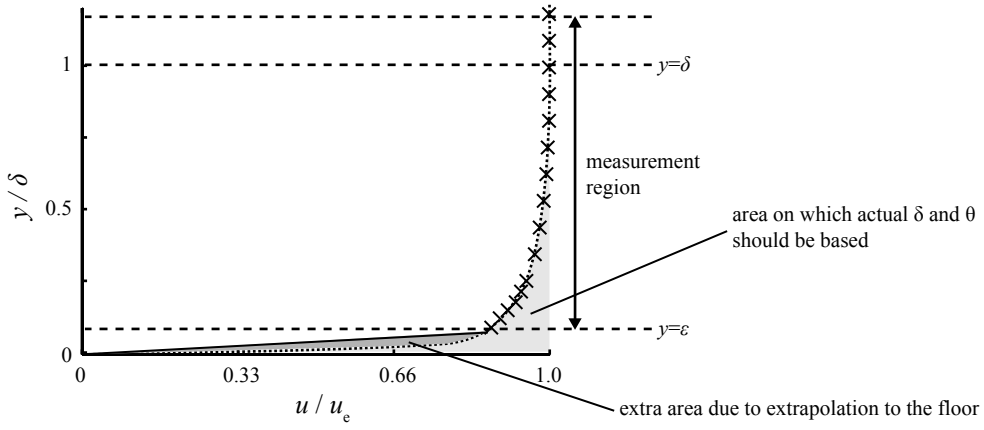

Figure 8.15: Determination of boundary-layer parameters from raw data

Consequently, when estimating boundary-layer parameters some assumption must be made about the profile below $y = \epsilon$. The simplest solution is to linearly interpolate between the data point at $y = \epsilon$ and the no-slip condition at $y = 0$. Although this is technically the raw boundary-layer parameters as experimentally measured, these values will almost certainly deviate significantly from those of the actual boundary layer. This deviation is illustrated in figure 8.15 which shows how the interpolation introduces a significant error to an equilibrium boundary layer. In such instances, the displacement thickness, δ^*, is generally overestimated (by the area shown in dark grey) as the actual δ^* should be based on the region shown in light grey. In contrast, the momentum thickness, θ, is underestimated as the interpolation assumes lower momentum near the wall. The shape factor, $H = \delta^*/\theta$, is, therefore, usually significantly overestimated (it should be noted that this interpolation will not necessarily have the same influence on non-equilibrium boundary layers; however, in this investigation boundary-layer parameters were only calculated for inflow profiles close to equilibrium).

In addition, the errors increase rapidly with ϵ, the location of the first datapoint. Hence, measurements obtained using a Pitot probe tend to be less accurate than LDV data.

When the boundary-layer is near equilibrium estimates of the boundary-layer parameters can be much improved by curve-fitting the measured data to a family of analytically derived boundary layers. Here the measured data was fitted to the analytical boundary layer distribution of Sun and Childs (1973) using a least squares regression, which curve fits the logarithmic and wake regions of the flow to estimate the boundary-layer thickness, δ_{sc}, and the wall-shear velocity, u_τ. This estimate for the wall shear velocity can then be used to estimate the wall shear stress. This analytical profile is given by

$$\frac{u}{u_{\mathrm{e}}} = \frac{1}{\sigma^{1/2}} \sin\left[\sin^{-1}\sigma^{1/2}\left(1 + \frac{1}{\kappa}\frac{u_\tau}{u_{\mathrm{e}}^*}\left\{\ln\eta + \frac{2(1-\eta^a)^{1/2}}{a} - \frac{2}{a}\ln(1+(1-\eta^a)^{1/2})\right\} - \frac{\Pi}{\kappa}\frac{u_\tau}{u_{\mathrm{e}}^*}(1+\cos\pi\eta)\right)\right] \tag{8.16}$$

where

$$a = 1 \quad , \quad \sigma = \frac{\frac{\gamma-1}{2}M_{\mathrm{e}}^2}{1+\frac{\gamma-1}{2}M_{\mathrm{e}}^2} \quad , \quad \frac{u_\tau}{u_{\mathrm{e}}^*} = \frac{\left(\frac{c_{\mathrm{f}}}{2}\frac{\sigma}{1-\sigma}\right)^{1/2}}{\sin^{-1}\sigma^{1/2}} \quad ,$$
$$\frac{\Pi}{\kappa} = \frac{1}{2}\left[\frac{u_{\mathrm{e}}^*}{u_\tau} - \frac{1}{\kappa}\ln\left(\frac{\delta u_\tau}{\nu_{\mathrm{w}}}\right) - B + \frac{0.614}{a\kappa}\right] \tag{8.17}$$

and where, under adiabatic conditions, as assumed throughout, the van Driest effective velocity (van Driest (1951)) is given by

$$u^* = \frac{u_{\mathrm{e}}}{A}\sin^{-1}\left(\frac{Au}{u_{\mathrm{e}}}\right) \quad \text{with} \quad A^2 = 1 - \frac{T_{\mathrm{e}}}{T_{\mathrm{aw}}} \tag{8.18}$$

An example of a Sun and Childs curve fit is presented in figure 8.16. It can be seen that the curve fit correlates well to the raw data and nicely matches the van Driest modified log-law in figure 8.16b. Yet, this curve fit is only valid down to the logarithmic region, and in the boundary-layer profiles measured here the logarithmic region ends at around $y^+ = 100$ ($y^+ = yu_\tau/\nu_w$) or $y = 0.2$ mm. Consequently, another fit is required for the sublayer and buffer layer as details below 0.2 mm are important for accurately determining boundary-layer parameters. The sublayer and buffer region were approximated using the composite formula of Spalding (1961) modified to include the van Driest effective velocity, giving

$$y^+ = u^{*+} + e^{-\kappa B}\left[e^{\kappa u^{*+}} - 1 - \kappa u^{*+} - \frac{(\kappa u^{*+})^2}{2} - \frac{(\kappa u^{*+})^3}{6}\right] \quad \text{where } u^{*+} = \frac{u^*}{u_\tau} \tag{8.19}$$

For this fit, the wall-shear velocity, u_τ, is obtained from the Sun and Childs curve fit (equation 8.16). Although data could not be obtained close enough to the wall to verify the validity of the Spalding fit (equation 8.19), this fit does nicely overlap with the Sun and Childs fit used for the logarithmic and outer wall regions shown in figure 8.16.

The large differences between the curve-fitted and raw boundary-layer parameters are illustrated by the numbers shown in table 8.7. This table shows data obtained using LDV with the first measurement away from the wall at $\epsilon = 0.2$ mm. The extent to which the displacement thickness is overestimated is clearly visible while the under-prediction of the momentum

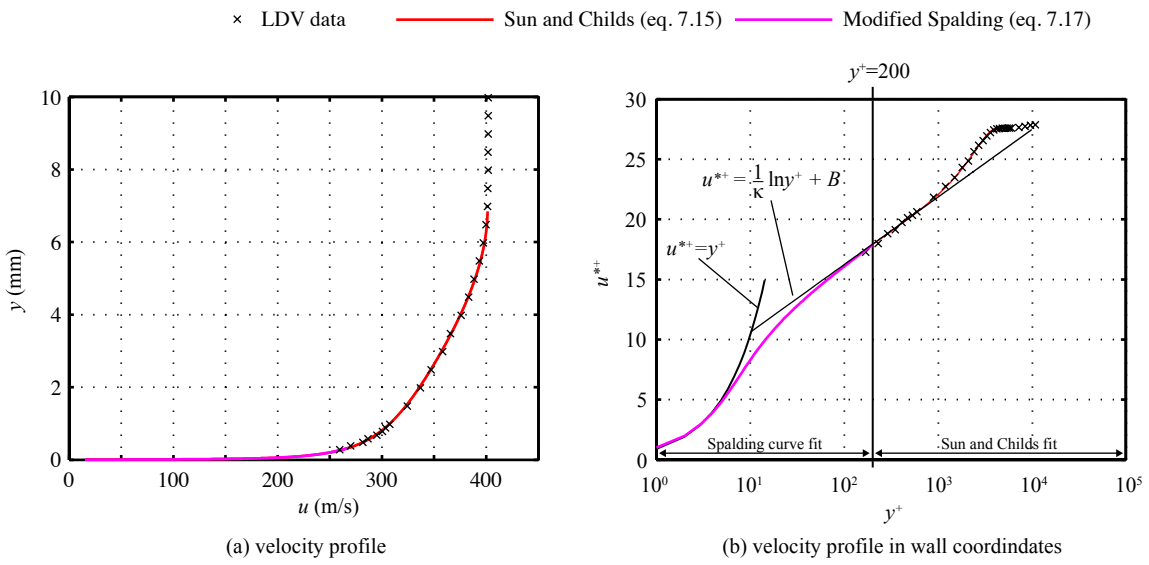

(a) velocity profile

(b) velocity profile in wall coordindates

Figure 8.16: Example of curvefitting to LDV dataset

quantity	raw data	curve-fitted data
δ^*	0.92	0.82
θ	0.62	0.63
H	1.48	1.30

Table 8.7: Difference in boundary-layer parameters with and without near-wall model

thickness is actually very small. The small error on the momentum thickness occurs because $u/u_e \to 0$ at the wall, meaning that the region right near the wall is not as important as for the displacement thickness (however the near-wall region is still important). The overestimate of the shape factor that results due to these factors is also clearly visible.

8.8.2 Sources of error

Errors in the calculation of the boundary-layer parameters from both LDV and Pitot are shown in table 8.8. As has been discussed above, the main source of error are inaccuracy in the floor position and the position of the first measurement. For the equilibrium boundary layer examined in this investigation, the inaccuracy in the floor location with the LDV system is ± 0.02 giving an inaccuracy of $\pm 2\%$ on δ^*. More importantly, however, the difficulty in obtaining measurements below 0.2 mm results in an overestimate of 10 to 14% on δ^*. Due to the same errors, θ is slightly underestimated, -2.5 to -0.5%, and H is overestimated by 12 to 17%. Using the curve-fit these overestimates can be substantially reduced (under the assumption the near-wall region is well behaved) and consequently you are left with errors of $\pm 2\%$ on δ^*, $\pm 1\%$ on θ, and $\pm 2\%$ on H.

With the Pitot probe the errors are even higher as all data below 1 mm is thought to be inaccurate. Consequently, there are very high errors for the Pitot probe raw data. Using the curve-fitting method, these can be substantially reduced to errors of $\pm 6\%$, $\pm 6\%$, and $\pm 4\%$ on δ^*, θ, and H respectively.

quantity	sources of error	error
LDV		
δ	floor location ($\pm$0.02 mm)	$\pm$1%
δ^*	u	negligible
	floor location ($\pm$0.02 mm)	$\pm$ 2%
	first measurement point, $\epsilon = 0.2$mm	+10–14%
δ^*	total (raw data)	+10–14%
δ^*	total (curve-fitted)	$\pm$ 2%
θ	total (raw data)	-2.5–-0.5%
θ	total (curve-fiited)	$\pm$ 1%
H	total (raw data)	+12–17%
H	total (curve-fitted)	$\pm$2%
Pitot		
δ	floor location ($\pm$0.15 mm)	$\pm$2%
δ^*	p_0	negligible
	T	negligible
	floor location ($\pm$0.15 mm)	$\pm$ 6%
	first measurement point, $\epsilon = 1$mm	+54–66%
δ^*	total (raw data)	+54–66%
δ^*	total (curve-fitted)	$\pm$ 6%
θ	total (raw data)	-18–-30%
θ	total (curve-fitted)	$\pm$ 6%
H	total (raw data)	+110–120%
H	total (curve-fitted)	$\pm$4%

Table 8.8: Boundary-layer parameters measurement errors

Chapter 9

Inflow Characterization

9.1 Introductory comments

The incoming boundary layer has been characterized with both LDV and a flat-head Pitot probe (see sections 8.4 and 8.6 for details of these measurement techniques). These measurements were taken to determine the boundary-layer characteristics at start of the SWBLI as well as to establish the quality (uniformity) of the wind tunnel flow. These measurements are thought to be more extensive than previous investigations using this wind tunnel and should be beneficial for CFD studies on this and similar configurations.

9.2 Boundary-layer characterization

Incoming boundary layer measurements were undertaken at a variety of streamwise and spanwise locations. While the majority of data were taken in the boundary layer on the tunnel floor, some measurements were also taken of the sidewall boundary layer. A schematic diagram showing the locations at which boundary-layer traverses were performed is shown in figure 9.1.

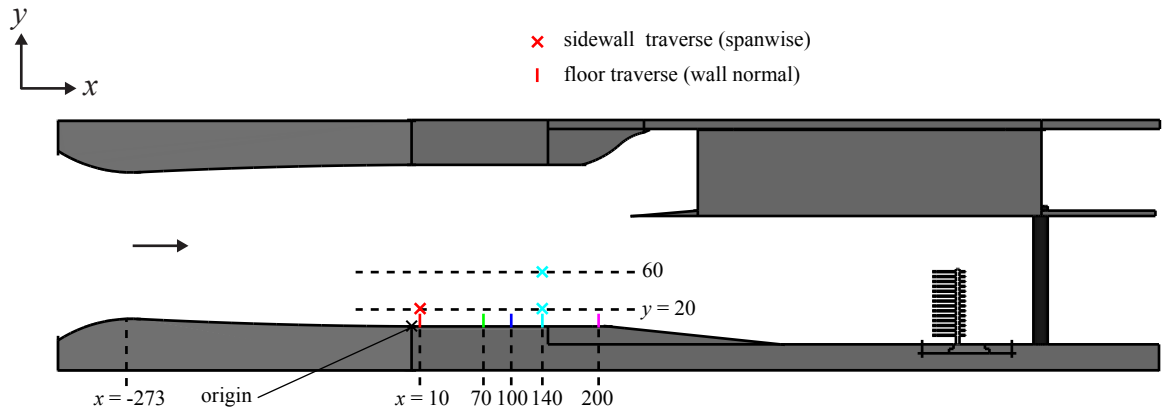

Figure 9.1: Schematic diagram of incoming boundary layer measurement locations (in addition to centre-span measurements for all streamwise locations a number of spanwise traverses were conducted at $x = 140$ mm)

Details of the streamwise evolution of the floor boundary layer downstream of the nozzle are

shown in figure 9.2. These boundary-layer profiles were obtained using LDV at five streamwise locations along the centre-span . Measurements were obtained from just downstream of the nozzle exit (x = 10 mm) to near the entrance of the diffusing section (x = 200 mm). These five profiles are shown in figure 9.2a along with their corresponding Reynolds number based on both θ and Δx_{throat} (where Δx_{throat} is the distance between the measurement location and the geometric throat, $x - x_{\text{throat}}$).

From these profiles it can be seen that the boundary layer grows slowly in thickness as it travels downstream and that there is a small reduction in the freestream velocity (due to the effective contraction caused by the boundary layer growth).

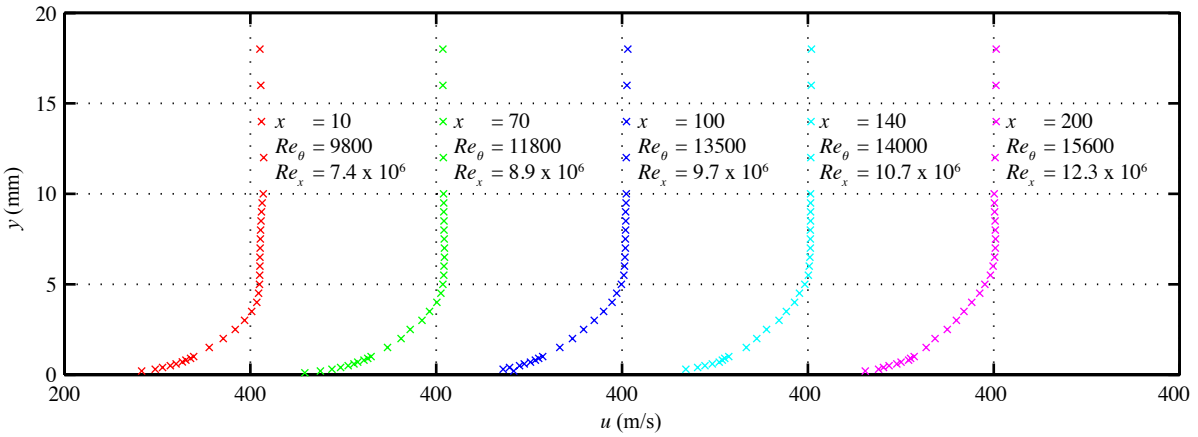

(a) Velocity profiles (outer coordinates)

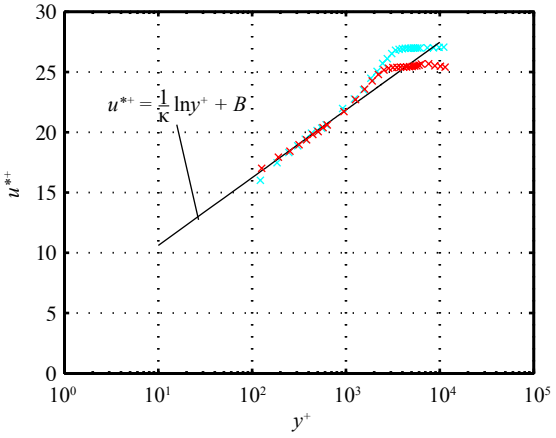

(b) Velocity profiles (wall/inner coordinates)

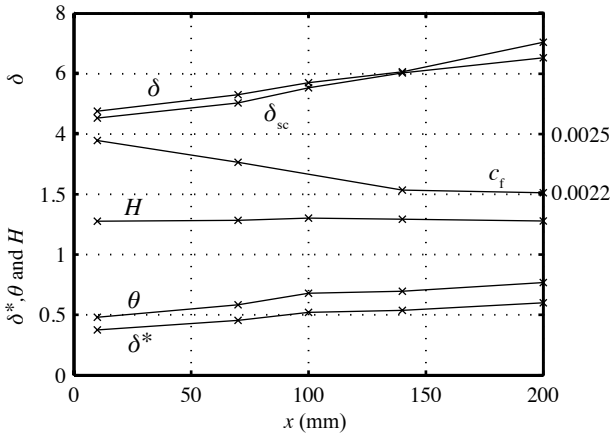

(c) Boundary layer properties

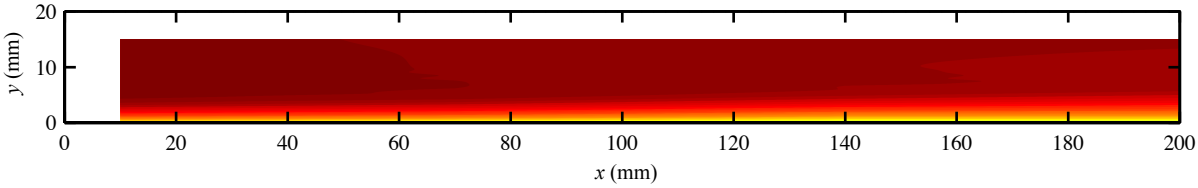

(d) Streamwise contour plot

Figure 9.2: Streamwise variation of the boundary layer at centre-span ($z = 0$)

The boundary layer profiles at $x = 10$ and $x = 140$ mm are presented in wall-coordinates form in figure 9.2b. The good agreement between the law of the wall and the lower portion of the boundary layer measurements helps to verify that the data obtained is of good quality. Furthermore, the movement of the wake region upward as the flow travels downstream suggests a slight adverse-pressure-gradient which is in agreement with the observed decrease in the freestream velocity.

The boundary-layer parameter data (resulting from the curve-fitted data as described in section 8.8) are presented in figure 9.2c. It can be seen that δ rises slowly from about 4.5 mm at the nozzle exit to around 6.5 mm near the entrance to the diffuser. The boundary-layer thickness at the start of the SWBLI, δ_0, will therefore be close to 6.5 mm. Both δ^* and θ increase in a similar fashion: δ^* rising from 0.38 to 0.60 mm and θ from 0.48 to 0.77 mm. Yet, H remains almost constant close to 1.30, and this indicates that the boundary layer is in a 'quasi' equilibrium state. As expected, the wall shear decreases slowly with streamwise distance; c_f dropping from 0.0025 to 0.0022.

The constriction of the flow due to the boundary layer is also nicely illustrated in figure 9.2d which shows contours of streamwise velocity. The growth of the boundary layer is visible in tandem with the slight decrease in freestream velocity.

While figure 9.2 presents data obtained at centre-span, some indication of the spanwise variation in the boundary layer can be gauged from figure 9.3 which shows LDV measurements at $x = 140$ mm at three spanwise locations: $z = -10$, $z = 0$, and $z = 10$ mm. From this figure, it can be seen that there is some spanwise variation, with the boundary layer slightly thicker either side of centre-span. It is nice to see, however, that the profiles at $z = -10$ and $z = 10$ mm are very similar—the first indication that the flow is relatively symmetric. This fact is verified by the wall coordinates plot in figure 9.3b.

The excellent match between the Sun and Childs curve-fits and the raw data is also visible in figure 9.3a: compare the solid lines from the curve-fit with the crosses which are the measured data points.

Although these data present some information about the spanwise variation of the boundary layer, it is desirable to have data further than 10 mm from the centre-span. Unfortunately, the seeding used for the LDV system is only able to produce good seeding density within this range, and, consequently, it was not possible to obtain LDV data outside of this range. As a result, instead of using LDV, a flat-head Pitot probe was used to obtain data further off-centre-span.

These data are presented in figure 9.4 and figure 9.5. In figure 9.4a Pitot pressure profiles are shown for $x = 140$ mm at the spanwise location $z = -40$, $z = -25$, $z = -10$, $z = 10$, $z = 25$, and $z = 40$ mm. These were then converted to velocity profiles via the method described in section 8.7 assuming zero wall-normal pressure gradient and these profiles are shown in figure 9.4b. From these plots it is evident that there is only a small spanwise variation in the inflow: the profiles lie close to one another and both the thickness of the boundary layer and the freestream velocity are in close agreement.

The quality of the incoming boundary layer is better illustrated by figure 9.5 which shows the variation of boundary-layer parameters from the curve-fitted Pitot probe data. Although there is some variation across the span, this is quite small with a maximum variation in δ, δ^*, and θ of 10 % across the section of the span measured. This is thought to be relatively low and

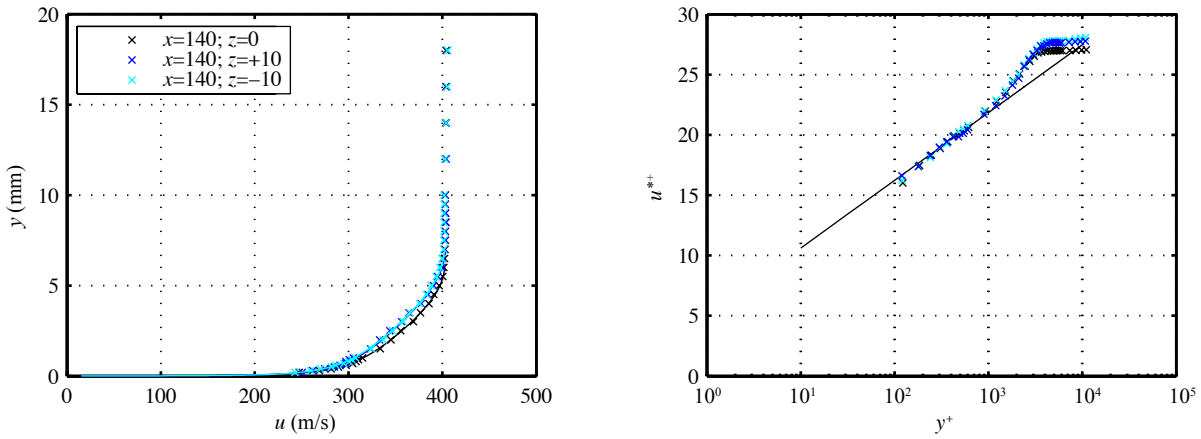

(a) Velocity profiles (outer coordinates)

(b) Velocity profiles (wall/inner coordinates)

Figure 9.3: Spanwise variation of the boundary layer at $x = 140$ mm from LDV

indicates that the wind tunnel has good flow distribution with no significant flow distortion. In addition, the flow, again, exhibits good symmetry about centre-span.

Thus far only the boundary layer on the wind tunnel floor has been considered. Although it is the interaction of this boundary layer that is of upmost interest, the influence of the sidewall boundary layers is also important (see section 3.2.4 for a discussion of the importance of three-dimensional effects). Consequently, measurements were also taken of the sidewall boundary layer. As optical (and seeding) limitations restricted the use of the LDV for this task, the same Pitot probe as used for the tunnel floor was used. However, instead of being mounted in the floor, the probe was mounted on the door with the motor and mounting bracket mounted outside the tunnel. As the door had to be specially modified for this purpose it was only possible to take measurements on one sidewall (the sidewall at $z = +57$ mm).

Data taken at two streamwise positions $x = 10$ and $x = 140$ mm are shown alongside centre-span tunnel floor data at the same streamwise location in figure 9.6. In the data taken near the nozzle exit (figure 9.6a) there is a small difference between the measured sidewall boundary layer ($y = 20$ mm) and the floor boundary layer. However, by $x = 140$ mm the sidewall profiles taken at both $y = 20$ and $y = 60$ mm are almost identical to the floor boundary layer. These measurements suggest that there is little difference between the floor and the sidewall boundary layer. Furthermore, the fact that the two sidewall profiles are so closely matched at $x = 140$ mm is evidence that there may also be relatively little variation in the sidewall boundary layer itself.

It is perhaps slightly surprising that there is such a good match between the two boundary layers as they do develop in a different manner due to the geometrical constraints of the two-dimensional nozzle blocks. Nevertheless, it appears that this is relatively insignificant—especially by 140 mm downstream of the nozzle exit.

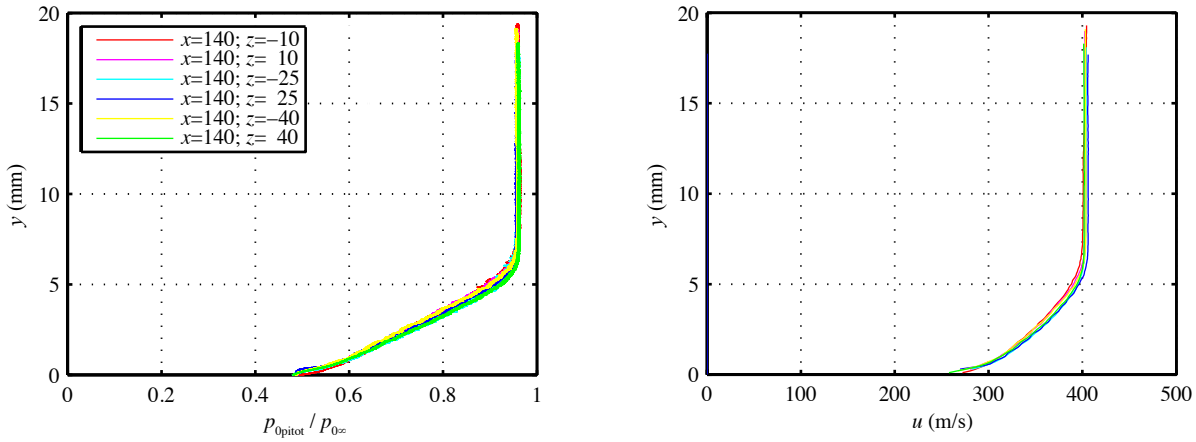

(a) Pitot pressure profiles

(b) Velocity profiles

Figure 9.4: Spanwise variation of the boundary layer at $x = 140$ mm from the Pitot probe

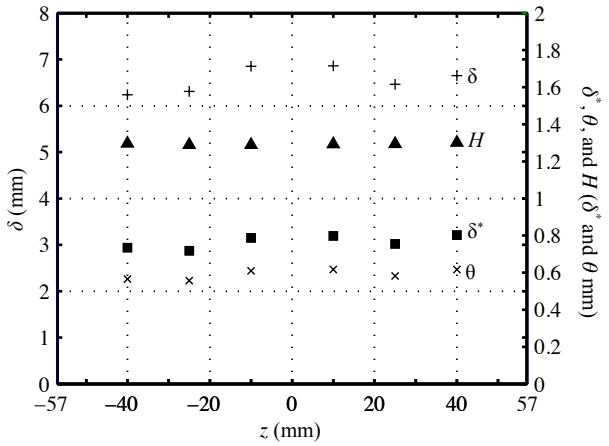

Figure 9.5: Spanwise variation of boundary layer parameters at $x = 140$ mm

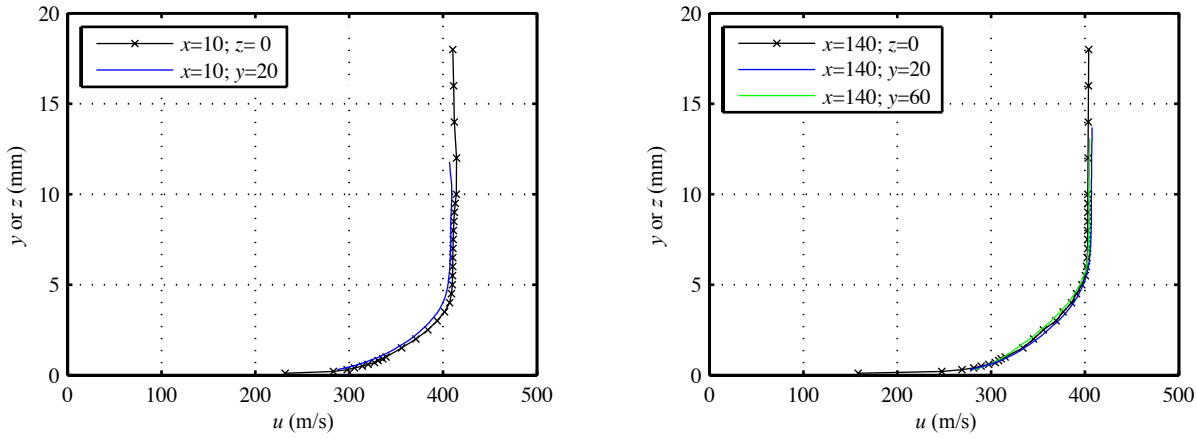

(a) Velocity profiles; $x = 10$ mm

(b) Velocity profiles; $x = 140$ mm

Figure 9.6: Comparison of floor and sidewall boundary layers

Chapter 10

Results

10.1 Introduction

The main results of this investigation are presented and discussed in this chapter. The first portion of the results detail the design of the baseline or uncontrolled case. This is conducted to determine whether the baseline case is appropriate for a flow control study and, if it is, to fully characterize the flow-field. Only once the uncontrolled case is characterized can the full benefits and drawbacks of adding flow control be ascertained. Flow control in the form of VGs is then added and its advantages and disadvantages are established.

10.2 Uncontrolled interactions

To determine the influence of integrating a diffuser downstream of the normal shock (which, as previously discussed, is thought to be influential in determining the severity of the interaction), the shock holder and therefore shock position was varied relative to the diffuser. The three shock positions examined were approximately $5\delta_o$ upstream of the diffuser entrance, 0, and $5\delta_o$ downstream. Positions 1, 2, and 3 respectively.

Flow visualizations for these three uncontrolled cases are presented in figures 10.1, 10.4, and 10.7. In each of these figures, schlieren and oil-flow visualization have been combined to qualitatively illustrate the features of the flow-fields.

The flow-field produced with the shock in the most upstream position, position 1, is shown in figure 10.1. In the schlieren image of this figure, it can be seen that the shock wave is near-vertical and straight at a location just slightly in front of the shock holder. Yet, as the floor is approached the flow is influenced by viscous effects, and this is most apparent from the bifurcation of the shock which results because of the thickening of the boundary layer across the shock wave. Furthermore, downstream of the shock, weak shocklets are visible near the boundary-layer edge, indicating that the boundary-layer thickening across the shock is strong enough to reaccelerate the flow to a sonic velocity. What is more, there is little indication that the flow follows the profile of the diffuser as the boundary-layer edge appears to continue almost horizontally within the area viewable by the window. These features illustrate that viscous phenomena are strongly modifying the flow—in particular, the growth of the viscous regions is clearly modifying the effective geometry of the channel.

More information about the flow-field can be gauged from the oil-flow visualization of the

channel floor. This image is shown directly below the schlieren image to orientate the shock position relative to the surface-flow visualization. This surface-flow visualization is presented again in figure 10.2 with its key features labelled, and to highlight these features further, a sketch of the near-wall streamlines is shown in figure 10.3. This interpretation of the near-wall flow topology (and all subsequent interpretations) are based on the still images taken of the oil-flow visualizations and on videos taken during the running of the wind tunnel.

The following observations are made with reference to these figures: From the surface-flow visualization in position 1, it can be seen that there is no large-scale separation in the central part of the channel floor—neither beneath the shock nor in the diffuser. Yet, beneath the shock, there is a very small region of reversed flow and a lighter region indicating a low shear stress; the whole centre-span region appears to be on the verge of separation.

Flow separation is, however, visible in the corners at the junction of the floor and sidewalls. These separations originate at a streamwise location close to that of the front leg of the lambda-foot, and this signifies that the corner separations are shock-induced. The locations of the nodes of separation and the shock-foot are labelled in figure 10.2 and are shown in the topology sketch of figure 10.3. These shock-induced corner separations grow quickly with streamwise distance and by the end of the diffuser their footprint covers more than 50 % of the channel span (their extent from each sidewall being approximately $6\delta_o$). The large spanwise extent of the corner separations and the spanwise variations they induce is the first sign that the flow produced here is highly three-dimensional. In spite of this the flow is close to symmetric and this is why only half the topology is shown in figure 10.3.

Also visible in the oil-flow visualization is a reduction in the growth of the corner separation between the shock and the diffuser entrance, and this is consistent with a reduction in the adverse-pressure-gradient in this short region. It can therefore be concluded that with the shock in this position the boundary layers have some time to recover from the adverse-pressure-gradient of the shock before the adverse-pressure-gradient of the diffuser. Furthermore, while there is little in the schlieren image to suggest that the flow 'feels' the diffuser, the change in the growth of the corner separation at the diffuser entrance indicates that the flow does feel the diffuser's presence. Although not shown here, the flow on the sidewall is similar with attached flow away from the corners.

The flow-field can be made more severe for the boundary layers by reducing the extent of the recovery region region (i.e., the distance between the shock the diffuser). The flow visualizations that result when the shock is moved downstream to position 2 are shown in figure 10.4. When the shock is moved closer to the diffuser, the schlieren image illustrates that there is a slight increase in the thickening of the boundary layer across the interaction (most visible by the accompanying increase in the size of the shock-foot), and, again, the boundary-layer edge does not follow the profile of the diffuser.

While the general features of the schlieren image are much the same as before, the oil-flow visualization suggests that the flow-field is significantly different. Oil-flow visualizations for this position are displayed in figure 10.4 through 10.6. These figures illustrate that once again corner separations start at the leading edge of the shock-foot. Yet, they grow more quickly than before: even before the diffuser entrance, the corner separations are large. The growth of the corner separations continues inside the diffuser, and they soon cover 50 % of the span. In addition,

each corner separation has a clear focus 3–4δ_o downstream of the diffuser entrance. The flow is clearly more three-dimensional than in position 1.

Not only are the corner separations much enlarged compared to position 1; there is also no longer an attached channel between the two corner separations on the channel floor. Instead, a saddle point is present around 10δ_o downstream of the shock-foot—well into the diffuser. This saddle point and its corresponding separation line demarcate the incoming flow from that in the majority of the diffuser, which is fully reversed travelling from right to left. The incoming and reversed flow regions are separted by a separation line which runs from the saddle point to a focus—one for each half of the flow. The flow spiralling into each focus will result in a vortex which will quickly become orientated in the streamwise direction resulting in upwash near the sidewall and downwash near centre-span. Again, the flow is highly symmetric. Flow attachment is also clearly visible in the oil-flow visualization, but does not occur until a significant streamwise distance downstream, downstream of the end of the diffuser, where a single saddle point is visible on the channel floor. The streamwise extent of separation is approximately 190 mm or 30δ_o. Nevertheless, much like position 1 there is no separation directly beneath the shock-foot. The floor boundary-layer is clearly able to negotiate the flow turning required at the entrance to the diffuser.

As well as the complex floor topology, a complex flow pattern is visible on the sidewall. Like the channel floor flow, the topology is dominated by a focus near the diffuser entrance. However, the focus is confined to a region closer to the wall and has a more elongated form. Further away from the wall, the wall remains attached, but is deflected over the corner and floor separation.

To examine the impact of moving the shock further downstream, the shock was moved to position 3 into the diffuser region. The resulting schlieren and channel floor oil-flow visualization are shown in figure 10.7. The schlieren image in this figure demonstrates that the amplification of the viscous flow is once more increased by further movement of the shock downstream: the shock-foot is much larger due to more abrupt boundary-layer thickening; and in addition, the shock is more curved (now certainly a strong oblique rather than normal shock wave). In fact, the shock is so curved that even with the shock holder 30 mm downstream of the diffuser entrance, the leading edge of the shock-foot is still upstream of the diffuser leading edge. Hence, there is no expansion ahead of the shock at the diffuser entrance.

The continued enhancement in viscous effects as the shock is moved downstream is back up by the surface-flow visualizations of the channel flow (figures 10.8 and 10.9). In the surface-flow visualizations, the corner separations are again clearly visible. Once more, the corner separations originate near to the leading edge of the shock-foot. Furthermore, they grow quickly—soon covering the majority of the span. At the same time, the separation location at centre-span has moved upstream to a position beneath the shock-foot. As a direct consequence of these two factors, the flow from the corner and the centre-span regions are more interlinked than ever. Accordingly, the flow is now the most three-dimensional of any configuration. The sidewall oil-flow visualization in position 3 looks similar to that in position 2 but with a larger deflection of the attached sidewall flow away from the corner. This is further evidence that the interaction is now even more severe.

Nevertheless, the overall flow topologies between positions 2 and 3 are quite similar. Despite the introduction of centre-span separation under the shock and small differences in the corner

separation foci in terms of location and shape, the flow throughout the remainder of the diffuser is similar to position 2. Further, the reattachment location is almost identical. As a result, the streamwise extent of separation is only extended by the movement of the initial separation saddle point upstream to $x_{\text{sep}} = 220$ mm. The total extent of separation was therefore around 240 mm ($37\delta_{\text{o}}$).

The wall-pressure measurements obtained on the channel floor for the three positions are presented in figure 10.10 (wall-pressure measurements taken using both pressure transducers and PSP are shown). What is immediately apparent is that in all cases the pressure rise falls well short of the inviscid pressure rise which should be the same in each case (see figure 10.10). This result verifies that the viscous flow has a strong bearing on the effective area of the duct in all cases, as a consequence of the boundary-layer thickening and flow separation—both of which cause a blockage effect and reduce the effective area of the channel. As the shock is moved downstream, this influence becomes more severe as the blockage is increased due to the increasing amount of separation. This reduction in the effective area causes the flow in the subsonic region downstream of the shock to accelerate and this leads to a corresponding reduction in the wall-pressure—with a near linear change of close to $0.05p/p_{0\infty}$ observed between each position. These wall-pressure measurements are fully consistent with the observations from the surface-flow visualizations.

Another informative comparison between the three positions can be attained by overlaying the three distributions so that their pressure rises all start at the same location. The pressure distributions in this form are also displayed in figure 10.10. In addition to the pressure distributions for positions 1, 2, and 3, the pressure distribution in the absence of a diffuser is also included in figure 10.10. In this figure, it is visible that all the curves collapse to a single line in the first part of the interaction (and this is in agreement with the Free Interaction Concept which was also observed in section 3.2.3). However, after the first rapid pressure rise, the distributions start to diverge from one another. The most pronounced difference is the very low pressure rise for position 3. Strikingly, the pressure rise is even lower than the constant-area duct case, and this suggests that the flow does not even 'notice' the diffuser which would normally be expected to increase the pressure over the constant-area channel. The only explanation is that the flow separation is so severe in this case that the effective geometry is reduced when compared to the constant-area channel case.

On the other hand, the profiles for position 1, position 2, and the constant-area channel overlay each other for longer. Only when position 1 enters the diffuser, at the inflexion in the distribution, where the effect of the diffuser starts to be felt does this distribution diverge upwards. Additionally, this change in slope at the diffuser entrance and the fact the distribution starts to rise above the constant-area case is further evidence that the diffuser is not stalled in position 1, i.e., no/little separation. (Strangely, the distribution for position 2 actually follows very closely to the constant-area channel, even once the flow enters the diffuser. It appears that the thickening of the boundary layer is almost exactly counteracts the diffuser in this case).

Wall-pressure measurements obtained using the PSP system are shown in figures 10.11 through 10.13, together with the schlieren image for each position. (Unfortunately, in the time available it was only viable to use PSP on the channel floor due to the presence of the windows and the lack of static pressure ports on the sidewall). In each of the figures, it can be

seen that the shock-foot lines up well with the region of rapid pressure rise in the PSP. What is more, the leading-leg of the shock-foot tends to lie somewhere between the initial pressure rise in the corners and at centre-span (and this is to be expected as the schlieren image gives an average representation of the shock-foot across the span). Examining the wall-pressure maps themselves, in addition to the reduction in wall-pressure recovery as the shock wave is moved downstream (which is illustrated by the change in colour of the downstream region from red to light orange), there is also an increase in three-dimensionality in the shock-foot region. As the shock is positioned closer to the diffuser, the curvature of the shock-foot increases, with the pressure rise occurring earlier in the corners. This observation is in agreement with the surface-flow visualizations, which also exhibited enhanced three-dimensionality as the shock was moved downstream. To compare the PSP images and the surface-flow visualizations directly, the points of initial separation taken from the surface-flow visualizations are indicated on these PSP maps. This comparison shows that the corner flow separation occur just downstream of the initial pressure rise, and this is evidence that the corner flows are not able to negotiate much of the shock-induced pressure rise before separating in all three configurations.

In general, these wall-pressure data nicely illustrate the increase in the effective constriction of the channel due to increased flow separation as the shock is moved downstream.

The extent of the stagnation pressure losses between positions are best illustrated by measurements of the stagnation pressure at the simulated AIP. The stagnation pressure contours measured at this plane are presented in figure 10.14. The axes bounding each of the contour maps at the bottom and sides are at the same location as the channel floor and sidewalls respectively. In each contour map, the losses near the floor and sidewalls are apparent, as is the increase in losses as the shock is moved successively downstream. This is again in agreement with the data presented thus far.

In position 1, it can be seen by looking at figure 10.14a that the sidewall and floor losses are similar (in terms of both their extent away from the wall and the magnitude of the losses), and this suggests that the viscous effects on the sidewalls and floor are comparable. There is a region of higher loss in each of the corners, though, and this supports the conclusion from the oil-flow visualization of the presence of corner separations.

As the shock is moved downstream (firstly to position 2 and then to position 3), the losses in the vicinity of the channel floor increase rapidly (compare figures 10.14a through figure 10.14c), and this is very much supports the observations from the wall-pressure and flow visualizations.

On the other hand, the sidewall losses are only slightly enhanced. This result indicates that the floor flow is more susceptible to separation than the sidewall in these configurations. This tendency may be due to the channel turning on the channel floor which is not present on the sidewalls: this leads to the need for a local increase in the adverse-pressure-gradient to accommodate the flow turning, and this therefore increases the susceptibility of the floor boundary layer to separation.

The increase in the losses in the floor region as the shock is moved closer to the diffuser can also be seen in figure 10.10d. In this figure, the stagnation pressure profiles at centre-span for the three shock locations are compared. A large increase in the thickness of the viscous layer, from around $4\delta_o$ in position 1 to $8\delta_o$ in position 3, is observed.

Also indicated in figure 10.14 are the area-averaged stagnation pressure recovery and dis-

tortion for each shock position (see chapter 2, equations 2.2 and 2.3). The pressure recovery drops from 88.4% in position 1 to 83.5% in position 3 and the distortion rises from 0.233 to 0.335. To estimate the increase in losses caused by separation, as a crude approximation, it can be assumed that the drop in pressure recovery between the positions is solely due to turbulent losses caused by flow separation (this assumes that shock losses and frictional losses are unchanged—which is not a terrible assumption). Using this approximation the separation loss in position 2 is 2.4% and in position 3 it is 4.9%. These numbers, while very approximate, are important because they give an estimate of what the maximum possible improvement that can be obtained by flow control which is only capable of separation mitigation (such as VGs). Thus using these configurations the maximum improvement that should be expected in this study is 2.4% and 4.9% for shock positions 2 and 3, respectively.

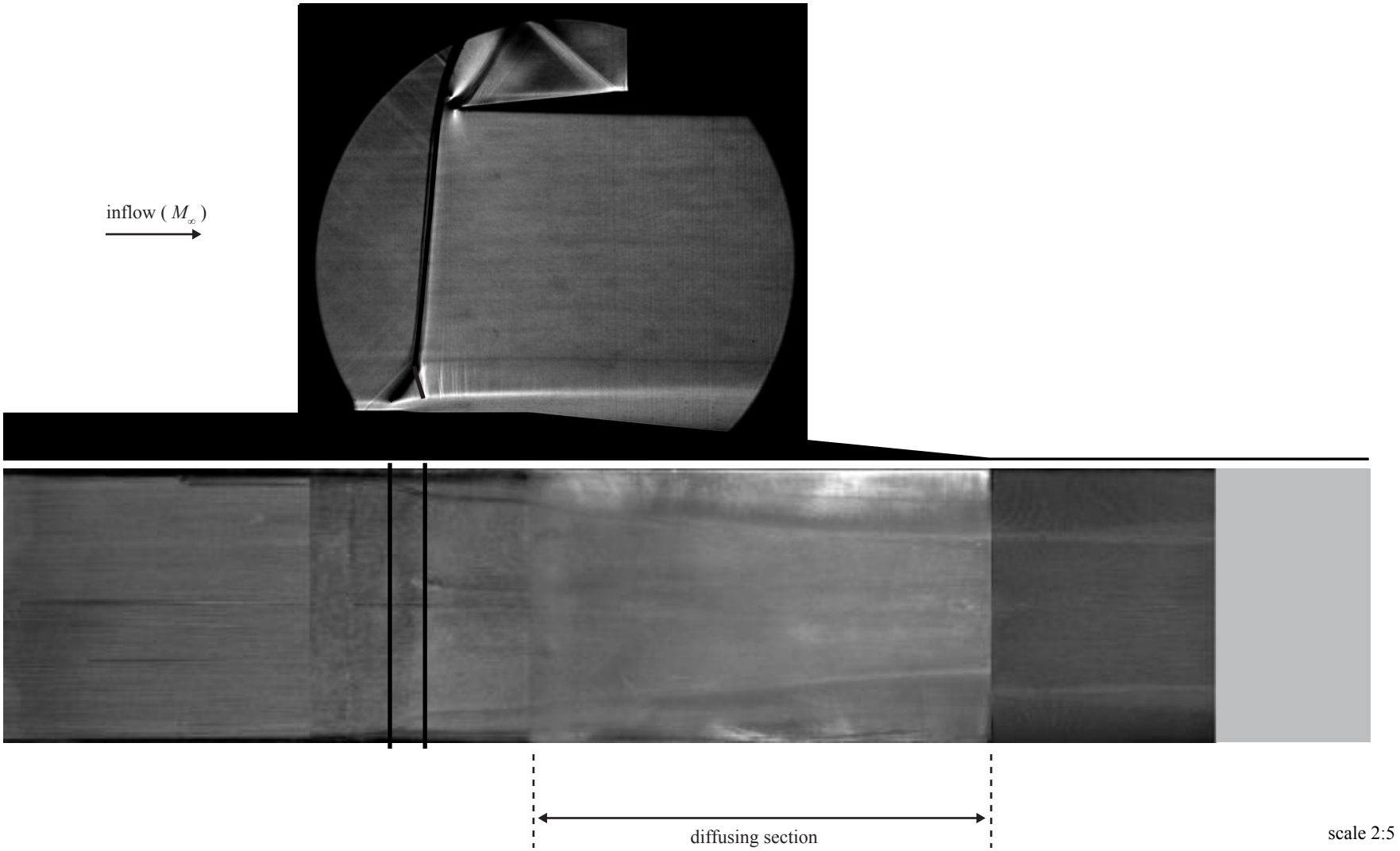

Figure 10.1: Flow visualizations with the shock holder in position 1 (30 mm upstream of the diffuser entrance)

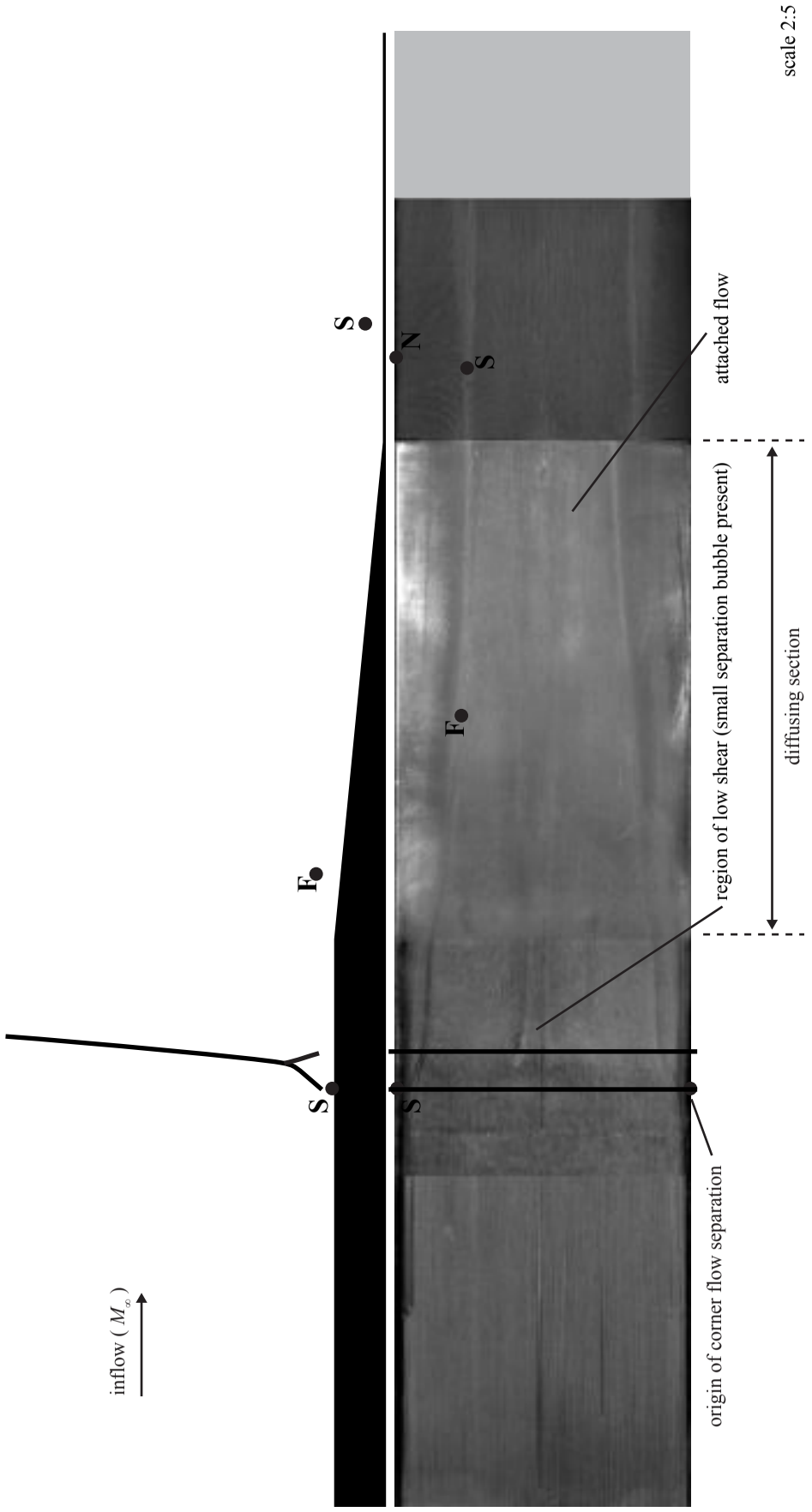

Figure 10.2: Flow visualizations with the shock holder in position 1 (30 mm upstream of the diffuser entrance)

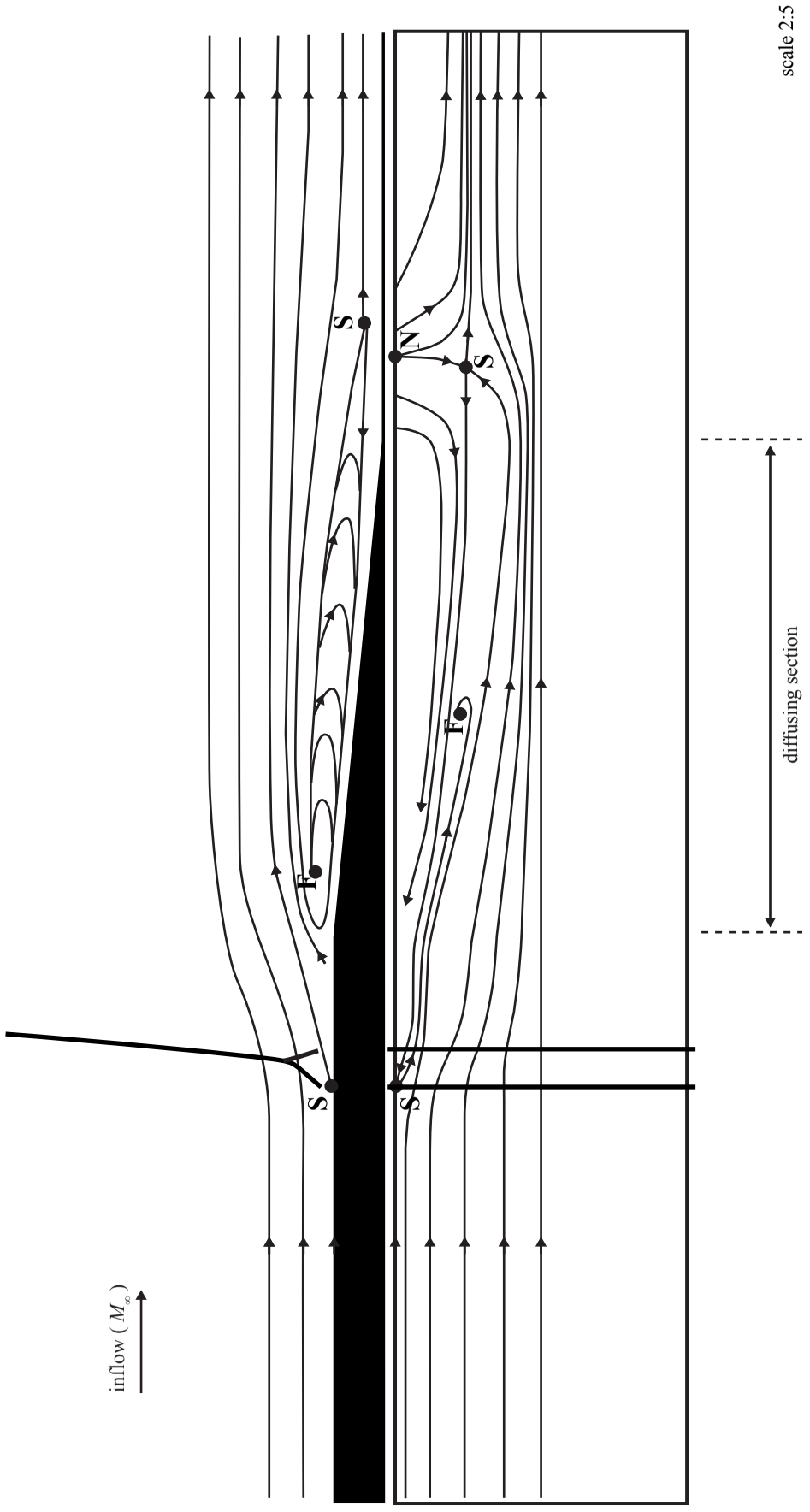

Figure 10.3: Topological interpretation of oil-flow visualization for position 1

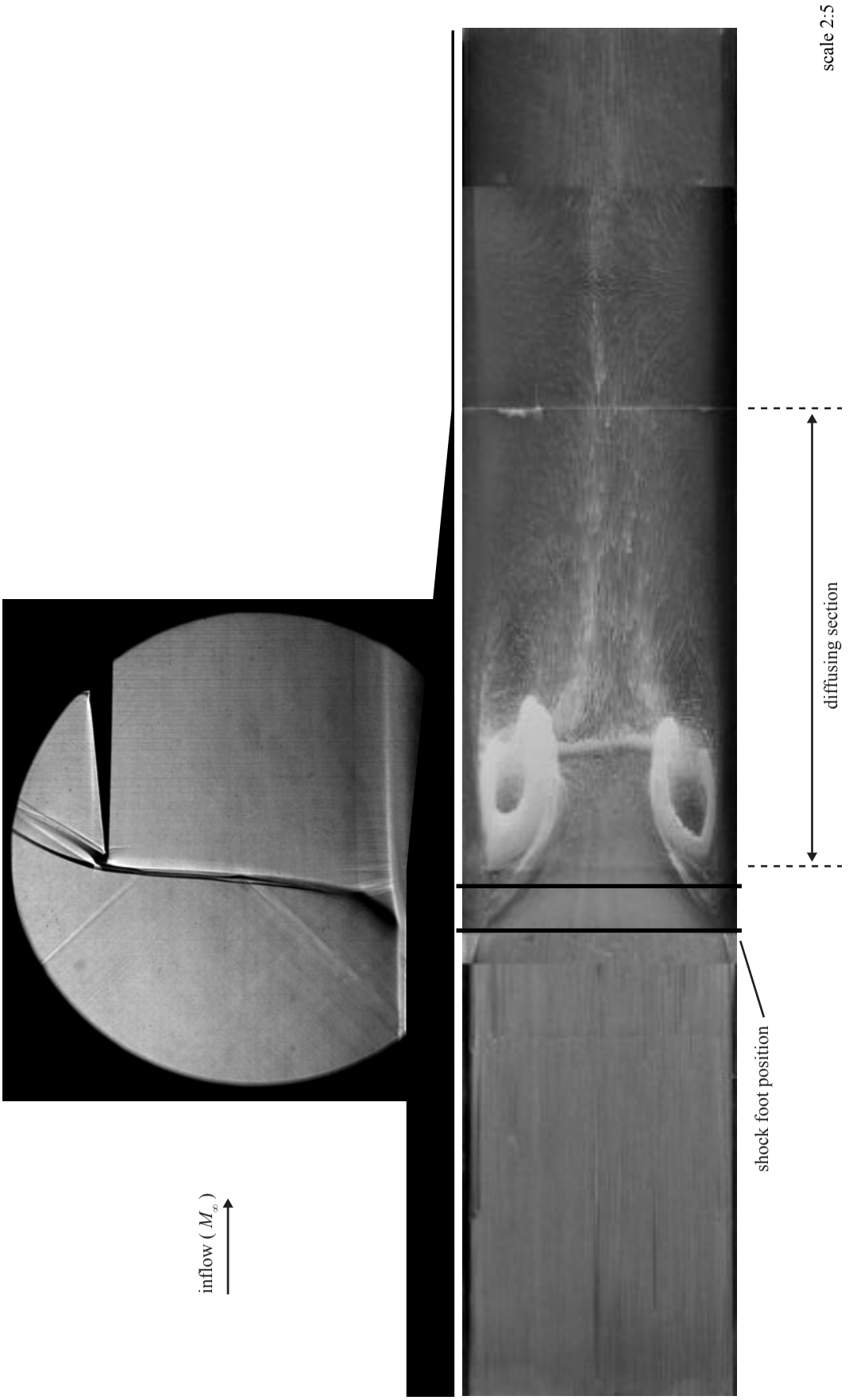

Figure 10.4: Flow visualizations with the shock holder in position 2 (at the same streamwise location as the diffuser entrance)

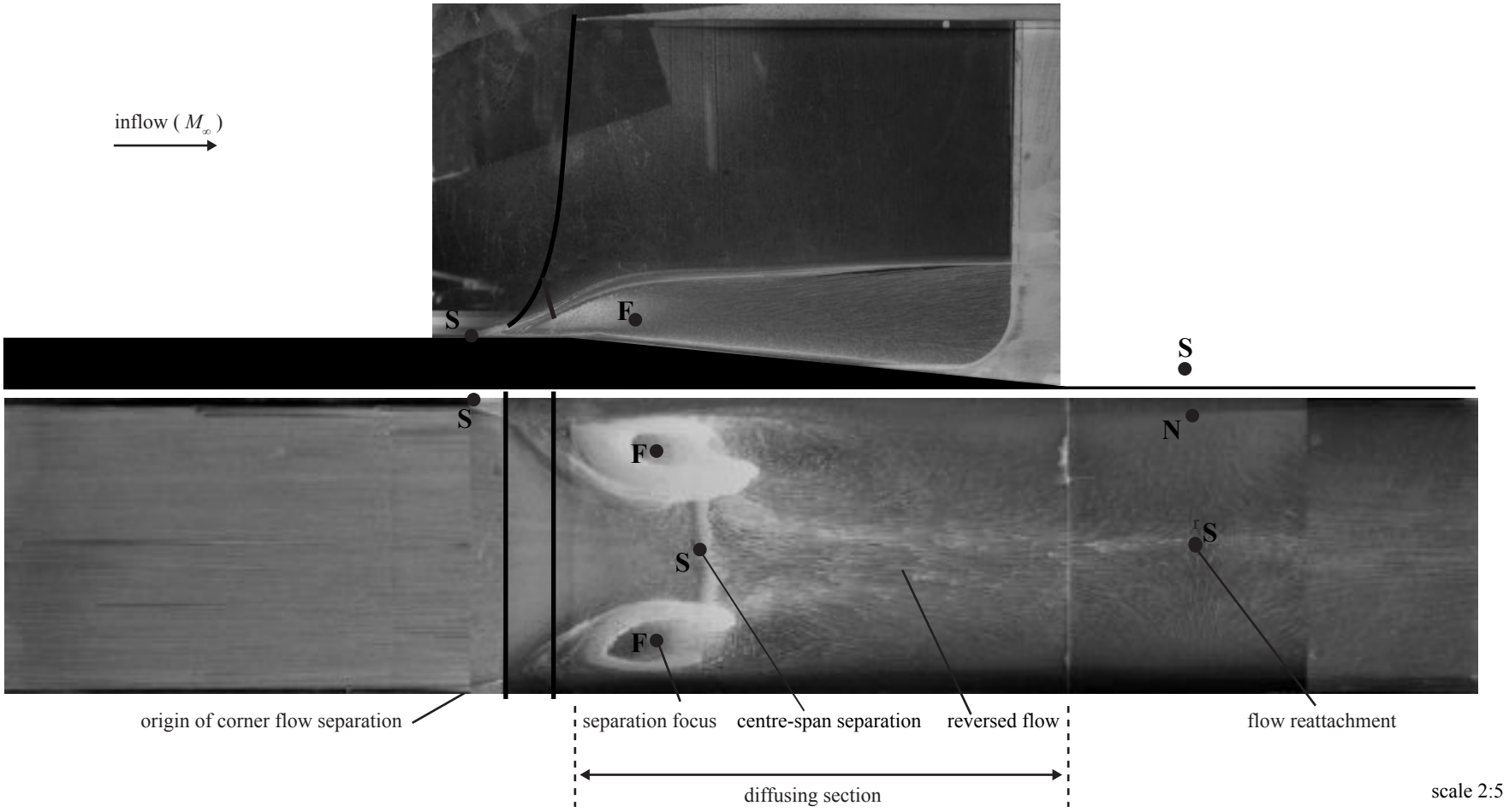

Figure 10.5: Flow visualizations with the shock holder in position 2 (at the same streamwise location as the diffuser entrance)

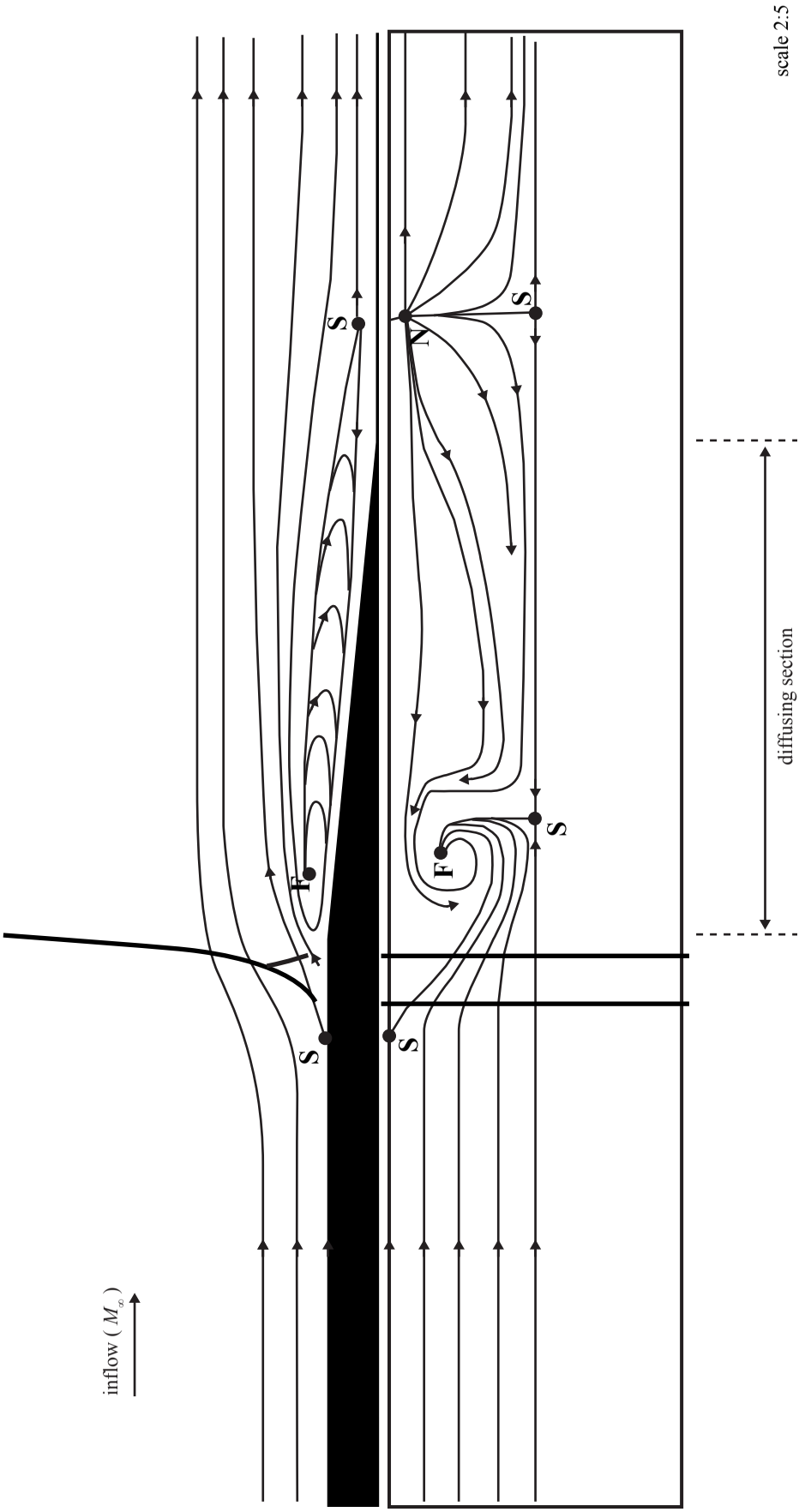

Figure 10.6: Topological interpretation of oil-flow visualization for position 2

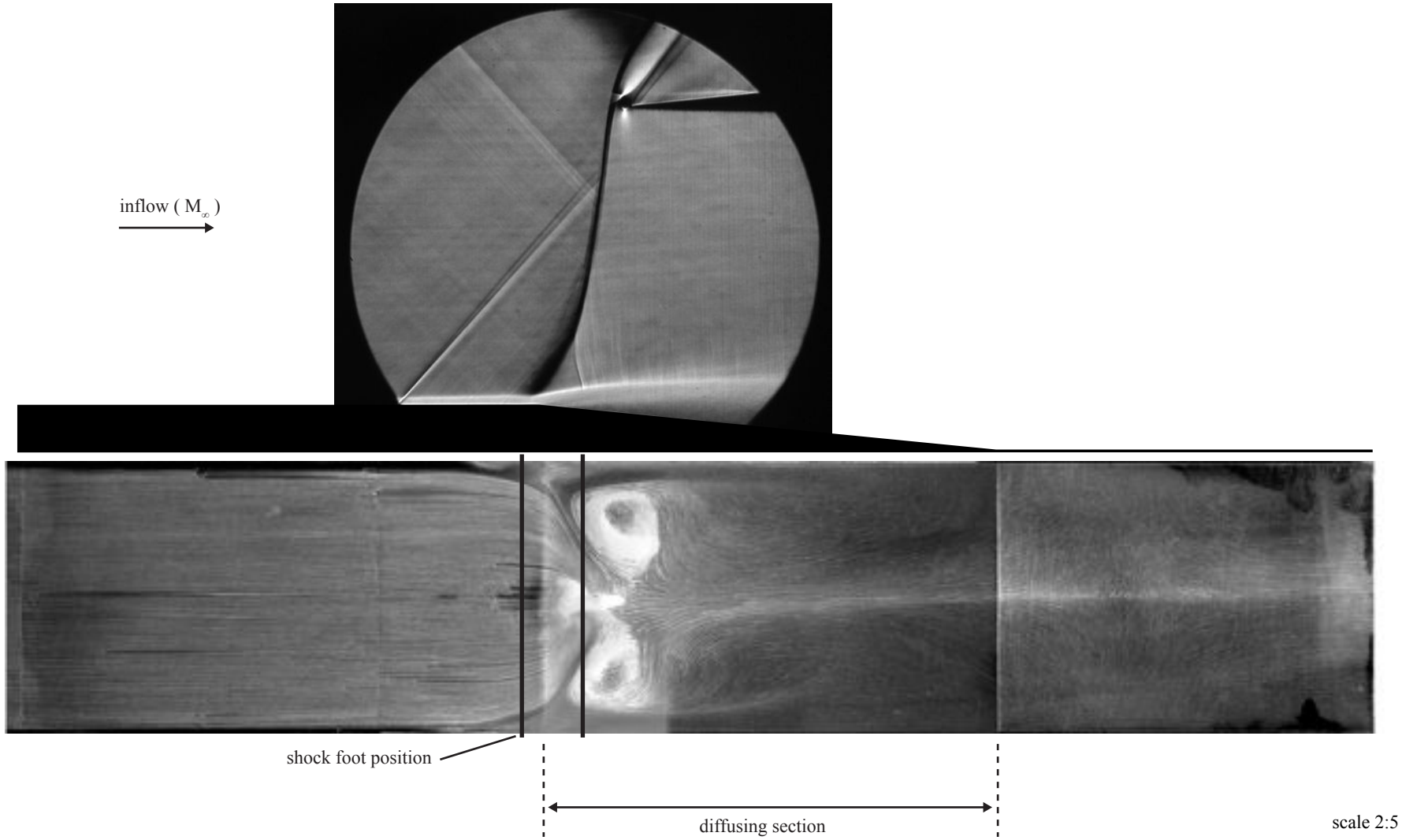

Figure 10.7: Flow visualizations with the shock holder in position 3 (30 mm downstream of the diffuser entrance)

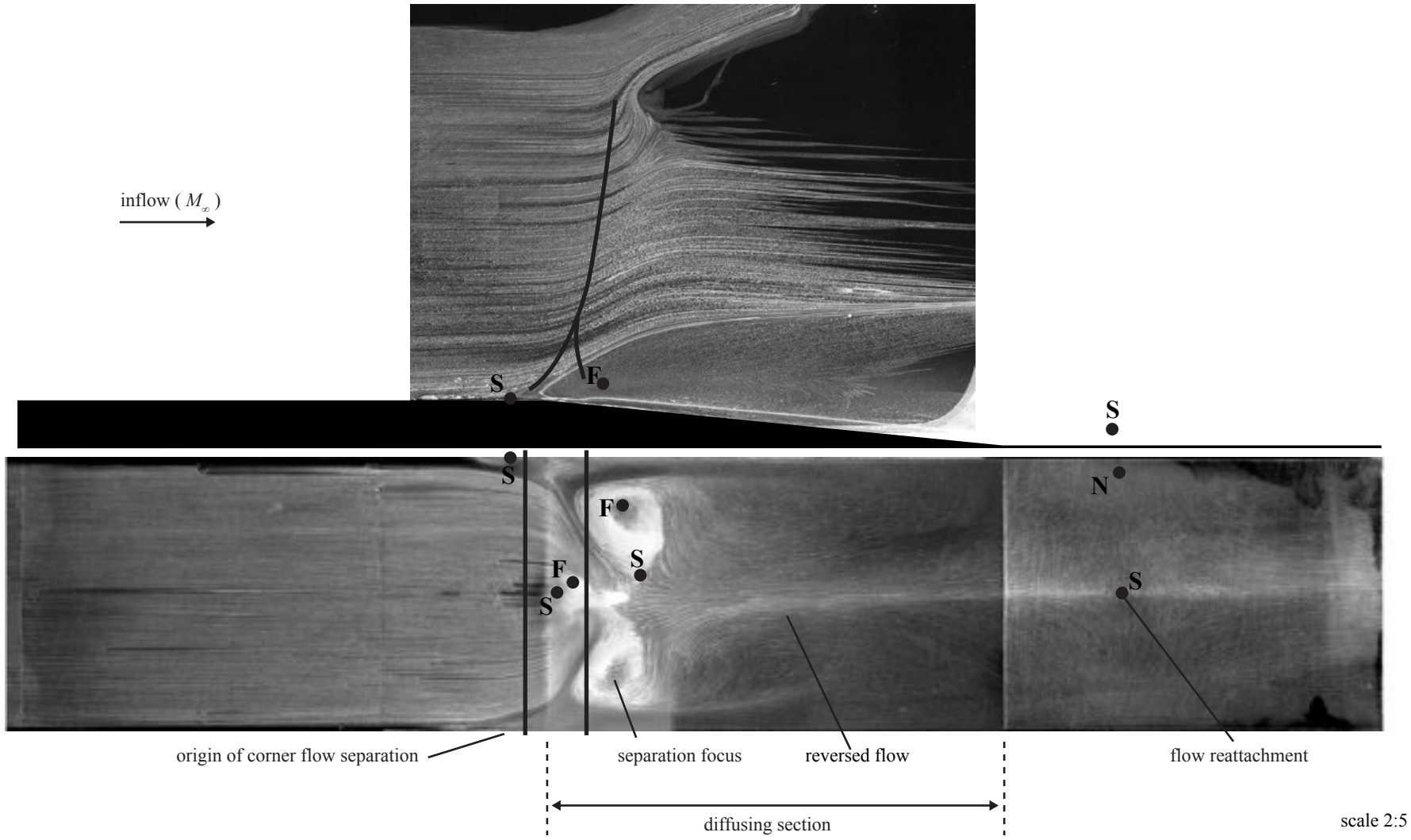

Figure 10.8: Flow visualizations with the shock holder in position 3 (30 mm downstream of the diffuser entrance)

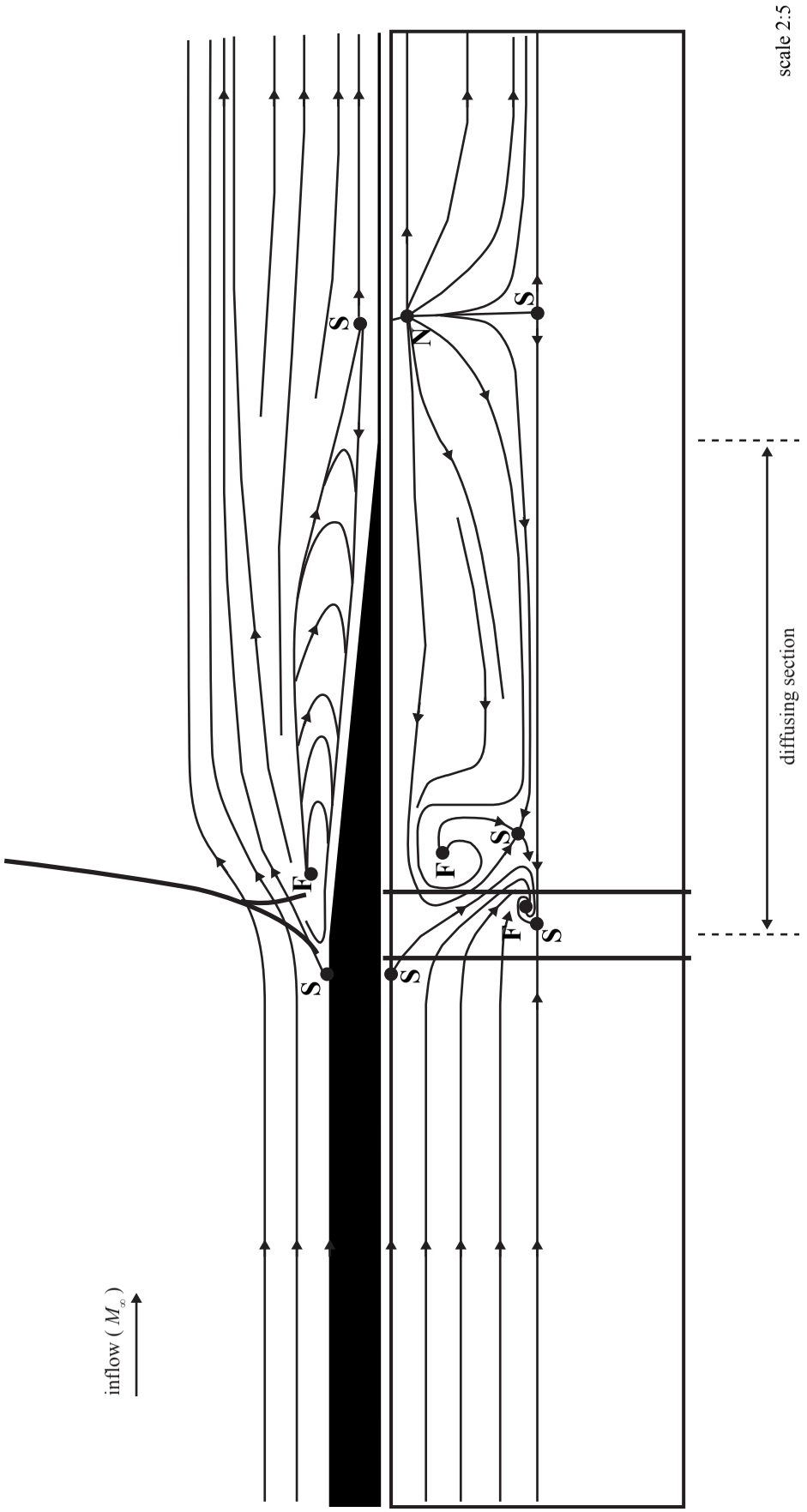

Figure 10.9: Topological interpretation of oil-flow visualization for position 3

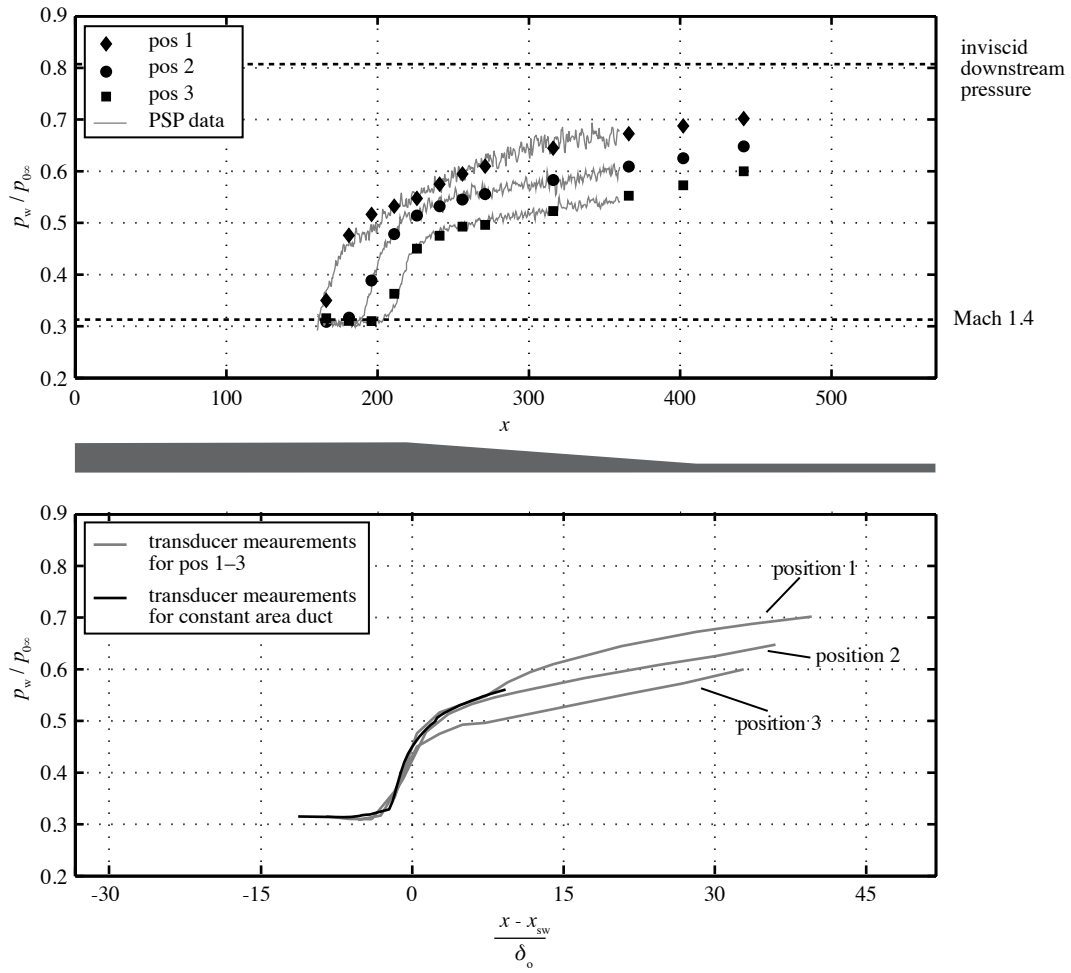

Figure 10.10: Wall-pressure measurements for the uncontrolled cases

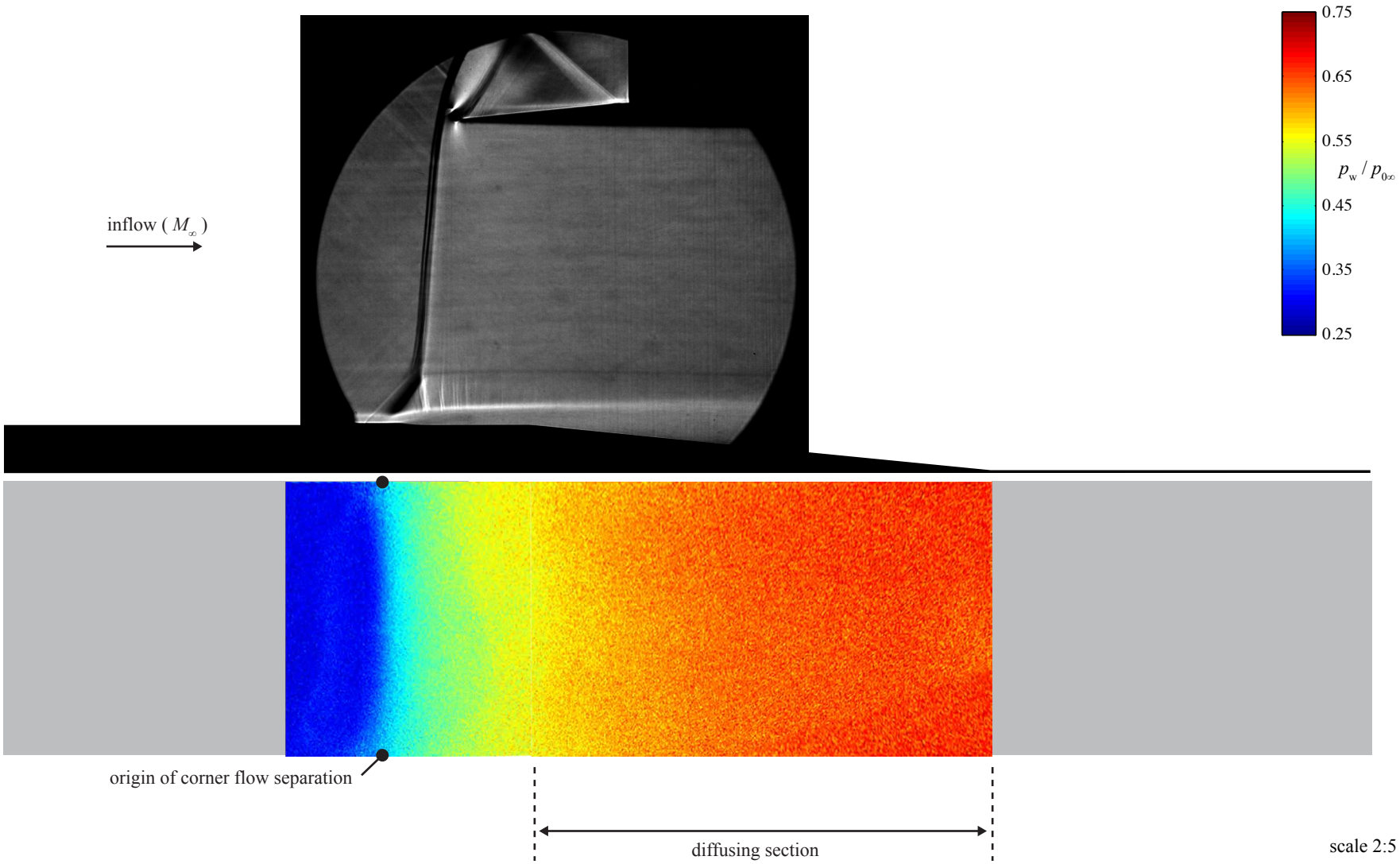

Figure 10.11: Schlieren and channel floor wall-pressure map with the shock holder in position 1

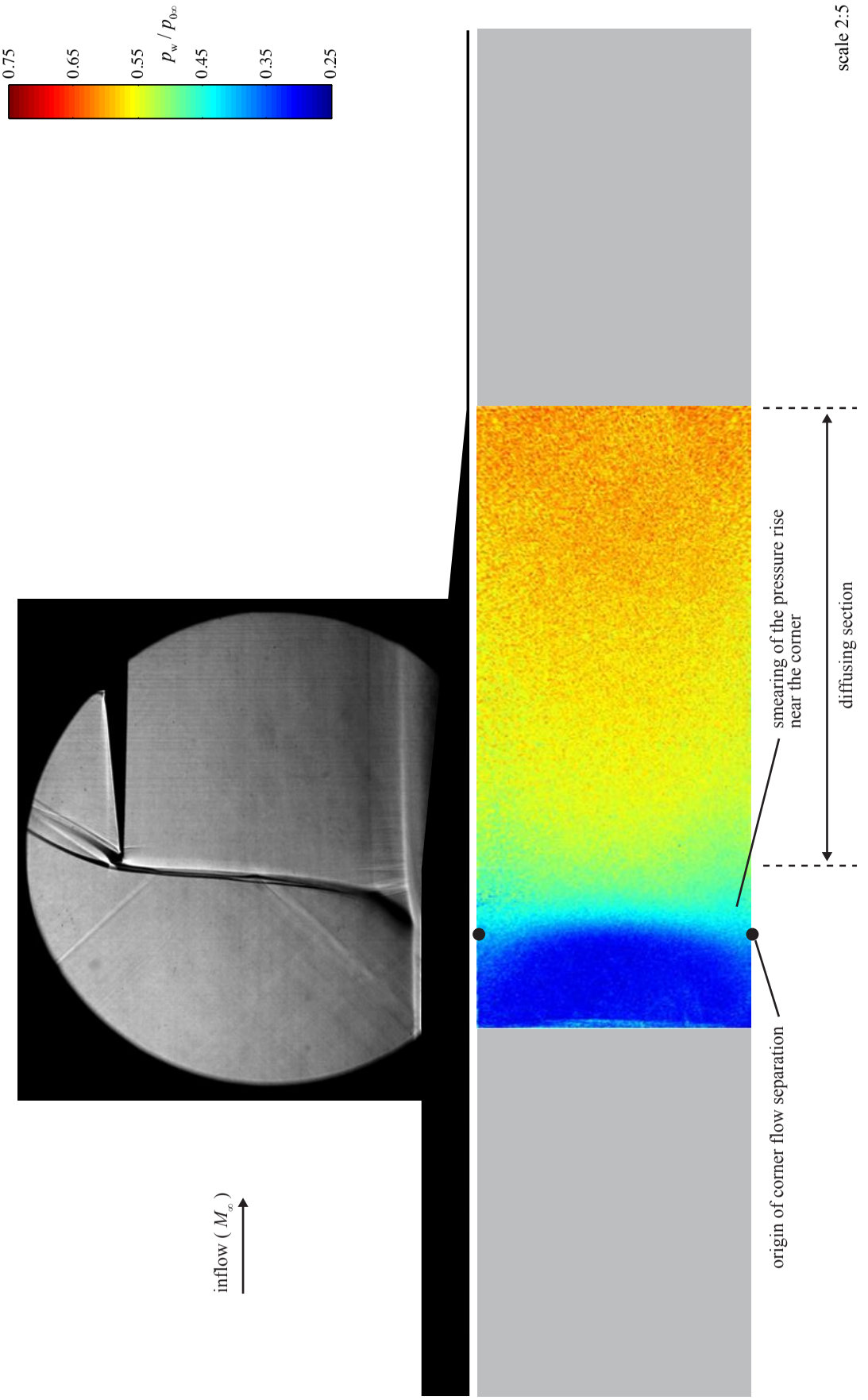

Figure 10.12: Schlieren and channel floor wall-pressure map with the shock holder in position 2

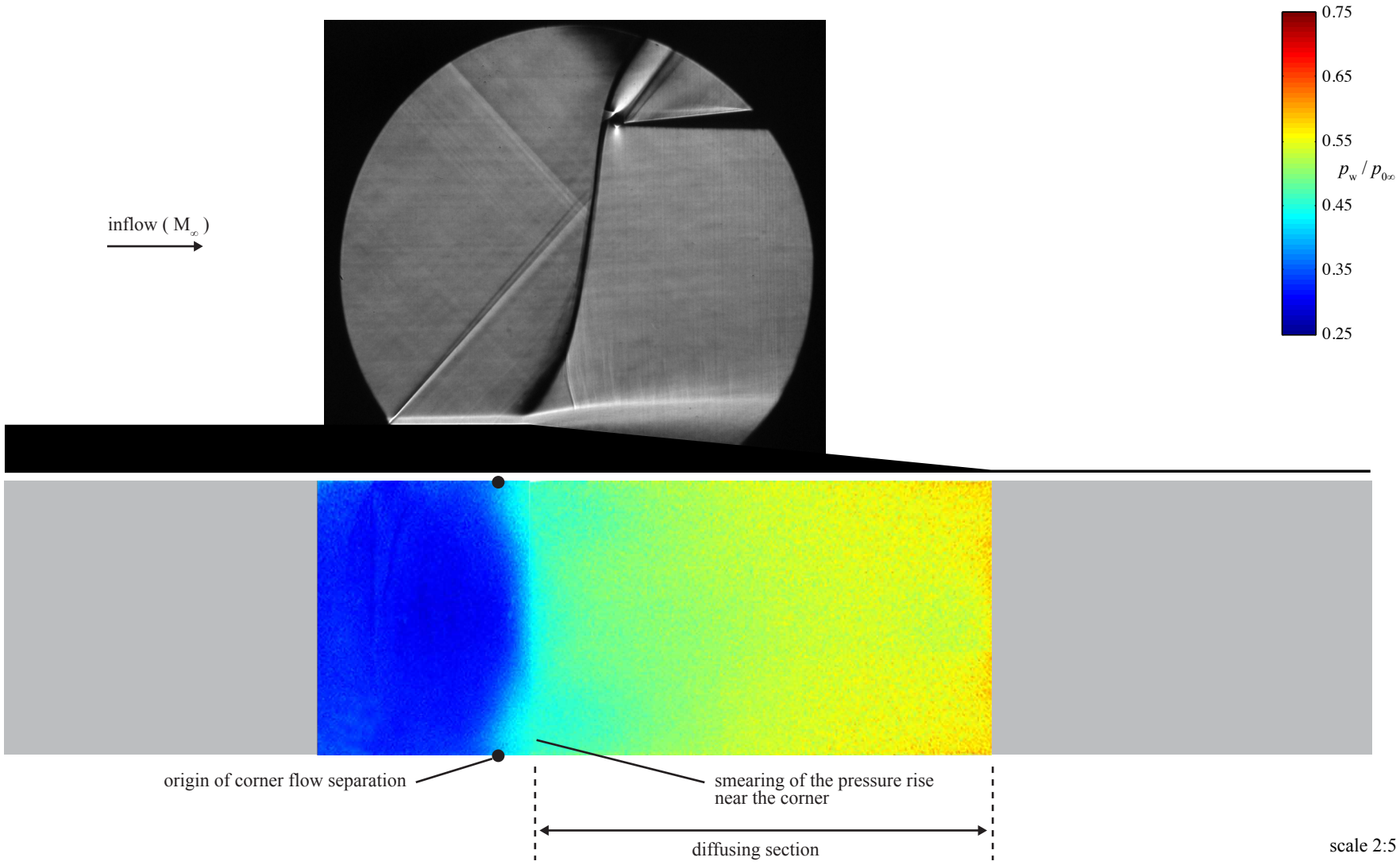

Figure 10.13: Schlieren and channel floor wall-pressure map with the shock holder in position 3

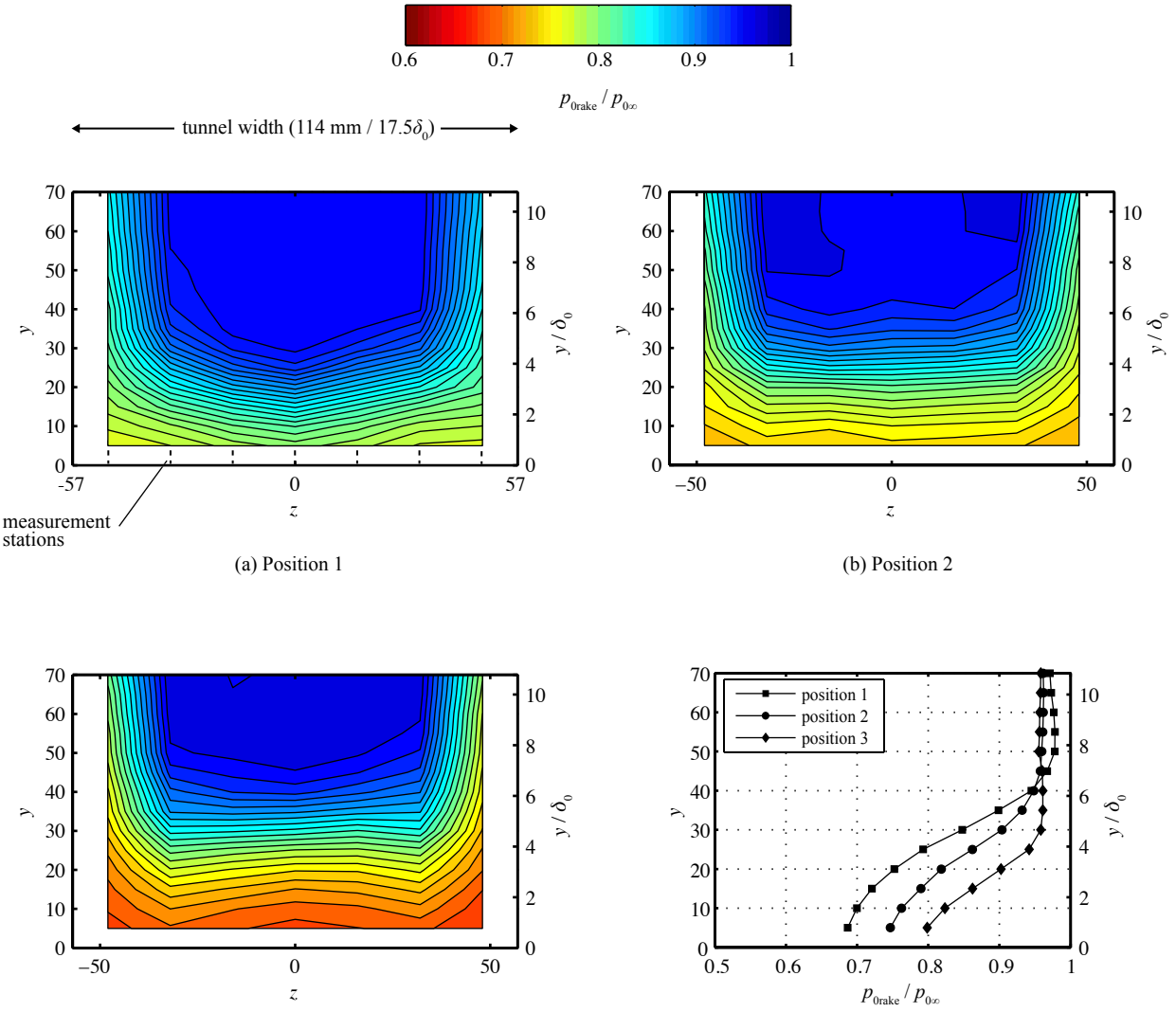

(a) Position 1

(b) Position 2

(c) Position 3

(d) Centre-line profiles

position	recovery (%)	total loss (%)	shock loss (%)	additional to shock losses (%)
pos 1	88.4	11.6	4.2	7.4
pos 2	86.0	14.0	4.2	9.8
pos 3	83.5	16.5	4.2	12.3

Figure 10.14: Pitot pressure measurements at the simulated AIP

10.3 The interaction in the presence of vortex generators

As the uncontrolled cases exhibited the most significant flow separation on the floor of the channel, it is thought that this region would benefit most from flow control. Such a situation is presented in figure 10.15, where flow visualizations with the shock in position 3 in the presence of an array of ramped vanes on the channel floor are shown. The VGs were positioned as described in section 7.4. These flow visualizations should be directly compared with those in figure 10.7.

When comparing figures 10.7 and 10.15, it can be seen that the flow is significantly modified by the presence of the VGs. Firstly, what is immediately apparent in the shadowgraph image of figure 10.15 are both the VGs and the shock waves associated with the VGs, which appear to originate near the leading edges of the VGs. Downstream of the VGs, but upstream of the shock wave, thickening of the boundary layer is also evident. Furthermore, the shock wave is more normal than in the uncontrolled case. As a result, the shock-foot stands closer to the diffuser entrance. Nevertheless, much like before, there is substantial thickening through the interaction, and the edge of the viscous region behind the shock does not follow the profile of the diffuser. Yet, the interaction region is somewhat more blurred than in the uncontrolled case—both the shock itself and the boundary-layer edge appear less sharp and more smeared than before. Video footage of the interaction, however, indicated that there was no increase in unsteadiness. Instead, it is thought that the increased blurring is due to more spanwise non-uniformity than before and that the blurring results as a product of the averaging process of the shadowgraph image across the span.

In addition to the channel floor surface-flow-visualization shown in figure 10.15, a sidewall surface-flow visualization is shown alongside the floor surface-flow visualization in figure 10.16. Examination of the surface-flow topology reveals a number of changes to the near-wall flow when compared to the uncontrolled interaction. This difference is particularly visible when comparing the topological interpretation of the surface-flow-visualization in the presence of VGs presented in figure 10.17 with the topological interpretation of the uncontrolled case of figure 10.9. The main difference is what appears to be an attached channel of flow along the channel floor (with the exception of some very small owl-face separations immediately downstream of the diffuser entrance). Although this attached channel is relatively wide at the diffuser entrance, inside the diffuser, it is quickly constricted by the large corner separations which again grow rapidly with streamwise distance and consequently dominate the flow-field inside the diffuser. Much like the uncontrolled case, these corner separations originate in the vicinity of the shock-foot. On the sidewall, the flow topology looks more similar to the uncontrolled case. However, the separation line is deflected further from the floor than before. This suggests that, if anything, the corner separations are even larger than before.

The wall-pressure distribution for this case is compared to the uncontrolled case in figure 10.19. From this figure, it can be seen that with this VG configuration that there is no improvement in the overall wall-pressure recovery over the uncontrolled case. This indicates that the effective area remains unchanged compared to the uncontrolled case. Thus, if there has been a small reduction in separation along the centre-span with the VGs, at the same time, the corners must be slightly worse.

While the overall pressure rise remains unchanged, the distributions are not identical: the

start of the interaction has clearly moved downstream in the case with VGs which is in agreement with the shadowgraph image. This downstream movement allows an expansion to take place at the entrance to the diffuser. In spite of this, the expansion is soon swallowed by the terminal shock wave (also visible in the shadowgraph image: figure 10.15), and, as a result, its influence on the inviscid pressure rise is thought to be relatively negligible. (The majority of the shock still 'sees' an upstream Mach number of 1.4 as the expansion is confined to a small region close to the floor). After this, the wall pressure rises rapidly to a similar level to the uncontrolled interaction. Again, the pressure plateaus well below the inviscid level due to the blockage effect caused by the extensive separation.

The effects of the VGs are also visible in the wall-pressure map shown in figure 10.18 alongside the shadowgraph image. Again the area with the largest spanwise variation occurs close to the shock. In this region, the low pressure region just downstream of the diffuser entrance apparent in the centre-span distribution is clearly visible. This low pressure region does not extend to the side-walls, however, because of the smearing that is observed in the corners, much like the uncontrolled case. If anything compared to the uncontrolled case, there is more smearing (the green region extents further into the diffuser than the uncontrolled case: compare figure 10.18 with figure 10.13). This suggests that the corner separations are even more prominent in this case, which agrees with the behaviour observed in the sidewall flow visualization. While there is significant spanwise variation in the vicinity of the shock, this variation is eradicated by the middle of the diffuser, which illustrates that the subsonic diffuser cannot support substantial spanwise pressure gradients for long.

Comparing the floor surface-flow visualization of figure 10.16 and wall-pressure map of figure 10.17, it can be seen that there is good agreement between the position of the initial corner separations and the start of the shock smearing. This helps to confirms that the smearing is caused by this separation.

As an aside the low pressure cores of the vortices shed by the VGs are clearly visible until the shock location. The fact that they disappear at the shock location suggests that they are largely dissipated by the shock, however, more detailed measurements are required to confirm this.

Measurements taken at the AIP are presented in figure 10.20. From the centre-span plot in figure 10.20b, it is visible that flow control has reduced the stagnation pressure loss along the centre-span. This reduction in losses is consistent with the observed channel of attached flow in the floor surface-flow visualization. While this improvement is welcome, towards the side-walls, if anything, there is increased loss, and as a result there is almost no change in the overall pressure recovery or distortion.

It can be concluded that while the VGs have been able to energize the central channel, their presence has made the corners slightly worse. As a consequence, once again, the corner flows dominate. It is clear that control of the corner separations is required.

As previous attempts to reduce corner flow separations in similar flows with VGs have proved unsuccessful and because there is a general lack of experimental or computational studies to help guide a successful control scheme for the corner, it was decided that traditional boundary-layer suction should be used in the corners, which was considered the most likely candidate for success. The implementation of corner suction is discussed in the next section.

Figure 10.15: Flow visualizations for the case controlled by VGs on the channel floor (schlieren and channel floor surface-flow visualization)

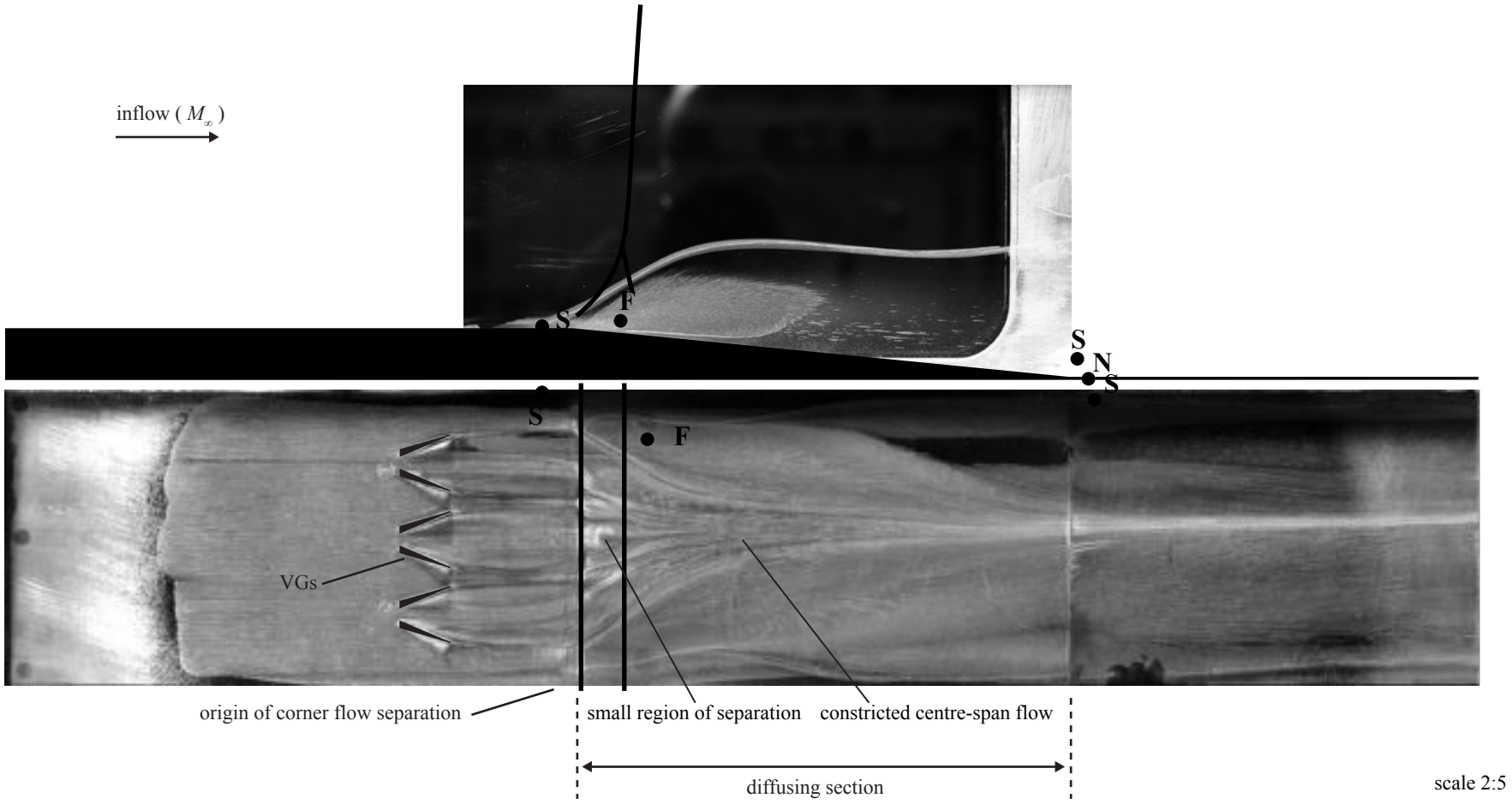

Figure 10.16: Flow visualizations for the case controlled by VGs on the channel floor (side-wall and channel floor surface-flow visualizations)

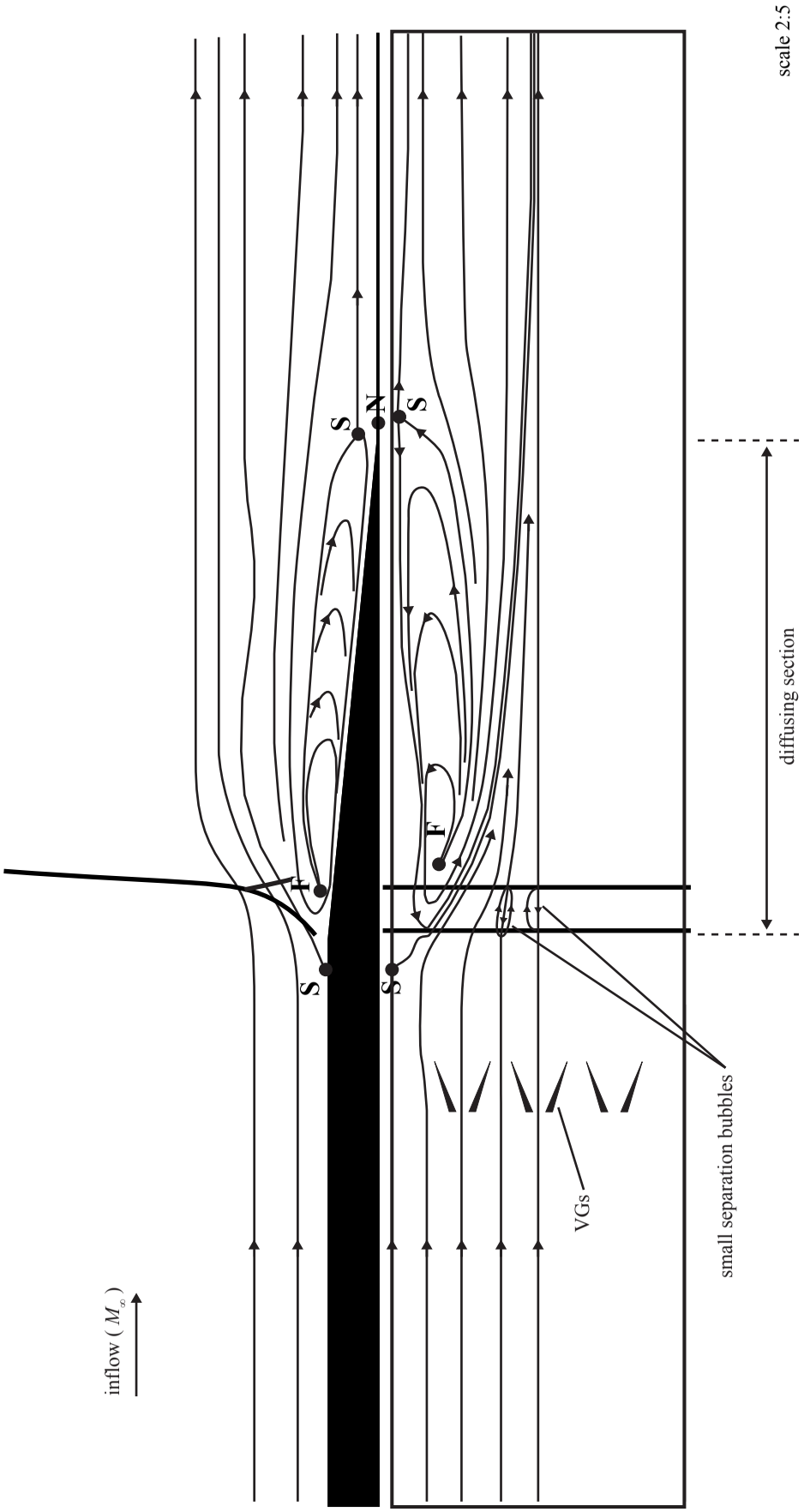

Figure 10.17: Topological interpretation of oil-flow visualization for the case controlled by VGs on the channel floor

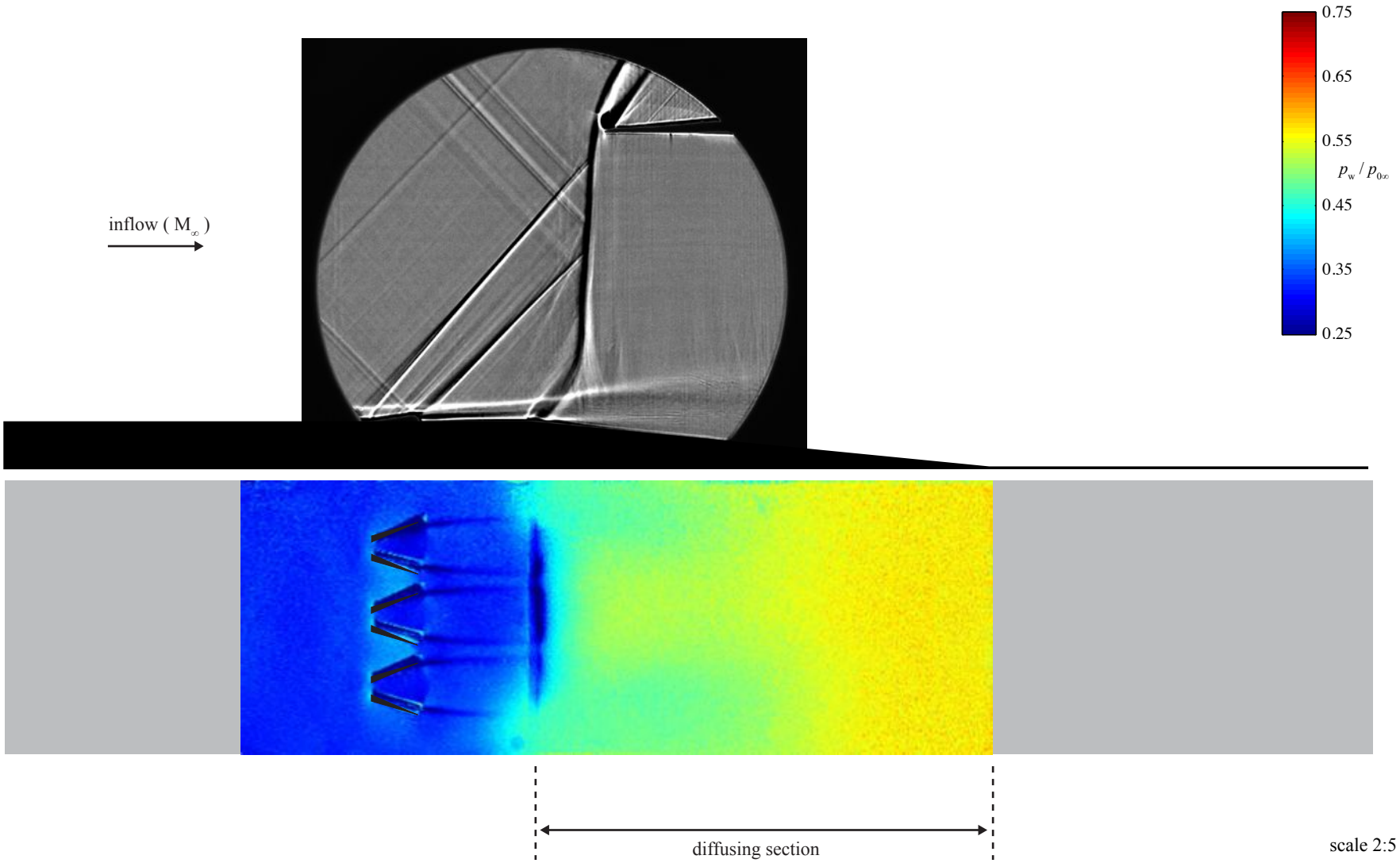

Figure 10.18: Schlieren and channel floor wall-pressure map for the case controlled by VGs on the channel floor

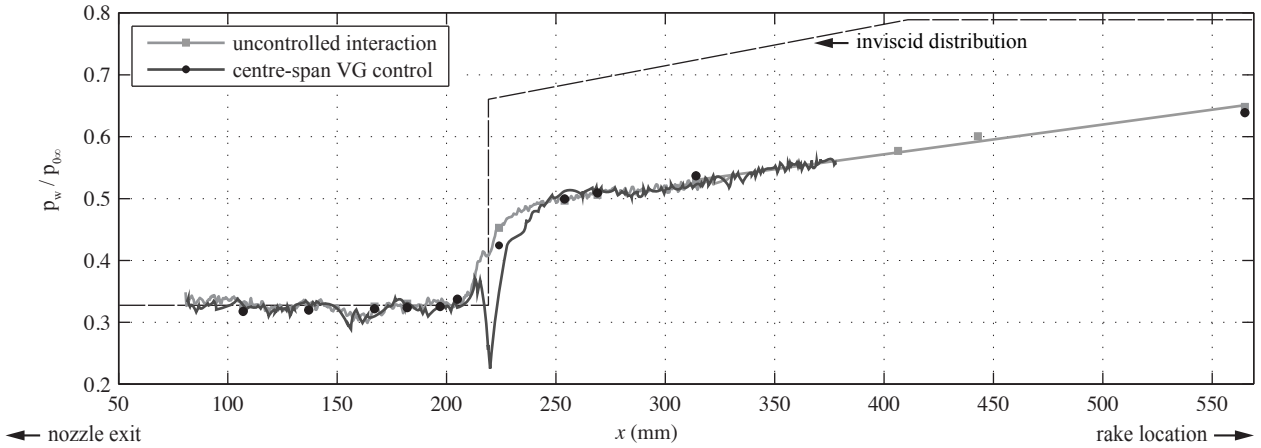

Figure 10.19: Floor wall-pressure distribution for the case controlled by centre-span VGs (lines indicate PSP; symbols pressure transducers)

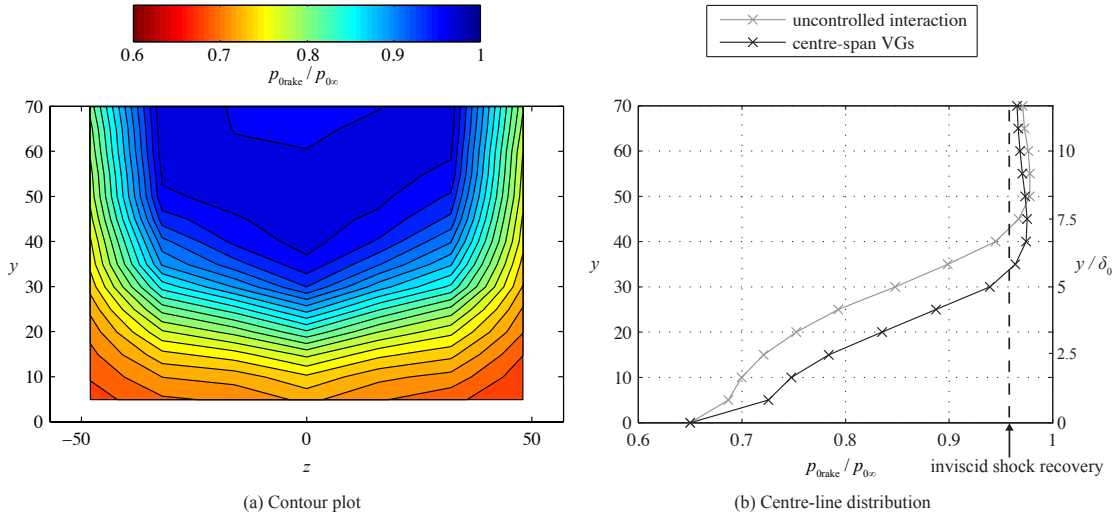

(a) Contour plot (b) Centre-line distribution

Figure 10.20: Pressure recovery contour plot and centre-line profile for the case controlled by centre-span VGs

10.4 The interaction in the presence of corner control using suction

The shadowgraph and channel floor surface-flow visualization for the case controlled by corner suction are presented in figure 10.21. Unfortunately, the corner slots are just outside the visible area with the shadowgraph setup; however, they can be seen in the surface-flow visualization.

In the shadowgraph image of figure 10.21 the initial boundary-layer thickness, thickening across the interaction, and downstream shear layer are indistinguishable from the uncontrolled case. Yet, two faint shock waves originating from the slots can be seen.

Like the previous cases, the surface-flow-visualization on the floor and sidewall are presented in figure 10.22 and a topological interpretation of the near-wall flow is sketched in figure 10.23. The impact of the corner suction on the flow-field is much more obvious in the surface-flow visualizations. No longer are there large corner separations. Instead, the extensive separation in the diffuser is initiated in the centre-span region. As a consequence, the streamlines approaching the upstream saddle point are pushed away from the centre-span towards the sidewalls where they then wrap up into a focus. This focus and its associated vortex are also of the opposite rotation to that in the uncontrolled case. In addition to this, the surface streamlines are more two-dimensional than previously observed, and the corners' influence is limited to a smaller portion of the span. These features are most clearly demonstrated in the topological interpretation of figure 10.23. The floor reattachment point is once again located downstream of the diffuser at a very similar streamwise location to the uncontrolled case. Whilst the location of reattachment is similar to the uncontrolled case, the reattachment topology is more complex. Instead of a single reattachment saddle point there now appears to be two reattachment saddle points straddling an attachment node at centre-span.

From the floor surface-flow visualization it is unclear whether there is separation in the corners at all. The sidewall surface-flow visualization does suggest that there is some separation in the corner region upstream of the diffuser entrance. Its extent is much reduced compared to the uncontrolled case, however. This reduction, combined with the lack of evidence for corner separation in the floor flow visualization indicates that the slots have been successful at reducing the separation in the corners.

Regardless of the dramatic changes in the near-wall topology, the extent of flow separation at centre-span and across the centre-span region remains much the same as the uncontrolled case at 240 mm ($37\delta_o$).

Wall pressure measurements are presented in figure 10.24 and figure 10.25. From the centre-span wall-pressure distributions shown in figure 10.25, apart from some deviation in the vicinity of the corner slots, it can be seen that there is little, if any, difference in the wall-pressure rise. This is a sign that the effective area in the diffuser remains unchanged, which is in agreement with the surface-flow visualizations which suggests a similar separation length. The difference between the wall-pressure distributions in the vicinity of the slots comes about due to a local expansion and subsequent compression at the leading and trailing edges of the slot respectively. This local variation is especially evident from the pressure map shown in figure 10.24. Nonetheless, overall, the slots appear to leave the Mach number just upstream of the shock unchanged, i.e., the shock strength is unchanged. (This is thought to be because the removed mass flow is relatively low, and therefore has little impact on the core flow).

While the centre-span distributions look much the same, in the vicinity of the shock, clear differences are visible when comparing the wall-pressure maps (compare figure 10.13 and figure 10.24). Upon inspection of the wall-pressure variation near the side-walls in the presence of suction, it is visible that there is no longer substantial shock smearing in the corners. This further substantiates the conclusion that the corner separations are much reduced by the corner slots. Instead of being smeared, the footprint of the shock is just curved in much the same way as the separation line in the flow-visualization, and occurs just upstream of the separation line.

The pressure recovery measured at the AIP in this configuration is presented in figure 10.26. A comparison of this case with the uncontrolled case demonstrates that there is no substantial change to the overall flow. As a direct consequence, the pressure recovery and distortion remain very similar to before at 84.0% and 0.374 respectively. Despite this, on closer inspection some differences in the variation of losses across the span are visible between the two: in the case with corner suction a slight reduction in the channel floor losses is seen as the sidewalls are approached, which is in contrast to a small increase in the uncontrolled case. Nevertheless, the similarity between these two cases is especially evident in figure 10.26b, which shows a comparison of the centre-span profiles obtained with and without corner suction. It can be seen that the profiles are similar.

In summary, while the structure of the separation and therefore the losses in the diffuser has altered considerably by introducing corner suction, their overall extent has not. Instead, reduced corner separation is replaced by increased centre-span separation. As a consequence, there is very little change in overall pressure recovery. For this reason, there appears to little to be gained from using corner suction in isolation in this particular configuration.

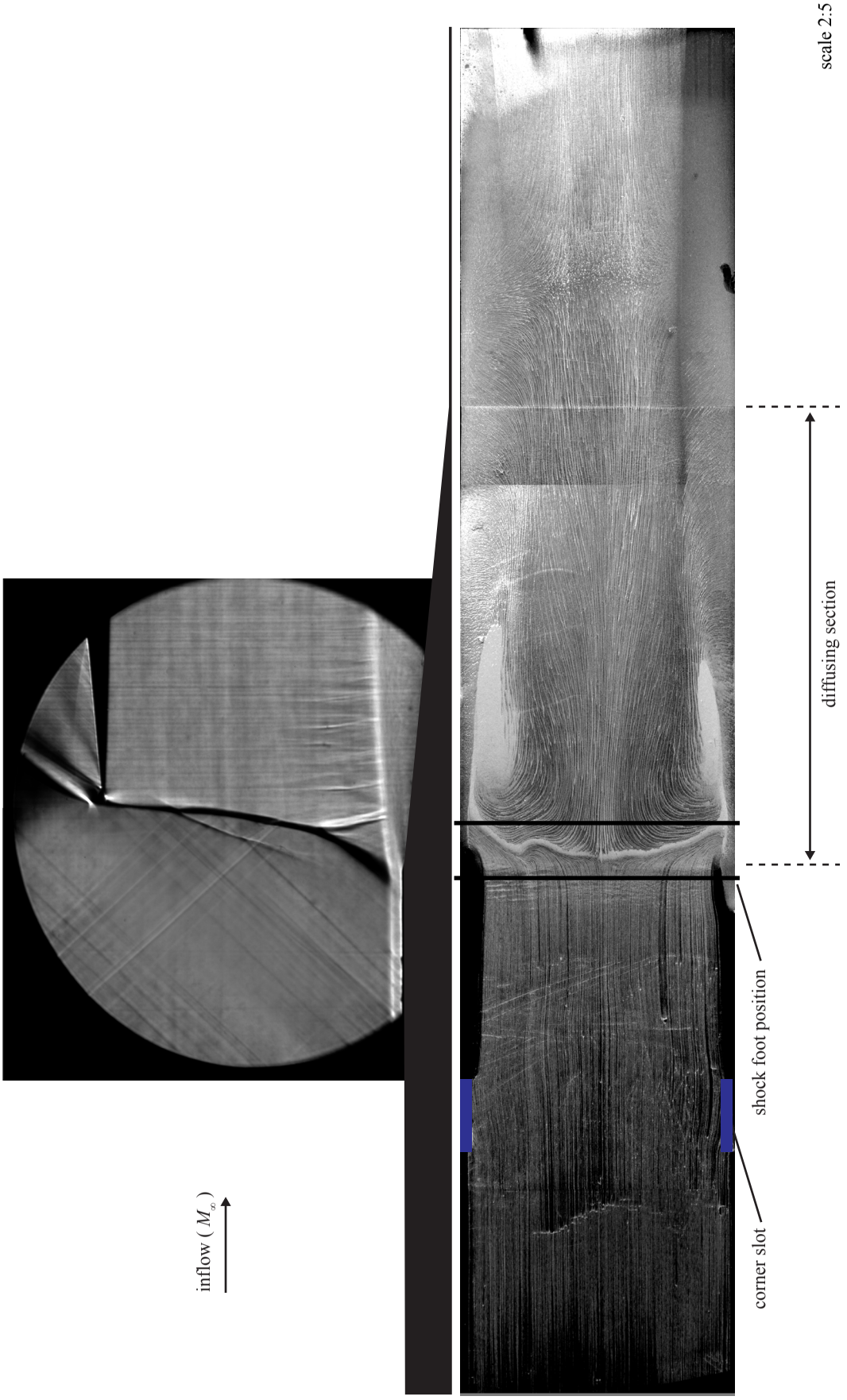

Figure 10.21: Flow visualizations for the case controlled by corner suction (schlieren and channel floor surface-flow visualization)

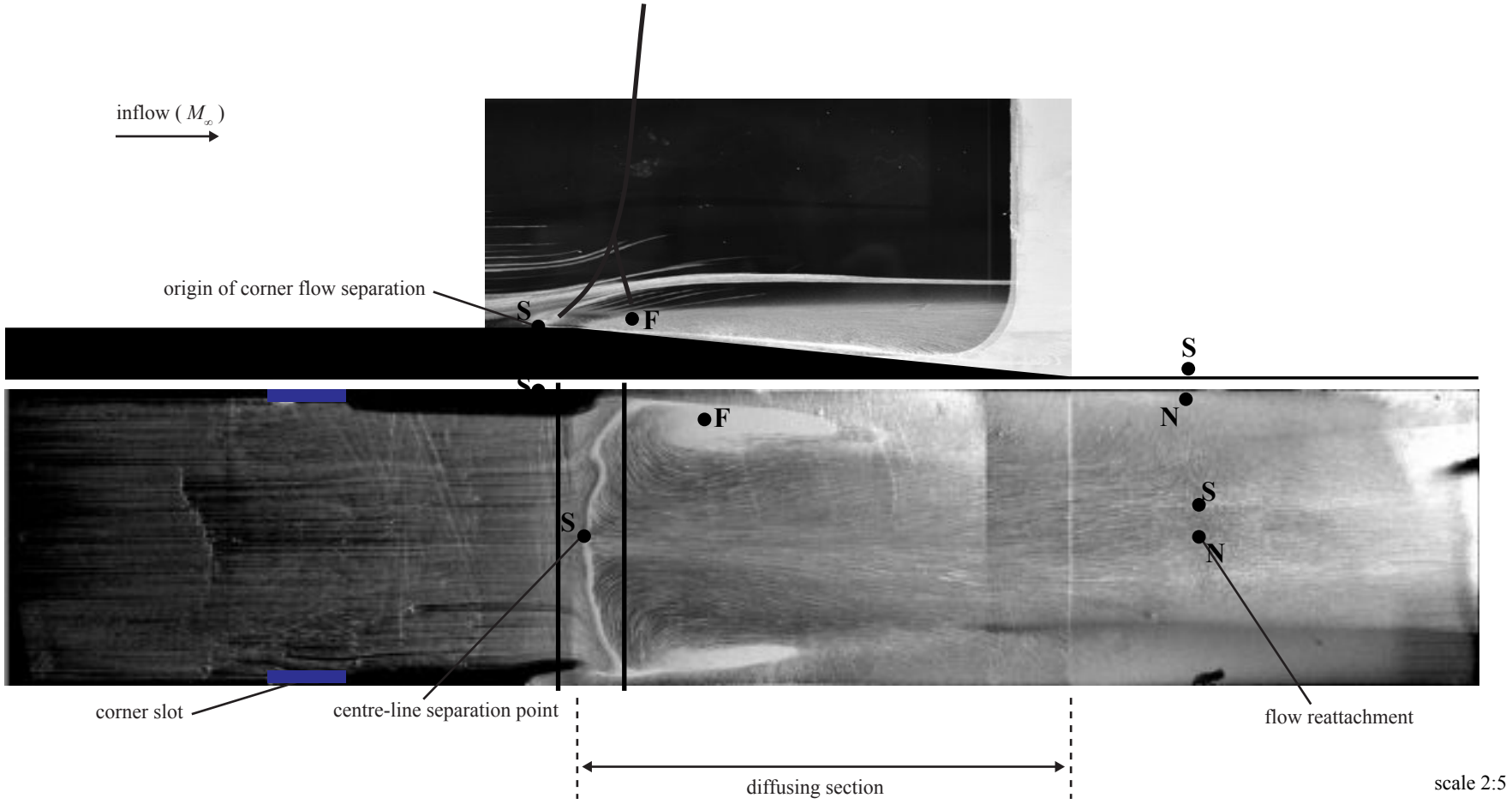

Figure 10.22: Flow visualizations for the case controlled by corner suction (side-wall and channel floor surface-flow visualizations)

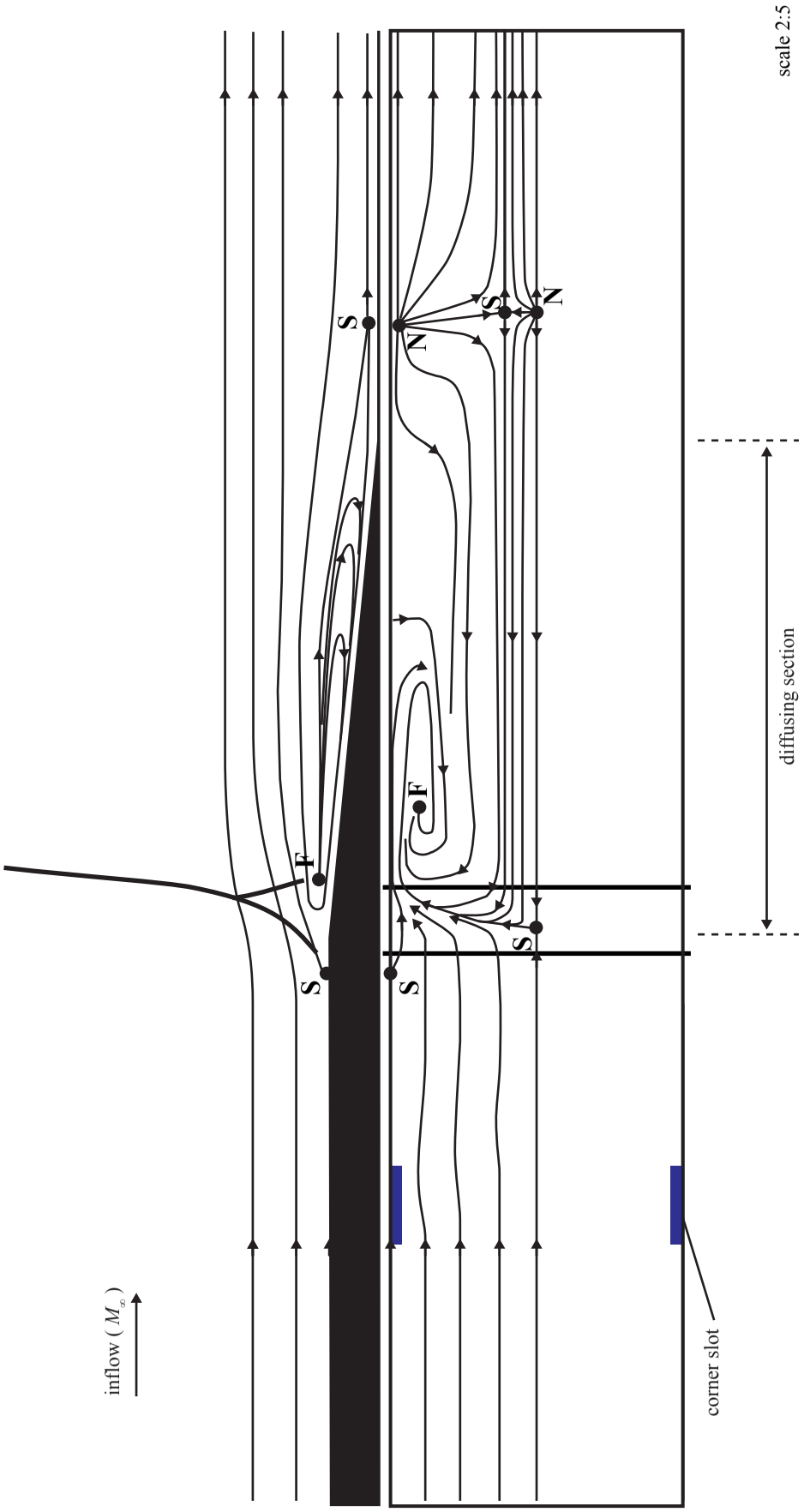

Figure 10.23: Topological interpretation of oil-flow visualization for the case controlled by corner suction

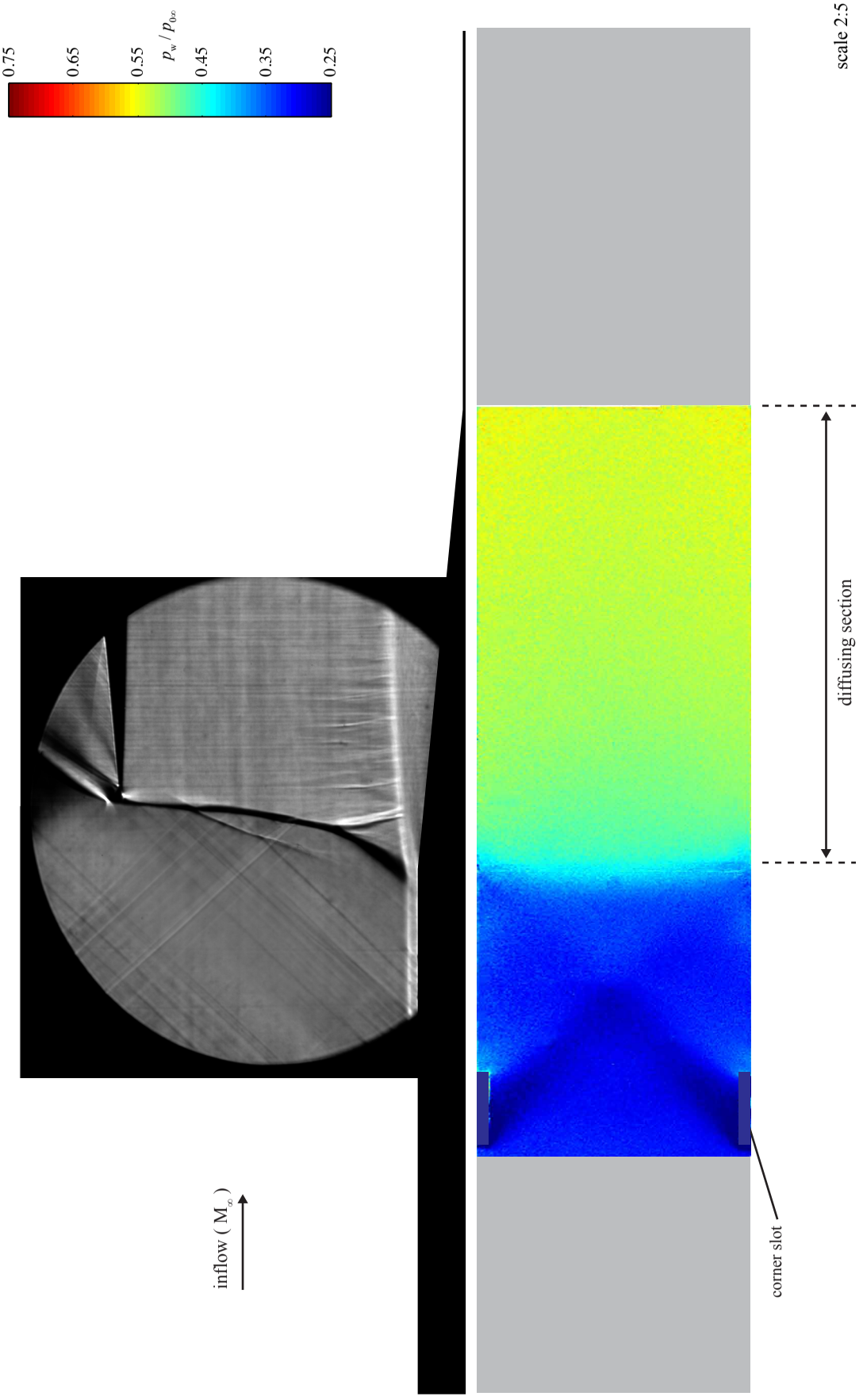

Figure 10.24: Schlieren and channel floor wall-pressure map for the case controlled by corner suction

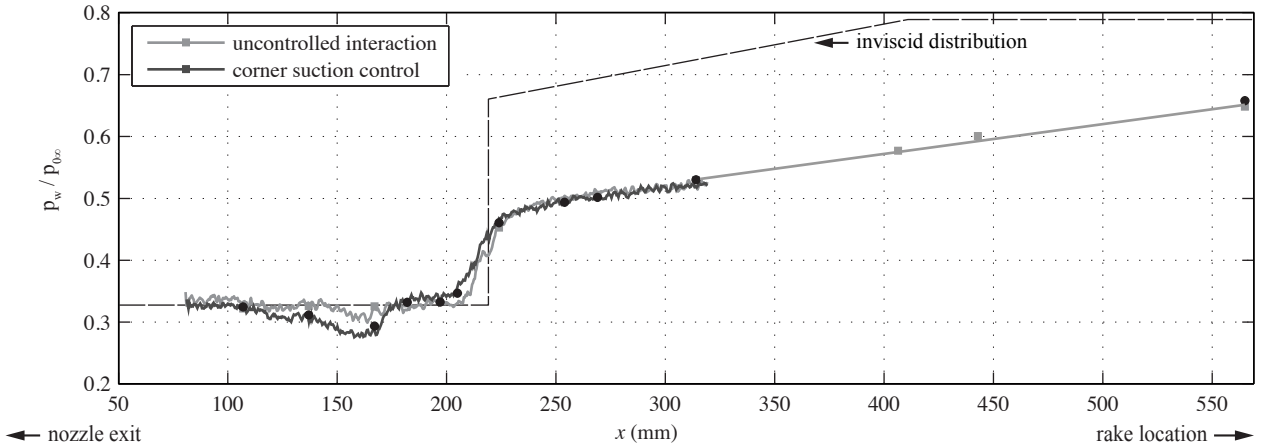

Figure 10.25: Floor wall-pressure distribution for the case controlled by corner suction (lines indicate PSP; symbols pressure transducers)

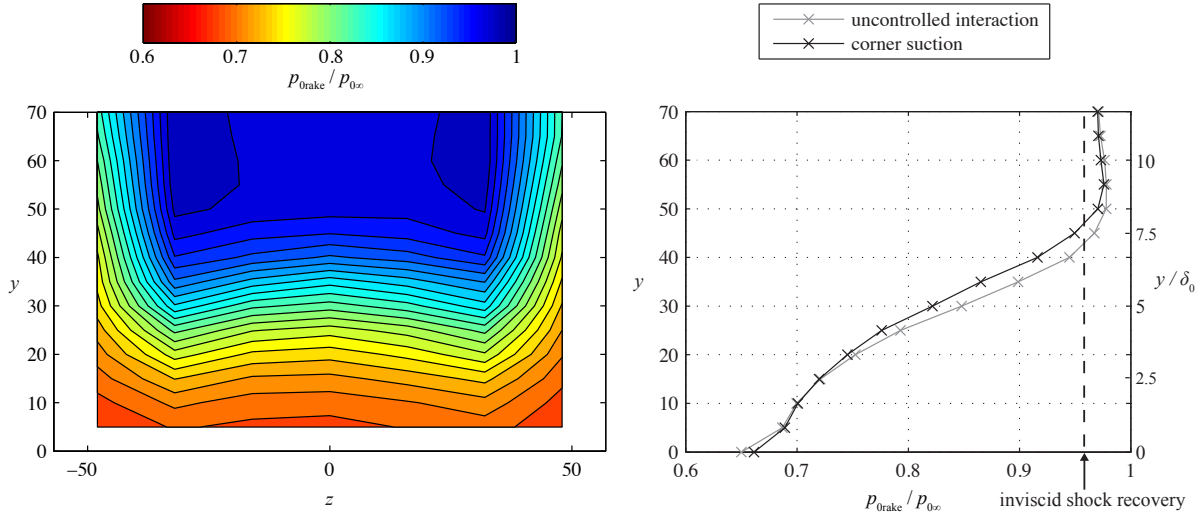

(a) Contour plot

(b) Centre-line distribution

Figure 10.26: Pressure recovery contour plot and centre-line profile for the case controlled by corner suction

10.5 The interaction with combined centre-span and corner control

In light of the results obtained with flow control applied to one area, it is suggested that flow control is required in all regions of the flow where there is the potential for significant losses to be generated (although these regions may not always be particularly easy to discern). However, in the experiments presented thus far, significant losses have been obtained in two regions: the corners and the centre-span region on the floor. Consequently, in this section, the corners and centre-span region are controlled simultaneously.

In an attempt to eradicate flow separation completely, corner suction and centre-span VGs have been applied in combination to control the centre-span and corner flows respectively. The results with this combined control configuration are presented in figures 10.27 through 10.32.

In the shadowgraph image shown in figure 10.27, the interaction appears at first similar to that with just centre-span VGs—although, as expected, both the shock waves from the suction slots and the VGs are now visible. More importantly, however, on close inspection there does appear to be a slight reduction in the amount of thickening of the viscous region downstream of the terminal shock wave when compared to the other cases (this difference is somewhat difficult to see though, as it is relatively small).

The reduction in separation is much more clearly illustrated in the surface-flow visualization where it can be seen that the surface streamlines are drastically different compared to the previous configurations: For the first time, there is a substantial spanwise extent of attached flow throughout the diffuser, bar some small localized owl-face separations that again occur at the diffuser entrance. These separations are small though and should not take away from the fact that unlike the previously examined configurations in this instance there has been a dramatic reduction in the separation.

Although the corner separations have not been entirely eradicated, they are much smaller than in the case controlled by centre-span VGs alone. This reduction in the corner separation is also visible in the sidewall surface-flow visualization presented in figure 10.28. These visualizations demonstrate that the corner suction is somewhat effective, but is not totally able to totally eradicate separation in the corners. There is also now some asymmetry in the corners. Importantly, unlike the previous cases there is now separation on the sidewall. This is evidence that there is now an increased pressure rise, which the sidewall boundary layer is not able to cope with.

Wall-pressure measurements for this configuration are shown in figure 10.30 and figure 10.31. An improvement over the uncontrolled case can be most easily observed by examining the centre-span distribution of figure 10.31. It can be seen that there is a strong pressure rise across the shock and the pressure soon overtakes that of the uncontrolled case—halfway into the diffuser the wall-pressure in the combined case is notably above the uncontrolled case and this improvement is retained to the simulated AIP. By the time the flow reaches the AIP there is more than a 6% increase in wall pressure from $0.65p_{0\infty}$ to $0.69p_{0\infty}$. This improvement in wall-pressure confirms that there has been a significant increase in the effective area of the channel, which is in agreement with the corresponding reduction in separation observed in the surface-flow visualization.

By comparing the wall-pressure map of figure 10.30 to that of the uncontrolled case (fig-

ure 10.13) and the case with only centre-span VGs (figure 10.17) a clear the reduction in the smearing near the corners is discernible. This is not to say that there is no smearing: the expansion around the diffuser is contained to the centre-span region by smearing in both corners. Nevertheless, these factors are further evidence that the corner separations have been reduced but not entirely eradicated.

Alongside these observations, the measurements taken at the AIP presented in figure 10.32 also indicate that the separation has been reduced. Immediately apparent is the lack of a red low pressure region close to the floor like the uncontrolled case (figure 10.14). A marked improvement is maintained across the central half of the span, in precise agreement with the floor surface-flow visualization. In addition, the losses in the corners are also reduced which further agrees with the data presented thus far. The centre-span profile at the AIP in figure 10.32b illustrates how much the combined control case improves the flow: the boundary layer here is now the thinnest of any configuration at about $5\delta_o$ (32 mm). And unlike the case controlled by VGs alone this improvement is sustained across appreciable part of the span.

There is now some asymmetry at the AIP, though. This can be seen by noting that the extent of the losses pertaining to each sidewall are not of the same thickness. In fact, the boundary layer on the right-hand sidewall is much thicker. This suggests that the right-hand sidewall boundary layer may now be close to separation or even slightly separated. This increased susceptibility of the sidewalls to separation should have been foreseen though as these regions have been left uncontrolled and are now exposed to an increased pressure rise. Yet, it is not known why this the right-hand sidewall is more vulnerable than the left-hand sidewall, or for that matter why the corner flows have become asymmetric. It is likely that these two factors are linked, though.

The overall result of the combined control, however, is still overwhelmingly positive. There is an improvement in the pressure recovery to 86.0% and a reduction in distortion to 0.310. Compared to the uncontrolled case, the stagnation pressure loss has been reduced by 15% and there has been a nearly 20% drop in steady-state distortion.

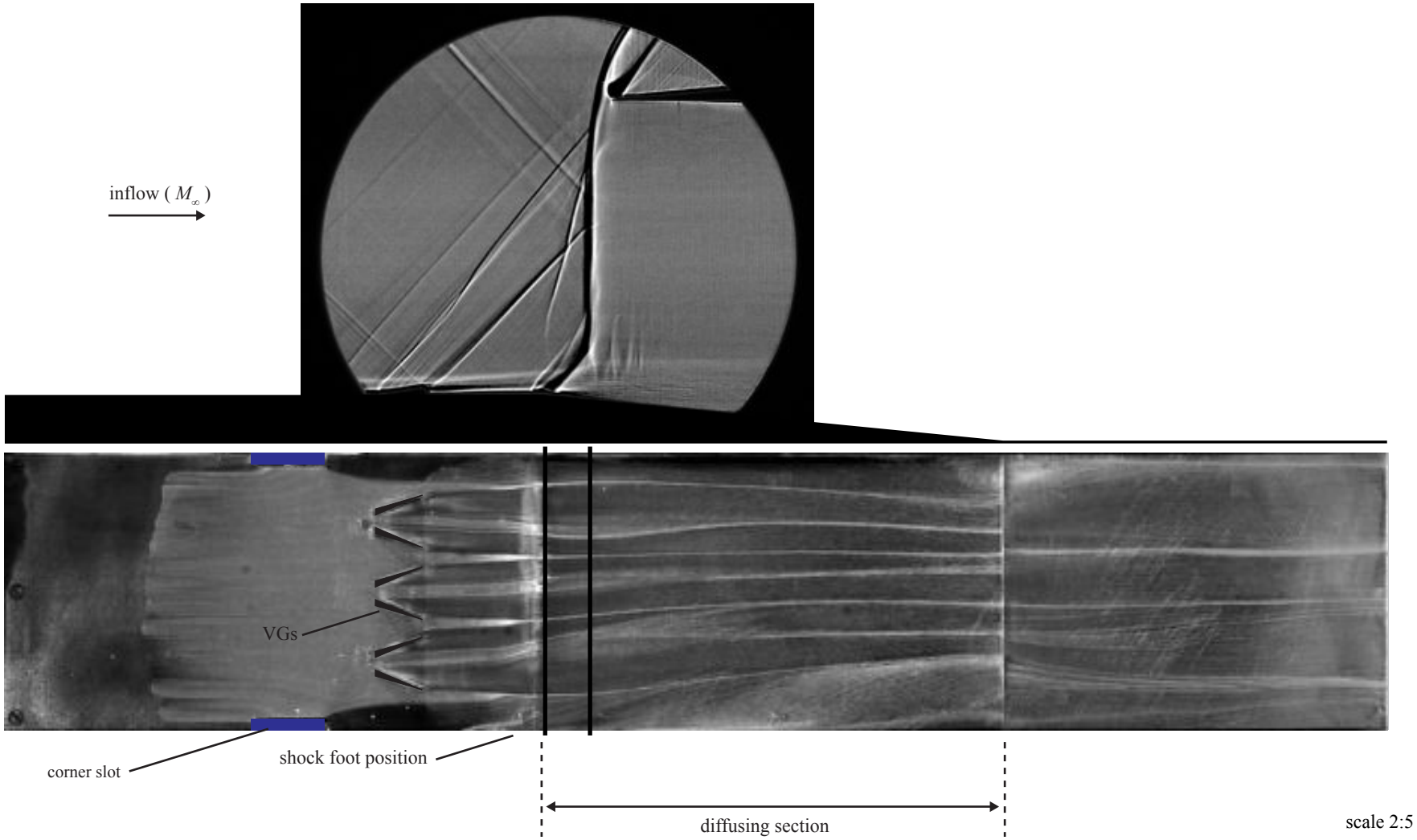

Figure 10.27: Flow visualizations for the combined control case (schlieren and channel floor surface-flow visualization)

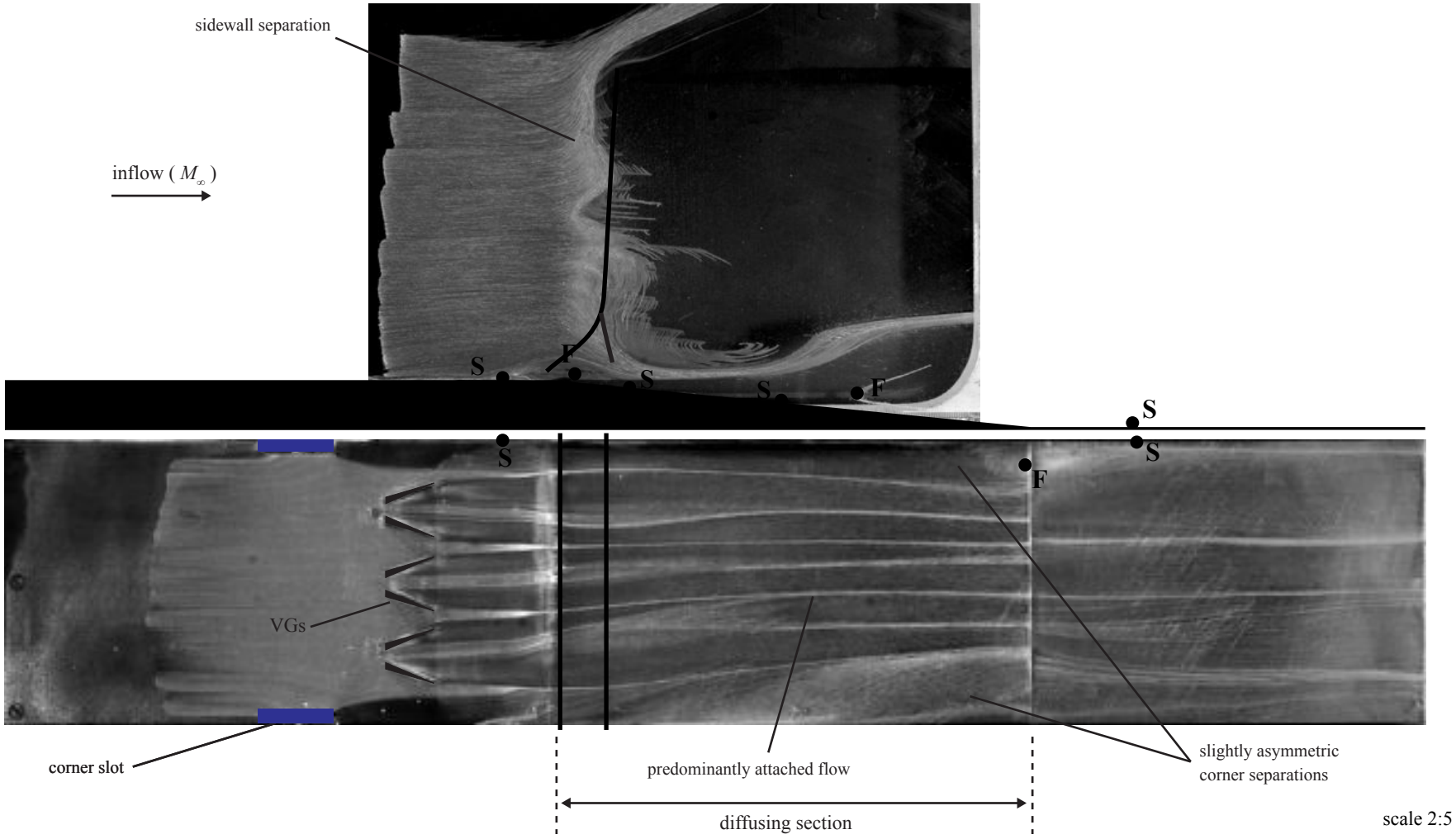

Figure 10.28: Flow visualizations for the combined control case (side-wall and channel floor surface-flow visualizations)

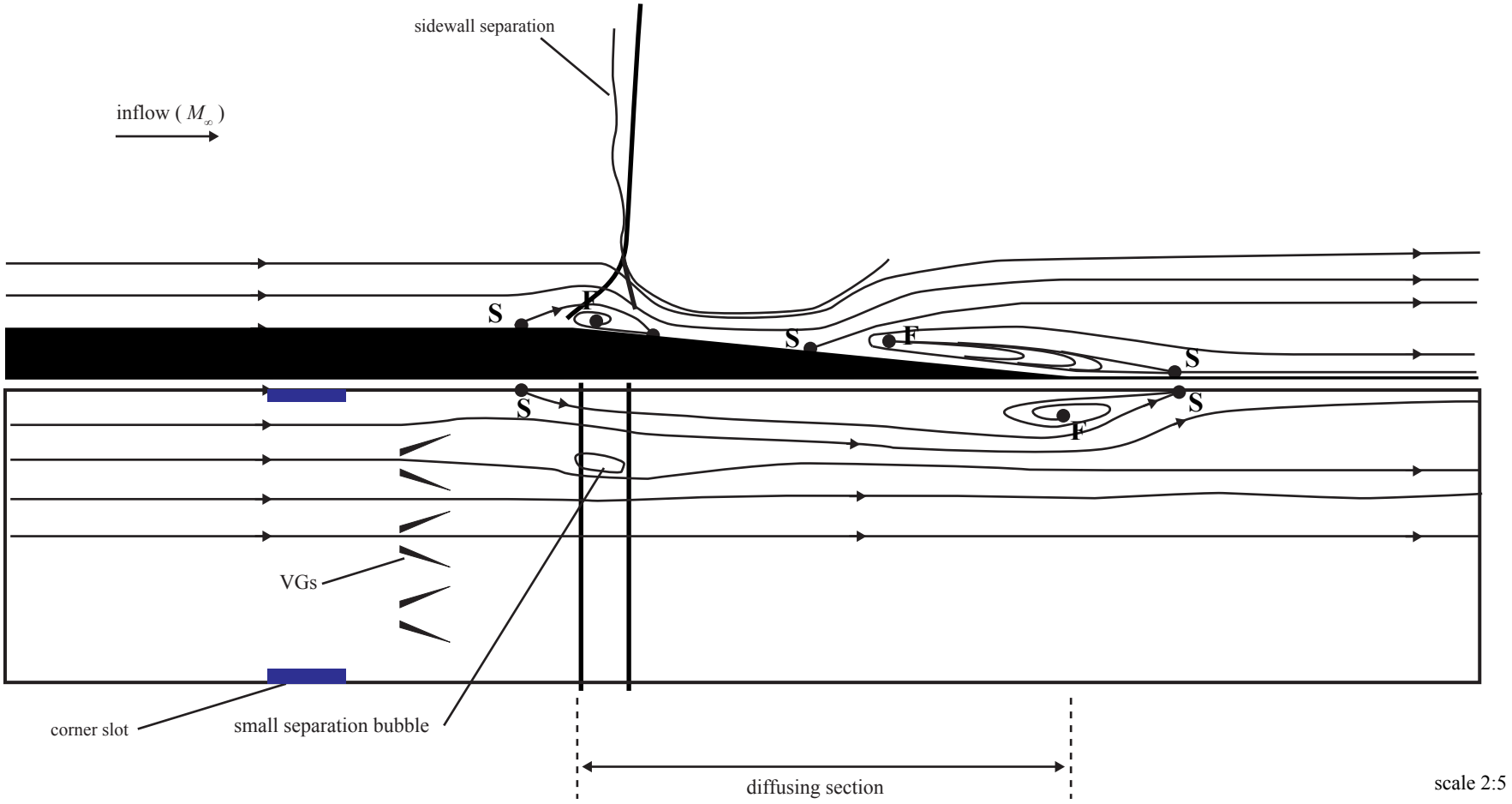

Figure 10.29: Topological interpretation of oil-flow visualization for the combined control case

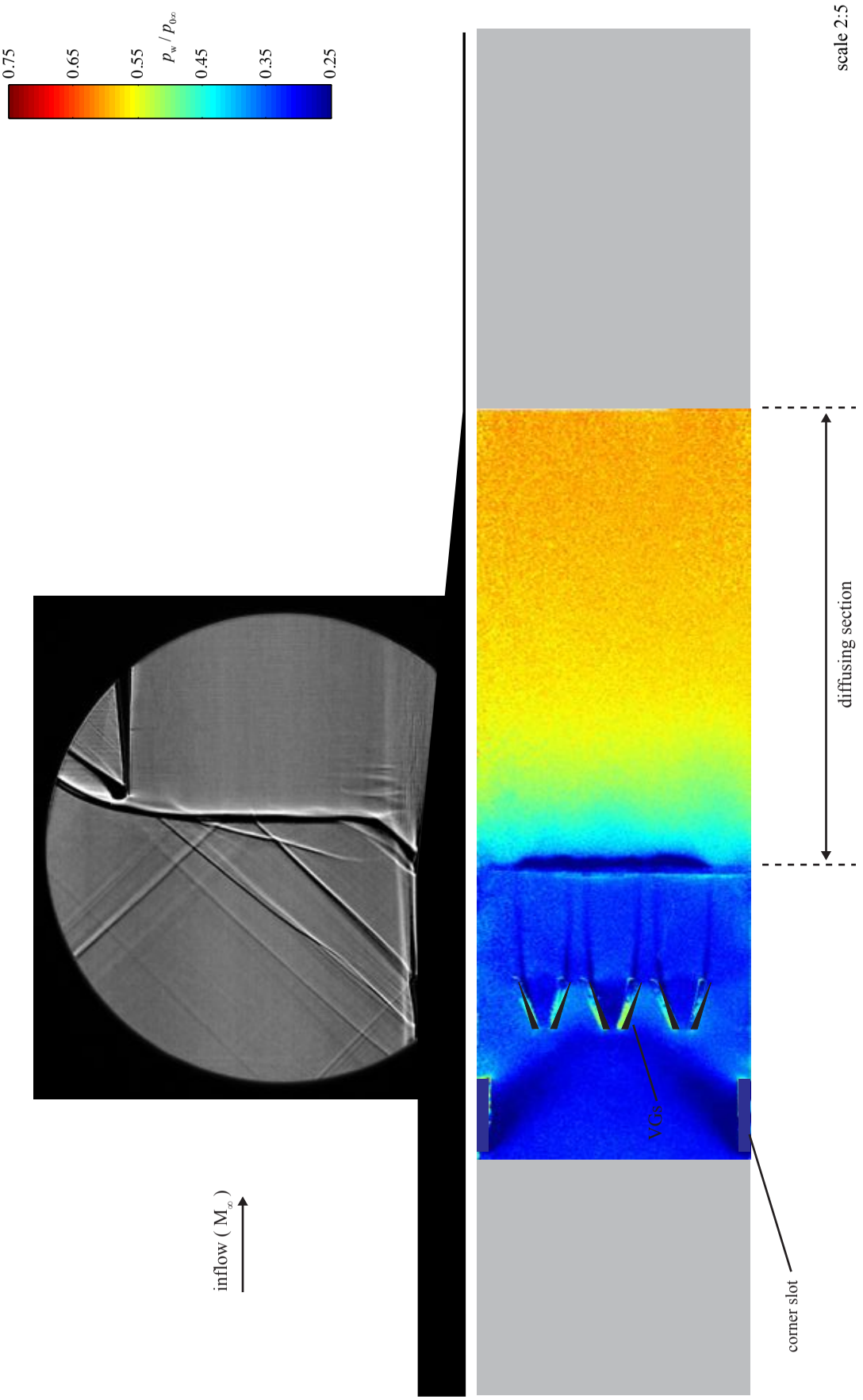

Figure 10.30: Schlieren and channel floor wall-pressure map for the combined control case

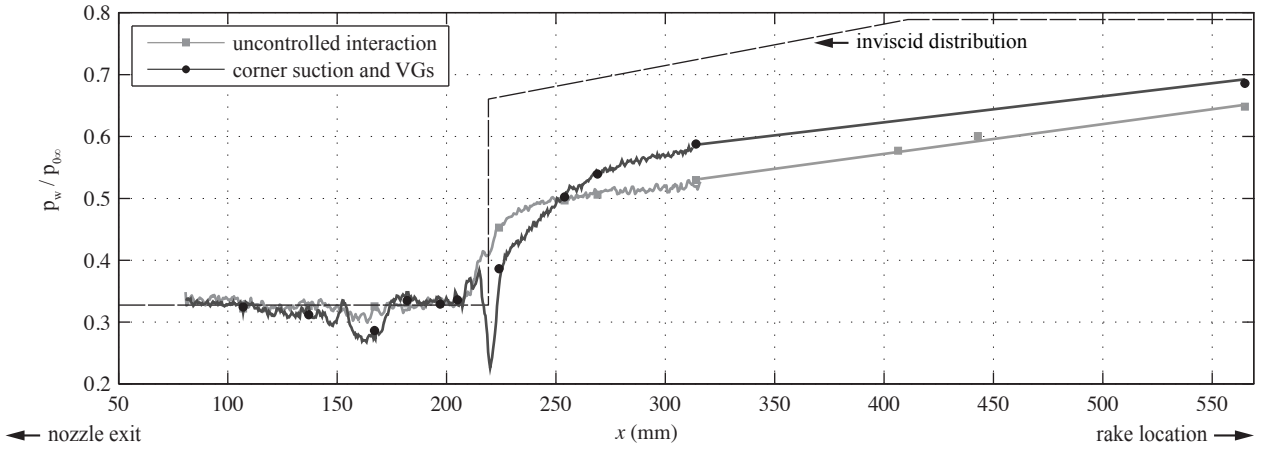

Figure 10.31: Floor wall-pressure distribution for the combined control case (lines indicate PSP; symbols pressure transducers)

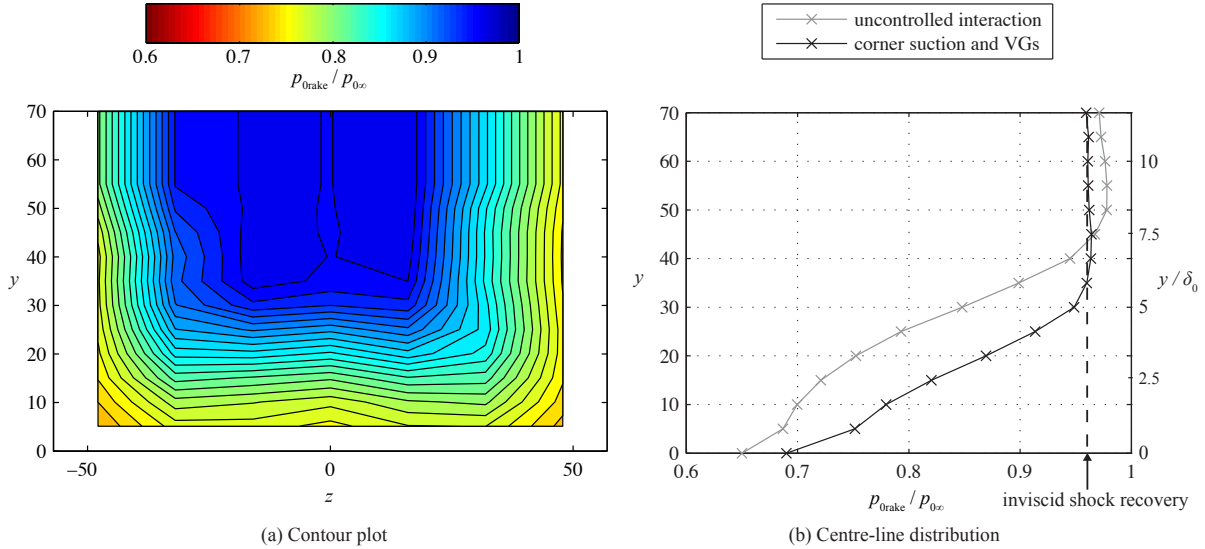

(a) Contour plot

(b) Centre-line distribution

Figure 10.32: Pressure recovery contour map and centre-line profile for the combined control case

Chapter 11

Further Discussion

11.1 Introduction

The results presented in this investigation are discussed in more detail in this section. The results are compared to investigations in a number of other facilities and particular emphasis is placed on the implications of the results obtained here to inlet aerodynamics.

11.2 Discussion of uncontrolled interactions

The uncontrolled flow configurations examined have helped to detail a number of the less well understood aspects of normal SWBLIs.

Firstly, by varying the position of the normal shock relative to the diffuser, the strong influence of the post-shock geometry and therefore post-shock adverse-pressure-gradient has been documented. By moving the position of the shock wave from far upstream to the diffuser entrance, it has been demonstrated that the positioning of the shock relative to the subsonic diffuser is critically important.

When the shock is far enough upstream, in this case around $6\delta_o$, of the diffuser, the flow is relatively benign, with little, if any, separation at centre-span. Wall-pressure measurements indicated that the adverse-pressure-gradient from the shock and diffuser are separated in space and that prior to the diffuser entrance the interaction did not vary from that of the constant area duct. In addition to this, the flow visualizations do not look dissimilar to the constant-area duct case, and these are shown here in figure 11.1 to illustrate this. The fact that the flow with the shock in position 1 behaves similarly to that in the constant-area duct case is further evidence that the adverse-pressure-gradient from the downstream diffuser is having little influence on the SWBLI.

The reason why the floor boundary layer does not separate at this Mach number, although Mach 1.4 is higher than the traditionally accepted limit of Mach 1.3, can be nicely illustrated using the plot of shock-induced separation limit based on geometry presented by Bruce et al. (2011). Adding the configuration examined here to this plot results in a position below the line which demarcates unseparated and separated flow. This fact is shown in figure 11.2.

However, when the shock is moved downstream to position 2, where the shock is only δ_o upstream of the diffuser entrance, the flow is entirely different to that of the constant-area duct. The corner separations become very large and extensive separation is introduced in the centre-

span region. The cumulative detrimental effect of the shock-induced pressure rise and diffuser pressure rise in quick succession gives the boundary layer little time to recover and the boundary layer separates in the diffuser.

Further movement of the shock downstream to position 3 results in a flow where the two pressure rises have effectively merged. As a result, centre-span separation occurs underneath the shock due to the combined effect of the shock and diffuser. Although the strength of the shock itself remains unchanged—the incoming Mach number is still Mach 1.4—the combination of the two adverse-pressure-gradients results in a very strong interaction with a substantial length of fully reversed flow.

While the minimum distance required between the shock and the diffuser for the floor boundary layer not to separate has not been determined, it must lie somewhere between δ_o and $6\delta_o$ for this configuration.

The importance of the downstream area variation has consequences for the shock-induced separation limit predicted by Bruce et al. (2011). Unfortunately, figure 11.2 does not in any way take into consideration the influence of downstream pressure gradients. For this reason, figure 11.2 cannot be used as a definitive estimator of shock-induced separation. The importance of downstream geometry indicates that it may not even be a good estimator as the position of the line dividing attached from separated interactions will inevitably move depending on the post shock geometry. Nevertheless, this should not detract from the observed trend by Bruce et al. (2011) of increasing shock-induced separation limit with increasing three-dimensionality, large $\delta^*/w_{\text{tunnel}}$.

The changes in the flow-field that are observed as the shock is moved closer to the diffuser clearly demonstrate that this flow-field is not only a function of the upstream Mach number, but also a strong function of geometry. The streamwise area variation and therefore downstream pressure gradient is having a strong bearing on the interaction. While this in itself is not necessary unexpected, the extent of the separation produced, $37\delta_o$, and accompanying losses increase, a nearly 5% increase, is undoubtably noteworthy.

Turning our attention to the observed near-wall flow topologies: once conditions are such that separation is initiated in the vicinity of the shock, a comparison of the separation topology observed here in position 3 with that observed by Sawyer and Long (1982) (presented in figure 3.3) exemplifies a large deviation between the two cases. While the flow-field produced here is dominated by separation originating in the corners, the separation in the case of Sawyer and Long (1982) is initiated near centre-span. It is not immediately clear though why this is the case; clearly there must be a difference in the separation mechanisms at work. Interestingly, however, the separation topologies observed on the sidewalls are not too dissimilar.

To help determine why such a variation in the near-wall topologies exists between these two cases, a number of other studies in which the separation topology was investigated were collated. Some of the surface-flow visualizations by these authors are shown in figure 11.3. During this search of the literature, the author could only find one other study, that of Doerffer and Dallmann (1989), where a similar flow topology was obtained to that observed in this investigation. Two examples of typical flow visualizations obtained by Doerffer and Dallmann (1989) are shown in figure 11.3. The surface flow topology of figure 11.3a most closely resembles the flow topology obtained here in positions 2 and 3; figure11.3b is only included for completeness because a

corresponding topological interpretation was provided by the authors and is shown here in figure11.3c. The topologies of Doerffer and Dallmann (1989) are quite similar to those obtained here: much like in this investigation, separation is initiated in the corners; the centre-span flow is entrained into the foci on either side of the centre-line; and the separation is terminated by a single separation saddle point (in the symmetric case).

Other than the investigation of Doerffer and Dallmann (1989), in instances in the literature where surface-flow visualizations were available, the flow topology tends to look more similar to that obtained by Sawyer and Long (1982). Two further examples of this type of topology are shown in figure 11.3. These topologies shown in figure11.3d and 11.3e and f were performed by Zare Shahneh and Motallebi (2009) and Schofield (1985) respectively. In each of these cases, flow separation is initiated at centre-span and the reversed flow near the initial separation line travels towards the two sidewalls before being entrained into a focus on each side. In these cases the foci rotate in the opposite direction to the flow-fields presented here and those of Doerffer and Dallmann (1989).

To determine why such topological variations exist, the test conditions and geometric parameters for this investigation is compared with those of the other investigations presented in figure 11.3 in table 11.1.

Table 11.1: Test conditions for a variety of transonic SWBLIs

Investigation	M_∞	configuration	$Re \times 10^{-6}$	C	$\delta^*/w_{\text{tunnel}}$	AR
This investigation	1.40	spillage-diffuser	31.5	0.13	6	0.93
Sawyer and Long (1982)	1.54	constant-area duct	10	0.16	4.5	1.20
Schofield (1985)	1.40	duct-diffuser	30	0.08	3.7	1.8
Doerffer and Dallmann (1989)	1.43	2D bump	16.7	0.18	6.4	0.4
Zare Shahneh and Motallebi (2009)	1.40	duct-diffuser	16	0.23	6	1

Inspection of table 11.1 demonstrates, unsurprisingly, that all these investigations were performed under different conditions. However, there is one factor that differentiates this investigation and that of Doerffer and Dallmann (1989) from the others, and this is the wind tunnel aspect ratio. While this investigation and that of Doerffer and Dallmann (1989) utilized a working section where the tunnel is taller than it is wide ($AR < 1$), all the other utilized facilities with a working section wider than they are tall ($AR > 1$). These results indicate that the wind tunnel aspect ratio is influential in the establishment of the separated flow topology. Nevertheless, following this argument further one might expect the sidewall topology of a configuration with $AR > 1$ to be similar to that of the floor flow for $AR < 1$, i.e., the separation topology in the entire duct is the same but rotated through 90^o. However, this is not the case: for example, the sidewall topologies in position 2 and 3 do not look like the floor flow of Sawyer and Long (1982) or vice versa. The flow physics is more complicated than a direct switch between the floor and sidewall.

What is more, the use of $\delta^*/w_{\text{tunnel}}$ as a first approximation of the importance of the corner separations used by Bruce et al. (2011) fails to deliver a trend in this instance: the experiment

here and that of Zare Shahneh and Motallebi (2009) have a very similar value of $\delta^*/w_{\text{tunnel}}$, but the topology is not similar. This is perhaps surprising as it is the prominence of the corner separations which differentiates the two differing topologies.

It is difficult to conclude from the available data why these topological variations exist. The observed trend with aspect ratio cannot be easily explained and requires further examination. It is possible that this trend is a coincidence as only five investigations have been compared. This is unfortunately due to the fact that most SWBLI investigations do not include surface-flow visualizations. What is clear is the strong three-dimensionality in all of these interactions, and this clearly demonstrates the need to achieve three-dimensional measurements whenever possible.

These results have a number of implications for SWBLI studies that are designed to be relevant to supersonic inlet aerodynamics. Due to the importance of downstream geometry, the constant-area channel normal SWBLI, which has been widely used as a test-case for inlet SWBLIs and flow control studies, is unlikely to be a good representation of typical inlet conditions as these rarely include a constant area section. Thus matching the upstream Mach number is not enough as inlets very often have post terminal shock divergence and flow turning. It is therefore important to set up more realistic flow conditions. The flow-field investigated here is thought to be a step in the right direction, because it imposes a more realistic adverse-pressure-gradient (without the added complication of an actual inlet geometry). And it is the adverse-pressure-gradient which is of foremost importance to the flow-field. In addition to this, it has been shown that by altering the shock position relative to the diffuser in this configuration the severity of the adverse-pressure-gradient can be nicely adjusted.

In spite of the advantages to this configuration just discussed, the configuration here exhibited very prominent corner separations, which is not necessarily typical of an inlet. The importance of the corner separations here is in large part due to the low aspect ratio of this wind tunnel, and real inlets do not have such low aspect ratios (see figure 6.6). As a result, the flow-field established here has three-dimensional effects that are not typical of most inlet flows—especially axisymmetric inlets which have very little three-dimensionality. Yet, as already discussed, fundamental geometries have an important role to play in helping to improve our understanding of inlet SWBLIs. Hence, it is very important to appreciate corner interactions and their influence on the performance of small-scale geometries. This is important if we are to interpolate effectively from small-scale test data to real inlet performance.

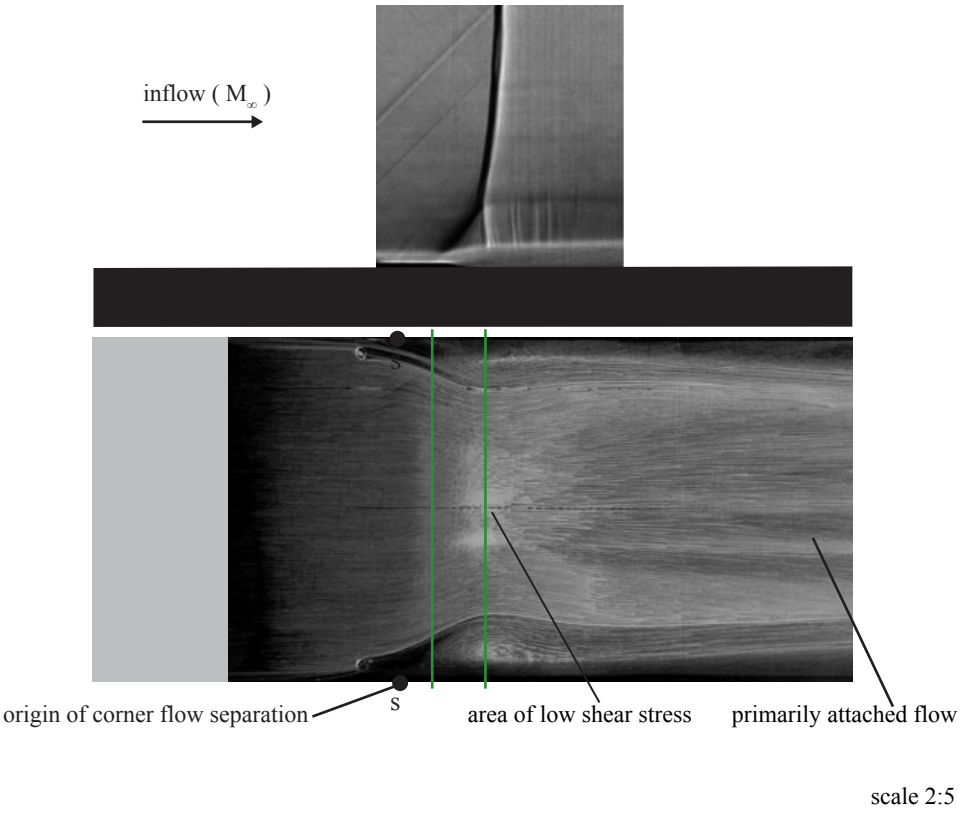

Figure 11.1: Flow visualizations in the constant-area duct case (Bruce (2008))

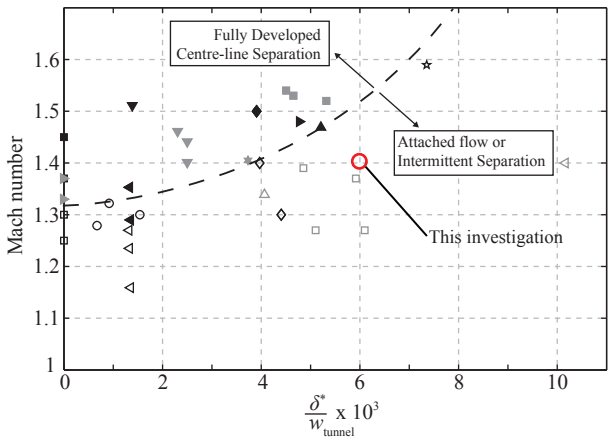

Figure 11.2: Experimental shock induced separation limit, Mach number vs geometry ($\delta^*/w_{\text{tunnel}}$); unseparated flows (open symbols) and separated flows (closed symbols); adapted from Bruce et al. (2010))

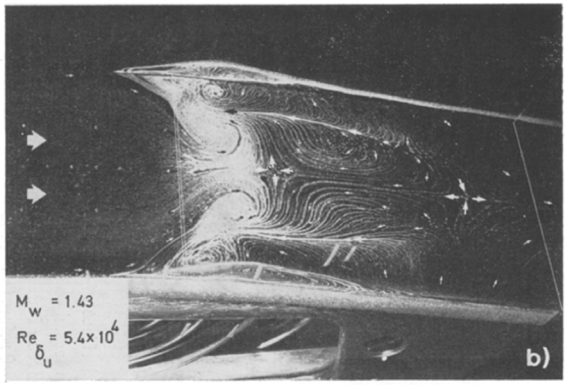

(a) Doerffer and Dallmann (1989)

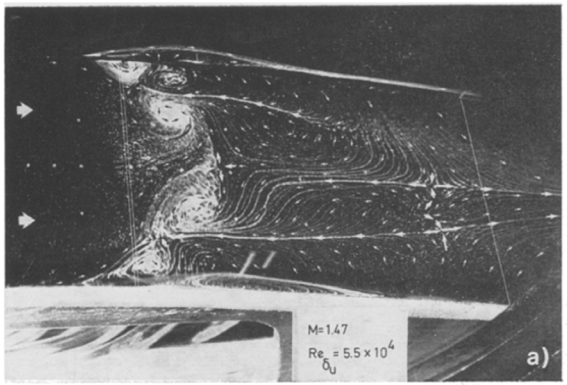

(b) Doerffer and Dallmann (1989)

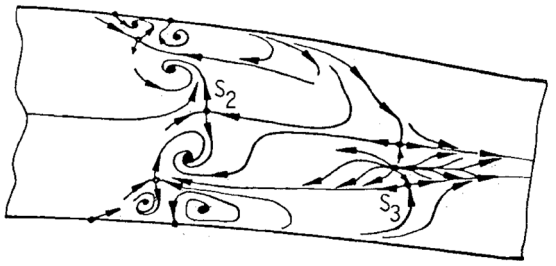

(c) topological interpretation of the flow in (b)

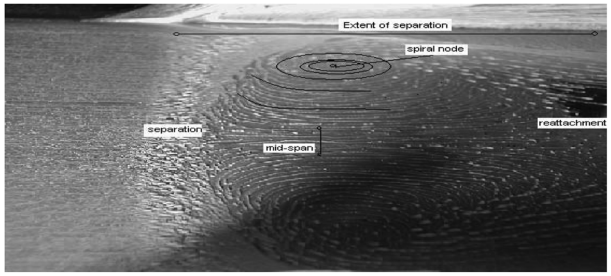

(d) Zare Shahneh and Motallebi (2009)

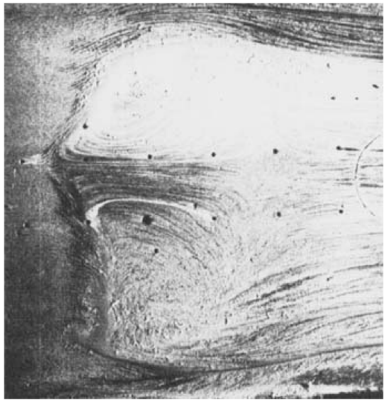

(e) Schofield (1985)

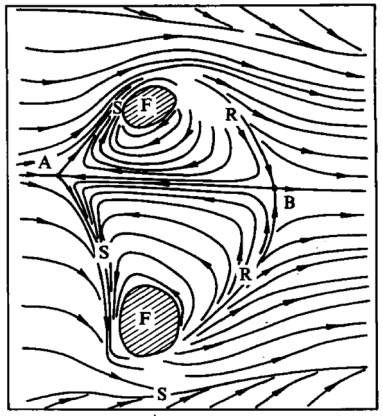

(f) topological interpretation of the flow in (e)

Figure 11.3: Surface-flow visualizations from a variety of transonic facilities

11.3 Discussion of results with flow control

From the results presented with one control method, it can be concluded that neither VGs in the centre-span region nor corner suction can alone eliminate, or even appreciably reduce, the flow separation present in the current configuration. Yet, in each case, the flow control was able to somewhat improve the flow in its local vicinity: the VGs were able to improve the centre-span flow and the corner suction did manage to reduce the losses towards the sidewall.

Nevertheless, it is clear that in both cases improvements in the local flow led to a deterioration in other areas of the flow-field: With VGs in the centre-span region of the channel floor the corner separations were even more pronounced, while with corner suction a contrasting scenario was observed as a reduction in the corner separations introduced a large centre-span separation.

It is thought that this phenomenon can be explained using the following argument: When introducing flow control to one particular area the intended goal of reducing flow separation in this region will inevitably lead to an increase in the static pressure, stagnation pressure, and the effective flow geometry in this area. This, the desired outcome of the flow control, leads to an 'effective' increase in the pressure rise through the diffuser. As the flow-field cannot support large variations across the flow (due to its subsonic nature), if this effective pressure rise is to be maintained other regions must be able to support this stronger adverse-pressure-gradient. Thus, these areas, which may have previously experienced a benign pressure rise, are now more vulnerable to flow separation. This stronger adverse-pressure-gradient increases losses in these other regions (especially if separation is initiated where there previously was none), and this counteracts the improvements (both static and stagnation pressure) produced in the areas where flow control was originally implemented. Consequently, there may be little overall improvement, even though the structure of the flow-field can vary significantly.

The above experiments strongly back-up this hypothesis: introducing VGs to the centre-span region leaves the corners uncontrolled. As a result, the improvement in the centre-span in counteracted by the increased losses in the corners. On the other hand, when suction is only introduced in the corners, the centre-span is left uncontrolled, and therefore the improvement in the corners is counterbalanced by enhanced loss in the centre-span region.

The change in the near-wall flow topology produced with the introduction of the corner suction is considerable. In fact, the topology in this configuration looks more similar to the majority of normal SWBLIs as discussed above in section 11.2. This is evidence that it is the flow in the corners which is having an influential impact been the investigations discussed in section 11.2. However, the relationship of this factor to the observed influence of aspect ratio is not known at this time.

The results obtained when VGs were employed in tandem with corner suction allow it to be concluded that only when flow control is employed to all problem areas simultaneously can significant performance improvements be obtained. In this instance, corner suction successfully mitigated corner separations and VGs were able to suppress separation in the centre-span region.

While the overall improvement in stagnation pressure recovery may not appear to be huge, 83.6% to 86.0%, it is important to remember as previously discussed that the role of VGs is restricted to separation prevention. As was detailed in section 10.2 the separation losses in this configuration without flow control were only of the order of 5%. The 2.4% improvement

obtained here with VGs, therefore, represents a 50% reduction in the separation losses. In this light, this result is more impressive.

It is probably possible to improve the performance beyond that obtained here by optimizing the VG configuration, something which has not been undertaken here. Nevertheless, it should be noted that some improvement due to separation reduction will inevitably be counteracted by drag produced by the VGs themselves. At the current time, the balance of this trade-off is unknown. It is therefore difficult at this time to conclude how much more of an improvement could be obtained. Further studies are required to determine the full extent of the success of the configuration investigated here.

Now that an increased pressure rise has been induced in this configuration, the sidewall boundary layers are now vulnerable to separation as is demonstrated in the sidewall surface-flow visualization. In addition, the pressure data at the AIP above indicates that the right-hand sidewall is now, if anything, in a worse condition than the floor boundary layer. As a consequence, serious consideration should be given to implementing flow control on the sidewalls as well as the floor.

Centre-span plots of Pitot pressure for the four configurations examined with the shock in position 3 are presented in figure 11.4. From this figure, it can be concluded that the configuration employing both VGs and corner suction performed most favourably. However, it should be remembered that the flow in all configurations is highly three-dimensional and extreme care should be taken when making generalizations about flow-field performance from data obtained at one location within the flow-field.

Table 11.2 presents a summary of the pressure recovery and flow distortion for all the configurations examined for reference. From this table it can be seen that the combined VG and corner suction configuration results in a pressure recovery similar to that obtained in position 2. This result indicates that flow control could help to maintain internal performance but with the benefit of a more compact inlet design. However, this is one of many trade-offs of flow control for inlet design which require further investigation. Unfortunately, the combined control case did not result in as high a pressure recovery as position 1, and this is because the corner suction was not able to entirely eradicate the corner separation. In addition, flow separation started to emerge on the sidewalls. To obtain a level of performance similar to position 1, these regions which are currently under-controlled would need to be dealt with.

Table 11.2: Summary of results

Configuration	Pressure recovery (η_f)	Flow distortion (D)
pos 1	88.4	0.23
pos 2	86.0	0.25
pos 3	83.5	0.34
pos 3 + VGs	83.4	0.37
pos 3 + corner suction	84.0	0.37
pos 3 + VGs and corner suction	86.0	0.31

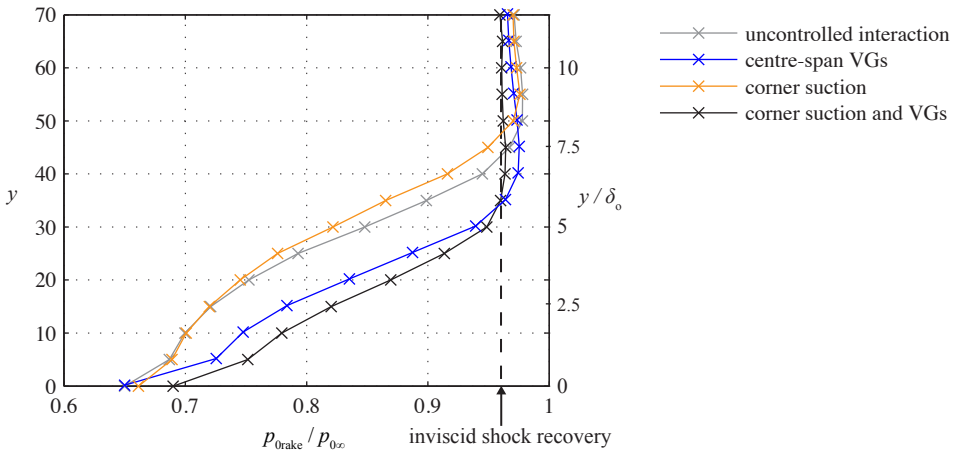

Figure 11.4: Centre-span Pitot profiles in position 3 for all configurations

Chapter 12

Conclusions

12.1 Conclusions of this study

With the help of an extensive literature survey, a simple yet inlet relevant flow-field has been developed as a test-bed for the evaluation of inlet boundary layer flow control techniques. This flow-field combines a terminal shock wave with a subsequent subsonic diffuser in a small rectangular working section wind tunnel. This configuration is thought to be important because it incorporates two adverse-pressure-gradients which are influential in many inlet designs: the terminal shock wave which has the highest pressure rise, thickest boundary layers and hence losses of any SWBLI; and the subsonic diffuser which is the last adverse-pressure-gradient before the engine-face and therefore crucially effects AIP performance. In addition, this setup allows the coupling between these two adverse-pressure-gradients to be ascertained.

Using preliminary experimentation and a survey of current and previous inlet designs as a guide, the experimental setup that was settled on included a Mach 1.4 terminal SWBLI followed by an adverse-pressure-gradient created by a 6 degree diffuser. Using this setup, data was obtained from schlieren and oil-flow visualizations, wall-pressure measurements using both tappings and PSP, and Pitot pressures at a simulated AIP.

Firstly, a detailed evaluation of the flow-field was undertaken in the absence of flow control. Three uncontrolled configurations were examined by varying the position of the shock wave relative to the diffuser. It was found that the position of the shock wave is highly influential in determining the resulting interaction and that the severity of the losses could be nicely controlled by adjusting the shock wave's position relative to the diffuser; the closer the shock wave is placed to the diffuser the higher the losses become.

In the most upstream shock wave position, the shock wave and diffuser are separated by enough of a stream-wise extent that their influences on the flow is not coupled. Consequently, the flow through the SWBLI behaves similarly to the constant-area terminal SWBLI at the same Mach number in the same wind tunnel. In this upstream position, there is neither large-scale separation underneath the shock wave nor in the diffuser in the central part of the flow. Nevertheless, there is separation in the corners of the working section, where the sidewall meets the floor. As the shock wave is moved downstream towards the diffuser, the adverse-pressure-gradients from the shock wave and diffuser combine, and separation is initiated in the centre-span region in the diffuser. Further movement of the shock wave downstream such that the shock-foot

resides directly above the diffuser entrance brings the separation forward to a position underneath the shock-foot. Alongside these observations of the floor topology, with each movement downstream the recovery of both wall and stagnation pressure is reduced. It can be concluded that only when the floor boundary layer is given enough time to recover from the initial shock wave (in this instance around $5\delta_o$ is required) is separation avoided.

In each of the uncontrolled configurations, separation is first observed in the corners. These corner separations are prevalent in all three positions, but tend to dominate the flow more as the shock wave is moved closer to the diffuser. In addition, the three-dimensionality is also increased as the shock wave is positioned closer to the diffuser.

In the first instance, VGs were employed in the centre-span region on the tunnel floor. Although the VGs were able to introduce small region of attached flow the corner flows still dominated the flow-field—and, if anything, were more prominent than in the uncontrolled case. Consequently, neither the wall-pressure or overall pressure recovery was improved.

Suction slots upstream of the SWBLI were utilized to control the corner separations. These were particularly successful at reducing the size of the corner separations, and only a very low mass flow rate (approximately 0.2% of the inflow) was required to significantly reduce the corner separations. Yet, while the corner separations were reduced, the overall amount of separation, wall-pressure and stagnation pressure recovery remained near unchanged. Instead of significant corner separations, a separation originating in the central part of the channel and of very similar extent was introduced. This separation is more two-dimensional than in the uncontrolled case.

The results obtained when utilizing both centre-span VGs and corner suction in isolation reveal that there is a strong coupling between the centre-span and corner flow regions in this configuration—improvements in one area being cancelled out by increased losses in another area. The reason for this is thought to be as follows: When flow control is effectively applied to one problem area there is an effective increase in the pressure recovery here. This pressure rise cannot necessarily be supported by other regions of the flow-field, and this can cause these (potentially uncontrolled) regions to grow and perhaps even separate where there previously was no separation. This, in turn, counteracts the pressure-rise in the controlled region, and, consequently, there is little or no improvement throughout the flow-field. As a result, it is imperative to employ flow control in all potential problem areas, if an overall improvement is to be obtained.

The redistribution of losses from one area to another is nicely illustrated by the exchange of separation from one region to another and by the relative span-wise uniformity of the wall-pressure downstream of the SWBLI.

To apply flow control to all potential problem areas, VGs were employed alongside corner suction. In this configuration, appreciable improvements to the flow-field were obtained. A substantial stream-wise extent of attached flow was produced and notable improvements in both wall-pressure and stagnation pressure recovery were obtained. To the author's knowledge, this combined control configuration has illustrated for the first time that VGs can significantly mitigate shock-induced separation. Compared to the uncontrolled case, the stagnation pressure loss at the AIP was reduced by 15% and there was a nearly 20% drop in steady-state distortion. In addition this time, there was a 6% increase in the wall-pressure at the AIP.

These results are evidence that VGs do have the potential to reduce our dependence on

boundary-layer bleed for the purpose of separation suppression.

12.2 Future work

As ever, further experimental and computational work is required on fundamental SWBLIs; especially pertaining to the effects of three-dimensionality. One significant gap in our understanding that remains is the lack of understanding as to when and why some wind tunnel configurations are more susceptible to corner separations than others. The mechanisms behind this are unknown. Accordingly, this area would profit significantly from a three-dimensional mapping of SWBLI flow-fields such as those presented here. These data would also be highly beneficial for CFD validation purposes, which are required to further develop computational codes in this field.

In tandem to improving our understanding of corner flows, corner flow control techniques other than bleed require development. Although the corner slots used here were successful, they are undesirable for a number of reasons including incrased weight due to structural considerations and reduced flexibility. As a first step, an improvement could probably be obtained by utilizing distributed suction. As a result, it is worth considering this configuration.

Despite making a step forward from the constant-area SWBLI experiments to one more relevant to inlet aerodynamics, the configuration presented here lacks the combined effects of two shock adverse-pressure-gradients. Such an experimental setup, for example a reflected shock followed by a terminal shock would be highly beneficial to this field.

In terms of continuing the development of VGs, studies are still required to determine their effect on shock unsteadiness. This subject has not been discussed here and is certainly important—particularly from a temporal distortion point of view. Although it is probable that a reduction in separation will also lead to a reduction in unsteadiness this phenomenon needs to be quantified and analyzed in detail. It would also be worthwhile re-investigating this configuration but with the addition of VGs mounted on the sidewalls.

Finally, it is important to try and benchmark other types of boundary-layer control, such as VGs, against bleed (for the purpose of separation mitigation). A step in this direction would be to utilize the results of these experiments in conjunction with further investigations using this setup employing only bleed (both centre-span and corner). If care is taken to improve the flow-field to a similar level to that obtained here, this would give a first-order approximation as to the trade-off between VGs and bleed.

12.3 Final remarks

It is worth noting that although some success has been obtained here in the implementation of VGs, it is important not to set overreaching aims for the potential for VGs to replace bleed. Bleed has the ability to offer many advantages other than separation suppression which VGs cannot. Although seemingly obvious, this fact is sometimes overlooked, and it is perceived that VGs can give you the same control authority as bleed. This is not the case. VGs cannot remove the losses associated with attached boundary layers and they cannot reduce the displacement effect of a growing boundary layer or the beneficial matching influence of bleed. Consequently, when

determining whether VGs could help to provide an application with a better inlet configuration these factors should be taken on board.

With regard to the influence of three-dimensionality, although the coupling observed in these experiments would probably not be as prominent in a real inlet configuration (real inlet will not have as low aspect ratios), it is important to remember that many fundamental investigations that are required to further our knowledge in this area are conducted in small facilities. These often have rectangular working sections, due to ease of optical access amongst other factors. Thus, these three-dimensional factors will continue to be of important even if they are not encountered in the final product. To stop such effects inadvertently contaminating small-scale wind tunnel data, these effects must be better understood.

References

J. Ackeret, F. Feldmann, and N. Rott. Investigations of compression shocks and boundary layers in gases moving at high speed. TM-1113, NACA, January 1947.

I.E. Alber, J.W. Bacon, B.S. Mason, and D.J. Collins. An experimental investigation of turbulent transonic viscous-inviscid interactions. *AIAA Journal*, 11(5):620–627, May 1973.

Ames Research Staff. Equations, tables and charts for compressible flow. Report 1135, NACA, Washington.

B. H. Anderson and D. N. Bowditch. Performance of three isentropic all-internal-compression axisymmetric inlets designed for mach 2.5. TM X-259, NASA, Washington, 1960.

B. H. Anderson, J. Tinapple, and L. Surber. Optimal control of shock wave turbulent boundary layer interactions using micro-array actuation. AIAA-2006-3197, June 2006.

J. D. Anderson. *Modern Compressible Flow*. McGraw-Hill, 3 edition, 2004.

P. R. Ashill, J. L. Fulker, and K. C. Hackett. Studies of flows induced by sub boundary layer vortex generators (SBVGs). AIAA-2002-0968, January 2002.

P. R Ashill, J. L. Fulker, and K. C. Hackett. A review of recent delevopments in flow control. *Aeronautical Journal*, 109(1095):205–232, 2005.

C.J Atkin and L.C Squire. A study of the interaction of a normal shock wave with a turbulent boundary layer at mach numbers between 1.30 and 1.55. *European Journal of Mechanics, B/Fluids*, 11(1):93–118, 1992.

H. Babinsky and J. K Harvey, editors. *Shock Wave–Boundary-Layer Interactions*. Cambridge University Press, 2011.

H. Babinsky and H. Ogawa. Wind-tunnel setup for investigation of normal shock wave/boundary-layer interaction control. *AIAA Journal*, 44(11):2803–2805, November 2006.

H. Babinsky, Y. Li, and C. W Pitt Ford. Microramp control of supersonic oblique shock-wave/boundary-layer interactions. *AIAA Journal*, 47(3):668–675, March 2009.

W. H Ball. Propulsion system installation corrections. Affdl-tr-72-147 vol. 3, 1972.

M. A. Beheim and L. W. Gertsma. Performance of variable two-dimenisonal inlet designed for engine-inlet matching I–performance at design mach number of 3.07. RM-E56H23, NACA, November 1956.

L. H. Benedict and R. D. Gould. Towards better uncertainty estimates for turbulence statistics. *Experiments in Fluids*, 22:129–136, 1996.

S. L. Bragg. Effect of compressibility on the discharge coefficient of orifices and convergent nozzles. *Journal Mechanical Engineering Science*, 2(1):35–44, 1960.

C. S. Brown and E. L. Goldsmith. Measurements of the internal performance of a rectangular air intake with variable geometry at mach numbers from 1.7 to 2.5. CP 1243, Aeronautical Research Council, 1973.

P. Bruce. *Transonic Shock/Boundary Layer Interactions Subject to Downstream Perturbations*. PhD thesis, University of Cambridge, Cambridge, UK, 2008.

P. Bruce, D. Burton, N. Titchener, and H. Babinsky. Corner flows and separation in transonic channel flows. 45th Symposium of Applied Aerodynamics, Marseille, March 2010.

P. J. K. Bruce, D. M. F. Burton, N. A. Titchener, and H. Babinsky. Corner effect and separation in transonic channel flows. *Journal of Fluid Mechanics*, 679:247–262, 2011.

F.W Burcham Jr. and D. R. Bellman. A flight investigation of steady-state and dynamic pressure phenomena in the air inlets of supersonic aircraft. TM-X-67495, NASA, 1971.

D. Burton and H. Babinsky. Corner separation effects for normal shock wave/turbulent boundary layer interactions in rectangular channels. *Journal of Fluid Mechanics*, 707:287–306, 2012.

J. E. Calogeras and E. T. Meleason. Wind-tunnel investigation of techniques for reducing cowl drag of an axisymmetric external-compression inlet at Mach 2.49. TM-X-1516, NASA, March 1968.

R.C. Campbell. Performance of a supersonic ramp inlet with internal boundary-layer scoop. RM-E54I01, NACA, 1954.

D. R. Chapman, D. M. Kuehn, and H. K. Larson. Investigation of separated flow in supersonic and subsonic streams with emphasis on the effect of transition. TN-3869, NACA, March 1957.

C. Chatfield. *Statistics for technology : A Couse in Applied Statistics*. Chapman and Hall Ltd., third edition edition, 1983.

R. M. Chriss, W. R. Higst, A. J. Strazisar, and T. G. Keith Jr. A LDA investigation of three dimensional normal shock wave boundary-layer interaction. NASA Langley Research Center, Transonic Symposium: Theory, Application, and Experiment, Volume 1, Part 2, 741-764, NASA, 1989.

S. P. Colliss. Experimental investigation of the flow physics of three-dimensional shock control bumps. Internal Report, Cambridge University, August 2011.

J. F. Conners, G. A. Wise, and J. C. Lovell. Investigation of translating-double-cone axisymmetric inlets with cowl projected areas 40 and 20 percent of maximum at mach numbers from 3.0 to 2.0. RM-E57C06, NACA, May 1957.

J. M. Delery and J. G. Marvin. Shock-wave boundary layer interactions. AGARDograph 280, AGARD, February 1986.

J.M. Delery. Shock wave/turbulent boundary layer interaction and its control. *Progress in Aerospace Sciences*, 22:209–280, 1985.

P. Doerffer and U. Dallmann. Reynolds number effect on separation structures at normal shock wave/turbulent boundary-layer interaction. *AIAA Journal*, 27(9):1206–1212, 1989.

D. S. Dolling. Fifty years of shock-wave/boundary-layer interaction research: What next? *AIAA Journal*, 39(8):1517–1531, August 2001.

N. D. Domel, D. Baruzzini, and D. N. Miller. A perspective on mixed-compression inlets and the use of CFD and flow control in the design process. AIAA-2012-0014, January 2012.

F. Durst, A. Melling, and J. H. Whitelaw. *Principles and practice of laser-Doppler anemometry.* Academic Press, 2nd edition, 1981.

J. Dussauge, P. DuPont, and J. Debrieve. Unsteadiness in shock wave boundary layer interactions with separation. *Aerospace Science and Technology*, 10:85–91, 2006.

L. F. East. The application of a laser anemometer to the investigation of shock-wave boundary-layer interactions. AGARD Conference Proceedings 193, 1976.

W. H. Echols and J. A. Young. Studies of portable air-operated aerosol generators. NRL report 5929, U.S. Naval Research Laboratory, July 1963.

J. Erdos and A. Pallone. *Shock/boundary-layer interaction and flow separation.* Proceedings of the 1962 Heat Transfer and Fluid Mechanics Institute. Stanford University Press, 1962.

H. H. Fernholz and P. J. Finley. A critical commentary on mean flow data for two-dimensional compressible boundary layers. AGARDograph 253, 1980.

S. A. Fisher, M. C. Neale, and A. J. Brooks. On the sub-critical stability of variable ramp intakes at mach numbers around 2. R&M 3711, Aeronautical Research Council, 1972.

M. K. Fukuda, E. Roshotko, and W. R. Higst. Bleed effects on shock/boundary-layer interactions in supersonic mixed compression inlets. *Journal of Aircraft*, 14(2):151–156, February 1977.

Installation Handbook for Turbojet Engines, Ch. 8. GE, 1952.

S. Ghosh, J. Choi, and J. Edwards. Numerical simulations of effects of micro vortex generators using immersed-boundary methods. *AIAA Journal*, 48(1):92–103, January 2010.

E. L. Goldsmith. The effect of internal contraction, initial rate of subsonic diffusion, and cowl and centrebody shape on the pressure recovery of a conical centrebody intake at supersonic speeds. R & M 3204, Aeronautical Research Council, 1956.

J. E. Green. Interactions between shock waves and turbulent boundary layers. TR 69098, Royal Aircraft Establishment, 1969.

C. F. Griggs. An investigation of two methods of suppressing shock oscillations ahead of conical centre-body intakes. CP 605, Aeronautical Research Council, 1958.

G. R Hall, W. M Hurwitz, G. S Tiebens, W. P Norby, P. Singshinsuk, and C. E Wilt. Development of the F/A-18 E/F air induction system. AIAA-93-2152, June 1993.

J. W. Hamstra and B. N McCallum. Tactical aircraft aerodynamic integration. *Encylopedia of Aerospace Engineering*, 2010.

S. Hanson. Coherent detection in laser doppler velocimeters. *Opto-electronics*, 6(4):263–269, 1974.

J. E. Hawkins. YF-16 inlet design and performance. *Journal of Aircraft*, 13(6):436–441, 1976.

T. Herges, E. Kroeker, G. Elliot, and C. Dutton. Microramp flow control of normal shock/boundary-layer interactions. *AIAA Journal*, 48(11):2529–2542, November 2010.

W. W. Hinz, H. Huttenlocher, and P. M. Stiglic. The F-14A air inlet control system. AIAA-70-697, 1970.

S. M. Hirt, K. B. M. Q. Zaman, and T. J. Bencic. Experimental study of boundary layer flow control using an array of ramp-shaped vortex generators. AIAA-2012-0741, 2012.

D.W. Holder and R. J. North. Schlieren methods. Notes on applied science no. 31, National Physical Laboratory, 1963.

W. F. Imfeld. Development program for the f-15 inlet. *Journal of Aircraft*, 13(4):286–291, 1976.

G. R. Inger and W. H. Mason. Analytical theory of transonic normal shock/turbulent boundary-layer interaction. *Journal of Aircraft*, 14(9):1266–1272, 1976.

A. Kantrowitz and C. Donaldson. Preliminary investigation of supersonic diffusers. ACR L5D20, NACA, May 1945.

S J Kline, J G Bardina, and R C Strawn. Correlation of the detachment of two-dimensional turbulent bounday layers. *AIAA Journal*, 21(1):68–73, 1983.

J Koncsek and J Syberg. Transonic and supersonic test of a mach 2.65 mixed-compression axisymmetric intake. CR 1977, NASA, Washington, March 1972.

V. I Kornilov. Correlation of the separation region length in shock wave/channel boundary layer interaction. *Experiments in Fluids*, 23(6):489–497, 1997.

S. Lee, M.K Goettke, E. Loth, J. Tinapple, and J. Benek. Microramps upstream of an oblique-shock/boundary-layer interaction. *AIAA Journal*, 48(1):104–118, January 2010.

S. Lee, E. Loth, and H. Babinsky. Normal shock boundary layer control with various vortex generator geometries. *Computers and Fluids*, 49:233–246, 2011.

J Leynaert. Fonctionnement du plege a couche limite interne fonctionnement du piège à couche limite interne d'une prise d'air à compression supersonique externe. AGARDograph 103: also NASA English Translation TT F-9869, January 1966.

Y. Li. Internal Report, Cambridge University, 2008.

T. Liu, B. T. Campbell, S. P. Burns, and J. P. Sullivan. Temperature- and pressure-sensitive luminescent paints in aerodynamics. *Applied Mechanics Reviews*, 50(4):227–246, 1997.

E. Loth, R. Jaiman, C. Dutton, S. White, F. Roos, J. Mace, and D. Davis. Mesoflap and bleed flow control for a mach 2 inlet. AIAA-2004-0855, January 2004.

R. W. Luidens and R. J. Flaherty. Use of shock-trap bleed to improve pressure recovery of fixed and variable-capture-area interal-contraction inlets; mach number 2.0 to 3.0. RM E58D24, NACA, 1958.

C.J MacMiller. Investigation of subsonic duct distortion. Technical Report AFFDL-TR-69-21, 1969.

R. L. Maltby. Flow visualization in wind tunnels using indicators. AGARDograph 70, 1962.

J. L. Mark, M. A. McGarry, and P. V. Reagan. Research on a two-dimensional inlet for a supersonic v/stol propulsion system. CR 174945, NACA, 1989.

B. N. McCallum. F-16 inlet stability investigation. Number 89-2465 in 25th Joint Propulsion Conference, Monterey, CA, July 10 - 12 1989. AIAA/ASME/SAE/ASEE, AIAA.

D. C. McCormick. Shock/boundary-layer interaction control with vortex generators and passive cavity. *AIAA Journal*, 31(1):91–96, 1993.

B. G. McLachlan and J. H. Bell. Pressure-sensitive paint in aerodynamic testing. *Experimental Thermal and Fluid Science*, 10(4):470–485, May 1995.

G. A Mitchell. Experimental investigation of the performance of vortex generators mounted in the supersonic portion of a mixed-compression inlet. TM X-2405, NASA, Nov 1971.

M. V. Morkovin. *Effects of Compressibility on Turbulent Flows*, pages 367–380. Mecanique de la turbulence. 1962.

M. J. Morris, M. Sajben, and J. C. Kroutil. Experimental investigation of normal-shock/turbulent-boundary-layer interactions with and without mass removal. *AIAA Journal*, 30(2):359–366, February 1992.

E. A. Mossman and F. A. Pfyl. An experimental investigation at mach numbers from 2.1 to 3.0 of circular-internal-contraction inlets with translating centrebodies. RM A56G06, NACA, Washington, 1956.

J. Müller, R. Mümmler, and W. Staudacher. Comparison of some measurement techniques for shock-induced boundary layer separation. *Aerospace Science and Technology*, 5(6):383–395, September 2001.

M. C. Neale and P. S. Lamb. Tests with a two-dimensional intake having all-external compression and a design mach number of 2.0. CP 937, Aeronautical Research Council, 1963.

H. E Neumann, L. A Povinelli, and R. E Coltrin. An analytical and experimental study of a short s-shaped subsonic diffuser of a supersonic inlet. TM 81406, NASA, 1980.

T.J. Nussdorfer. Some observations of shock-induced turbulent separation in supersonic diffusers. RM E51L26, NACA, May 1956.

L. J. Obery and R.W. Cubbinson. Effectiveness of boundary-layer removal near throat of ramp-type side inlet at free-stream mach number of 2.0. RM E54I14, NACA, 1954.

L. J. Obery, G.W. Englert, and T.J. Nussdorfer. Pressure recovery, drag and subcritical stability characteristics of conical supersonic diffusers with boundary-layer removal. RM E51H29, NACA, 1952.

D. Om, J. R. Viegas, and M. E. Childs. Transonic shock-wave/turbulent boundary-layer interactions in a circular duct. *AIAA Journal*, 23(5):707–714, May 1985.

K. Oswatitsch. Pressure recovery for missiles with reaction propulsion at high supersonic speeds. TM 1140, NACA, 1944.

W. R. Pauley and J. K. Eaton. Experimental study of the development of longitudinal vortex pairs embedded in a turbulent boundary layer. *AIAA Journal*, 26(7):816–823, 1988.

H. H. Pearcey. *Shock-Induced Separation and Its Prevention by Design and Boundary Layer Control*, volume 2 of *Boundary Layer and Flow Control*, pages 1170–1344. Pergamon Press, 1961.

F. A. Pfyl and E. C. Watson. An experimental investigation of circular internal compression inlets with translating centrebodies employing boundary-layer removal at mach numbers from 0.85 to 3.50. MEMO 2-19-59A, NASA, 1959.

T. G. Piercy and H. W Johnson. A comparison of several systems of boundary-layer removal ahead of a typical conical external-compression side inlet at mach numbers of 1.88 and 2.93. RM E53F16, NACA, 1953.

A. Pope and K. L. Goin. *High-Speed Wind Tunnel Testing*. John Wiley and Sons, Inc, 1st edition, 1965.

D. Rao and T. Kariya. Boundary-layer submerged vortex-generators for turbulent flow separation control - an exploratory study. AIAA-88-3546-CP, 1988.

L. R. Reneau, J. P. Johnston, and S. J. Kline. Performance and design of straight two-dimensional diffusers. *ASME Journal of Basic Engineering*, 89(Series D):151–160, 1967.

M. Rybalko, E. Loth, R. V. Chima, S. M. Hirt, and J. R. DeBonis. Micro-ramps for external compression low-boom inlets. Technical Report TM-2010-216351, NASA, May 2010.

Gas Turbine Engine Inlet Flow Distortion Guidelines, ARP 1420 rev. b. SAE S-16 Committee, 2002.

M. Sajben, M. J. Morris, T. J. Bogar, and J. C. Kroutil. Confined normal-shock/turbulent-boundary-layer interaction followed by an adverse pressure gradient. *AIAA Journal*, 29(12): 2115–2123, December 1991.

J. T. Salmon, T. J. Bogar, and M. Sajben. Laser doppler measurements in unsteady, separated, transonic diffuser flow. *AIAA Journal*, 21(12):1690–1697, 1983.

K. Sami. *Physics of three-dimensional normal shock wave/turbulent boundary layer interactions in rectangular channels*. PhD thesis, University of Cambridge, 2012.

H. Sams. F-15 propulsion system design and development. AIAA-75-1042, 1975.

W. G. Sawyer and C. J. Long. A study of normal shock-wave turbulent boundary-layer interactions at mach numbers of 1.3, 1.4, and 1.5. TR 82099, RAE, 1982.

W. H. Schofield. Turbulent-boundary-layer development in an adverse pressure gradient after an interaction with a normal shock wave. *Journal of Fluid Mechanics*, 154:43–62, 1985.

J. Seddon and E. L. Goldsmith. *Intake Aerodynamics*. Blackwell Publishing, 2nd edition, 1999.

J. W. Slater, D. O. Davis, B. W. Sanders, and L. J. Weir. Role of CFD in the aerodynamic design and analysis of the parametric inlet. ISABE 1168, 2005.

D.B. Smeltzer, R.H. Smith, and R.W. Cubbinson. Wind tunnel and flight performance of the YF-12 inlet system. *Journal of Aircraft*, 12(3):182–188, 1975.

N. E Sorenson and D. P Bencze. Possibilities for improved supersonic inlet performance. *Journal of Aircraft*, 11(5):288–293, 1974.

N. E Sorenson and D.B Smeltzer. Investigation of a large-scale mixed-compression axisymmetric inlet system capable of high performance at mach numbers of 0.6 to 3.0. Technical Memorandum X-1507, NASA, Washington, February 1968.

D. B. Spalding. A single formula for the law of the wall. *Journal of Applied Mechanics*, 28: 455–457, 1961.

E. Stanewsky, J.M. Delery, J. Fulker, and W. Geissler. Euroshock: Drag reduction by passive shock control. *Notes on Numerical Fluid Mechanics*, 56, 1997.

L. E. Stitt and R. J. Salmi. Performance of a mach 3.0 external-internal-compression axisymmetric inlet at mach numbers from 2.0 to 3.5. TM X-145, NASA, Washington, 1960.

B. S Stratford. An experimental flow with zero skin friction throughout its region of pressure rise. *Journal of Fluid Mechanics*, 5:17–35, January 1959.

C. Sun and M. Childs. A modified wall wake velocity profile for turbulent compressible boundary layers. *Journal of Aircraft*, 10(6):381–383, 1973.

L.E Surber and C.P Robinson. Survey of inlet development for supersonic aircraft. AIAA-83-1164, 1983.

J. Syberg and L. Surber. Performance variations in high aspect ratio subsonic diffuser due to geometric constraints in supersonic tactical aircraft inlet installations. AIAA-80-1066, 1980.

H. D. Taylor. Summary report on vortex generators. United Aircraft Research Department, Ref. R-05280-9, 1950.

E. Tjonneland. The design, development, and testing of a supersonic transport intake system. AGARD-CP-91-71, paper no. 18, 1971.

E. R. van Driest. Turbulent boundary layer in compressible fluids. *Journal of the Aeronautical Sciences*, 18(3):145–160, 1951.

Intake Aerodynamics, volume 1 & 2, 1988. VKI Lecture Series 1988-04, von Karman Institute For Fluid Dynamics.

J.F Wasserbauer, R.J Shaw, and H. E Neumann. Design of a very-low-bleed mach 2.5 mixed compression inlet with 45 percent internal compression. TM X-3135, NASA, March 1975.

J.F. Wasserbauer, E. T. Meleason, and P. L. Burstadt. Experimental investigation of the performance of a mach-2.7 two-dimensional bifurcated duct inlet with 30 percent internal contraction. TM 106728, NASA, May 1996.

F. M White. *Viscous Fluid Flow*. McGraw-Hill Science, 3 edition, 2006.

B. P. Willis and D. O. Davis. Boundary layer development downstream of a bleed mass flow removal region. AIAA-96-3278, July 1996.

K. G. Winter and L. Gaudet. Turbulent boundary-layer studies at high reynolds numbers at mach numbers between 0.2 and 2.8. R&M 3712, Aeronautical Research Council, 1970.

W. F. Wong. The application of boundary layer suction to suppress strong shock-induced separation in supersonic inlets. AIAA-74-1063, October 1974.

A. Zare Shahneh and F. Motallebi. Effect of submerged vortex generators on shock-induced separation in transonic flow. *Journal of Aircraft*, 46(3):856–863, 2009.